

Copyright
by
Yuannian Wang
2009

**The Dissertation Committee for Yuannian Wang Certifies that this is the approved
version of the following dissertation**

**THREE-DIMENSIONAL ROCK-FALL ANALYSIS WITH IMPACT
FRAGMENTATION AND FLY-ROCK MODELING**

Committee:

Fulvio Tonon, Supervisor

Jon Olson

Krishnaswamy Ravi-Chandar

Kenneth H. Stokoe II

Zip Zavodni

**THREE-DIMENSIONAL ROCK-FALL ANALYSIS WITH IMPACT
FRAGMENTATION AND FLY-ROCK MODELING**

by

Yuannian Wang, M.S.

Dissertation

Presented to the Faculty of the Graduate School of

The University of Texas at Austin

in Partial Fulfillment

of the Requirements

for the Degree of

Doctor of Philosophy

The University of Texas at Austin

August, 2009

Dedication

To my lovely wife Lili and my beautiful daughter Ivy

To my parents Yeliu Wang and Daoshi Li

To all my family

Acknowledgements

I wish to express my deep and sincere gratitude to many individuals. This thesis would not have been completed without their contribution.

First and foremost, I would like to express my deepest gratitude to my advisor, Dr. Fulvio Tonon, for his valuable advice, constant encouragement and patience throughout the course of this study; for his support for my academic research; for providing me state-of-art computing resource; for introducing me to the professional society; and for his care for me personally. It has been an honor for me to work for such a knowledgeable professor. I will forever benefit the experience working with him.

I am grateful for the help and guidance provided to me by my advisory committee members, Dr. Jon Olson, Dr. Krishnaswamy Ravi-Chandar, Dr. Kenneth H. Stokoe II, Dr. John L. Tassoulas, Dr. Stephen Wright, and Dr. Zavis Zavodni. I have learned a great deal from each of these individuals. I would also give thanks to the other geotechnical engineering faculty members at The University of Texas, Dr. Gilbert, Dr. Mohtar, Dr. Olson, Dr. Rathji, and Dr. Zornberg for their great lectures that broaden and deepen my knowledge in geotechnical engineering.

To Dr. Shihai Li, for introducing me to the world of discrete element modeling and geomechanis.

To Dr. Kagawa (late), for bringing me to USA and supervising my research on modeling soil liquefaction.

To Dr. Krishnaswamy Ravi-Chandar, for providing me with Dynamic Lab to perform SHPB test and for his valuable discussion.

To Dr. Haitao Zhang, for his help on conducting SHPB tests overnight and valuable discussion on the dynamic fragmentation.

To Xin Xiang, for his valuable work on neural network modeling.

I would like to thank Songcheng Li, Min Jae Jung, Jiabei Yuan, Heejung Yoon, Pooyan Asodalli, Ran Chen, Xiaoming You, Sang Yeon, Seo, Seung Han Kim, Yucao Tang, Rui Wei, Xiaowei Luo and many others who made my life easier and happier at Austin. Thanks are also extended to Chris Trevino, Teresa Tice-Boggs, Johnie Williams and John Hall for their administrative support.

This research was funded by Rio Tinto, whose financial support is gratefully acknowledged. Special acknowledgments are extended to Dr. Zavis Zavodni (Chief consultant geotechnical engineer for Rio Tinto) for his support during this research: he provided his expertise and experimental data and samples.

Finally, I am most grateful to my dear wife, and eternal companion, Lili. Her encouragement, support and love in my life cannot be quantified. She is such a wonderful mother and wife. I am also grateful to my little one, Ivy, who is such a lovely and understanding girl, bringing me a lot of joy. I would also give thanks to my parents, Yeliu Wang and Daoshu Li, and my parents-in-law, Yuhai Zhu and Xuemei Liu, for their consistent support and concern. Their trips to Austin have been especially enjoyable and helpful for Lili, Ivy and me. I am especially indebted to my late grandmother, Zhengying Cheng, who passed away before she could see my achievement she was always willing to see, for her love, concern and bringing up in my life.

Three-Dimensional Rock-Fall Analysis with Impact Fragmentation and Fly-Rock Modelling

Publication No. _____

Yuannian Wang, Ph.D.

The University of Texas at Austin, 2009

Supervisor: Fulvio Tonon

The dissertation details work aimed toward the development and implementation of a 3-D impact fragmentation module to perform rock fall analysis by taking into account impact fragmentation. This fragmentation module is based on a database of a large set of impact simulations using a fully calibrated discrete element model (DEM), and is employed to predict impact fragmentation processes in rockfall analysis by either training a neural network model or linearly interpolating the database.

A DEM was employed to model impact fragmentation in the study. A DEM code was developed from scratch. The model was first calibrated and verified with experimental results to demonstrate the capability of modeling both quasi-static and dynamic material behavior. Algorithms to calibrate the model's micro-parameters against triaxial tests on rocks were presented. Sensitivity analyses were used to identify the deformability micro-parameters by obtaining relationships between microscopic and macroscopic deformability properties. The strength model parameters were identified by a global optimization process aimed at minimizing the difference between computed and

experimental failure envelopes. When applied to the experimental results of tested granite, this calibration process produced a good agreement between simulated and experimental results for both deformability and strength properties.

Dynamic compression and SHPB tests were performed to verify the dynamic model. A strain-rate-dependent dynamic strength was observed in the experimental results. This strain-rate-dependent dynamic strength was also confirmed by the numerical results. No rate-dependent constitutive model was used in the DEM to simulate dynamic behavior. This simulated rate-dependent dynamic strength can be attributed to material inertia because the inertia inhibits crack growth.

Some fundamental mechanisms of impact fragmentation associated with rockfalls were then numerically investigated. The developed DEM code was coupled with a simplified impact model inspired by the theory of dynamic foundations. It has been shown that the magnitude of impact velocity, the angle of the incidence, the ground condition all play very important roles in impact fragmentation.

Several case studies were performed to validate the developed impact fragmentation module in rock fall analysis. It has been demonstrated that the developed fragmentation module can reasonably predict impact fragmentation and perform some risk analysis in rock fall analysis.

Table of Contents

List of Tables	xiv
List of Figures	xv
Chapter 1 Introduction	1
1.1 Overview	1
1.1.1 Rockfall Analysis	1
1.1.2 Rockfall Fragmentation	3
1.1.3 Discrete Element Modeling	5
1.2 Motivation	7
1.3 Expected Contributions	8
1.4 Research Plan	9
Chapter 2 3-D Discrete Element Method	11
2.1 Introduction	11
2.2 Packing	11
2.3 General Formulation	14
2.3.1 Calculation Cycle	14
2.3.2 Force-Displacement Law	15
2.3.2.1 Normal Force Calculation	17
2.3.2.2 Shear Force and Moment Calculation	17
2.3.3 Failure Criteria	21
2.3.4 Equations of Motion	24
2.4 Timestep Determination	24
2.5 Damping	25
2.6 Wave Motions	28
2.7 Computational Time	31
Chapter 3 DEM Model Calibration	34
3.1 Introduction	34
3.2 Model Parameters	35

3.2.1 Deformability Parameters	35
3.2.2 Strength Parameters	38
3.3 Numerical Setup.....	38
3.3.1 Membrane Boundary for Applying Confining Pressure.....	39
3.3.2 Comparisons between Rigid and Membrane Boundaries.....	43
3.3.3 Simulation Procedures for Triaxial Tests	48
3.4 Static Calibration	49
3.4.1 Experimental Results	49
3.4.2 Identification of Micro Deformability Parameters	52
3.4.3 Identification of Micro Strength Parameters.....	56
3.4.4 Comparisons against PFC's BPM Model	64
3.4.5 Discussions on Model Calibration	68
3.5 Verification of dynamic problems	73
3.5.1 Introduction.....	73
3.5.2 Dynamic Tests	75
3.5.2.1 Dynamic Compression Tests	75
3.5.2.2 Split Hopkinson Pressure Bar Tests.....	77
3.5.2.2.1 Experimental Setup and Data.....	79
3.5.3 Verification of Dynamic Model with Dynamic Compression and SHPB Tests	85
3.5.3.1 Numerical Simulation of Compression Tests	86
3.5.3.2 Numerical Simulations of SHPB Tests.....	90
3.5.4 Fragment Size Distribution	92
3.5.4.1 Introduction.....	92
3.5.4.2 Fragmentation Detection in DEM Modelling	93
3.5.4.3 Results of Fragment Size Distributions	95
Chapter 4 Modeling Rock Fragmentation upon Impact	98
4.1 Introduction	98
4.2 Model of the Interaction between Rock Blocks and the Ground.....	98
4.3 Investigation on Mechanism of Impact Fragmentation	102
4.3.1 Model Setup.....	102

4.3.2 Effect of Impact Velocity.....	103
4.3.2.1 Magnitude of Impact Velocity	103
4.3.2.2 Incidence Angle	107
4.3.3 Effect of Ground Condition	109
4.3.4 Effect of Fracture Properties of Rock Block.....	112
4.3.4.1 Persistence.....	113
4.3.4.2 Fracture Aperture	115
4.3.4.3 Fracture Orientation	116
4.3.5 Energy Loss during Impact and Dynamic Interaction with the Ground	117
4.4 Conclusion	122
Chapter 5 Fragmentation Module	123
5.1 Introduction	123
5.2 Simulation Database Preparation.....	123
5.3 Neural Network Model	127
5.3.1 Overview.....	127
5.3.2 Multi-layer Feed Forward NN	128
5.3.2.1 Neuron Model	128
5.3.2.2 Network Architecture.....	129
5.3.2.3 Neural Network Training.....	131
5.3.3 Input and Output Neurons.....	131
5.3.4 Training and Testing Network	132
5.3.5 Performance of Trained Neural Networks	134
5.3.5.1 Performance of the First Stage NN Prediction	134
5.3.5.2 Performance of the Second Stage NN Prediction	134
5.4 Interpolation Method	138
5.4.1 Multilinear Interpolation.....	138
5.4.2 Performance	138
5.5 Fragmentation Module.....	141
5.5.1 Overview.....	141
5.5.2 Input and Output	141

5.5.3 Preprocessor	143
5.5.4 Postprocessor	144
Chapter 6 Case studies	145
6.1 Introduction	145
6.2 California Rockfall Tests	145
6.2.1 Overview	145
6.2.2 Model Calibration	148
6.2.3 Rockfall Analysis using HY-STONE	151
6.2.3.1 Input Data.....	152
6.2.3.2 Kinematic Modeling	153
6.2.3.3 Natural Variability and Uncertainty in the Input Data.....	154
6.2.3.4 Results.....	155
6.3 Rossing Drop Tests	161
6.3.1 Overview	161
6.3.2 Model Calibration	162
6.3.3 Impact Simulations	164
6.3.4 Conclusion	168
6.4 Argyle Rockfall Event	169
6.4.1 Introduction.....	169
6.4.2 Model Calibration for Intact Rock.....	171
6.4.3 Model Calibration for Equivalent Continuum Model.....	173
6.4.4 Impact Simulation.....	176
6.5 Improvement on Fragment Size Distribution	178
6.5.1 Rolling Stiffness and Strength Disorder	179
6.5.2 Fragment Size Distribution	180
6.6 Conclusion	180
Chapter 7 Conclusions and Recommendations.....	182
7.1 Overall Conclusions	182
7.2 Recommendations for Future Work.....	185

Appendix.....	187
Appendix A Transformation matrix.....	187
Appendix B Uniaxial Compressive Test Data on Sandstone for California Rockfall Tests	189
Appendix C Results Of Uniaxial Compression Tests with Elastic Modulus and Poisson’s Ratio Measurements by Means of Strain Gauges.....	190
References.....	191
Vitae	199

List of Tables

Table 3-1:	Model parameters used in simulations with membrane boundary and rigid boundary	44
Table 3-2:	Results of triaxial tests	50
Table 3-3:	Model parameters used in the simulations	56
Table 3-4:	Macro-properties of experimental and simulated results	56
Table 3-5:	Macro-properties of Lac du Bonnet granite	66
Table 4-1:	Number of fragments of different magnitude of impact velocity under normal incidence	104
Table 4-2:	Fragmentation of different incidence angles with the magnitude of impact velocity of 50 m/s	109
Table 4-3:	Fragmentation of different ground conditions under normal incidence	110
Table 5-1:	Comparisons of simulated impact fragmentation for two different sizes of block	125
Table 5-2:	Input parameters for impact simulations	127
Table 6-1:	Input data used for HY-STONE rockfall model in California case study	152

List of Figures

Figure 1-1: Front view of incident area and sketch of rockfall trajectories; A rock fall fatality happened on October 29th in 2003 at an open-cut mine in Mantos Blancos, Chile (from a report provided by Zavis Zavodni)...	4
Figure 1-2: The impact fragment striking the vehicle and causing the fatality; a rockfall fatality happened on October 29th in 2003 at an open-cut mine in Mantos Blancos, Chile (from a report provided by Zavis Zavodni)	4
Figure 1-3: Sketch of rockfall analysis with impact fragmentation.....	8
Figure 2-1: The 1 st step: Randomly generate 2500 spheres with artificially small radii in to prepare a cylindrical specimen with a radius of 25 mm and height of 100 mm	13
Figure 2-2: The 2 nd step: Expand each sphere to obtain a specific porosity with large overlapping	13
Figure 2-3: The 3 rd step: Cycle the spheres using a simple DEM model to obtain equilibrium	14
Figure 2-4: DEM calculation cycle employed in the developed code used for the research	15
Figure 2-5: Constitutive model of contact used in the developed code.....	16
Figure 2-6: Rotations of contact plane used in determination of contact shear forces (in 2D): (a) The 1 st rotation, and (b) The 2 nd rotation	18
Figure 2-7: Tensile failure criterion used in the developed code (modified after Donze (Hentz 2004)).....	22

Figure 2-8: Shear failure criterion used in the developed code (modified after Donze (Hentz 2004))	23
Figure 2-9: Effect of numerical damping on material behavior. Cylindrical specimen with a height of 3.2 cm and 1.6 cm diameter consisting of 2500 spheres; $E_c = 104.7 \text{ GPa}$, $K_s / K_n = 0.085$, $c = 429 \text{ MPa}$, $\varphi = 68^\circ$, $T = 34.2 \text{ MPa}$, and coefficient of interaction range of 1.3	26
Figure 2-10: Displacement vector fields for different numerical damping. Cylindrical specimen with a height of 3.2 cm and 1.6 cm diameter consisting of 2500 spheres; $E_c = 104.7 \text{ GPa}$, $K_s / K_n = 0.085$, $c = 429 \text{ MPa}$, $\varphi = 68^\circ$, $T = 34.2 \text{ MPa}$, and coefficient of interaction range of 1.3	27
Figure 2-11: Sketch of position of monitored particles in a cylindrical specimen (5 cm in diameter and 10 cm in height) consisting of 1,500 spheres	29
Figure 2-12: Histories of particle motions in the axial direction during the elastic stage (no contact failures)	30
Figure 2-13: Histories of particle motions in the axial direction at failure (many contact failures occur)	30
Figure 2-14: Effect of cell number on simulated results for triaxial tests. Cylindrical specimen with a height of 3.2 cm and 1.6 cm diameter consisting of 2500 spheres; $E_c = 104.7 \text{ GPa}$, $K_s / K_n = 0.085$, $c = 429 \text{ MPa}$, $\varphi = 68^\circ$, $T = 34.2 \text{ MPa}$, and coefficient of interaction range of 1.3	32
Figure 2-15: Computational time versus cell number. Cylindrical specimen with a height of 3.2 cm and 1.6 cm diameter consisting of 2500 spheres; $E_c = 104.7 \text{ GPa}$, $K_s / K_n = 0.085$, $c = 429 \text{ MPa}$, $\varphi = 68^\circ$, $T = 34.2 \text{ MPa}$, and coefficient of interaction range of 1.3	32

Figure 3-1: Sketch of deriving contact spring constant	36
Figure 3-2: Contact spring constant for different sphere sizes	37
Figure 3-3: Boundary particles identification using a cell algorithm in modeling membrane boundary for applying confining pressure	42
Figure 3-4: Results of identified boundary particles at post-peak stage for different boundaries: (a) Membrane boundary, and (b) Rigid boundary.....	43
Figure 3-5: Comparison of stress-strain curves between membrane boundary and rigid boundary conditions	44
Figure 3-6: Positions of boundary particles shown on a squeezed axial-radial plane for two different boundaries: (a) Rigid boundary, and (b) Membrane boundary	45
Figure 3-7: Confining pressures applied to individual boundary particles for two different boundary conditions: (a) Membrane boundary, and (b) Rigid boundary	46
Figure 3-8: Experimental failure envelope of granite used for DEM model calibration	51
Figure 3-9: Failure pattern (split) in uniaxial compression tests on granite	51
Figure 3-10: Failure pattern (shear) in triaxial compression tests on granite	52
Figure 3-11: The relationship between macro elastic properties and E_c	53
Figure 3-12: The relationship between macro elastic properties and K_s / K_n	54
Figure 3-13: Fitting results: material's Young's modulus vs. K_s / K_n	55

Figure 3-14: Fitting results: material's Poisson's ratio vs. K_s / K_n	55
Figure 3-15: Calibrated strength envelope using a global optimization method compared against the experimental one	58
Figure 3-16: Flow-chart of the inverse method for strength parameters identification using the global optimization package SNOBFIT	59
Figure 3-17: Simulated stress-strain curves using the calibrated model	61
Figure 3-18: History of contact failures during a simulated uniaxial compressive test with the calibrated model	63
Figure 3-19: Mobilization of the strength components (after ref. (Hajiabdolmajid et al. 2002))	63
Figure 3-20: Comparison against PFC's BPM model in calibrating Lac du Bonnet granite	66
Figure 3-21: Simulated stress-strain curves using the calibrated model	69
Figure 3-22: Effect of particle size on simulated macro properties: (a) Dependence of Young's modulus on particle size, and (b) Stress-strain curves for different mean particle sizes	71
Figure 3-23: Effect of random distribution of particles on simulated material behavior in DEM modeling	72
Figure 3-24: Regime of strain rates for different loading conditions (after (Hentz et al. 2004))	73
Figure 3-25: Strain rate effect on dynamic uniaxial compressive strength (after (Hentz et al. 2004))	74

Figure 3-26: Effect of strain rate on dynamic strength of dynamic compression tests: (a) Stress histories of different strain rates, and (b) Relationship between dynamic strength and strain rate	76
Figure 3-27: Fragmentation under different strain rates in dynamic uniaxial compression tests	77
Figure 3-28: Sketch of SHPB test setup used to determine material's dynamic properties at high strain rates	78
Figure 3-29: Failure process recorded by a high-speed camera for the test with stain- rate of 53.4 s^{-1}	80
Figure 3-30: Failure process recorded by a high-speed camera for the test with stain- rate of 80.1 s^{-1}	81
Figure 3-31: Recorded strain histories for the test with 300 kPa controlling pressure generating an average strain rate of 53.4 s^{-1}	82
Figure 3-32: Recorded strain histories for the test with 450 kPa controlling pressure generating an average strain rate of 80.1 s^{-1}	83
Figure 3-33: Calculated force histories applied on the input bar head at two different strain rates	83
Figure 3-34: Calculated force histories applied on the output bar end at two different strain rates	84
Figure 3-35: Calculated particle velocity histories at the input bar end at two different strain rates	84
Figure 3-36: Calculated particle velocity histories at the output bar head at two different strain rates	85

Figure 3-37: Effect of strain rate on dynamic strength observed from both experimental and numerical results	86
Figure 3-38: Stress-strain curves for different applied strain rates (both stresses on top end and on bottom end were recorded as indicated in the figures)...	88
Figure 3-39: Failure evolution by monitoring contact failures at different stages corresponding to the simulation case (c) in Figure 3-38. The black points represent locations of failed contacts.	89
Figure 3-40: Strain-rate dependent dynamic strength for both experimental results and simulated results in modeling dynamic compression tests with a 600-sphere packing	90
Figure 3-41: Numerical and experimental SHPB stress-strain curves for the strain rate of 53.4 s^{-1}	91
Figure 3-42: Numerical and experimental SHPB stress-strain curves for the strain rate of 80.1 s^{-1}	92
Figure 3-43: Flowchart of fragmentation block detecting scheme in DEM modeling	94
Figure 3-44: Detected fragments after a simulated impact (some very tiny fragments are not shown).....	95
Figure 3-45: Normalized size distributions for the generated fragments in dynamic tests at different strain rates	96
Figure 3-46: Normalized fragment size distributions and fitted curves with two-parameter Weibull equation for different strain rates	97
Figure 3-47: Comparison of experimental and numerical fragment size distributions at different strain rates	97

Figure 4-1: Surface motion due to a transient point source (after (F. E. Richart 1970)).....	99
Figure 4-2: Sketch of impact model with springs and dashpots attached to each impacting particle in both normal and shear directions to simulate dynamic interactions between rock block and the ground.....	101
Figure 4-3: Fragmentations of different magnitude of impact velocity after the block (in green) bouncing off the ground (in white)	105
Figure 4-4: Histories of impact stress and system kinetic energy for different impact velocities	106
Figure 4-5: Fragmentation, and histories of impact stress and system kinetic energy for different incidence angles.....	108
Figure 4-6: Fragmentation, and histories of impact normal stress and system energy for different ground conditions under normal incidence	111
Figure 4-7: Impact of homogeneous rock block on the ground after the block (in green) bouncing off the ground (in white).....	112
Figure 4-8: Sketch of “X” and “+” shape fractures in a spherical block used for numerically investigating the effect of fracture patterns on impact fragmentation	113
Figure 4-9: Impact fragmentation for different fracture persistence after the block (in green) bouncing off the ground (in white): (a) 80% persistence (46 fragments), (b) 90% persistence (55 fragments), and (c) 100% persistence (196 fragments)	114
Figure 4-10: Impact fragmentation for opening fractures with 80% persistence after the block (in green) bouncing off the ground (in white).....	116

Figure 4-11: Impact fragmentation for different persistence of “+” shape fractures after the block (in green) bouncing off the ground (in white): (a) 90% fracture persistence with 224 fragments (“+” shape), and (b) 100% fracture persistence with 317 fragments (“+” shape)	117
Figure 4-12: System energy transformation and energy loss due to failure and geometric damping during impact	120
Figure 4-13: Histories of impact stresses resulted from spring and dashpot in normal direction for different ground conditions	121
Figure 5-1: Comparisons of simulated stress-strain curves of uniaxial compression test for two different scales of specimen.....	124
Figure 5-2: A neuron with vector input used in neural network model.....	128
Figure 5-3: A typical multi-layer feed forward NN with two hidden layers	129
Figure 5-4: A multi-layer neural network	130
Figure 5-5: Convergence characteristics of training for the two neural networks: (a) First stage prediction with 27 hidden neurons, and (b) Second stage prediction with 20 hidden neurons.....	133
Figure 5-6: Network performance for the number of fragments in the first trained neural network	135
Figure 5-7: Network performance for the mass of the largest fragment (the 1 st output) in the 2 nd trained neural network	135
Figure 5-8: Network performance for the V_z component of the largest fragment (the 2 nd output) in the 2 nd trained neural network	136

Figure 5-9: Statistic distribution of fragment mass in the database of impact simulation.....	137
Figure 5-10: Statistic distribution of fragments velocity component in the Z direction in the database of impact simulation.....	137
Figure 5-11: Performance of interpolation method for the number of fragments (1 st output)	139
Figure 5-12: Performance of interpolation method for the mass of the largest fragment (2 nd output)	140
Figure 5-13: Performance of interpolation method for the velocity component in Z direction of the largest fragment (3 rd output)	140
Figure 6-1: 3D topographic map of the test site in Brisbane, CA with the sketch of two cross-sections used for dropping tests.....	146
Figure 6-2: Geological map of the test site in Brisbane, CA.....	146
Figure 6-3: Cross section of F-F' for dropping tests	147
Figure 6-4: Cross section of G-G' for dropping tests	147
Figure 6-5: Material properties of generalized sandstone with RockData	149
Figure 6-6: Calibrated and experimental failure envelopes of sandstone for California case study.....	151
Figure 6-7: Full view (NE) of simulated 3D rockfall trajectories with activating fragmentation along cross-section FF' using HY-STONE	156
Figure 6-8: Front view of simulated 3D rockfall trajectories with activating fragmentation along cross-section FF' using HY-STONE. Trajectories are represented as points, classified by translational velocity.	157

Figure 6-9: Front view of simulated 3D rockfall trajectories without activating fragmentation module along cross-section FF' using HY-STONE. Trajectories are represented as points, classified by translational velocity.....	157
Figure 6-10: NE-view of simulated 3D rockfall trajectories with activating fragmentation module along cross-section FF' using HY-STONE. Trajectories are represented as points, classified by translational velocity.....	158
Figure 6-11: Full view (NE) of simulated 3D rockfall trajectories with activating fragmentation along cross-section FF' using HY-STONE	158
Figure 6-12: Top view of simulated 3D rockfall trajectories with activating fragmentation module along cross-section FF' using HY-STONE. Trajectories are represented as points, classified by translational velocity.....	159
Figure 6-13: Top view of simulated 3D rockfall trajectories without activating fragmentation module along cross-section FF' using HY-STONE. Trajectories are represented as points, classified by translational velocity.....	159
Figure 6-14: N-view of simulated 3D rockfall trajectories with activating fragmentation module along cross-section FF' using HY-STONE. Trajectories are represented as points, classified by translational velocity.....	160
Figure 6-15: N-view of simulated 3D rockfall trajectories without activating fragmentation module along cross-section FF' using HY-STONE. Trajectories are represented as points, classified by translational velocity.....	160

Figure 6-16: Average height of flying fragments of each cell with activating fragmentation module along cross-section FF'	161
Figure 6-17: Testing arrangement for Rossing dropping tests.	162
Figure 6-18: Experimental and calibrated failure envelopes for the high-bound properties.....	164
Figure 6-19: Experimental and calibrated failure envelope for the lower-bound properties.....	165
Figure 6-20: Simulated high-bound marble block after bouncing off the ground for dropping onto the scree-covered surface	166
Figure 6-21: Simulated high-bound marble block after bouncing off the ground for dropping onto the hard rock surface.	166
Figure 6-22: Simulated low-bound marble block after bouncing off the ground for dropping onto the scree-covered surface.	167
Figure 6-23: Simulated low-bound marble block after bouncing off the ground for dropping onto the hard rock surface.	168
Figure 6-24: Rock fall damage to Motor Control Center with impact fragmentation at an Argyle mine	169
Figure 6-25: Location of rockfall incident with possible impact point	170
Figure 6-26: An oblique view of the local site of the rockfall incident.....	171
Figure 6-27: A CT scanned cross section of the tested quartzite sample	172
Figure 6-28: Experimental and calibrated of failure envelopes of the tested intact quartzite sample	173

Figure 6-29: Material properties of quartzite rock mass obtained based on intact rock properties and characterization of fractured rock	174
Figure 6-30: Comparison between the calibrated and generalized failure envelopes for fractured quartzite	175
Figure 6-31: Sketch of impact simulation with coordinate reference system.....	176
Figure 6-32: Simulated intact block rolling down a slope and impacting against a horizontal placed big boulder.....	177
Figure 6-33: Simulated equivalent fractured block rolling down a slope and impacting against a horizontal placed big boulder	178
Figure 6-34: Fragmentation size distribution of simulated rock impact using improved model with rolling stiffness	181

CHAPTER 1 INTRODUCTION

1.1 OVERVIEW

Rock fall is a common natural hazard causing sometimes loss of life and significant damage to infrastructures, such as roads, construction sites, working faces in open pit mines and so on. Rock fall mitigation measures, such as restraining nets, catch benches and other protection barriers, are thus important in protecting highways, construction sites and working faces. In order to design effective rock fall mitigations, it is necessary to understand the rock fall dynamics, such as rock fall trajectory, bouncing height, kinetic energy of boulders and impact fragmentation.

1.1.1 Rockfall Analysis

Depending on the initiation of the detached rock block and the geomorphic conditions of the slope, a rock fall trajectory is the combination of three main processes, namely: sliding or rolling, free falling and impact. These processes are controlled by well-known physical laws and can be described by simple equations and hence easily simulated if these processes are free of fragmentation. However, if fragmentation occurs during the rock falling, the process will be much more complicated to simulate.

Generally, there are two approaches to evaluate rock fall dynamics: experimental methods and numerical analyses (Agliardi and Crosta 2003; An and Tannant 2007; Bozzolo and Pamini 1986; Crosta 2003; Dorren 2003; Giacomini et al.; Giani et al. 2004; Mougin et al. 2005; Nocilla et al. 2008). Experimental methods include field tests and empirical studies. Usually, field tests are carried out to determine rock fall trajectories and runout distances, and sometimes to evaluate the efficiency of protective measures. Field test is undoubtedly effective, but it is expensive and time-consuming. It is also

impossible to test many scenarios: initial conditions (velocity, mass, location), natural and design topography and ground properties. Therefore, field tests are typically used to calibrate numerical models. By using the calibrated numerical models, statistical and parametric analyses may be performed to improve the understanding of rock fall events. Numerical analysis mainly focuses on the evaluation of the trajectories of detached blocks for different morphological and geologic conditions. It becomes increasingly popular and powerful because of the development of computer technology and relevant information technology.

Several computer programs either in 2D and 3D have been developed and tested for rockfall analysis (Guzzetti et al. 2002). Most of the programs implement either a lumped mass or a rigid body approach. Despite the fact that impact fragmentation and its relevant fly-rock have often been cause of damage and unexpected accidents, so far, there are no programs which can simulate rockfall with a function of modeling rock fragmentation.

The program STONE is a three-dimensional simulation program that can produce simple maps useful to assess rockfall hazard; it uses GIS technology to manipulate existing thematic information available in digital format. The program requires as input a digital terrain model, the location of rock-fall detachment areas, the dynamic friction coefficient used to simulate the loss of velocity during rolling, and the coefficients for normal and tangential energy restitution at the impact points (Guzzetti et al. 2002). STONE has been extensively verified and then validated using actual case histories ranging in scale from the local to the regional (Agliardi and Crosta 2003; Crosta 2003; Guzzetti et al. 2002). However, like all other rockfall analysis tools, STONE cannot take into account impact fragmentation and analyze its potential hazard.

With a good understanding of rock fall dynamics for a specific site condition, different mitigation measures may be designed against rock fall, such as rock restraining nets, catch walls and deformable barriers. Generally, the design of the defense system is determined on the basis of the estimated rock fall trajectories, of their energy and of the identified arrest areas.

1.1.2 Rockfall Fragmentation

Rock fragmentation is frequently observed during rock fall events. However, rock fragmentation upon impact is usually not accounted for in the design of a defense structure. This lack of consideration explains why the study of fragmentation is still in its early age despite it being a natural and frequent phenomenon. Fragmentation can be facilitated by the presence of discontinuities in the boulders and by high impacting energy and rigid ground conditions. The trajectories of rock fragmentation are much different from that of the intact block (used to design the barrier) and are more difficult to predict with an increase in the risk of causing damage to properties and lives. Agliardi and Crosta (Agliardi and Crosta 2003) have experimentally observed that “the smaller rock fragments are characterized by observed velocities greater than the computed maximum velocities” and that “the high observed velocities could be due to the momentum increase occurring as a consequence of fragmentation at impact”.

A rock fall fatality happened on October 29th in 2003 at an open-cut mine in Mantos Blancos, Chile. As shown in Figures 1-1 and 1-2, a rock block from a waste dump was initiated and fell down. It impacted against a bench and fragmented. One of the projectile fragments struck a light vehicle on the driver’s side on the door pillar, entering through the windows and striking the driver.



Figure 1-1. Front view of incident area and sketch of rockfall trajectories; a rockfall fatality happened on October 29th in 2003 at an open-cut mine in Mantos Blancos, Chile (from a report provided by Zavis Zavodni)



Figure 1-2. The impact fragment striking the vehicle and causing the fatality; a rockfall fatality happened on October 29th in 2003 at an open-cut mine in Mantos Blancos, Chile (from a report provided by Zavis Zavodni)

There is a real need to improve our understanding of fragmentation mechanisms in order to strengthen the protection against rock fall. In particular, predicting the possible size, shape and number of fragments generated under impact is fundamental to design more efficient protection systems.

1.1.3 Discrete Element Modelling

The behavior of rock is oftentimes complex, with a nonlinear failure envelope, a high ratio of uniaxial compression strength to tensile strength (Hoek 1983), and a strain-rate dependent dynamic strength. Currently, it is very difficult, if not impossible, to fully model this complex behavior, which has a complicated failure evolution process. Discrete element method (DEM) is a popular tool used in modeling rock behavior, because it can deal with the material failure naturally by modeling failure evolutionary process from micro crack to macro failure without any complex constitutive models. As a result, DEM is chosen to model the rock fragmentation upon impact in rock fall analysis.

DEM can be generally viewed (Cundall and Hart 1992) as a method that allows finite displacements and rotations of discrete bodies, and updates contacts automatically as the calculation progresses. The original application of DEM by Cundall and Strack (Cundall and Strack 1979) was to perform research into the behavior of granular material and blocky rock systems (Cundall 1971). Then it has been extended to solid mechanics to investigate the failure process of bonded geomaterials, like intact rock (Hajiabdolmajid et al. 2002; Potyondy and Cundall 2004) and concrete (Hentz et al. 2004a). Nowadays, DEM is widely used in geomechanics from soil (particulate type) to intact rock (relatively continuum type), to rock masses (assemblies of blocks) with applications in many areas, such as rock engineering, soil mechanics, mining and petroleum engineering (Cho et al. 2007; Cook 2004; Cundall and Strack 1979; Donze et al. 1997; Ng 2006;

Olson et al. 2002; Onate and Rojek 2004; Pierce et al. 2007). In modeling particulate materials, the element used in the model can be viewed as representing the true material particle. When modeling the behavior of intact rock, the elements used in the model do not represent the actual material particle size and the elements are bonded to each other with a specific strength.

While the method is versatile and attractive, it requires extensive calibration work. The calibration process in DEM includes parameter identification for both deformability and strength. Before modeling a specific case, the specimen should be prepared with specific micro parameters to be determined for a given packing so as to closely reproduce the specific macro material properties.

So far, there has been no satisfactory way to calibrate the DEM model in order to reproduce the complicated behavior of material like rock and deploy the versatility of DEM. Using sensitivity analysis, most of the researchers investigate the effect of one individual parameter (or a combined dimensionless parameter) while keeping other variables fixed, and then a general formula to determine micro-scale parameters based on specific macro material properties is determined (Fakhimi and Villegas 2007; Yoon 2007). Based on the author's investigation, when identifying micro deformability parameters, the problem is relatively simple and sensitivity analysis can be applied. However, when identifying micro strength parameters, the problem involves micro crack propagation, and hence it is more complicated. Indeed, the individual trend of one strength parameter may not be directly obtained by just fixing the values of all the other parameters since these parameters may not be independent. In Particle Flow Code (PFC) (Itasca 1999), for example, uniaxial compressive tests are used to reproduce the deformability behavior and the uniaxial compressive strength: as the authors note (Potyondy and Cundall 2004), "It should be noted that our current understanding of this

calibration process is still incomplete — i.e., we still do not know how to construct a PFC material that reproduces a given strength envelope or one that reproduces a given ratio of unconfined compressive strength to Brazilian tensile strength ...”.

In order to accurately model impact induced rock fall fragmentation, dynamic properties, such as strain-rate dependency, must be accounted for. So far, little work has been done on the simulations of dynamic properties of brittle materials, like rock, in DEM modeling. Hentz and his coworkers (Hentz et al. 2004a; Hentz et al. 2004b) have investigated the behavior of concrete subjected to dynamic loading using DEM in a very high level of strain rate. However, the model calibration process was not well defined; and the verification of the dynamic model was only limited to a relatively small range of high strain rate (350~700 sec.⁻¹).

1.2 MOTIVATION

Although, rock fragmentation is frequently observed during rock fall events and several authors have raised issues related to the impact of fragments on protection structures (Giacomini et al.; Mougín et al. 2005; Nocilla et al. 2008), this phenomenon is not accounted for when designing the rock fall mitigation measures. The impact fragmentation of falling rock (as shown in Figure 1-3 may increase the possibility of damage and the difficulties in predicting and preventing rock fall fatalities. In open pit mines, impact fragmentation of falling rock blocks and relevant fly-rock pose a daily hazard and have caused loss of life and property damage. Due to the complexity of impact fragmentation, it is still poorly understood and very few useful contributions can be found in the literature (Chau K.T. 2003; Zhang et al. 2000). An improvement in understanding the mechanism of rock fragmentation upon impact is of great need. Current rock fall analysis tools cannot account for impact fragmentation (Agliardi and

Crosta 2003; Guzzetti et al. 2002), which drive us to investigate the fundamental mechanism governing the impact induced rock fragmentation, and to develop a three-dimensional rock-fall analysis system that can take into account impact fragmentation and fly-rock.

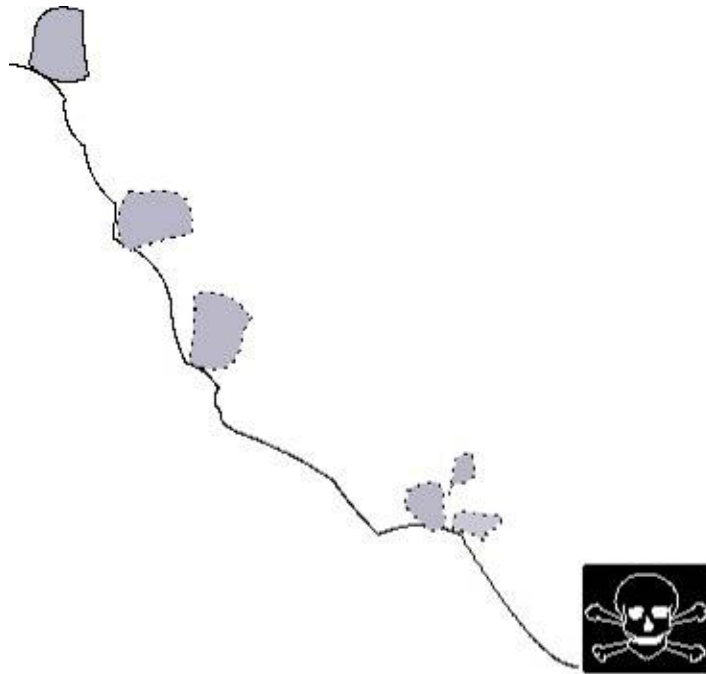


Figure 1-3. Sketch of rockfall analysis with impact fragmentation

1.3 EXPECTED CONTRIBUTIONS

The expected contributions of the proposed study include:

- 1) To enhance the understanding of the fundamental mechanism of impact induced rock fragmentation and its effect on post-impact rockfall process;

- 2) To deliver a state-of-the-art rockfall analysis system to take into account impact fragmentation and fly-rock, which will help property owners take control and alleviate the loss of life from rockfalls;
- 3) To provide some valuable advice on rockfall management.

1.4 RESEARCH PLAN

The work focuses on the development of a rock fragmentation model to investigate the fundamental mechanism that governs the process of impact fragmentation and its influence on post-impact rockfall process.

A new module that models impact fragmentation will be developed and added to the existing three-dimensional rock-fall analysis system HY-STONE developed by Dr. Giovanni Crosta and co-workers (Bicocca University, Milan, Italy). The new module is a neural network model trained with the simulation results of sphere impacts using a newly developed Discrete Element Model (DEM) code. The new module will be fully validated using laboratory and field tests.

The new module is essentially a trained neural network which can determine the mass and velocities of the fragments right after impact. Because running a DEM simulation of each block's impact will excessively slow down the HY-STONE execution time, a very large set of DEM impact simulations to train the neural network will be analyzed beforehand using high-performance computing systems at UT Austin. This set of simulations will use possible input ranges occurring in practical rock fall cases, such as impact velocity, rock properties and ground conditions. The trained neural network will be then used to predict the fragmentation when an impact happens during a rockfall analysis. Each fragment's subsequent trajectory will be then determined by the existing STONE algorithm.

The key work is to develop a DEM impact model and investigate the fundamental mechanics of impact fragmentation. The DEM model has been developed from scratch and is being validated with experimental results. The validated model can then be extended to simulate some case histories with impact fragmentation to demonstrate the capability of predicting the fragmentation during rockfall impact. With these fully verified DEM model, a large set of simulations will be performed to account for different possible scenarios by varying material properties of rock block, dynamic characteristics of impact and ground conditions. Each simulation will record the information on fragmentation after impact, such as number of fragments, mass and velocities of each fragment. The neural network will be implemented and trained with these simulation results.

CHAPTER 2: 3-D DISCRETE ELEMENT METHOD

2.1 INTRODUCTION

The Discrete Element Method (DEM), originally developed by Cundall and Strack (Cundall and Strack 1979) has proved to be a powerful tool in modeling the behavior of geomaterials especially for those characterized by some discontinuous units like jointed rock or directly at the particle level like soils. The method has also been recognized as a very useful tool to model the process of failure evolution, i.e. behavior from continuum to discontinuum. A large amount of research has been devoted to such problems including failure of concrete (Hentz et al. 2004b), and fragmentation of rock and other quasi-brittle materials due to blasting or high-speed impact (D'Addetta et al. 2001; Donze et al. 1997; Whittles et al. 2006).

The DEM discretizes a material into a system consisting of either rigid or deformable elements, which are typical in shape of a sphere (disc in 2D), but polyhedra (polygons in 2D) have also been used. This method is typically an ideal tool when dealing with problems which are inaccessible to traditional continuum-based numerical approaches such as finite differences and finite elements. In contrast to these continuum-based methods, the DEM shows particular advantages in investigating the failure mechanism in terms of micromechanics.

2.2 PACKING

Sphere packing is used to generate particle in a given domain to prepare virtual specimens. It is always important to DEM modeling as both the packing degree and the size distribution of particles will affect the ultimate assembly (rock material) behavior.

Several types of sphere packing approaches were compared, like CRP (Close Random Packing) (Jodrey 1985) and radii expansion (Itasca 1999) used in PFC. Among these alternatives, radius expansion method is fast, can produce dense packing of arbitrary shape, and was finally selected as the method for sphere packing. A brief idea about radius expansion packing method is introduced as follows.

A population of spheres with their radii distributed according to a Gaussian distribution is first generated with the specified upper and lower radius values corresponding to plus-and-minus one standard deviation, respectively, from the mean radius. The mean radius, R_m , is calculated to meet the specified porosity as

$$R_m = \frac{3(1-n)V}{4N\pi}, \quad (2-1)$$

where N is the number of spheres, n is the desired porosity, and V is the total volume of the container. Then, these spheres are shrunk artificially to smaller sizes and placed randomly within the specified volume; this packing has a larger porosity, n_0 . It is easy to place small-radius spheres in this manner, because the available void space is large. The spheres are then expanded to obtain the desired porosity, in which all radii are multiplied by a radius multiplier, m , in order to change the porosity from n_0 to n . The radius multiplier can be calculated as

$$m = \left(\frac{1-n}{1-n_0} \right)^{1/3}. \quad (2-2)$$

After the spheres are expanded, particles may overlap. Finally, the assembly is cycled by a simple DEM model to reduce the overlap and obtain equilibrium. Rigid boundaries are placed to confine the spheres in a specified volume.

As an example, a cylindrical sphere packing with a radius of 25 mm and height of 100 mm, a desired porosity of 0.4 and 2,500 spheres is obtained in the three steps shown in Figures 2-1 to 2-3.

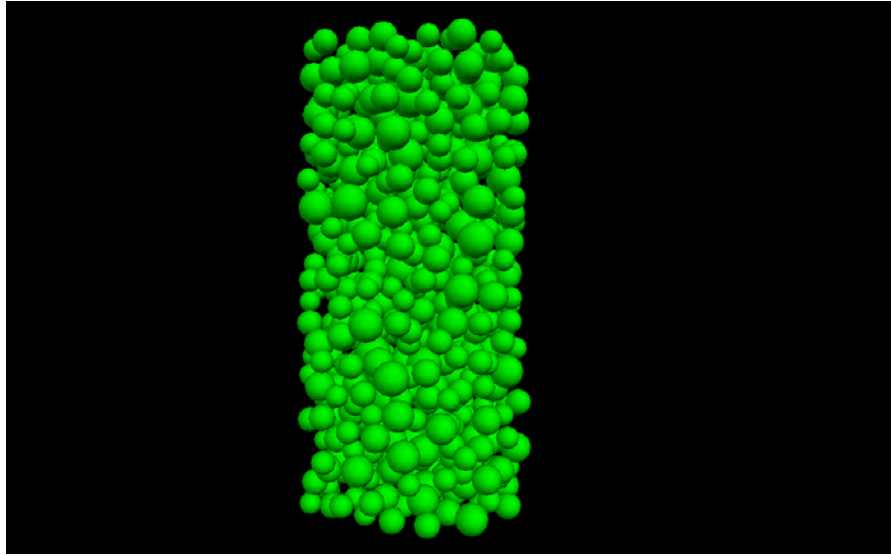


Figure 2-1. The 1st step: Randomly generate 2500 spheres with artificially small radii in order to prepare a cylindrical specimen with a radius of 25 mm and height of 100 mm

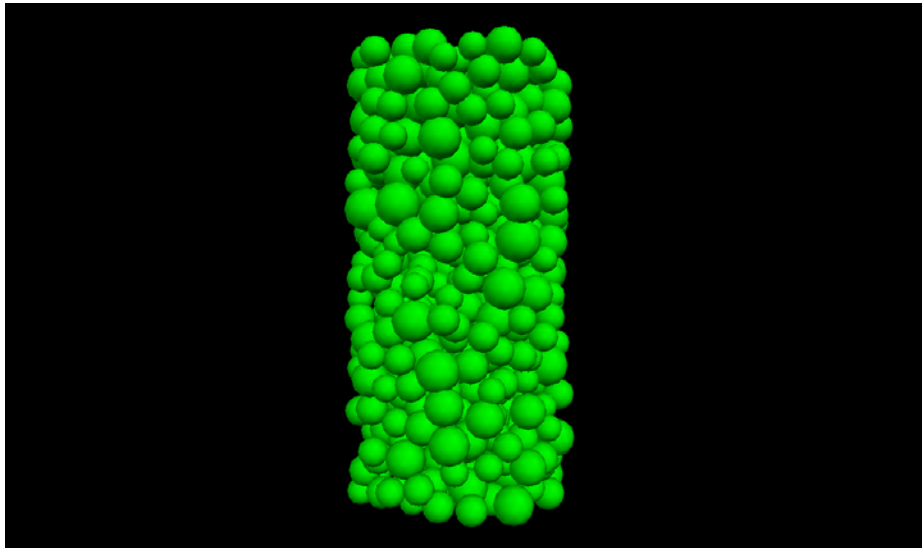


Figure 2-2. The 2nd step: Expand each sphere to obtain a specific porosity with large overlapping

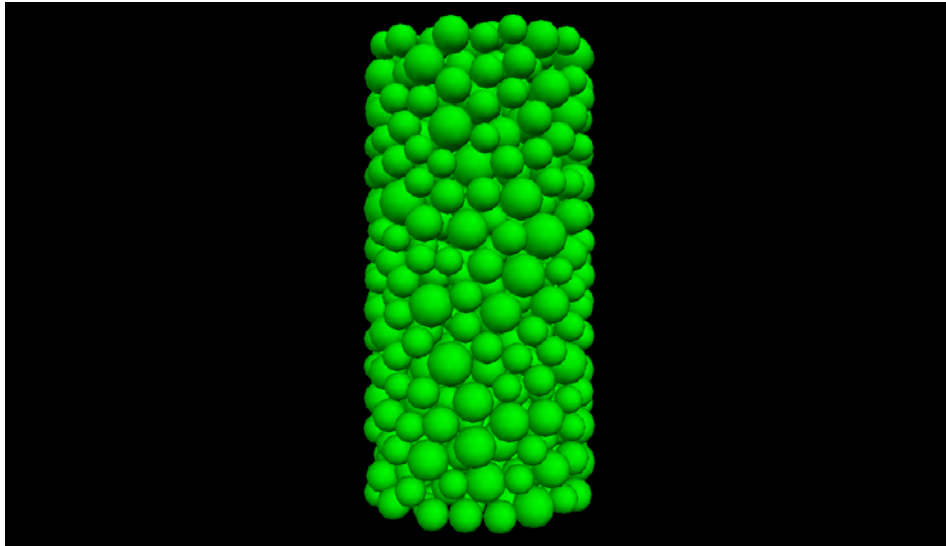


Figure 2-3. The 3rd step: Cycle the spheres using a simple DEM model to obtain equilibrium

2.3 GENERAL FORMULATION

2.3.1 Calculation Cycle

The calculation cycle used in DEM is a time-stepping algorithm (Cundall 1988; Cundall and Strack 1979; Itasca 1999): it integrates the differential equations of motion of each particle (the Newton's Second Law of Motion) in time by applying a contact constitutive model to each contact, updates particle positions and constant searches for contacts between two spheres or between a sphere and a boundary. The calculation cycle is illustrated in Fig. 2-4. At each time step, contacts are detected and updated from the known particle positions and boundary conditions. The contact constitutive model is then applied to each contact to update the contact forces. Based on the updated contact forces and boundary conditions, the law of motion is then applied to each particle to update its acceleration, velocity and position.

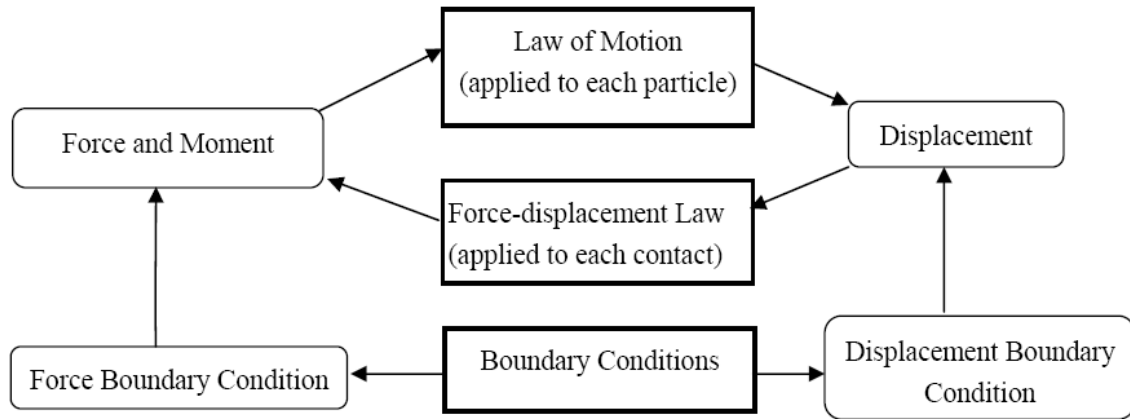


Figure 2-4. DEM calculation cycle employed in the developed code used for the research

2.3.2 Force-Displacement Law

The force-displacement law relates the relative displacement between two entities at a contact to the contact force acting on the entities (Hentz et al. 2004a). Here “Force-Displacement” is a general term including both Force-Displacement and Moment-Rotation. Depending on the type of contact, the force and moment acting on the particles at a contact are determined based on the relative displacement and contact constitutive model. There are different types of contact models to accommodate different material behaviors. When dealing with materials characterized by particulate or fractured elements, a frictional contact is used. However, in order to model a solid material with no initial crack, a bonded contact must be introduced. During the course of the simulation, if a bonded contact is broken according to the failure criterion to be described later, this bonded contact will be degraded to a frictional contact (provided that the two entities are still in contact).

A DEM algorithm has been implemented with the following features. The initial model is set up by using a spatially randomly distributed packing assembly of spheres, which yields the initial “zero stress” state. This is achieved by introducing an

“equilibrium distance”, $D_{eq}^{A,B}$ (Hentz et al. 2004a; Hentz et al. 2004b), between each pair of contact spheres A and B , which is equal to the distance between the centers of A and B at the end of the packing assembly (release of the locked-in stress). An interaction range is introduced into the model to simulate materials other than simple granular materials, in particular those which involve a matrix (Hentz et al. 2004a). Particles that are not in physical contact can still be bonded if they are within the interaction range, which makes the generated material behave more like a cemented material rather than a granular material.

Figure 2-5 shows the basic idea about the constitutive model implemented in the current algorithm, in which the springs represent the elastic responses to normal and shear forces, the slider and switch elements simulate the contact slide after shear failure and tensile crack after tensile failure, respectively. The constitutive model is detailed in next sections.

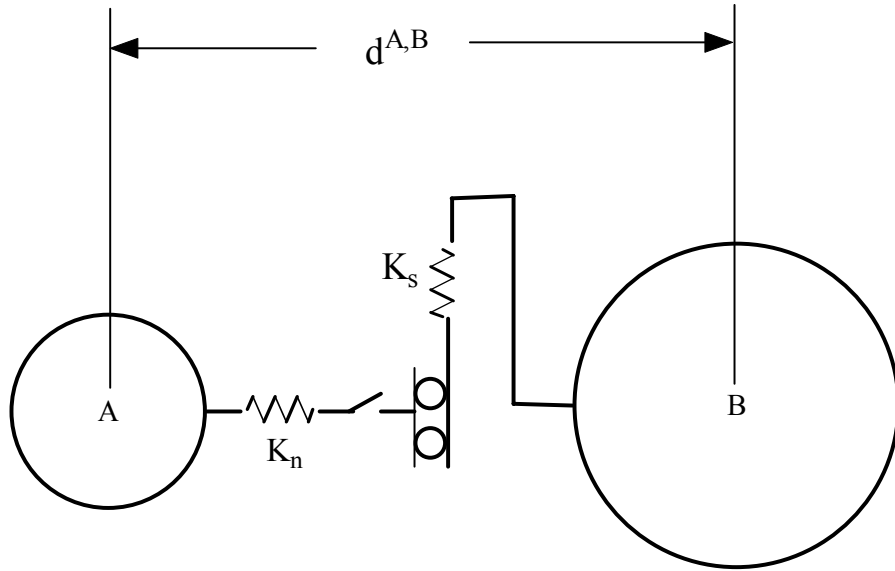


Figure 2-5. Constitutive model of contact used in the developed code

2.3.2.1 Normal Force Calculation

The relationship between contact forces and the relative displacements is assumed to be linear with the following interpretation (Cundall and Strack 1979; Hentz et al. 2004b; Itasca 1999). The contact forces consist of a normal component, \bar{F}_n , acting in the direction of the segment AB joining the two sphere centers, and a shear component, \bar{F}_s , acting in the plane perpendicular to AB at the point of contact. The force-displacement law relates these two force components to the corresponding components of the relative displacement via linear normal stiffness (K_n) and shear stiffness (K_s) at contact.

The normal force, \bar{F}_n , acting on sphere A is calculated as (Hentz et al. 2004a; Hentz et al. 2004b)

$$\bar{F}_n = K_n (D_{eq}^{A,B} - d^{A,B}) \bar{n}_{cont} , \quad (2-3)$$

where $D_{eq}^{A,B}$ is equilibrium distance between the two spheres A and B which is set when the contact is initially created, $d^{A,B}$ is the current distance between each pair of contact spheres A and B , and \bar{n} is the unit vector pointing from the center of sphere A to the center of sphere B . The contact is in tension when $d^{A,B} > D_{eq}^{A,B}$, and in compression when $d^{A,B} < D_{eq}^{A,B}$. The calculated new normal contact force is then added to the contribution of the resultant force and moment for both spheres. When tensile failure occurs at contact, the way to calculate the normal force will change, as described in Section 2.3.2.3.

2.3.2.2 Shear Force and Moment Calculation

The shear contact force is determined from an updated shear displacement on the contact plane, which is computed in an incremental fashion (Itasca 1999; Wang and Tonon 2009a; Wang and Tonon 2009b). The relative shear-displacement increment is

added to the current value of shear displacement in a vector form, which hence results in an increment in shear contact force. The motion of the contact should be taken into account during this procedure (Itasca 1999) because the current shear displacement vector always lies on the contact plane, which moves with the spheres in the global coordinate system.

The shear contact force vector, \vec{F}_s , should be updated to account for two rotations as shown in Figure 2-6.

- The first rotation is caused by the change from the old unit normal, \vec{n}^{old} , to the new normal, \vec{n}^{new} , which is due to the translational displacement of the sphere centers;
- The second rotation is caused by the rotation of both spheres around the normal vector, \vec{n}^{new} , (details about the transform matrix may be found in Appendix A).

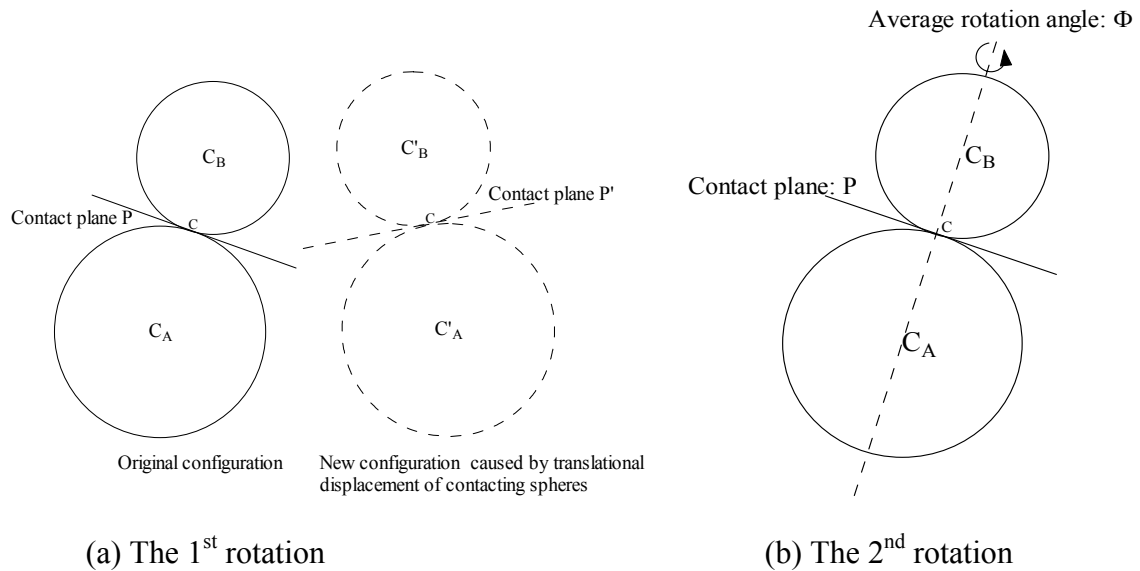


Figure 2-6. Rotations of contact plane (in 2D) used in determination of contact shear forces

Both of these rotations do not change the magnitude of the shear force between the two spheres; they only affect the direction of the contact shear force. The first rotation matrix can be obtained by rotating the local coordinate system about the unit vector \bar{v} , which is determined from the vector product of the old unit vector of contact plane, \bar{n}^{old} , and the new unit vector of contact plane, \bar{n}^{new} , as: $\bar{v} = \frac{\bar{n}^{old} \times \bar{n}^{new}}{l} = [v_x, v_y, v_z]$, in which $l = |\bar{n}^{old} \times \bar{n}^{new}|$, is the length of vector $\bar{n}^{old} \times \bar{n}^{new}$. The rotation angle θ is also calculated from the vector product of $\bar{n}^{old} \times \bar{n}^{new}$ as $\sin \theta = |\bar{n}^{old} \times \bar{n}^{new}| = l$. If one assumes that the rotation is very small, then $\cos \theta = 1$, and one may omit the higher order of the term of $\sin \theta$ in Eq. (A.1) (in Appendix A) to obtain the first rotation matrix:

$$M_1 = \begin{bmatrix} 1 & -lv_z & lv_y \\ lv_z & 1 & -lv_x \\ -lv_y & lv_x & 1 \end{bmatrix}, \quad (2-4)$$

which is a skew-symmetric matrix.

The second rotation matrix is calculated by using the average rotational speeds of the two contacting spheres as they rotate around the X-, Y- and Z- axes in a global Cartesian coordinate system. Let $\bar{\omega}^A = [\omega_x^A, \omega_y^A, \omega_z^A]^T$ and $\bar{\omega}^B = [\omega_x^B, \omega_y^B, \omega_z^B]^T$ denote the angular velocity of spheres A and B respectively. The rotational angles over the time increment Δt can be written as $\bar{\Theta} : [\theta_x, \theta_y, \theta_z]^T = \left(\frac{\bar{\omega}^A + \bar{\omega}^B}{2} \cdot \bar{n}^{new} \right) \cdot \bar{n}^{new} \Delta t$.

Again assume that rotations are very small at each time step. The second rotational matrix (A. 2) (in Appendix A) can be simplified as

$$M_2 = \begin{bmatrix} 1 & \theta_z & -\theta_y \\ -\theta_z & 1 & \theta_x \\ \theta_y & -\theta_x & 1 \end{bmatrix}. \quad (2-5)$$

Equations (2-4) and (2-5) apply only to small rotations. Considering that each contact is updated at each time step (which is very small to maintain computational stability in an explicit Euler time-integration scheme), the deformations will be sufficiently small for the approximation used in Equations (2-4) and (2-5). The time step is about one 10^{th} to one 100^{th} of the critical time step, $dt \sim \sqrt{m/K}$.

The total rotational matrix can then be determined as

$$\mathbf{M} = \mathbf{M}_1 \mathbf{M}_2 = \begin{bmatrix} 1 + l v_z \theta_z + l v_y \theta_y & \theta_z - l v_z - l v_y \theta_x & -\theta_y - l v_z \theta_x + l v_y \\ l v_z - \theta_z - l v_x \theta_y & l v_z \theta_z + 1 + l v_x \theta_x & -l v_z \theta_y + \theta_x - l v_x \\ -l v_y - l v_x \theta_z + \theta_y & -l v_y \theta_z + l v_x - \theta_x & l v_y \theta_y + l v_x \theta_x + 1 \end{bmatrix}. \quad (2-6)$$

To account for the motion of the contact plane, the new shear displacement, \vec{U}_s^{new} , is finally updated as

$$\vec{U}_s^{\text{new}} = \mathbf{M} \vec{U}_s^{\text{old}}. \quad (2-7)$$

The relative motion between two contact spheres along the new contact plane creates a shear displacement increment, $\Delta \vec{U}_s$, which is added to the shear displacement vector,

\vec{U}_s^{new} :

$$\vec{U}_s^{\text{updated}} = \vec{U}_s^{\text{new}} + \Delta \vec{U}_s. \quad (2-8)$$

The increment of shear displacement $\Delta \vec{U}_s$ for a given timestep can be computed by using the relative motion at contact. The relative contact velocity \vec{V}^c is given by

$$\vec{V}^c = \vec{V}_B^c - \vec{V}_A^c = (\vec{V}_B + \vec{\omega}^B \times \vec{r}_{BC}) - (\vec{V}_A + \vec{\omega}^A \times \vec{r}_{AC}), \quad (2-9)$$

where \vec{V}_A^c and \vec{V}_B^c are the translational velocities at the contact point for spheres A and B ,

\vec{V}_A and \vec{V}_B are the translational velocities of sphere centers A and B , $\vec{\omega}^A$ and $\vec{\omega}^B$ are the

rotational velocities for spheres A and B, and \vec{r}_{AC} and \vec{r}_{BC} are radius vectors from sphere centers to the contact point, C .

The relative contact velocity can be decomposed into normal (\vec{V}_n^c) and shear (\vec{V}_s^c) components with respect to the contact plane. The shear component is then calculated as

$$\vec{V}_s^c = \vec{V}^c - \vec{V}_n^c, \quad (2-10)$$

where $\vec{V}_n^c = (\vec{V}^c \cdot \vec{n}^{new}) \cdot \vec{n}^{new}$.

Finally, the increment of shear displacement $\Delta \vec{U}_s$ for a given timestep Δt is

$$\Delta \vec{U}_s = \vec{V}_s^c \Delta t. \quad (2-11)$$

The new shear contact force acting at contact point, C , is updated as

$$\vec{F}_s = -K_s (\vec{U}_s^{new} + \Delta \vec{U}_s), \quad (2-12)$$

where K_s is the shear stiffness of the contact. This newly updated shear contact force is added to the resultant force and moment for both spheres.

The moment applied on spheres A and B due to shear contact force, \vec{F}_s can be calculated respectively as

$$\begin{aligned} \vec{M}_A &= \vec{r}_{AC} \times \vec{F}_s \\ \vec{M}_B &= -\vec{r}_{BC} \times \vec{F}_s \end{aligned} \quad (2-13)$$

2.3.3 Failure Criteria

The strength criteria at contact used in the model comprise two parts, tensile failure and shear failure. These two kinds of failure jointly control the overall material strength. Tensile failure occurs when the magnitude of the contact normal force (in

tension) is greater than the product of tensile strength, T , times the contact area, A_c , which is calculated as:

$$A_c = \pi \left(\frac{R_A + R_B}{2} \right)^2, \quad (2-14)$$

where R_A and R_B are the radii of spheres A and B respectively.

After tensile failure, the contact force suddenly drops down to zero and the contact is de-bonded in tension, which means that the tensile strength is zero after the tensile failure. In the meantime, the cohesion part of shear strength will also degrade to zero. In order to model the softening behavior of the material, as shown in Figure 2-7, the contact force may gradually decrease rather than suddenly dropping to zero (used in this dissertation) after the contact force reaches the peak value.

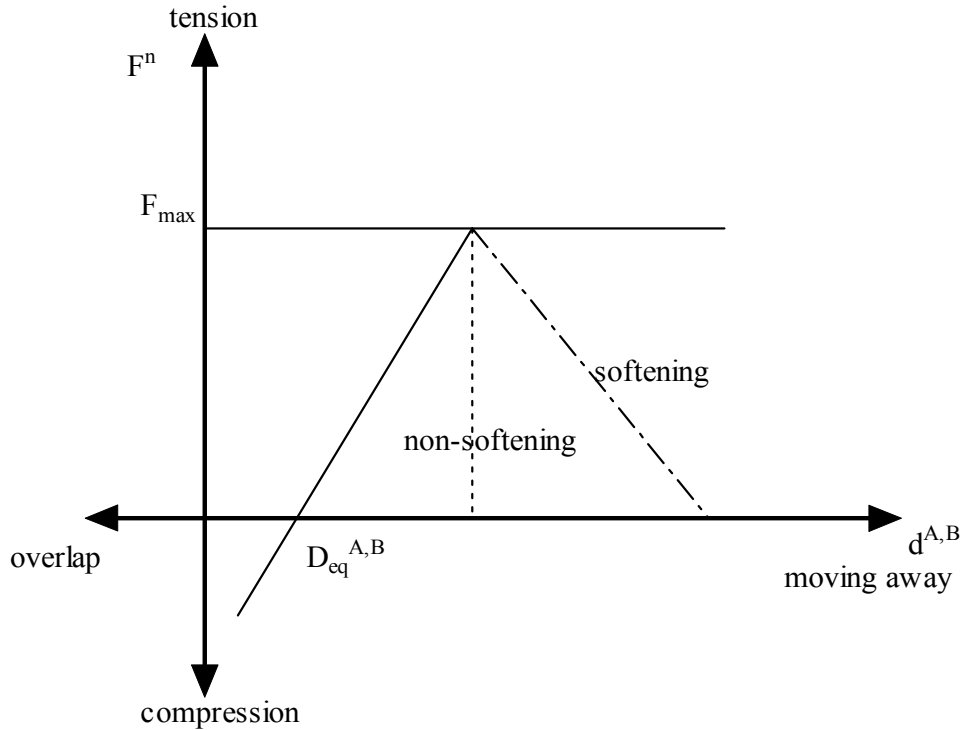


Figure 2-7. Tensile failure criterion used in the developed code (modified after Donze (Hentz et al. 2004a))

The shear failure follows the Coulomb criterion as shown in Figure 2-8. The maximum shear strength, τ_{\max} , is dependent on cohesion c , friction angle φ and also normal stress, σ_n , at contact (Hentz et al. 2004a).

$$\tau_{\max} = c + \sigma_n \tan \varphi \quad (2-15)$$

After shear failure, the cohesion is set to zero and the frictional angle can decrease to residual frictional angle φ_r .

The micro-level parameters used to describe the contact strength (T for tensile component and c , φ , and φ_r for shear component) are different from the values at the macro level, and need to be identified by a calibration process. In the cases presented, φ_r is taken as 50% of φ .

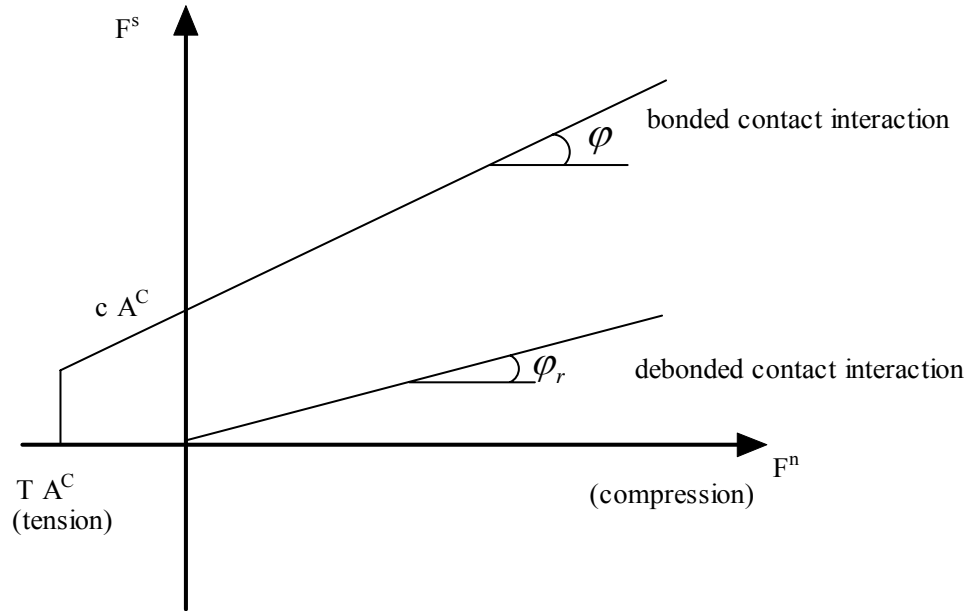


Figure 2-8. Shear failure criterion used in the developed code (modified after Donze (Hentz et al. 2004a))

2.3.4 Equations of Motion

In DEM, the equations of motion are applied to each individual particle, and can be expressed as two vector equations, i.e. translational motion equation and rotational motion equation. The vector form equation for translational motion is written as

$$m\ddot{\vec{u}} + c_1\dot{\vec{u}} = \vec{F} \quad (2-16)$$

where c_1 is damping for translational velocity; \vec{F} is the resultant force applied to a sphere (sum of all externally applied forces acting on the particle and body force); $\ddot{\vec{u}}$ and $\dot{\vec{u}}$ are translational acceleration and translational velocity respectively; m is the mass of the particle.

Because of symmetry of a solid sphere, each principal moment of inertia is the same. The equation for rotational motion can be then simply written as

$$I\dot{\vec{\omega}} + c_2\vec{\omega} = \vec{M} \quad (2-17)$$

where c_2 is damping for angular velocity; I is the moment of inertia of the sphere; $\dot{\vec{\omega}}$ is the angular acceleration; $\vec{\omega}$ is the angular velocity and \vec{M} is the resultant moment.

2.4 TIMESTEP DETERMINATION

In DEM, motion equations (2-16) and (2-17) are integrated using a centered finite-difference explicit scheme (Cundall 1971; Cundall and Hart 1992). The computed solution produced by these equations remains stable only if the timestep does not exceed a critical timestep, which is related to the minimum eigenperiod of the total system. For a static problem, the timestep is only associated with system's critical timestep. For a dynamic problem, the timestep should also be related to loading frequency in order to assure the accuracy in simulation. The actual timestep used in simulations is taken as a fraction of the minimum of this estimated critical timestep and the possible smallest period of loading, which can be expressed as

$$\begin{cases} \Delta t = \alpha \min[T_{system}, T_{loading}] & \text{(for a dynamic problem)} \\ \Delta t = \alpha T_{system} & \text{(for a static problem)} \end{cases} \quad (2-18)$$

where α is the fraction coefficient usually varying from 0.01 to 0.1, $T_{loading}$ is the possible smallest period of loading, and T_{system} is the minimum eigenperiod of all particle systems.

The minimum eigenperiod of all particle systems may not be easily calculated because each particle may have different contact configurations, not like a single mass-spring system. But the order of magnitude of T_{system} may be estimated as $\min(2\pi\sqrt{m/K})$, in which m is the mass of an element and K is the stiffness associated with that element (O'Sullivan and Bray 2004).

2.5 DAMPING

Because the DEM is a fully dynamic formulation, some form of damping is necessary to dissipate kinetic energy. For a dynamic problem, a specific damping needs to be known to correctly set up the model. For a quasi-static problem, the damping used in DEM is numerically used to dissipate the system energy as quickly as possible to reach the equilibrium state without affecting the final result. To improve the computational efficiency, a local non-viscous damping (Itasca 1999) is used in the current model to speed up the simulation of static problems, in which only the unbalanced forces are damped at each time step as follows:

$$m \cdot \ddot{\vec{a}} = \vec{F}_{unbalanced} - \alpha \cdot \text{sign}(\vec{v}) \cdot \text{abs}(\vec{F}_{unbalanced}) \quad (\text{in translation}) \quad (2-19)$$

$$I \cdot \ddot{\vec{\omega}} = \vec{M}_{unbalanced} - \alpha \cdot \text{sign}(\vec{\dot{\omega}}) \cdot \text{abs}(\vec{M}_{unbalanced}) \quad (\text{in rotation}), \quad (2-20)$$

in which m and I are mass and moment inertia of a spherical particle, respectively; $\ddot{\vec{a}}$ and $\ddot{\vec{\omega}}$ are translational and rotational accelerations, respectively; \vec{v} and $\vec{\dot{\omega}}$ are translational and rotational velocities, respectively; $\vec{F}_{unbalanced}$ and $\vec{M}_{unbalanced}$ are unbalanced resultant forces and moment.

For simplicity, the damping coefficients used in translational and rotational equations are the same and are indicated by α . The value of α should be between 0 and 1 to avoid numerical divergence. This kind of damping may be only suitable for static problems. For dynamic problems, usually a viscous damping is employed to decelerate local relative movements among neighboring particles (Fraige and Langston 2004).

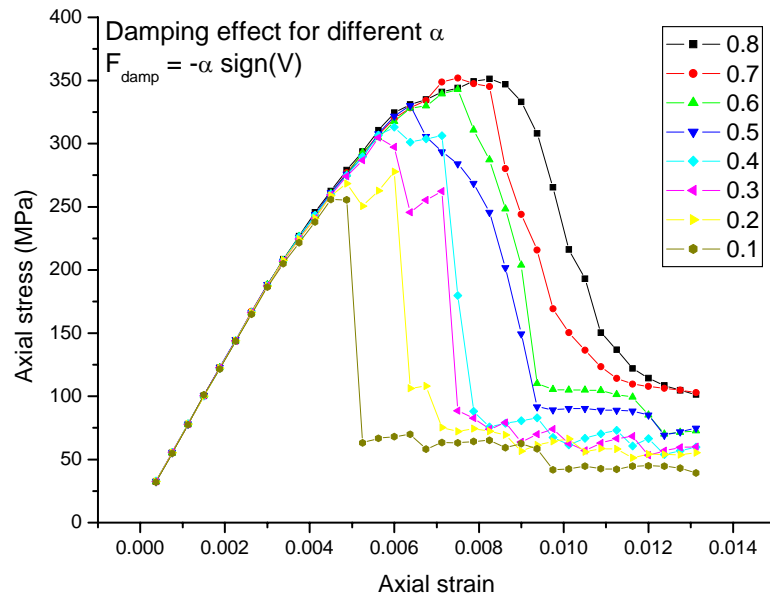


Figure 2-9. Effect of numerical damping on material behavior. Cylindrical specimen with a height of 3.2 cm and 1.6 cm diameter consisting of 2500 spheres; $E_c = 104.7 \text{ GPa}$, $K_s / K_n = 0.085$, $c = 429 \text{ MPa}$, $\varphi = 68^\circ$, $T = 34.2 \text{ MPa}$, and coefficient of interaction range of 1.3

Different values of damping coefficient, α , were used to investigate the effect of damping on static simulations. As depicted in Figure 2-9, simulated stress-strain curves show that material strength increases with damping, but material Young's modulus does not change with damping. Compared to lower damping, higher damping tends to decrease

the energy dissipation rate more quickly, and the loads are more gradually applied to the specimen to reach the equilibrium state. Hence, materials with lower numerical damping fail more easily and have lower strength. However, when $\alpha \geq 0.7$, damping has negligible effect on static strength (both peak and residual), whereas the post-peak softening is smoother for higher damping. It is to be noted that, for quasi-static problems, dynamic energy will be fully absorbed during loading and high damping ($\alpha \geq 0.7$) is typically used for the modeling.

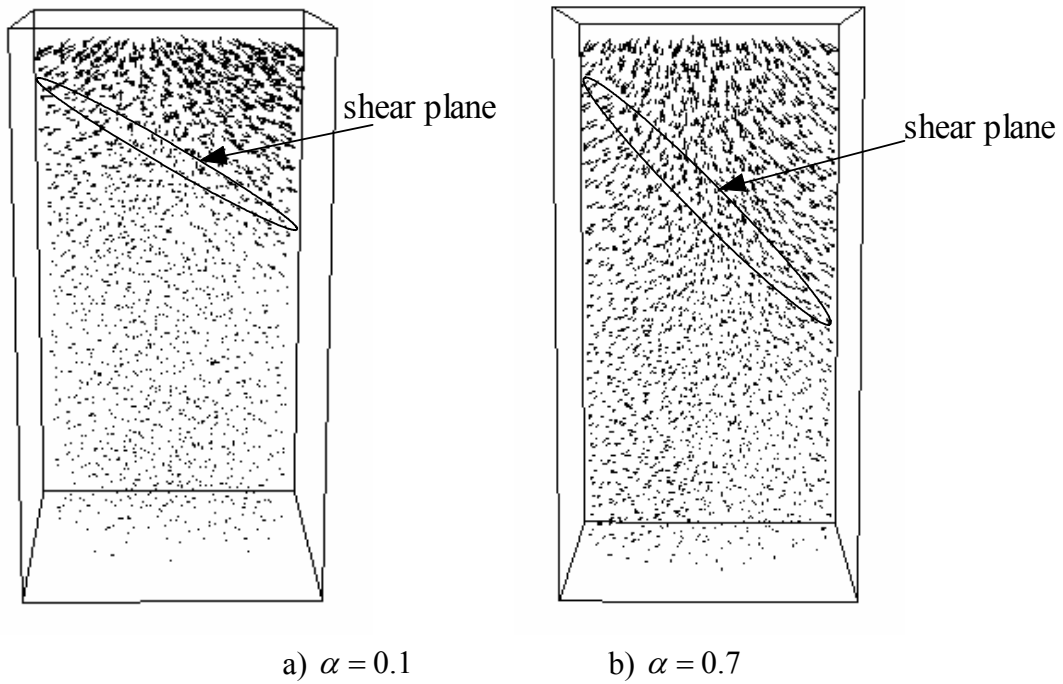


Figure 2-10. Displacement vector fields for different numerical damping. Cylindrical specimen with a height of 3.2 cm and 1.6 cm diameter consisting of 2500 spheres; $E_c = 104.7 \text{ GPa}$, $K_s / K_n = 0.085$, $c = 429 \text{ MPa}$, $\varphi = 68^\circ$, $T = 34.2 \text{ MPa}$, and coefficient of interaction range of 1.3

The numerical damping also affects the failure pattern, which is wedge shaped as shown in Figure 2-10. Lower damping decreases the energy dissipation from the top to the bottom (the load is applied from the top platen with the bottom end fixed), and hence the failure zone occurs at a relatively higher level than with higher damping.

It is expected that the higher damping should be used to mimic the actual test conditions, where, for quasi-static tests, the load is applied slowly enough to make the energy gradually transmitted to the whole specimen without causing any dynamic effects that may lead to failure.

The damping force is controlled by the non-dimensional damping constant, α , in which only accelerating motion is damped. This local non-viscous damping is similar to hysteretic damping, and can be directly related to the damping ratio, D , as $D = \frac{\alpha}{\pi}$, which is described in PFC manual (Itasca 1999).

2.6 WAVE MOTIONS

Discrete element modeling is a fully dynamic method (Cundall 1971; Cundall and Strack 1979). In modeling uniaxial compressive tests, loading is applied at the top of specimens while fixing the bottom of specimens in the vertical direction. The loading is applied in a step fashion by gradually increasing the axial displacement at the top end of specimen within 1000 timesteps and then waiting for the system to reach equilibrium before applying another step of displacement loading. A cylindrical specimen (5 cm in diameter and 10 cm in height) consisting of 1,500 spheres was employed and particle motions at different locations in the specimen were monitored. The histories of displacement in the axial direction (Z) for particles No. 904, 632, 880 and 592 (shown in Figure 2-11) were monitored for 2 different loading periods, namely, step 2 (elastic) and

step 18 (at failure). The histories of particle motions in the axial direction are shown in Figures 2-12 and 2-13. The results show that:

- 1) The displacement waves move from the top to the bottom and decay gradually.
- 2) For a given particle, the waves gradually die off due to damping and the system eventually reaches equilibrium in the elastic stage.
- 3) In the case of material failure, in addition to the general wave due to applied loading, there is also “noise” accompanied generated from many local micro fractures that behave like small free boundaries.

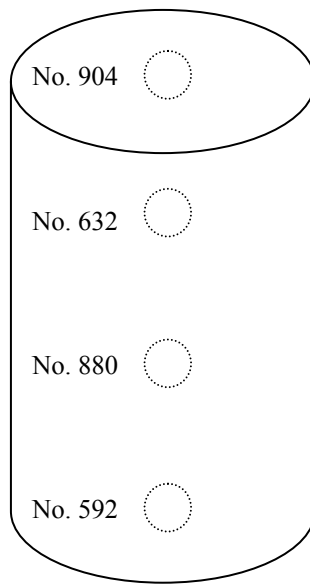


Figure 2-11. Sketch of position of monitored particles in a cylindrical specimen (5 cm in diameter and 10 cm in height) consisting of 1,500 spheres

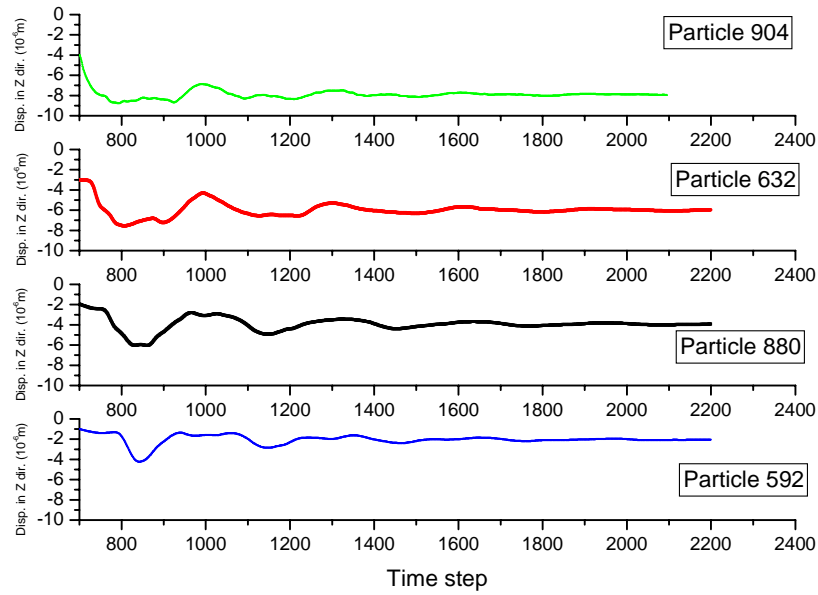


Figure 2-12. Histories of particle motions in the axial direction during the elastic stage (no contact failures)

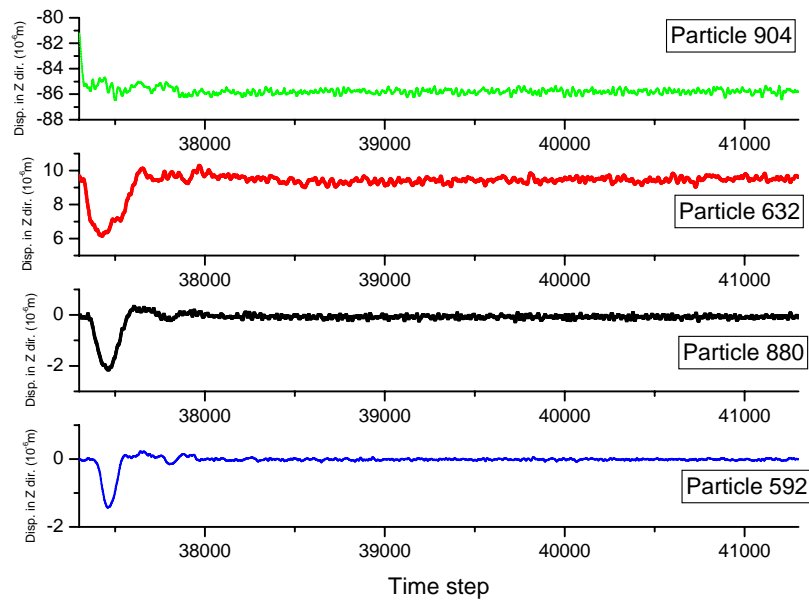


Figure 2-13 Histories of particle motions in the axial direction at failure (many contact failures occur)

2.7 COMPUTATIONAL TIME

In discrete element modeling, computational time is always a concern (Cundall 1988; Ferrez and Liebling 2001; Henty 2000). Extensive computational time is consumed by contact detection. The cell mapping technique (Cundall 1988), in which the whole domain is divided into many cells, is used to alleviate the computational burden due to contact detection in DEM. For a given cell, only the spheres located in neighboring cells and the cell itself need to be considered for contact detection without need to loop over all spheres. By doing this, each sphere is first mapped into a unique cell, and the contact detection is then carried out by looping these cells. The cell size is an important factor because an appropriate cell size can minimize the computational time. The algorithm may cause inaccuracy if the cell size is too small, thereby some contacts may not be detected. For example, two contacting spheres whose center distance is larger than the cell size may not be considered as a contact if these two centers are not located in neighboring cells or in the same cell. Hence, the cell size must be at least twice as large as the maximum sphere radius of the sphere packing.

The effect of cell size on both computational time and accuracy is investigated in a triaxial test example of a cylindrical specimen. All of the spheres are mapped into cells which are thin concentric disk dividing the specimen in the axial direction. The cell size is defined as the thickness of a thin disc, and the cell number is defined as the specimen height divided by the cell size. The simulated results shown in Figure 2-14 illustrate that the simulated material pre-peak behavior does not depend on the number of cells when the number of cells is smaller than 16. When the number of cells is larger than 16, which corresponds to a cell size of 2 mm (the maximum radius of the packing is about 1 mm), the calculated behavior dramatically changes because of failing to include all existing contacts. When the number of cells is smaller than 16, the differences in post-peak

behavior are caused by the fact that, after failure, the relative particle positions change much faster than in the pre-peak stage, and an even smaller cell number should be used. This aspect may not be of concern if the post-peak behavior is not important for the analyst.

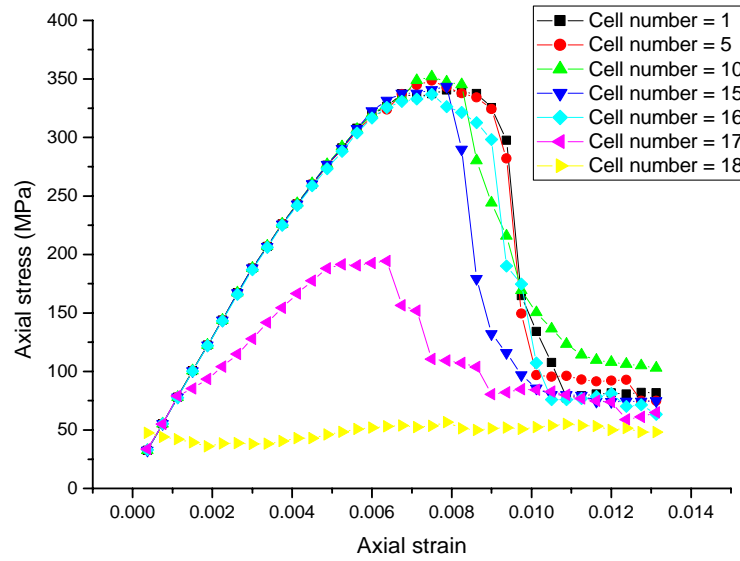


Figure 2-14. Effect of the number of cells on simulated results for triaxial tests. Cylindrical specimen with a height of 3.2 cm and 1.6 cm diameter consisting of 2500 spheres; $E_c = 104.7 \text{ GPa}$, $K_s / K_n = 0.085$, $c = 429 \text{ MPa}$, $\varphi = 68^\circ$, $T = 34.2 \text{ MPa}$, and coefficient of interaction range of 1.3

The computational times for different the number of cells are shown in Figure 2-15. It highlights that increasing the number of cells lowers the computational time needed. However, if the cell size is too small to the extent that some contacts are overlooked, inaccuracy may occur, and the computational time will increase.

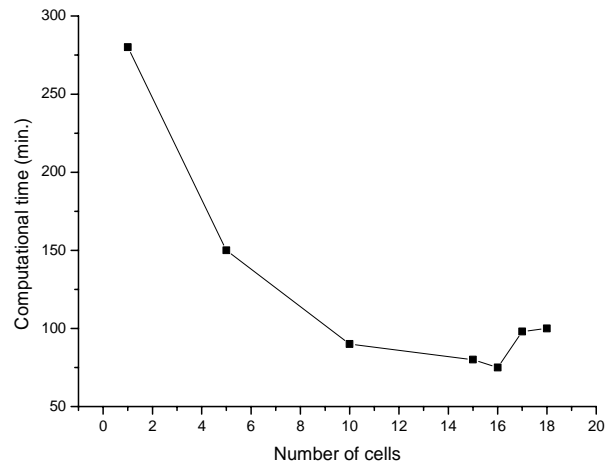


Figure 2-15. Computational time versus the number of cells. Cylindrical specimen with a height of 3.2 cm and 1.6 cm diameter consisting of 2500 spheres; $E_c = 104.7 \text{ GPa}$, $K_s / K_n = 0.085$, $c = 429 \text{ MPa}$, $\varphi = 68^\circ$, $T = 34.2 \text{ MPa}$, and coefficient of interaction range of 1.3

CHAPTER 3: DEM MODEL CALIBRATION

3.1 INTRODUCTION

DEM is attractive in modeling bonded geomaterials because it can naturally deal with the material failure by modeling the failure evolutionary process from micro crack development to macro failure without any complex constitutive models. While the method is versatile and attractive, it requires extensive calibration work.

The calibration process in DEM includes parameter identification for both deformability and strength. Before modeling a specific engineering system, a specimen should be prepared with specific macro elastic parameters and strength parameters, whose corresponding micro parameters are to be determined for a given packing to closely reproduce the specific macro material properties.

The calibration process is a typical inverse problem, and is currently carried out by trial and error using laboratory test results, which are compared with simulation results (Cooreman et al. 2007; Oreskes et al. 1994). There are a total of five micro parameters (they will be discussed in detail in Section 3.2) involved in determining the macro-scale emergent behavior for both deformability and strength. The packing structure (including particle shape, size and arrangement) will affect the material behavior. Usually, the behavior of geomaterials is complex, with a nonlinear failure envelope and a high ratio of uniaxial compression strength to tensile strength. Hence, it is hard to calibrate the model with the aim of accommodating all these micro parameters to match this complex behavior, and the micro model parameters can hardly be related directly to a set of material properties for all types of packing. Usually, this calibration process should be carried out for each different packing. From the mathematical point of view, the number

of experimental data points should be larger than or at least equal to the number of the model parameters to be determined.

Until now, there has been no satisfactory way to calibrate the DEM model in order to reproduce this complicated behavior and deploy the versatility of DEM. Using sensitivity analysis, most of the researchers just investigate the effect of one individual parameter (or a combined dimensionless parameter) while keeping other variables fixed, and then a general formula to determine micro-scale parameters based on specific macro material properties is determined (Fakhimi and Villegas 2007; Yoon 2007). However, the problem associated with determining these micro parameters is a multi-variable problem, in which the individual trend of one parameter cannot be directly obtained by just fixing the values of all the other parameters since these parameters may not be independent. A simple example to illustrate this problem could be: Provided that you have a topographic map, which gives the elevation at any point (x, y), it is impossible to obtain a unique relationship between elevation and x by fixing the value of y.

In this section, model parameters are first described. A typical calibration approach is then presented and employed to identify these model parameters at micro level for static problems. Experiments were carried out on granite by applying both static and dynamic loading. The experimental results were analyzed and used to calibrate and verify the model in both static and dynamic aspects.

3.2 MODEL PARAMETERS

3.2.1 Deformability Parameters

Deformability parameters include normal stiffness, K_n , and shear stiffness, K_s , that, to avoid local failures, are usually calibrated either under small loading conditions or by setting very high micro strength parameters. These micro deformability parameters are

calibrated to match the material macro deformability parameters: Young's modulus, E , and Poisson ratio, ν , which are determined from experiments. Based on our investigations from DEM simulation results, material Young's modulus is related to both K_n and the ratio $\frac{K_s}{K_n}$, while material Poisson's ratio is only related to the ratio $\frac{K_s}{K_n}$, which will be discussed in detail later.

A starting value for K_n may be calculated as spring constant as follows. As shown in Figure 3-1, consider a column consisting of N spheres having the same radius R , piled up vertically and subject to loading P at both ends. The spheres have Young's modulus E_c . The displacement of the assembly can be approximately determined as:

$$\Delta = \varepsilon L = \frac{P}{AE_c} 2NR = \frac{P}{\pi R^2 E_c} 2NR = \frac{2NP}{\pi R E_c}. \quad (3-1)$$

where A is the area of the effective cross section for the column.

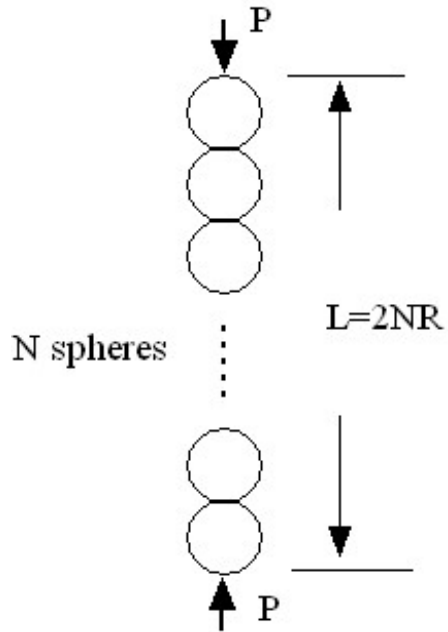


Figure 3-1. Sketch of deriving contact spring constant

Alternatively, the model can be simplified as series of $(N-1)$ springs with spring constant K . Each spring represents the material response between two neighboring sphere centers and is located at the contact. The displacement can be calculated as:

$$\Delta = (N-1) \frac{P}{K}. \quad (3-2)$$

By equating the displacements in Eqs. (3-1) and (3-2), the spring constant K can be determined as $K = \frac{\pi E_c R}{2}$ when N is large enough so that $N \approx N-1$.

As shown in Figure 3-2, consider a contact pair having different sizes with radii R_A and R_B , and contact equilibrium distance D_{eq} . The contact normal stiffness may be similarly approximated as

$$K_n = \frac{\pi E_c D_{eq}}{4}. \quad (3-3)$$

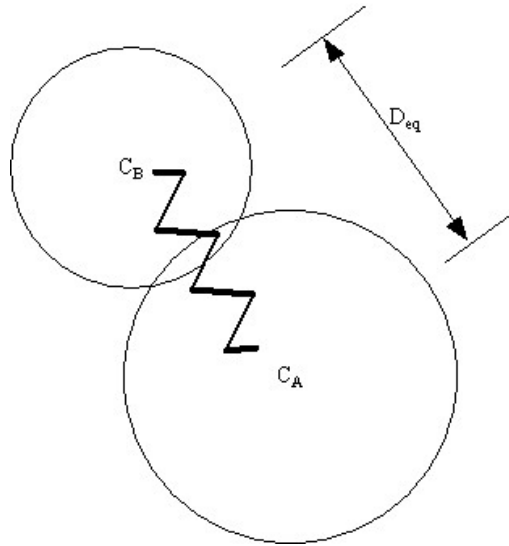


Figure 3-2. Contact spring constant for different sphere sizes

A relatively homogeneous response is obtained from a random packing assembly composed of different sphere sizes when E_c and $\frac{K_s}{K_n}$, rather than K_n and $\frac{K_s}{K_n}$, are used

as calibration parameters. Because if the same value of normal stiffness, K_n , is used for all contacts, the deformability properties between two sphere centers for contact pairs having different equilibrium distance, D_{eq} , are not uniform as can be seen from Eq. (3-3). The contact normal stiffness, K_n , is calculated using Eq. (3-3), and the contact shear stiffness, K_s , is determined from the ratio $\frac{K_s}{K_n}$ and K_n .

In summary, the deformability parameters to be calibrated are: E_c and $\frac{K_s}{K_n}$.

3.2.2 Strength Parameters

The two failure mechanisms of shear and tension can affect each other because either type of failure may change local stress conditions. This actually makes the failure process more complicated and makes it difficult to calibrate strength parameters.

Strength parameters include the contact tensile strength, T , and c and ϕ for shear components as already described in the failure criteria of the model (Section 2.3.3). These strength parameters are calibrated under different confining pressures to match a failure envelope obtained from experiments. This process is very time-consuming as each trial parameter set needs to be simulated under different confining pressures to reach the peak strength point of a stress-strain curve.

3.3 NUMERICAL SETUP

In order to calibrate the strength parameters, it is necessary to model triaxial tests of cylindrical specimens. Several techniques and algorithm developed for modeling a triaxial test are presented here.

3.3.1 Membrane Boundary for Applying Confining Pressure

One of the difficulties in modeling triaxial tests in DEM is applying confining pressure to realistically represent the test conditions. Currently, the conventional periodic, rigid, and flexible boundaries are commonly used to simulate triaxial tests.

Periodic boundary is commonly used in simulations with parallelepiped specimens, and is implemented by copying the boundary particles to the opposite side of the parallelepiped. The confining pressure is achieved by compacting the specimen to a specific pressure (Jensen et al. 1999). The periodic boundary is difficult to be implemented in a cylindrical specimen. The method used to achieve the desired confining pressures by compacting the specimen can significantly increase the computational effort, and it is difficult to keep the confining pressure constant during the shearing phase. “Rigid-wall” boundary treats boundaries as rigid walls, which may be either plane (parallelepiped specimen) or cylindrical (cylindrical specimen). The confining pressure is applied by moving these boundary walls laterally to reach the required confining pressure, which is defined as the average normal stress acting on the boundary particles (Itasca 1999; Potyondy and Cundall 2004). The drawbacks of rigid boundaries are that the boundary particles tend to be artificially aligned with the boundary wall, and that the material failure process and deformation may be overly constrained by such a boundary, which therefore are not fully representative of the actual test conditions.

Flexible boundary emulates the boundary in the conventional triaxial setup by using adjoining triangular plate elements, whose corners are placed at the centers of neighboring particles. Confining pressure is applied to each plate element, and the resultant force is then distributed among the three neighboring particles at the vertices of the plate element (Kuhn 1995). In addition to identifying boundary particles, the following operations must be performed: identify triangular elements, compute their

corresponding normal vectors and compute each interior corner angle and also take the issue of numerical instability into account. All these calculations must be repeated throughout the simulation to take into account the displacements of the membrane, and lead to a much higher computational expense than the proposed boundary model. Additionally, boundary particles are identified as those particles comprised in a thin layer parallel to the undeformed configuration. If the boundary undergoes large deformations (e.g. bulging or shear band), the boundary particles may not be correctly identified. Another type of flexible boundary was developed by Zhang and Sture (Zhang and Sture 1996) to simulate a rubber membrane by beam elements. In addition to the DEM, this algorithm calls for solving a set of matrix equations (associated with beam elements) at each time step. This type of flexible boundary can only be applied to simulate 2D problems.

All these conventional boundaries used in modeling confining pressure have difficulty representing the real confining conditions used in the laboratorial triaxial tests. A new approach to apply realistic fluid confining pressure has been developed for modeling triaxial tests on intact rock using the DEM. In order to overcome drawbacks of conventional boundaries, the new approach described here applies updated force boundary to simulate the confining pressure. The applied force only acts on the boundary particles, which are identified and updated periodically. The force applied to an individual boundary particle is directly determined (without any need for iteration) based on the input confining pressure and the sphere size.

The boundary particles are identified by using a cell algorithm developed by the author, in which the particles near the boundary are considered as the potential boundary particles, and are mapped into cells as shown in Figure 3-3, which, for clarity, only shows a 2D sketch on a horizontal cross section of a vertical cylindrical specimen. In order to

ensure that each cell has at most one boundary particle, the vertical (axial) and circumferential dimensions of a cell are selected as the minimum diameter of all spheres. Boundary spherical particles are mapped into cells according to their sphere centers, therefore, a sphere center can only be located in one cell, and it is of no concern if part of a particle is in one cell and part of it is in another cell. The cells make up a pipe-like boundary. The inner radius of the “pipe” is set as the original radius of the sample minus several times (twice used in the code) the maximum sphere diameter of all particles depending on the sphere size and specimen dimensions used in the simulation. However, the outside radial dimension of the “pipe” is not limited as shown in Figure 3-3, because the specimen may bulge during loading. By doing this, for each cell along the vertical (axial) and circumferential dimensions, there is at most one sphere center which can be placed in each cell. Along the radial direction, there could be several sphere centers located in a cell. For each cell, the outermost particle can then be easily identified as the particle with the largest radial distance, and marked as boundary particle.

Since identifying these boundary particles is time-consuming, the boundary particles are updated periodically rather than at each time step because they are not likely to change within a small time interval. The numerical investigations conducted revealed that updating the boundary particles every 100 timesteps is a good compromise between computational speed and accuracy, because it produces less than 1% discrepancy in axial stress while speeding up the simulation by about 3 times.

After identifying the boundary particles, the effect of the confining pressure is imposed by applying forces onto these boundary particles. The radial force applied onto the i^{th} individual boundary particle under membrane boundary condition, F_i^m , is

determined based on the value of input confining pressure, p , and the radius of the particle, R_i , as:

$$F_i^m = \pi R_i^2 \frac{A_b^m}{\sum_{i=1}^{N_b^m} \pi R_i^2} p \quad (3-4)$$

where A_b^m is the initial area of circumferential boundary of the specimen, N_b^m is the number of boundary particles, under membrane boundary condition. The boundary force, F_i^m , is applied at the center of its relevant sphere, and is directed radially.

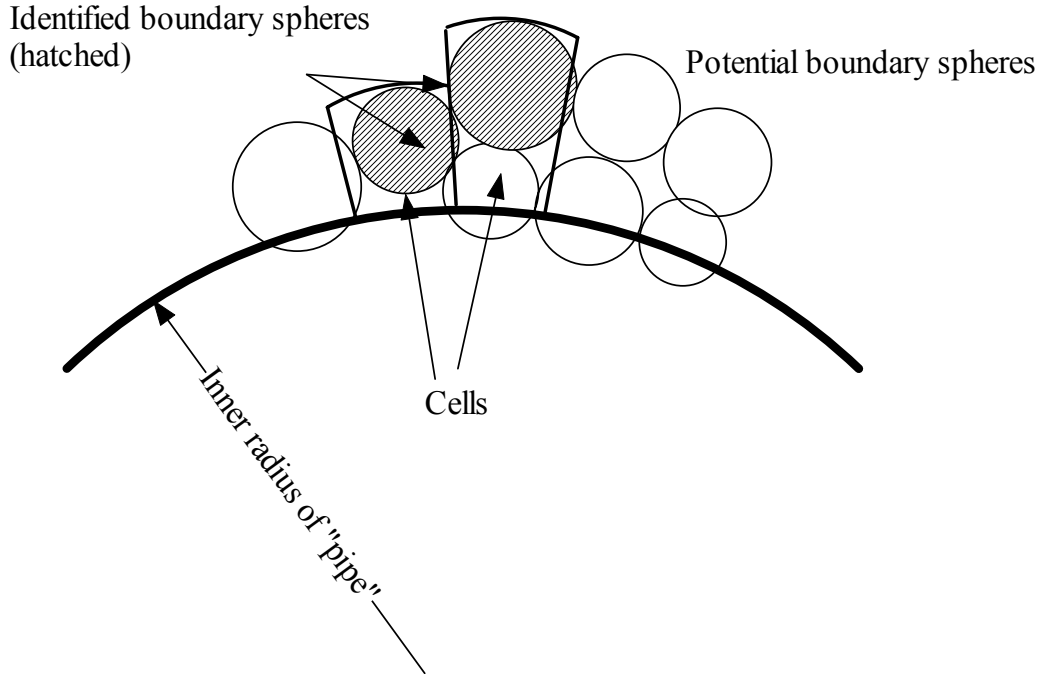
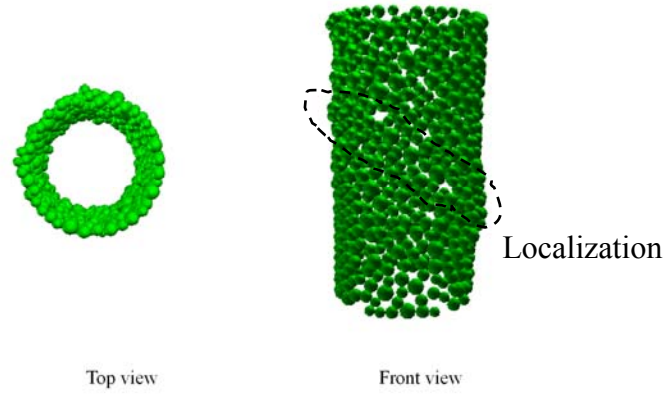


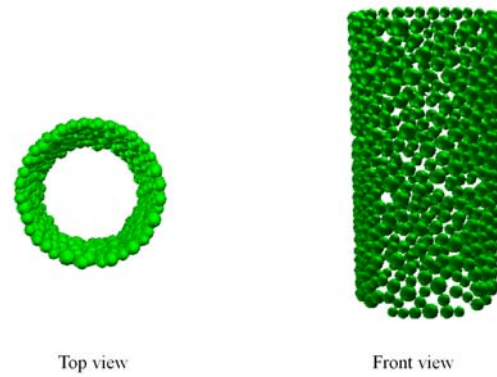
Figure 3-3. Boundary particles identification using a cell algorithm in modeling membrane boundary for applying confining pressure

Figure 3-4 (a) shows an example, in which the boundary particles are identified after loading a 2,500 sphere specimen to failure. The specimen bulges at several locations with formation of a shear plane (localization), which cannot be modeled by using

conventional boundary conditions, such as rigid boundary condition. Figure 3-4 (b) shows the boundary particles after failure under the rigid boundary condition.



(a) Membrane boundary



(b) Rigid boundary

Figure 3-4. Results of identified boundary particles at post-peak stage for different boundaries

3.3.2 Comparisons between Rigid and Membrane Boundaries

Comparisons between rigid and membrane boundaries were made with the same packing assembly, model parameters and loading conditions. The simulations model a triaxial test with a confining pressure of 10 MPa. A 2,500 sphere specimen is considered

here, which is 3.2 cm in height and 1.6 cm in diameter for the purpose of comparison against other simulations (Hentz et al. 2004a; Hentz et al. 2004b). The model parameters are shown in Table 3-1, which were calibrated for Lac du Bonnet granite (Wang and Tonon 2008).

Table 3-1. Model parameters used in simulations with membrane boundary and rigid boundary

Model parameter	$E_c (GPa)^*$	$\frac{K_s}{K_n}$	$c (MPa)$	ϕ	$T (MPa)$
Value	107.3	0.085	429	68^0	34.2

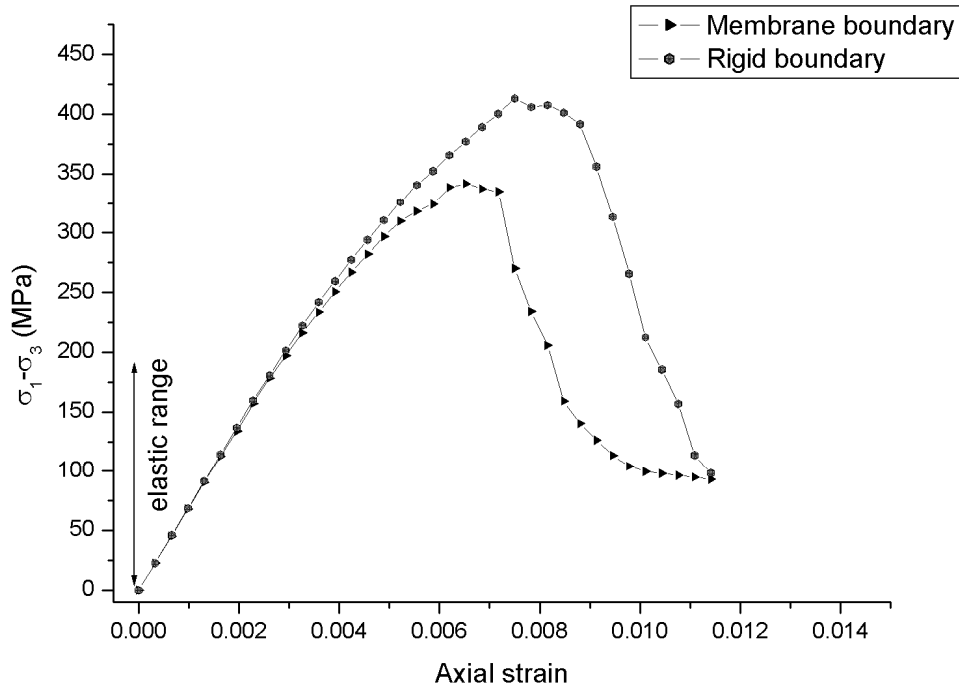
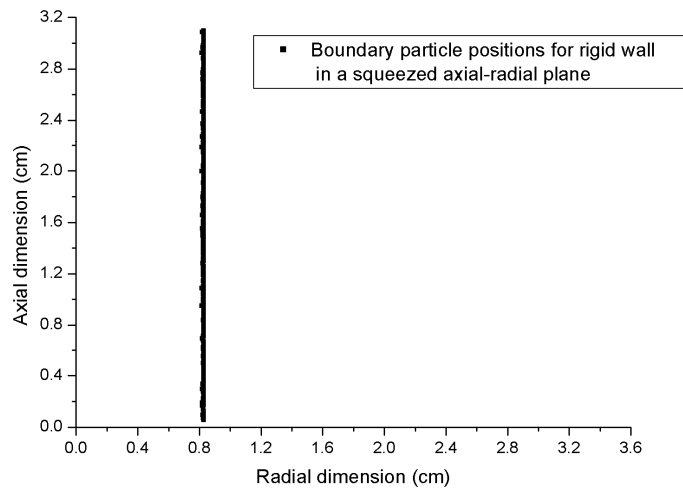
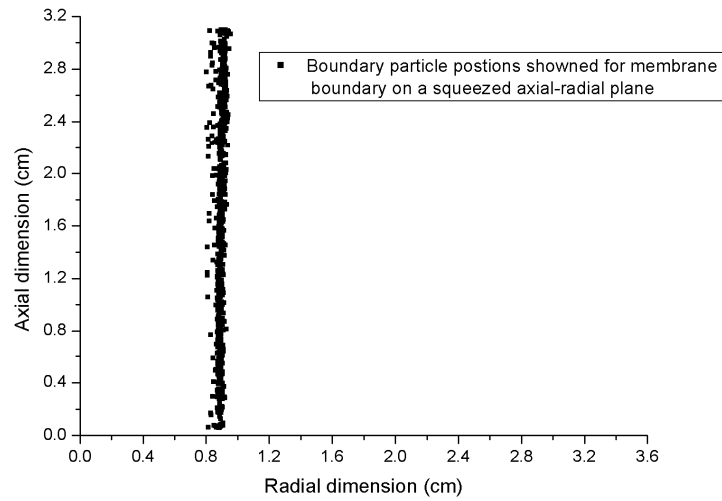


Figure 3-5. Comparison of stress-strain curves between membrane boundary and rigid boundary conditions

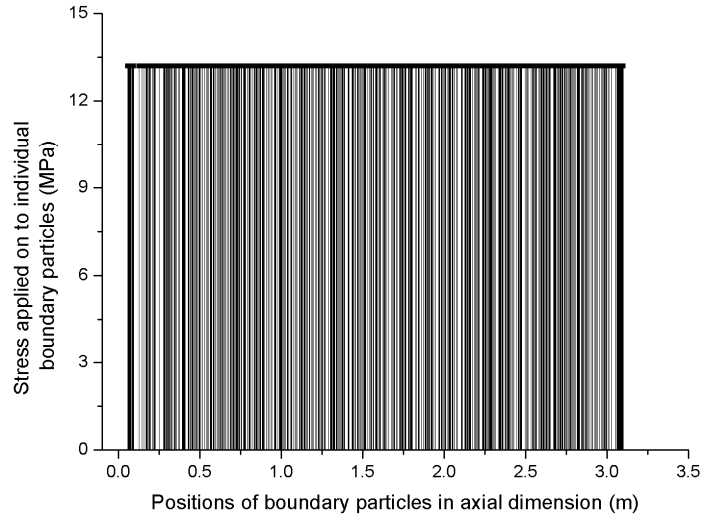


(a) Rigid boundary

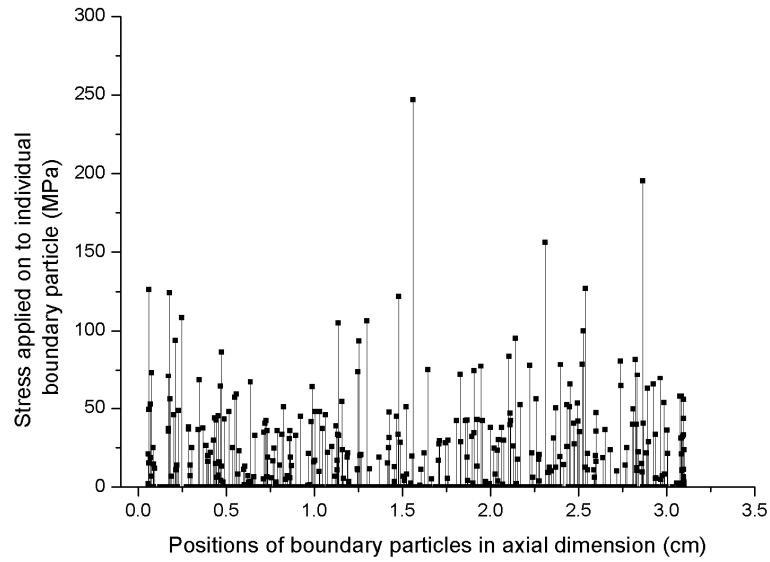


(b) Membrane boundary

Figure 3-6. Positions of boundary particles shown on a squeezed axial-radial plane for two different boundaries



(a) Membrane boundary



(b) Rigid boundary

Figure 3-7. Confining pressures applied to individual boundary particles for two different boundary conditions

The monitored stress-strain curves in Figure 3-5 show that the material under a rigid-wall boundary condition exhibits a higher strength than when membrane boundary conditions are applied: 418 MPa as compared to 352 MPa. Failure occurs at a relatively larger strain under rigid-wall boundary condition than under membrane boundary condition (0.8% versus 0.65%). Although less noticeable than strength, deformability is also affected by the boundary conditions. In the initial elastic loading range, the material has a slightly larger Young's modulus under rigid-wall boundary condition than under membrane boundary condition. After initial elastic loading range, the stiffness of the material drops faster under membrane boundary condition than under rigid-wall boundary condition.

The reason for the differences in both strength and deformability between rigid-wall and membrane boundary conditions lies in the interaction between the boundary and the specimen. In order to further investigate the boundary interaction, the positions of the boundary particles (Figure 3-6) and the stresses applied to each boundary particle (Figure 3-7) are monitored for the two different boundary conditions. The stress applied to the i^{th} boundary particles, σ_i^r , under rigid boundary condition is determined as:

$$\sigma_i^r = \frac{F_i^r}{\pi R_i^2} \frac{\sum_{i=1}^{N_b^r} \pi R_i^2}{A_b^r} \quad (3-5)$$

where F_i^r is the contact force calculated from the overlap between rigid wall and the boundary particle; A_b^r is the initial area of circumferential boundary of the specimen; N_b^r is the number of boundary particles (under membrane boundary condition); and R_i is the radius of boundary particle.

As depicted in Figure 3-7 (a), confining pressures applied to membrane boundary particles are the same for each particle, and are equal to 13.2 MPa, which is a weighted

value to approximately obtain the effect of input confining pressure (10 MPa). However, the confining pressures applied by using rigid-wall boundary particles vary largely: from zero to 250 MPa (Figure 3-7 (b)). For rigid-wall boundary, the boundary particles are artificially aligned to a rigid wall. This rigid-wall boundary constrains the failure and deformability processes, and introduces a highly inhomogeneous state of stress (Figure 3-7 (b)). Depending on the material type and loading condition, the failure pattern of a cylindrical specimen under triaxial loading conditions may vary, but during the shearing phase the circumferential boundary will no longer be cylindrical. A rigid-wall boundary, which is always cylindrical, hence overly constrains the boundary and tends to produce higher strength and stiffness than the actual condition does. During shearing, when membrane boundary condition is applied, some boundary particles tend to expand out (Figures 3-4 (a) and 3-6 (b)) at constant applied stress (Figure 3-7 (a)). However, when a rigid boundary condition is applied, these particles are constrained to a rigid wall (Figures 3-4 b) and 3-6 (a)), which produces higher stress applied to these particles (Figure 3-7 (b)). On the other hand, when a rigid boundary condition is applied, some boundary particles may have lower, even zero, stresses (Figure 3-7 (b)), because the confining pressure is mainly taken by those boundary particles which tend to expand out.

3.3.3 Simulation Procedures for Triaxial Tests

The confining pressure is first applied on all boundary particles (all-around pressure) to reach an equilibrium state. Under this all-around confining pressure, the specimen develops a displacement at the top end of the specimen. Then an axial displacement is applied incrementally while keeping the confining pressure constant on circumferential boundary particles.

The shearing phase for a triaxial test is simulated by applying an incremental displacement at the top end of specimen while the bottom end is fixed in the vertical direction. At each incremental step, the top-end displacement is increased by a certain amount, and the displacement is then kept constant until the system reaches equilibrium. The equilibrium state can be indicated by monitoring either the system energy history or the balances between the stresses applied at the two ends of the specimen. In the simulations carried out in this research, the latter one was used to check the equilibrium state during a simulation; displacement increment was increased if the relative difference of stresses calculated at the two ends of specimen is smaller than 1%. By monitoring the normal stress and strain in the axial direction, the stress-strain curve can be easily obtained, which is then used to analyze the macro material properties of the model specimen, i.e., deformability and strength.

3.4 STATIC CALIBRATION

In order to simulate a specific quasi-static problem, the micro parameters of the DEM model should be calibrated to reproduce similar macro material properties as desired. There are two types of micro parameters to be determined in DEM, i.e., deformability and strength parameters. These micro parameters are calibrated with uniaxial tests and triaxial tests (axi-symmetric).

3.4.1 Experimental Results

In order to make the dynamic model calibration consistent with the static model calibration, sets of experiments, including both quasi-static and dynamic tests, were carried out on the same kind of rock, in UT Rock Lab by using the GCTS RDS-300 system. The tested material is granite, which is fairly homogeneous, so no large scatter in

material properties such as deformability and strength due to fractures will be expected. The specimens used in the tests are cylindrical with dimensions of diameter in 50 mm and height in 100 mm.

Several triaxial tests under different confining pressures of 0, 1, 2 and 5 MPa, respectively, have been carried out. These relatively low confining pressures were typically used for quasi-static model calibration because high confining pressures are not to be expected in rock fall analyses. All the tests were tested at a strain rate of $1.0 \times 10^{-5} \text{ s}^{-1}$.

Table 3-2. Results of triaxial tests

σ_3 (MPa)	$\sigma_{1, failure}$ (MPa)	E (tangent modulus at 50% of failure load)(GPa)	ν (at 50% of failure load)	$\varepsilon_{, axial failure}$ (%)
0	162.4	22.4	0.26	1.08
1	172.5	23.5	0.24	0.71
2	186.7	27.1	0.27	0.77
5	208.7	22.7	0.19	0.71

The test results are shown in Table 3-2, and the failure envelope is shown in Figure 3-8. The failure mode for uniaxial compression test ($\sigma_3 = 0$) is different from that under confining pressure: under uniaxial compression, the specimen failed in “split” mode (Figure 3-9), which is typical for brittle material, whereas under triaxial compression, the classical “shear” failure mode was observed (Figure 3-10).

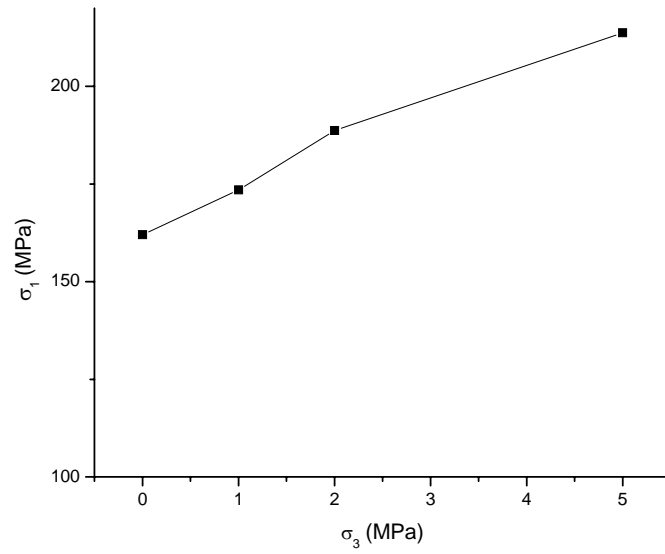


Figure 3-8. Experimental failure envelope of granite used for DEM model calibration



Figure 3-9. Failure pattern (split) in uniaxial compression tests on granite



Figure 3-10. Failure pattern (shear) in triaxial compression tests on granite

3.4.2 Identification of Micro Deformability Parameters

In the calibration process, the experimental data shown in Table 3-2 and Figure 3-8 were used to calibrate both deformability and strength parameters of the model.

A cylindrical specimen with a height of 100 mm and 50 mm diameter was prepared for calibration using a random packing of 2,500 spheres. The size of the specimen is the same as the one used in the experiments. The density is $2,600 \text{ kg/m}^3$ as measured. The coefficient of interaction range was chosen as 1.1.

Deformability parameters include particle's Young's modulus, E_c , and the ratio of normal stiffness over shear stiffness at contact, K_s / K_n , where the contact normal stiffness is determined by

$$K_n = \frac{\pi E_c D_{eq}^{A,B}}{4}. \quad (3-6)$$

These micro deformability parameters are calibrated to match the material's macro deformability parameters: Young's modulus, E , and Poisson's ratio, ν , which were determined from experiments as $E = 23.9$ MPa and $\nu = 0.24$, respectively.

The identification of deformability parameters was carried out under non-failure condition by means of DEM uniaxial compressive tests. The average stresses in the assembly can be determined either by the method of Liao (to determine the full stress tensor) (Liao 1997) or simply by averaging the contact forces on both the bottom and top ends to get the axial stress. The latter one was used in the simulations carried out in this research.

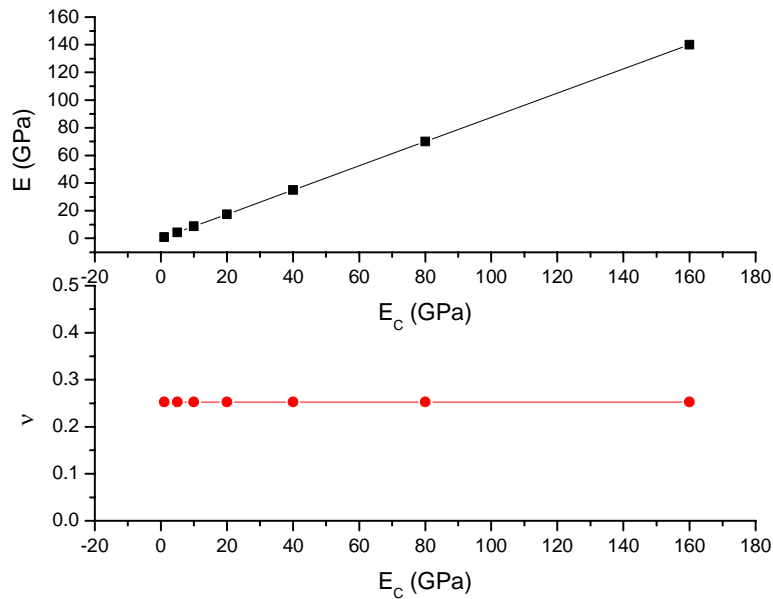


Figure 3-11. The relationship between macro elastic properties and E_c

As can be seen in Figures 3-11 and 3-12, material's Young's modulus, E , is related to both particle's Young's modulus and the ratio K_s / K_n , while material's Poisson ratio ν is only related to the ratio K_s / K_n . When determining material's

Young's modulus, E , particle's Young's modulus and the ratio K_s / K_n are independent of each other. This allows us to investigate this individual effect on E and then combine those effects together to determine material's Young's modulus E as follows.

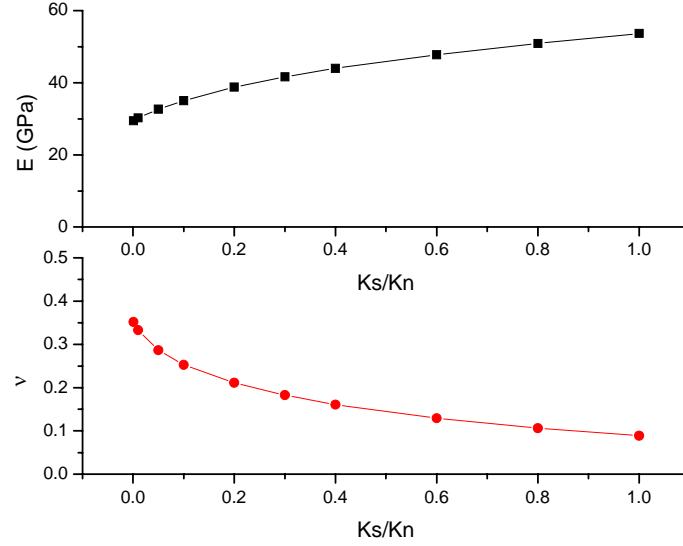


Figure 3-12. The relationship between macro elastic properties and K_s / K_n

Different combinations of E_c and K_s / K_n are used to set up a series of simulations for a given random packing. A sensitivity analysis is carried out by varying one of the factors and fixing the other factor. As seen in Figure 3-11, the material's macro Young's modulus, E , increases linearly with particle's Young's modulus, E_c , and the material's macro Poisson's ratio does not change with particle's Young's modulus, E_c . By fitting the simulation results (as shown in Figures 3-13 and 3-14), the following relationships are obtained based on formulas presented by Liao (Liao 1997) :

$$E = 0.937 E_c \left(\frac{0.794 + 2.589 \frac{K_s}{K_n}}{1 + 1.380 \frac{K_s}{K_n}} \right) \quad (3-7)$$

$$\nu = 0.544 \left(\frac{0.634 + 0.192 \frac{K_s}{K_n}}{1 + 3.732 \frac{K_s}{K_n}} \right) \quad (3-8)$$

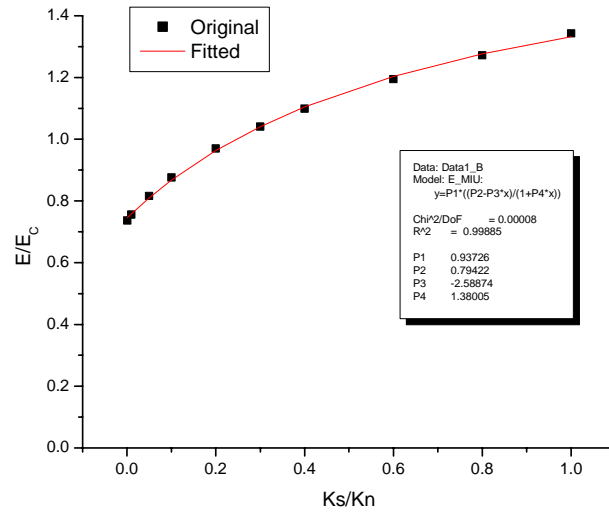


Figure 3-13. Fitting results: material's Young's modulus vs. K_s / K_n

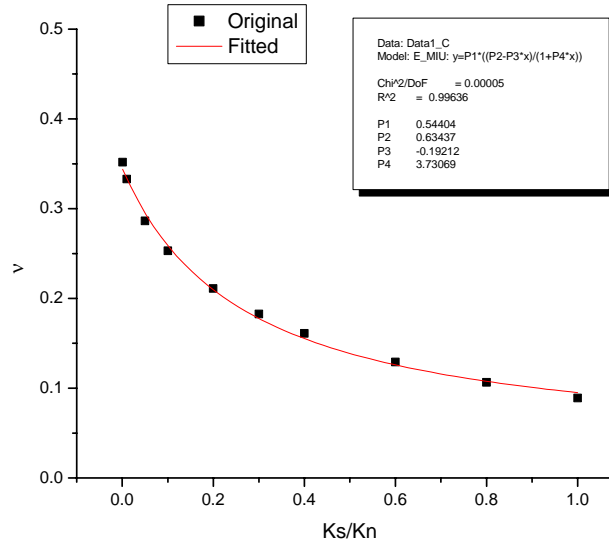


Figure 3-14. Fitting results: material's Poisson's ratio vs. K_s / K_n

Equations (3-7) and (3-8) can be solved for the micro deformability parameters, which are found to be equal to $E_c = 27.2 \text{ GPa}$ and $\frac{K_s}{K_n} = 0.098$ (as shown in Table 3-3).

With these model parameters, the simulated macro properties are as shown in Table 3-4 (third row, columns 2 and 3), which are very close to the experimental results. These two equations are only valid for a given packing structure including the number of particles, particle sizes and size distribution.

Table 3-3. Model parameters used in the simulations

Model parameter	$E_c \text{ (GPa)}$	$\frac{K_s}{K_n}$	$c \text{ (MPa)}$	φ	$T \text{ (MPa)}$
Value	27.2	0.098	385.0	60°	110.2

Table 3-4. Macro-properties of experimental and simulated results

Property	$E \text{ (GPa)}$	ν	$q_u \text{ (MPa)}$	$\varphi \text{ (degree)}$	$c \text{ (MPa)}$
Experimental	23.9	0.24	162.4	40.0	15.2
Calibrated	23.7	0.25	160.0	37.8	18.3

3.4.3 Identification of Micro Strength Parameters

There are two kinds of failure mechanisms, i.e. shear and tension, controlling the material failure. They can affect each other because either type of failure may change local stress conditions. This actually makes the failure process more complicated and makes it difficult to calibrate strength parameters. Strength parameters include the contact tensile strength, T , and c and φ for shear components as already described in the failure criteria of the model, (Section 2.3.3). These strength parameters are calibrated under

different confining pressures to match a failure envelope obtained from experiments. This process is very time-consuming as each trial parameter set needs to be simulated under different confining pressures to reach the peak strength point of a stress-strain curve.

In order to identify the strength parameters, an inverse method is used. The main objective of the inverse method used here is to identify a selected set of unknown modeling parameters in DEM to improve the agreement with experimental data. The experimental failure envelope is usually obtained by setting up a set of triaxial tests with different confining pressures to get the ultimate strength. In order to match the experimental failure envelope, some representative points, $(\sigma_{1_exp}^i, p^i)$, from the experimental failure envelope are selected to delineate the envelope as shown in Figure 3-15, where $\sigma_{1_exp}^i$ is the ultimate axial strength under confining pressure p^i ($i = 1, 2, 3 \dots n$), and n is the number of points chosen to describe the envelope. The corresponding confining pressures, p^i , are used for DEM simulation setup. For a given set of micro strength parameters, $[c, \phi, T]$, the simulated ultimate strength under confining pressure p^i , is denoted as $\sigma_{1_sim}^i$. The objective function

$$f(c, \phi, T) = \sqrt{\frac{1}{n} \sum_{i=1}^n \left(\frac{\sigma_{1_exp}^i - \sigma_{1_sim}^i}{\sigma_{1_exp}^i} \right)^2} \quad (3-9)$$

is used to evaluate the difference between experimental and simulated failure envelopes.

The global optimization package SNOBFIT (Neumaier 2008) is utilized in the calibration process, in which an optimization problem is solved with objective function $f(V)$ subject to $V \in [L, U]$, where V is the parameters set, $[c, \phi, T]$, to be identified, and $[L, U]$ is the parameter space, which is bounded by using specified ranges as

$$\begin{bmatrix} c_{low} & c_{up} \\ \phi_{low} & \phi_{up} \\ T_{low} & T_{up} \end{bmatrix}.$$

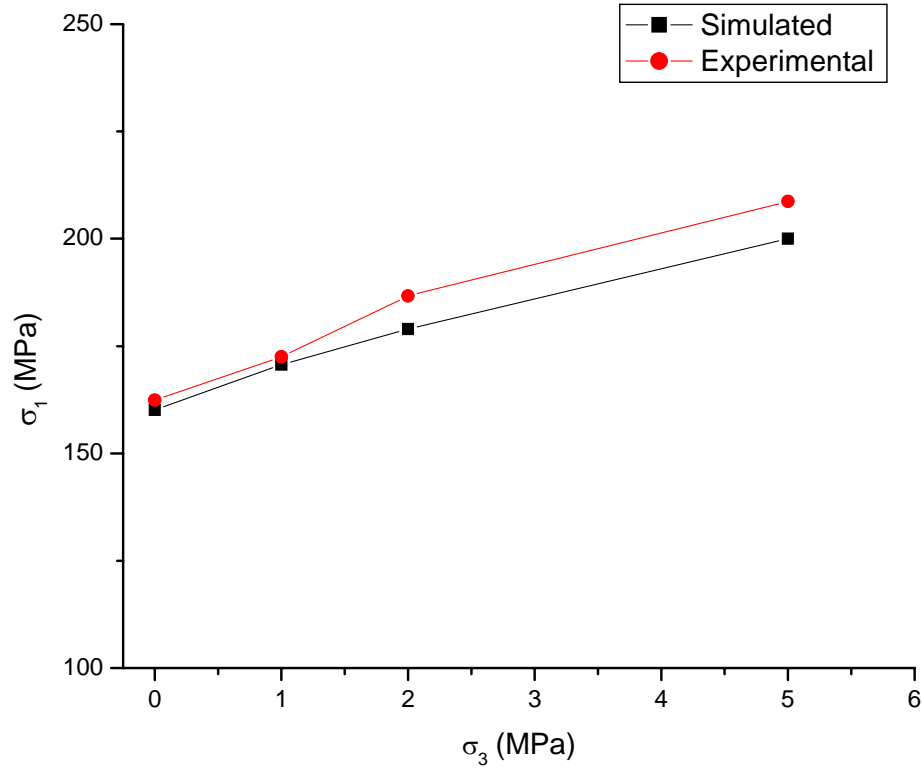


Figure 3-15. Calibrated strength envelope using a global optimization method compared against experimental one

SNOBFIT performs global and local search by branching and local fits to find the global optimal point. This technique is especially suitable for optimizing problems with multiple local optimal points. In the calibration of strength parameters, the objective function in Equation (3-8) is not available in an analytical form because a DEM code accounting for an intricate physical process is utilized to compute the failure envelope with specified micro strength parameters. SNOBFIT is the only global optimization code that handles non-analytical objective functions. The way in which the micro strength parameters affect the material strength is far complex, and the relationships of these strength parameters involved in determining the objective function, $f(c, \varphi, T)$, may not

be monotonic. Extensive numerical simulations have shown that SNOBFIT is capable of optimizing this complicated objective function to find the micro strength parameters.

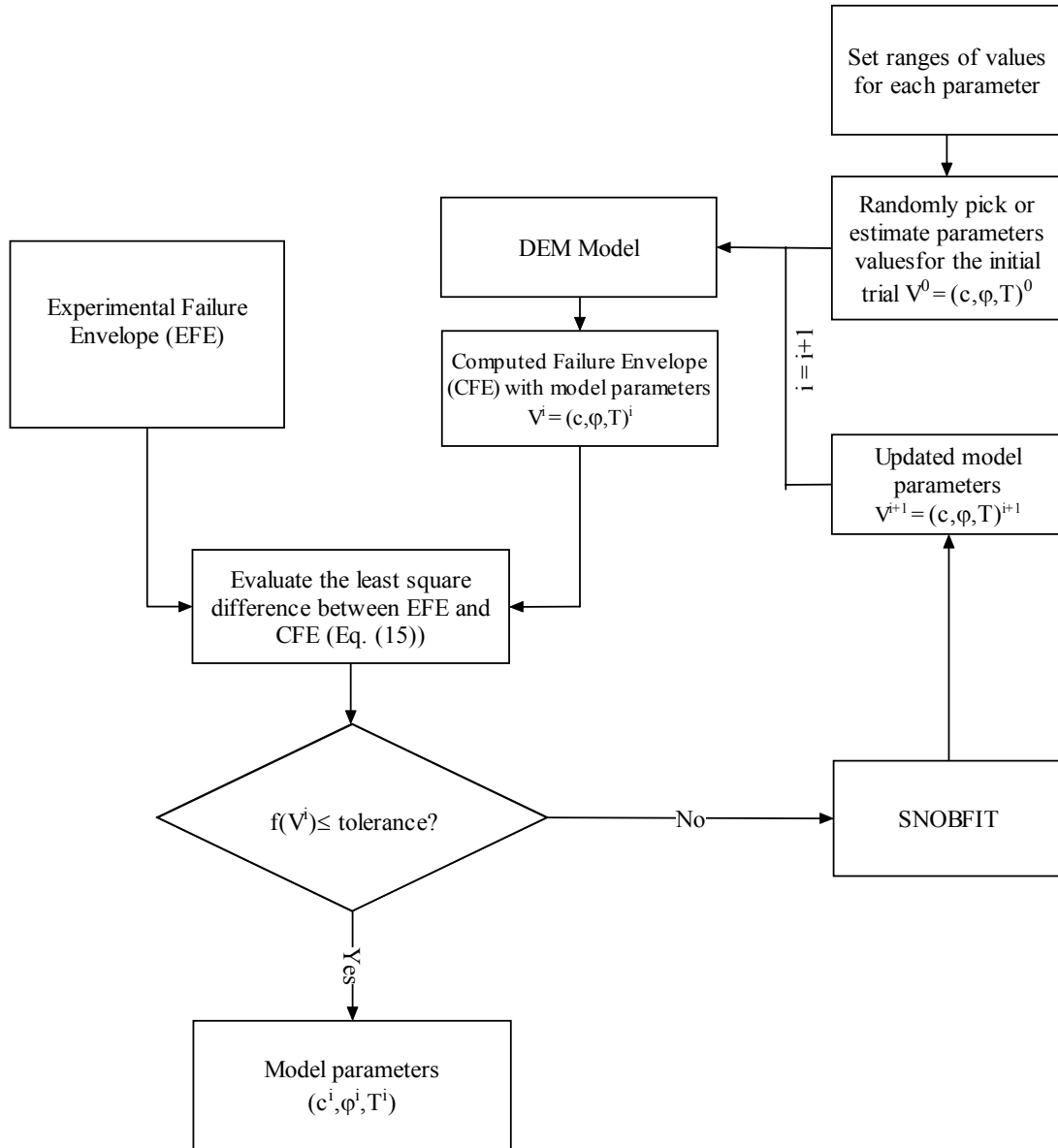


Figure 3-16. Flow-chart of the inverse method for strength parameters identification using the global optimization package SNOBFIT

At each step of the optimization process, SNOBFIT generates a specified number of evaluation points, and then proceeds by successively partitioning the parameter space and building local quadratic models of the objective function. The search process is terminated when a given minimal objective function value is reached or if no better solution can be found after a specified number of steps. Compared to typical stochastic algorithms, SNOBFIT does not require as many function evaluations and is therefore applicable to problems with expensive function evaluations, such as a DEM to obtain a failure envelope.

The overall calibration procedure proceeds iteratively. With reference to Figure 3-16, one starts from either an initial guess of model parameters or parameter values randomly chosen in parameter space. Then, the unknown parameters V are iteratively updated to find the optimized parameters: at the i^{th} iteration, the DEM code is invoked to obtain a computed failure envelope (CFE) corresponding to parameters V^i . The CEF is then compared to the experimental failure envelope (EFE) by evaluating the objective function $f(c, \varphi, T)$ (Equation 3-9). If the value of the objective function is smaller than the given tolerance, optimized model parameters will be output. Otherwise, the model parameters are updated by calling SNOBFIT. In the calibration process, the DEM code and SNOBFIT are repeatedly invoked until CFE matches EFE by meeting the tolerance criterion, which is set as 5% because of the intensive computational effort involved in obtaining the value of the objective function. In the calibration work presented in this

research, $\begin{bmatrix} c_{low} & c_{up} \\ \varphi_{low} & \varphi_{up} \\ T_{low} & T_{up} \end{bmatrix} = \begin{bmatrix} 10 \text{ MPa} & 500 \text{ MPa} \\ 10^0 & 80^0 \\ 10 \text{ MPa} & 150 \text{ MPa} \end{bmatrix}$ is used for the parameter ranges for the

tested granite, which are roughly estimated based on available experimental strength data. The number of points, n , chosen to delineate the failure envelope is 4.

All the simulations for strength parameter calibration use the deformability parameters identified in Table 3-3 (column 2 and 3). The calibrated strength parameters are $c = 385 \text{ MPa}$, $\varphi = 60^\circ$ and $T = 110.2 \text{ MPa}$. The calibrated failure envelopes are shown in Figure 3-15, which shows that the simulated envelope with calibrated micro strength parameters matches well the experimental one. A total number of 65 iterations were necessary to find the calibrated micro strength parameters with a tolerance criterion of 5%, i.e. 65 failure envelopes were generated, each corresponding to different strength parameter combinations.

The corresponding stress-strain curves under different confining pressures are plotted in Figure 3-17. It shows that specimens under higher confining pressure fail at larger strain and under higher deviator stress ($(\sigma_1 - \sigma_3)_{\text{failure}}$).

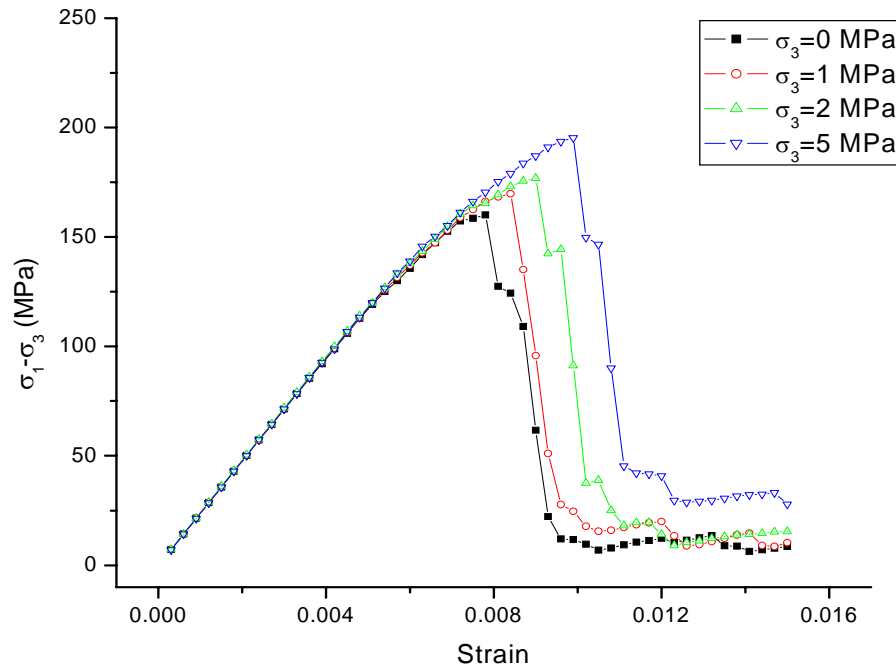


Figure 3-17. Simulated stress-strain curves using the calibrated model

The calibrated DEM model can be a good tool to investigate the failure of a brittle material by shedding light on the following aspects.

The macro failure of a brittle material is caused by the evolution and propagation of local cracks, which can be identified by the history of the number of contact failures (cracks). When a specimen fails in a simulation, a failure zone forms, along which, contacts are broken apart by tensile failure cracks and particles are rearranged. For triaxial compressive tests, the stress-strain curve can be divided into three distinct stages (Figure 3-18) based on the generated cracks:

Stage I: Very few cracks are generated and the material behaves elastically.

Stage II: Tensile cracks are gradually generated over a strain-loading increment; cohesion component of the cracked contact is destroyed, and the material behaves plastically.

Stage III: The frictional strength (residual contact shear strength) starts to mobilize gradually until the residual shear strength of the material is reached along a shear band, which is made up of those particle contacts firstly broken by tensile failure followed by loss of cohesion in the shear strength at contact. In this stage, the newly generated contact failures in tension are very few because the additional strain mainly takes place in the shear band, which is formed by broken contacts. This stage characterizes the post-peak behavior of compression test.

When the loading increases, the cohesion component of shear strength is gradually destroyed by tensile cracking. The normal stress-dependent frictional strength (residual shear strength at contact) is only mobilized after the specimen reaches macro failure (peak strength), when the cohesional component of shear strength is significantly reduced, and the rock fragments can move relative to each other in shear. In other words,

the residual frictional strength at contact (micro level) only affects the post-peak behavior for brittle materials.

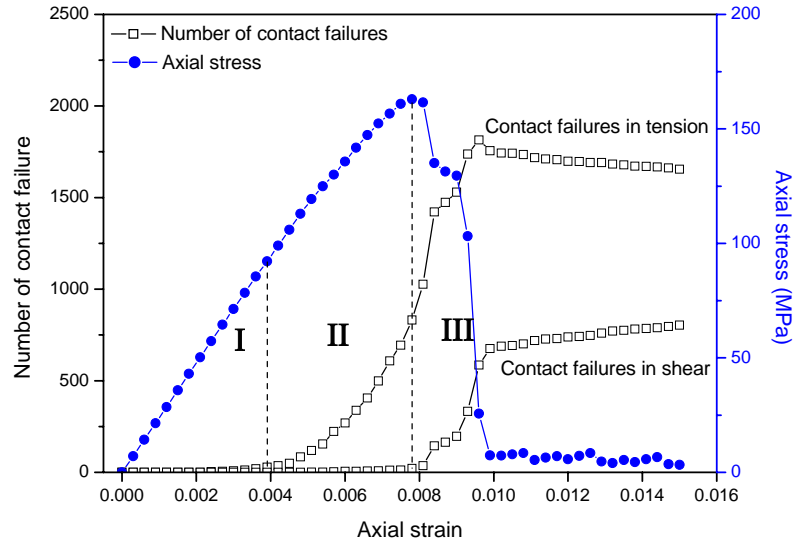


Figure 3-18. History of contact failures during a simulated uniaxial compressive test with the calibrated model

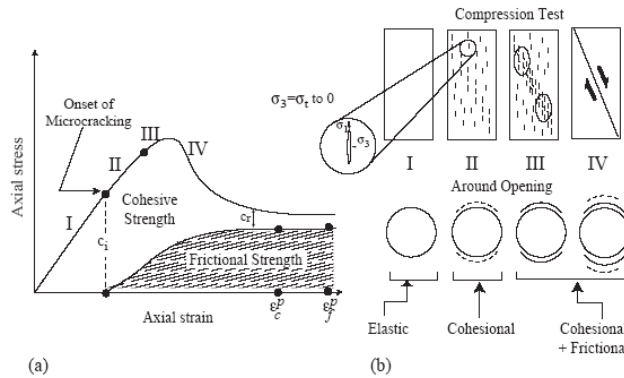


Fig. 10. Mobilization of the strength components in the CWFS model: (a) in the laboratory compression tests, (b) around underground openings: c_i and c_r are the initial and residual cohesion, respectively, and ϵ_c^p and ϵ_f^p represent the plastic strain components when the frictional and cohesive strength components have reached these ultimate values [10].

Figure 3-19. Mobilization of the strength components (after ref. (Hajiabdolmajid et al. 2002))

The results of failure process for compression test shown in Figure 3-18 can be compared with the investigations made in (Hajiabdolmajid et al. 2002) (on page 736 and Fig. 10) (Figure 3-19), in which Hajiabdolmajid, et al. concluded that, in relatively low confinement environments, the delay in frictional strength mobilization is characteristic of brittle failure in geomaterials. They argue that “The cohesive component of strength is the predominant strength component at the early stage of brittle failure and cohesion loss is the predominant failure process leading to the observed brittle behavior. The cohesive strength is gradually destroyed by tensile cracking and crack coalescence. The normal stress-dependent frictional strength can only be fully mobilized after the cohesive component of strength is significantly reduced, much damage has accumulated, and when the rock fragments can move relative to each other in shear.” These investigations agree well with the author’s observations obtained by modeling the failure behavior of brittle materials. Based on the author’s investigations, in brittle materials tensile cracks at particle contacts dominate the failure process before reaching the peak strength. When the loading increases, the cohesion component of shear strength is gradually destroyed by tensile cracking as shown in Figure 3-18. The normal stress-dependent frictional strength (residual shear strength at contact) is only mobilized after the specimen reaches macro failure (peak strength), when the cohesive component of strength is significantly reduced, and the rock fragments can move relative to each other in shear. In other words, the residual frictional strength at contact (micro level) mainly affects the post-peak behavior of brittle materials.

3.4.4 Comparisons against PFC’s BPM Model

The developed DEM model and calibration algorithm was compared against PFC’s BPM model (Potyondy and Cundall 2004) by calibrating the behavior of Lac du

Bonnet granite. PFC's BPM is often used to model intact rock behavior. However, if clusters of spheres are not used, it has difficulties in modeling the behavior of Lac du Bonnet granite, whose strength envelope displays a high slope, and which has a high ratio of compressive strength to tensile strength.

A cylindrical specimen with a height of 3.2 cm and 1.6 cm diameter was prepared for calibration using a random packing of 2,500 spheres. To allow comparison, the size of the specimen is the same as the one used in Hentz et al.'s work (Hentz et al. 2004a). The coefficient of interaction range was chosen as 1.3 for this case rather than 1.1 used in previous case. The model was calibrated against the macro properties of Lac du Bonnet granite shown in Table 3-5. The calibrated micro deformability parameters are $E_c = 104.7 \text{ GPa}$ and $\frac{K_s}{K_n} = 0.085$, and the calibrated micro strength parameters are $c = 429 \text{ MPa}$, $\varphi = 68^\circ$ and $T = 34.2 \text{ MPa}$ (also shown in Table 3-1). The calibrated failure envelopes are shown in Figure 3-20, which shows that the simulated envelope with calibrated micro strength parameters matches well the experimental one. The results demonstrate a prominent pressure-dependent behavior compared to PFC model results (Table 1 and Fig. 12 (Potyondy and Cundall 2004)). Potyondy and Cundall (Potyondy and Cundall 2004) concluded that: "This discrepancy may arise from the use of circular and spherical grains in the present model, and it could be reduced by using grain shapes that more closely resemble the complex-shaped and highly interlocked crystalline grains in granite." When using clusters of spheres, a good match with experimental envelope slope was obtained, but other problems, like discrepancy in dilation and post-peak behavior, were observed. It turns out that, in the model used in this research, the author can reproduce the behavior of Lac du Bonnet granite by an effective calibration technique (Figure 3-20). Unlike in author's model, the shear strength in BPM model is not pressure-

dependent (it only includes cohesion), which might cause the difficulty in modeling a high strength envelope slope.

Table 3-5. Macro-properties of Lac du Bonnet granite

Property	E (GPa)	ν	q_u (MPa)	ϕ (degree)	c (MPa)	σ_t (MPa)
Experimental results	69	0.26	216	59	30	9.3
Author's DEM model	71	0.25	220	58	32.6	19.1
PFC3D BPM model	69.2	0.256	198.8	32.1	55.1	27.8

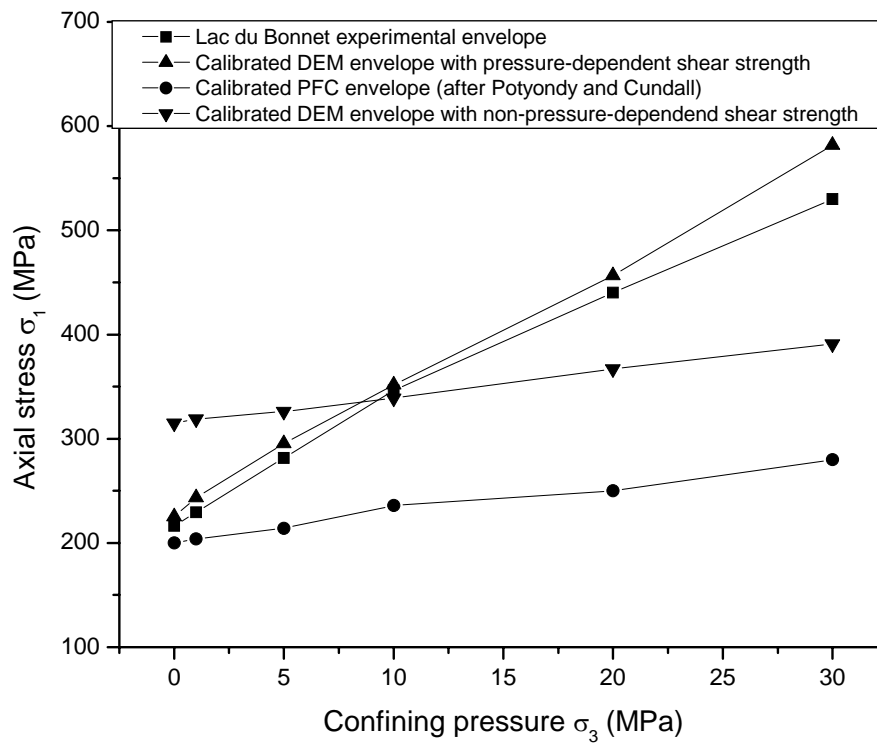


Figure 3-20. Comparison against PFC's BPM in calibrating Lac du Bonnet granite

In order to understand the importance of pressure-dependent shear strength in simulating a high strength envelope slope, a DEM model with a non-pressure-dependent shear strength ($\varphi = 0$ in Equation (2-15)) was calibrated against the experiment data of Lac du Bonnet granite as used above. The values of micro deformability parameters are the same as those identified previously. Now only two parameters are involved in strength parameter identification, i.e., c , and T .

The optimum result obtained after 100 iterations has strength parameters equal to $c = 239$ MPa, and $T = 47$ MPa and its failure envelope is shown in Figure 3-20 (failure envelope for non-pressure-dependent shear strength). It shows that the Lac du Bonnet granite experimental failure envelope cannot be modeled by only using model strength parameters c and T . This model is still different from PFC's BPM model because of the concepts of equilibrium distance and interaction range used in the model, therefore the identified model strength parameters cannot be directly compared to those used in the BPM model. It is concluded that pressure dependent micro shear strength is critical to correctly simulate high slope failure envelopes.

In practice, the Brazilian test is usually carried out to determine the material tensile strength. However the strength parameters calibrated from triaxial tests to determine material tensile strength cannot be directly used to model the Brazilian test. Because the packing assembly used for the Brazilian test (disk) is different from packing assembly used for triaxial test (cylinder), the calibrated strength parameters for the triaxial test specimen may not be suitable for a disk specimen any more.

From a numerical point of view, a direct tension test can be easily set up to determine tensile strength. With the calibrated strength parameters, a direct tension test is simulated by applying incremental tensile displacement loading. The tensile strength between specimen ends and loading platens (interface) are set high enough to make sure

that no failure can occur at the interface. As shown in Figure 3-21, the simulated tensile strength is about 19.1MPa (for mean particle radius of 0.70 mm), which is higher than the experimental value of 9.3MPa obtained from Brazilian tests. The tensile strength simulated by PFC3D in Potyondy's work (Potyondy and Cundall 2004) was about 28 MPa. The difference in the simulated tensile strength may be caused by different reasons. First, the model used in this work is different from PFC's BPM in several ways, such as concepts of equilibrium distance and interaction range, and pressure-dependent shear strength. Further, Potyondy and Cundall used different specimens used for simulating triaxial and Brazilian tests, and hence the internal packing structures were different. As highlighted in this dissertation, in order to model a specified material, different packing structures should have different micro model parameters. However, Potyondy and Cundall used the model parameters identified for uniaxial tests even in modeling Brazilian tests. Lastly, the tensile strength obtained from Brazilian tests is normally higher than that obtained from direct tension test because Brazilian tests introduce biaxial state of stress, in which some micro cracks may be due to compressive load. Usually, it is difficult to fully model a material behavior with very high ratio of uniaxial compressive strength over tensile strength. However, the ratio of uniaxial compressive strength to tensile strength of about 12 obtained here is a representative value for intact rock material.

3.4.5 Discussions on Model Calibration

This section follows the previous section of comparisons against PFC's BPM model with the example of modeling Lac du Bonnet granite to discuss some important aspects associated with DEM model calibration.

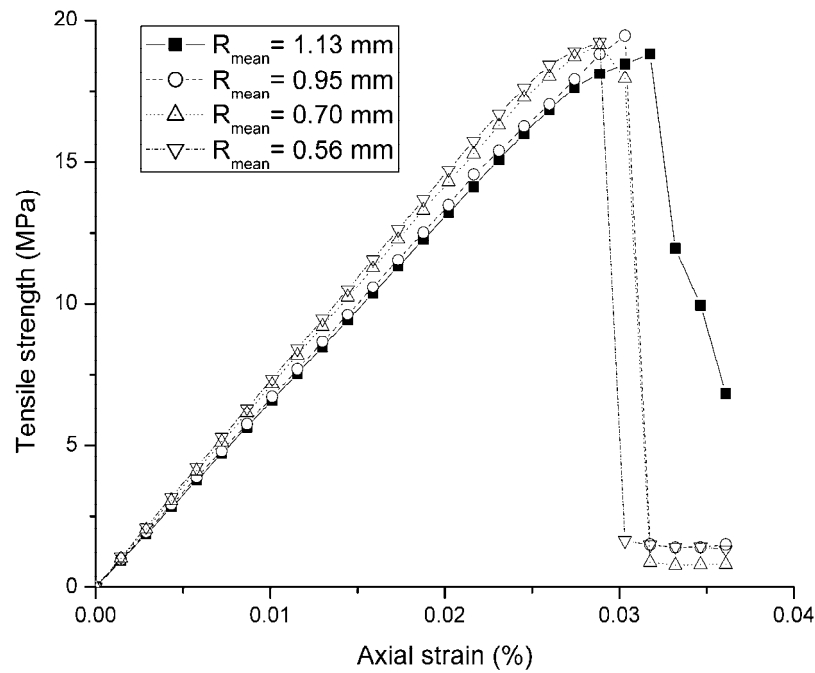


Figure 3-21. Simulated stress-strain curves for direct tension test with different particle sizes for Lac du Bonnet granite

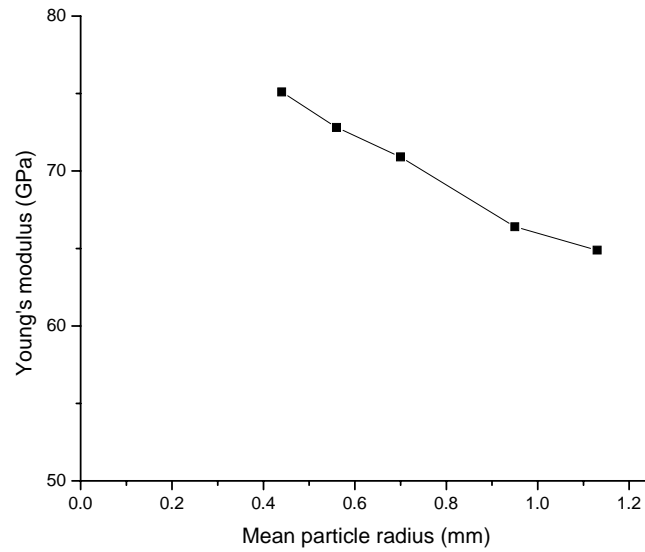
It should be noted that the calibrated values of micro strength parameters in DEM model are different from the ones at macroscopic level. In DEM modeling, failure either in tension or shear is initiated from those highly stressed contact bonds and propagates subsequently. Hence, calibrated micro strength parameters could be much higher than effective strengths, as can be seen from the strength parameter calibration of Lac du Bonnet granite, in which the calibrated model strength parameters c , ϕ and T are all much higher than macroscopic ones as shown in Table 3-5.

Unlike other numerical methods such as finite element method, in which model parameters can be directly derived from experimental results, DEM deformability and strength parameters used at the micro level are different from the material properties at

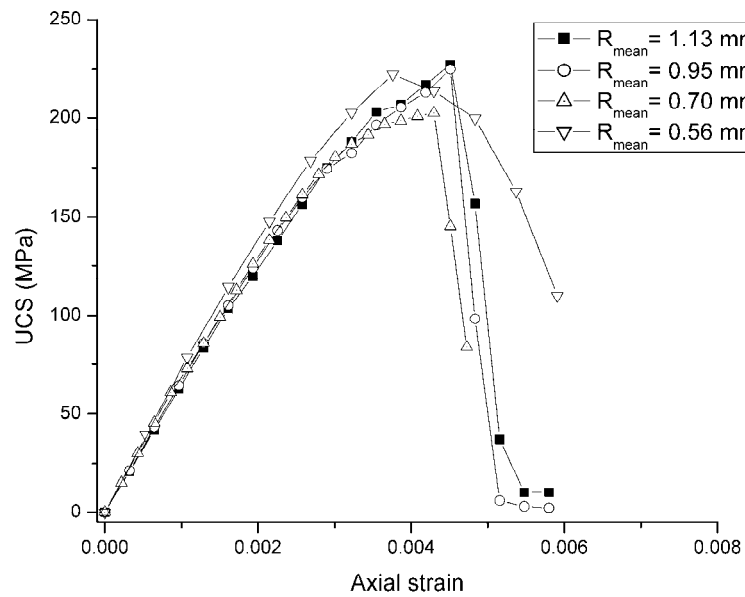
the macro level. That is why special calibration algorithms were proposed. In DEM modeling, specimens are prepared by random sphere packing. Different packings have different internal structures even for the same number of particles. These internal packing structures can affect the macroscopic behavior of packing assemblies. As a result, in DEM modeling, every packing specimen must be calibrated by using the algorithms discussed above to match the desired properties before using it in actual simulations. Usually, different packings should have different micro model parameters to match specific material properties.

The effect of internal packing structures on macro material properties was investigated in this section in terms of particle size and random process in packing. The investigation demonstrates that internal packing structure is an intrinsic part of material characterization in discrete element modeling.

First, packing assemblies with different mean particle sizes were considered while keeping all other micro parameters fixed. The mean particle radii for the five different packing assemblies are 0.44 mm, 0.56 mm, 0.70 mm, 0.95 mm, and 1.13 mm, respectively. Simulated results show that the particle size can affect macro properties in both deformability and strength. The Poisson's ratio is independent of particle size, while the Young's modulus exhibits a clear dependency upon particle size, with E decreasing from 75.1 GPa to 65.2 GPa as particle size increases from 0.56 mm to 1.13 mm (Figure 3-22 (a)). The reason to this dependence is unknown, but it should be related to the internal structure of random packing, because such dependence is not observed while using regular packings, in which spheres are in the same size and face centered. The simulated uniaxial unconfined compressive strength and tensile strength exhibit no clear increasing or decreasing trends with particle size as shown in Figures 3-21 and 3-22 (b).



(a) Dependence of Young's modulus on particle size



(b) Stress-strain curves for different mean particle sizes

Figure 3-22. Effect of particle size on simulated macro properties

Different random processes in packing can also cause changes in internal packing structures. A set of triaxial simulations ($\sigma_3 = 10$ MPa) were performed with packing assemblies generated by different random processes while using the same type of particle sizes. Figure 3-23 shows that the difference in ultimate deviator stress ($(\sigma_1 - \sigma_3)_{\text{at failure}}$) resulted from random arrangement can be up to 15%. However, this random process has negligible effect on Young's modulus and Poisson's ratio.

Another important factor which can affect the model calibration is the coefficient of interaction range. The higher the coefficient of interaction range is, the lower values of the calibrated micro strength parameter are.

In conclusion, internal packing structures can affect macro material properties provided other micro-properties are fixed, and have to be taken into account in model calibration.

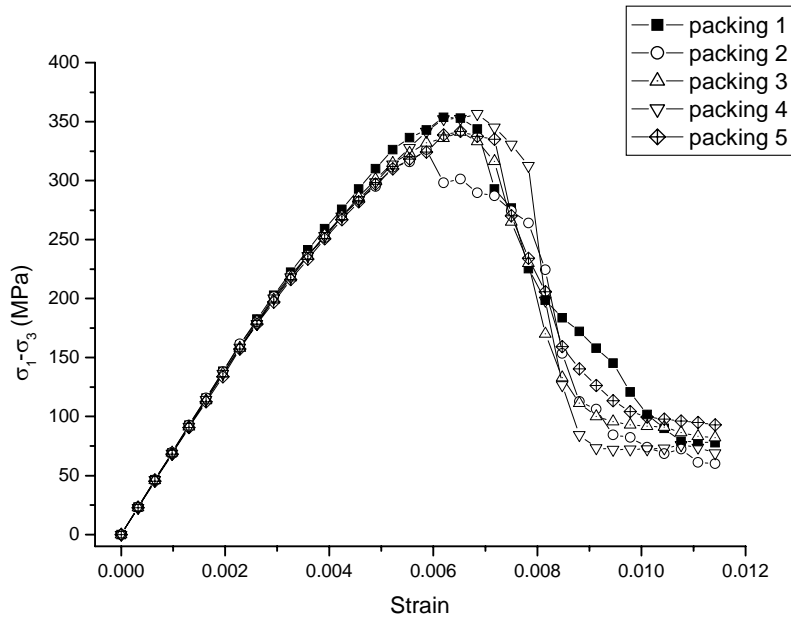


Figure 3-23. Effect of random distribution of particles on simulated material behavior in DEM modeling

3.5 VERIFICATION OF DYNAMIC PROBLEMS

3.5.1 Introduction

One of the key points of this research is to investigate the mechanisms that control impact fragmentation. Hence the dynamic behavior of rock materials under impact loading condition is of the great concern. One of the main features of dynamic behavior of rock materials is the loading-rate dependent dynamic strength, which a model must reproduce. The understanding of this rate effect has been the purpose of many experimental works, as well as of numerical models.

As indicated in Figure 3-24, the strain rate for rock falls ranges from about 0.5 to several hundred s^{-1} , but this is probably only for the case of rock block impact against hard rock (hard impacts). For rock falls onto a soft ground, most of kinetic energy dissipates via the ground by creating a plastic zone and by wave scattering, which tend to extend the impact duration. Hence, the loading and the loading rate applied to rock blocks are very low for rock falls onto soft grounds. Moreover, for rockfall impact, the strain rate mentioned here only refers to the impact zone, which accounts for a very small portion of the rock block. The remaining major portion of the rock block is subjected to very low strain rates. But it is the locally highly strain-rate loaded zone that initiates cracks and drives the propagation of cracks to create the general fragmentation process.

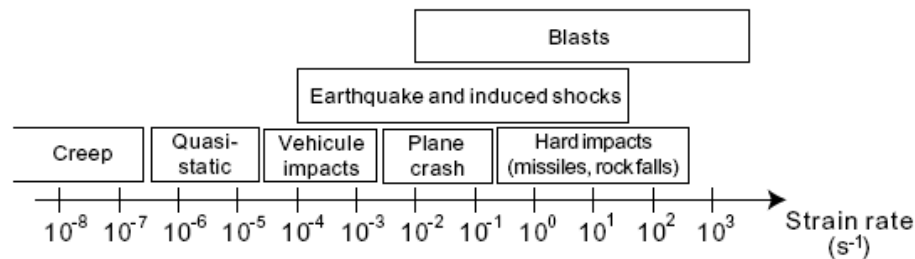


Figure 3-24. Regime of strain rates for different loading conditions (after (Hentz et al. 2004b))

Various experimental devices have been used to explore a wide range of strain rates (Giacomini et al.; Hentz et al. 2004a; Lankford 1980; Zhao 2003; Zhao et al. 1999). Compression tests have been performed, from static loading up to strain rates of 10^{-1} s^{-1} , with a hydraulic servo-controlled testing machine. With Drop Weight Impact tests, rates of 10^1 s^{-1} may be reached, but the energy transmitted to the specimen is limited by the size of the device. Higher strain rates as large as 10^2 s^{-1} can be obtained with a Split Hopkinson Pressure Bar (SHPB) test which has now become very popular.

As shown in Figure 3-25, a large number of experimental results on concrete were compiled by Hentz et al in terms of the dynamic strength over static strength ratio. These results show that at relatively lower strain rates, the strength increment with strain rate is less prominent than that at higher strain rates, where a sharp rise occurs at around the strain rate of 30 s^{-1} .

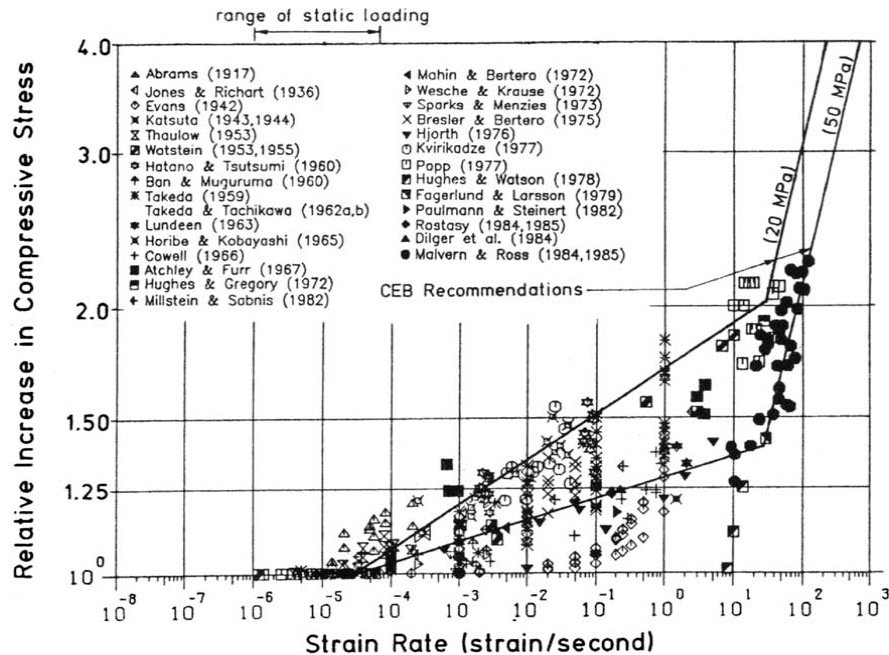


Figure 3-25. Strain rate effect on dynamic uniaxial compressive strength (after (Hentz et al. 2004b))

In order to make sure that the calibrated DEM model can also be used to model the dynamic behavior of rocks, dynamic tests using both a compression testing machine at low strain rates and a SHPB apparatus at higher strain rates were performed to verify the code on the same material used in triaxial tests for calibrating the quasi-static model (Section 3.4).

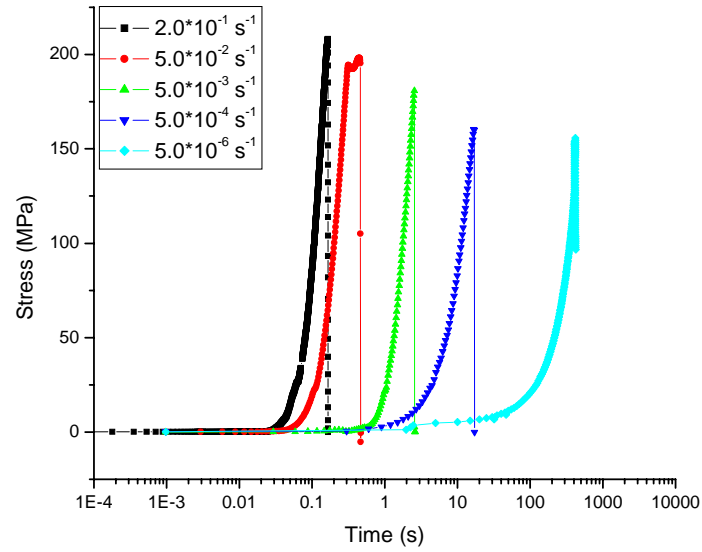
3.5.2 Dynamic Tests

3.5.2.1 Dynamic Compression Tests

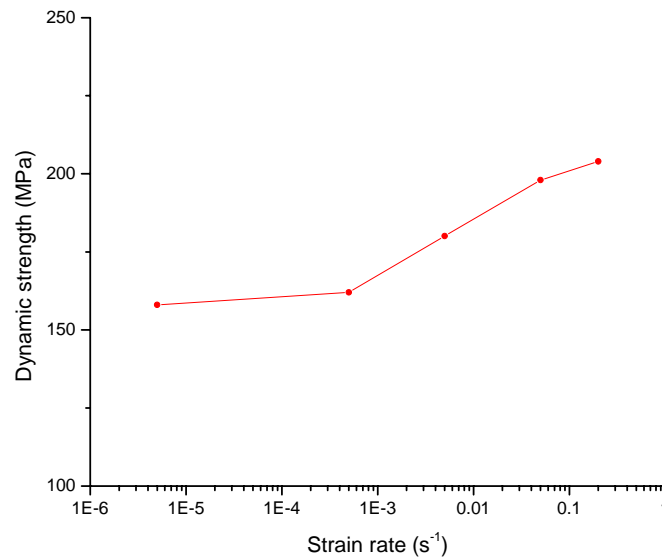
The specimens used for dynamic compression tests are the same size as the one used for triaxial tests. Five different strain rates were used in the uniaxial compression tests, namely, 5.0×10^{-6} , 5.0×10^{-4} , 5.0×10^{-3} , 5.0×10^{-2} and $2.0 \times 10^{-1} \text{ s}^{-1}$. The tests were conducted by controlling the displacement of the loading platen using the GCTS RDS-300 system in UT Rock Lab. The tested results given in Figure 3-26 show a clear effect of strain rate on dynamic strength especially when the strain rate is larger than $5.0 \times 10^{-4} \text{ s}^{-1}$. The dynamic strength does not increase much when strain rate increases from $5.0 \times 10^{-6} \text{ s}^{-1}$ to $5.0 \times 10^{-4} \text{ s}^{-1}$, and this range is typically considered as quasi-static state. The results shown in Figure 3-15 were obtained at strain rate of $1.0 \times 10^{-5} \text{ s}^{-1}$, in which the uniaxial strength is very close to the values obtained at strain rates of $5.0 \times 10^{-6} \text{ s}^{-1}$ to $5.0 \times 10^{-4} \text{ s}^{-1}$ as shown in Figure 3-26. When the strain rate is larger than $5.0 \times 10^{-4} \text{ s}^{-1}$, the dynamic strength is linearly dependent on strain rate in a logarithmic scale as shown in Figure 3-26 b).

Another interesting observation on these dynamic tests is that the size and number of fragments are directly related to the strain rate. As depicted in Figure 3-27, the higher the applied strain rate is, the larger number of fragments and the smaller size of the

fragments are generated. The further analysis on the effect of strain rate on the fragment size distribution will be addressed in Section 3.5.4.



(a) Stress histories of different strain rates



(b) Relationship between dynamic strength and strain rate

Figure 3-26. Effect of strain rate on dynamic strength of dynamic compression tests



a) $5.0 \times 10^{-6} \text{ s}^{-1}$



b) $5.0 \times 10^{-3} \text{ s}^{-1}$



c) $5.0 \times 10^{-2} \text{ s}^{-1}$

Figure 3-27. Fragmentation under different strain rates in dynamic uniaxial compression tests

3.5.2.2 Split Hopkinson Pressure Bar Tests

A typical SHPB experimental setup is outlined in Figure 3-28. It consists of two long aligned metallic bars with a short specimen placed between them. A projectile

impacts the free end of the input bar thus developing a compressive longitudinal incident wave $\varepsilon_i(t)$. Once this wave reaches the bar-specimen interface, part of it, $\varepsilon_r(t)$, is reflected, whereas the other part travels through the specimen and develops the transmitted wave $\varepsilon_t(t)$ in the output bar. These three waves are recorded by two strain gauges cemented on the input and output bars respectively. The recorded waves are then used to deduce the force and velocity at two ends of the specimen.

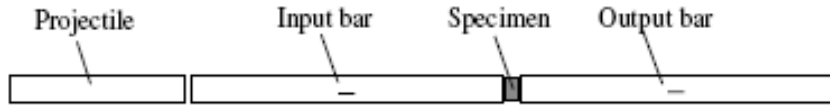


Figure 3-28 Sketch of SHPB test setup used to determine material's dynamic properties at high strain rates

As the three waves are not measured at bar-specimen interfaces, the recorded data have to be shifted in time and distance from the position of the strain gages to the specimen faces. Based on one dimensional wave propagation theory and the superposition principle, the forces $(F_{input}(t), F_{output}(t))$ and the velocities $(V_{input}(t), V_{output}(t))$ at both faces of the specimen are given by the following equations (Frew et al. 2001; Zhao 2003)

$$\begin{cases} F_{input}(t) = A_B E (\varepsilon_i(t) + \varepsilon_r(t)) \\ F_{output}(t) = A_B E \varepsilon_t(t) \\ V_{input}(t) = C_0 (\varepsilon_i(t) - \varepsilon_r(t)) \\ V_{output}(t) = C_0 \varepsilon_t(t) \end{cases} \quad (3-10)$$

where A_B , E and C_0 are the bar's cross-sectional area, Young's modulus, and the elastic wave speed.

In order to identify the material properties of tested materials (specifically, stress-strain relationship), Zhao (Zhao 2003) showed that a so-called three-waves formula give a correct average stress imposed on the specimen

$$\begin{cases} \dot{\epsilon}_s(t) = \frac{V_{output}(t) - V_{input}(t)}{l_s} \\ \sigma_s(t) = \frac{F_{output}(t) + F_{input}(t)}{2A_s} \end{cases} \quad (3-11)$$

where l_s and A_s denote the length and the cross-sectional area of specimen, respectively.

3.5.2.2.1 Experimental Setup and Data

SHPB tests were carried out at the Dynamic Lab of the Department of Aerospace Engineering and Engineering Mechanics at The University of Texas at Austin. The same granite material as used previously for model calibration was used (Section 3.4) for SHPB tests. The rock specimens that were used are cylindrical with a height of 13.1 mm and a diameter of 21.6 mm. The density is 2,600 kg/m³ and the average compressive wave speed is about 3,031 m/s deduced based on the Young's modulus of 23.9 GPa determined from quasi-static tests. The wave speed of the bars is 4,871 m/s and the Young's modulus is 193.7 GPa. The diameter of the input and output bars is 12.4 mm. The diameter of specimens were chosen much larger than the bar diameter so as to meet the ASTM standard D 4543 (ASTM 2007) in which the specimen diameter should be at least six times the maximum particle diameter in the material. In order to test a specimen with diameter of 21.6 mm, two adapters were used. But this will introduce some noise which should be considered in analyzing the recorded waves.

A high-speed camera was used to capture the failure process of the specimen and also to correlate the particle velocities at interfaces calculated from Equation (3-10) to the ones measured based on the movements of bars from captured pictures. As shown in

Figures 3-29 and 3-30, a typical failure process of the specimen was clearly captured with several cracks being initiated, then propagating, and eventually the whole specimen shattering into particles.

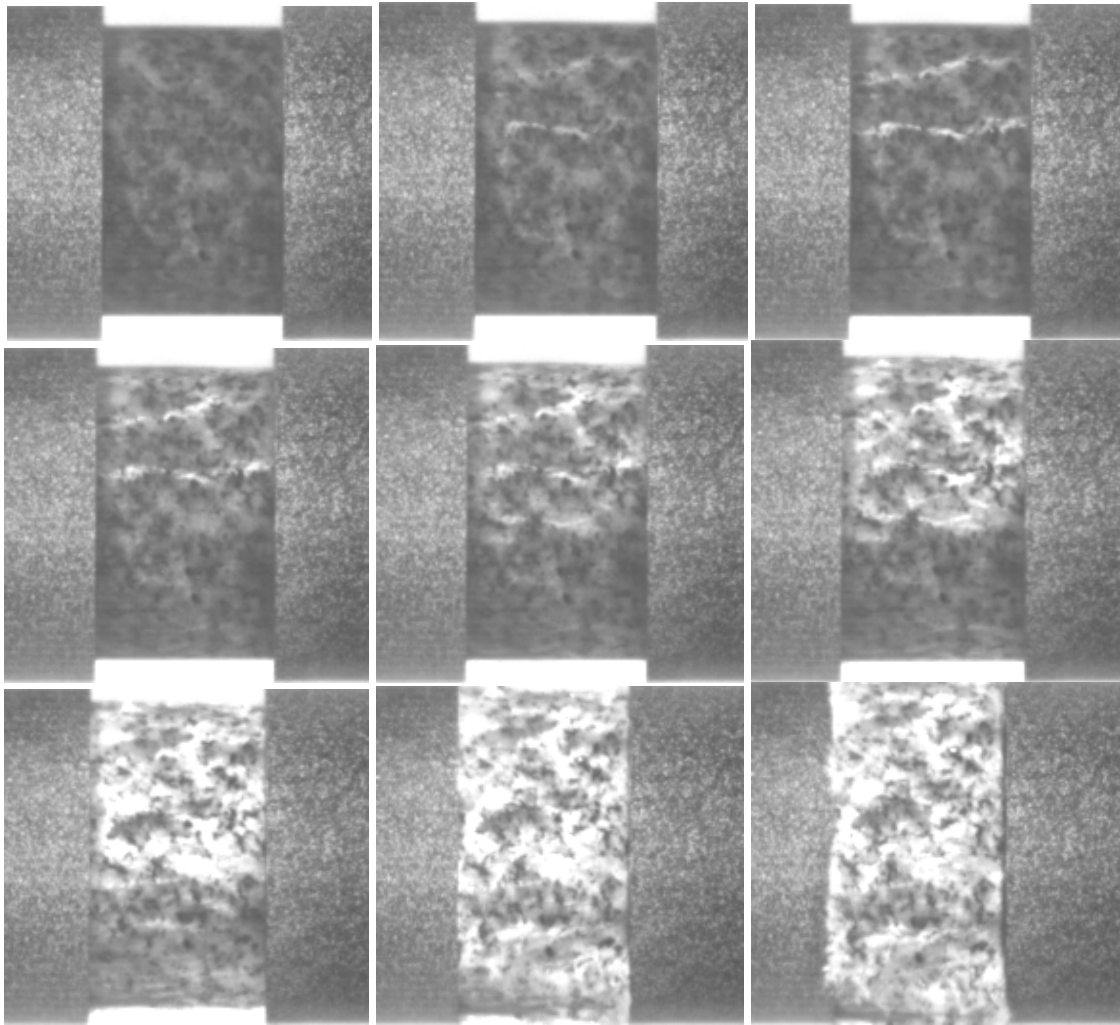


Figure 3-29. Failure process recorded by a high-speed camera for the test with a strain rate of 53.4 s^{-1} (time interval of 10 micro-seconds)

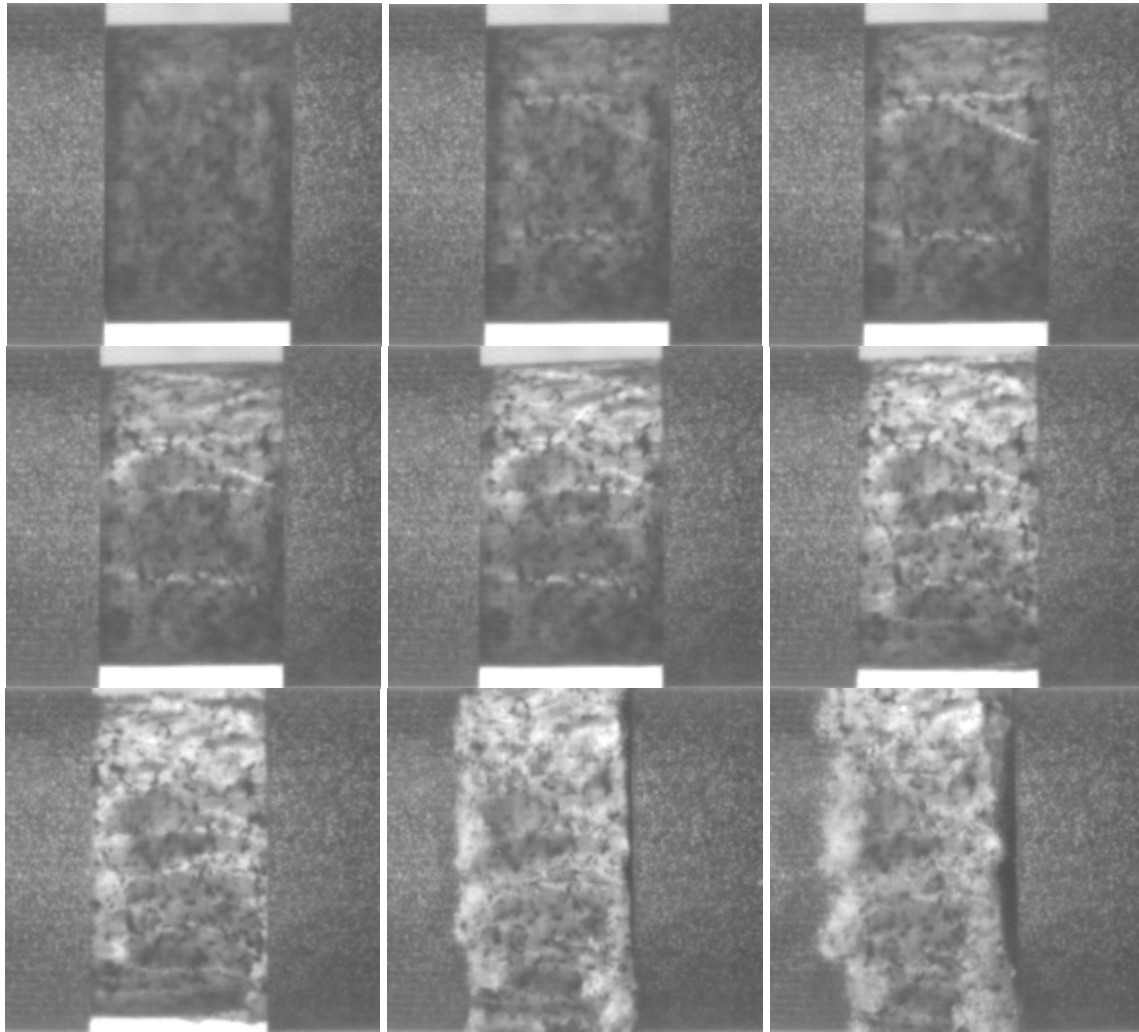


Figure 3-30. Failure process recorded by a high-speed camera for the test with a strain rate of 80.1 s^{-1} (time interval of 10 micro-seconds)

Pulse shapers (Frew et al. 2002) have been found to be a very useful tool to obtain smooth and well behaved stress-strain curves in brittle materials. The pulse shapers used in the tests were thin copper disks with a thickness of about 1 mm and a diameter of 6 mm. The pulse shaper is placed between the projectile and the incident bar. The pulse shaper slows down the load rate and extends the rise time, which is the time from starting

to load the specimen to reaching the peak value, giving the specimen more time to reach a quasi-steady (or equilibrium) state needed.

The projectile was triggered by a pressure gun. The strain rate could not be directly controlled in the tests. Instead, different pressures to trigger the projectile were used to achieve different strain rates. But the strain rates are not linearly dependent on the pressures to trigger the projectile. Two loading experiments respectively under 300 and 450 kPa controlling pressure were performed. Recorded strain histories from strain gauges and deduced force and velocity histories at bar-specimen interfaces are plotted in Figures 3-31 to 3-36.

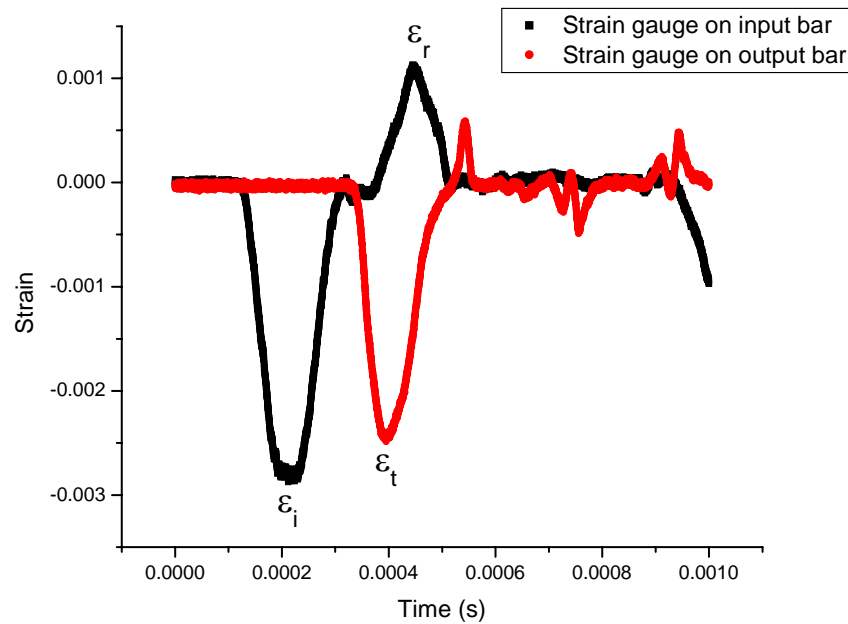


Figure 3-31. Recorded strain histories for the test with 300 kPa controlling pressure generating an average strain rate of 53.4 s^{-1}

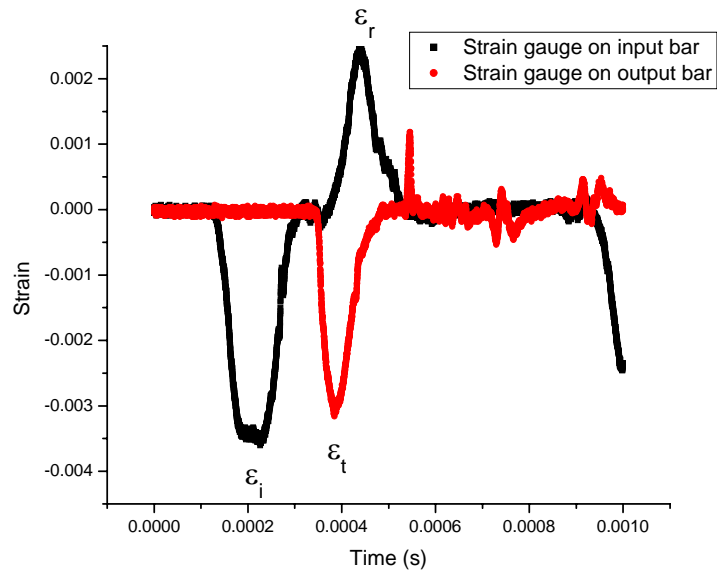


Figure 3-32. Recorded strain histories for the test with 450 kPa controlling pressure generating an average strain rate of 80.1 s^{-1}

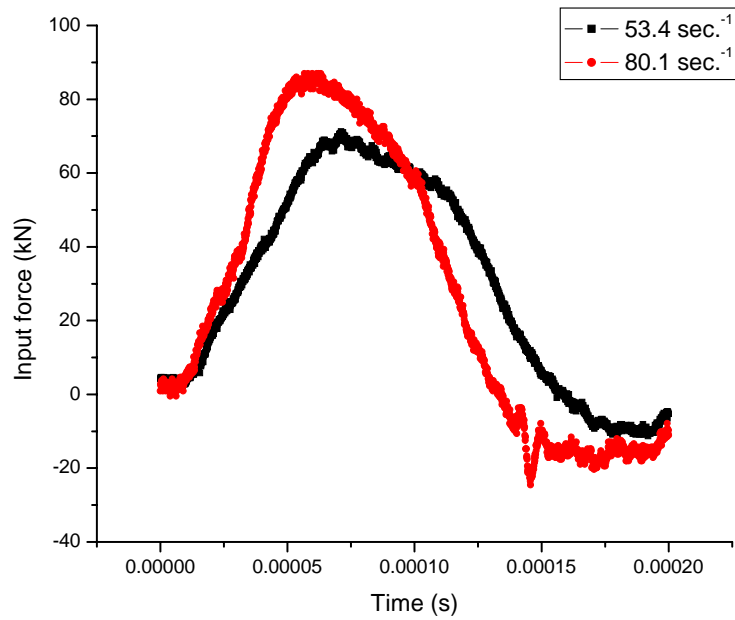


Figure 3-33. Calculated force histories applied on the input bar end at two different strain rates

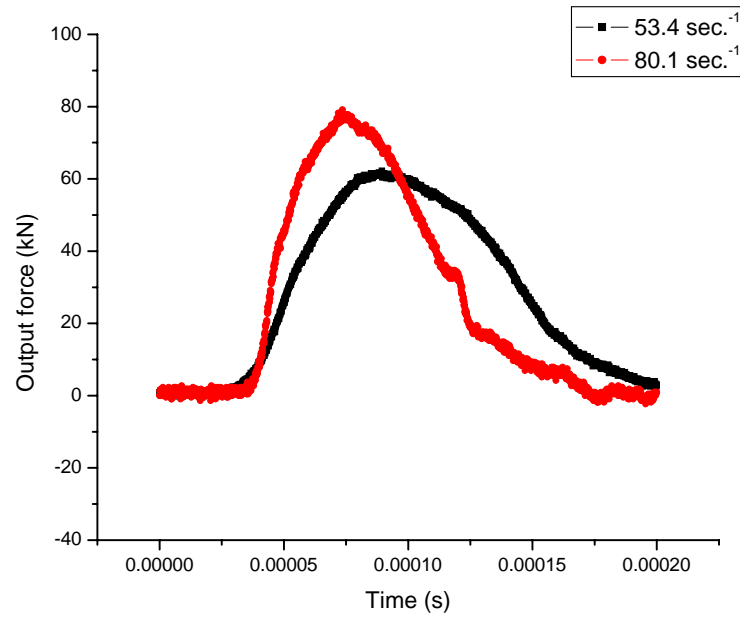


Figure 3-34. Calculated force histories applied on the output bar head at two different strain rates

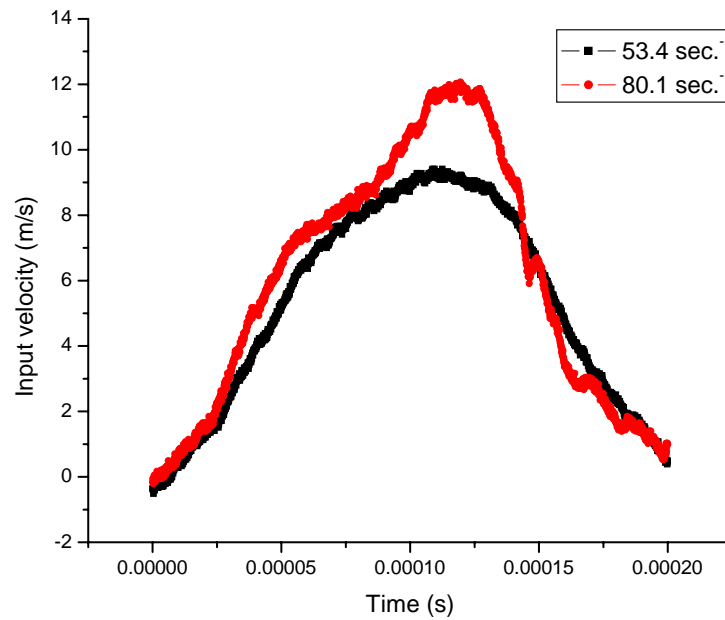


Figure 3-35. Calculated particle velocity histories at the input bar end at two different strain rates

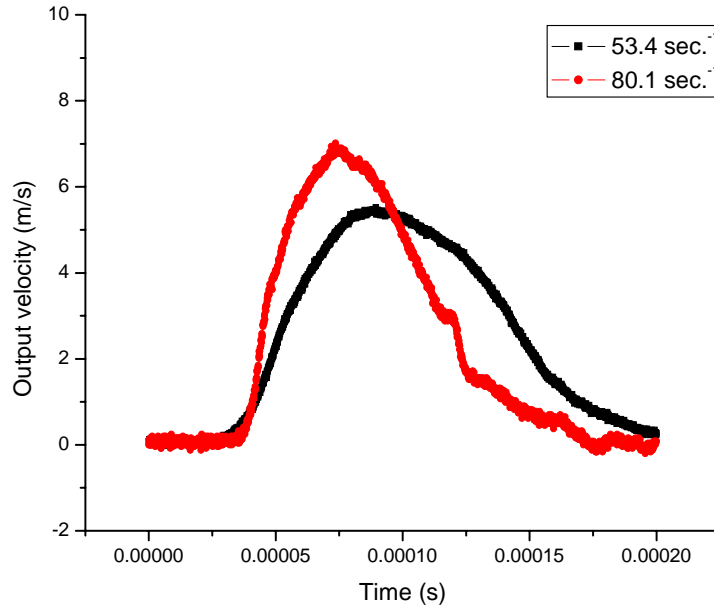


Figure 3-36. Calculated particle velocity histories at the output bar head at two different strain rates

3.5.3 Verification of Dynamic Model with Dynamic Compression and SHPB Tests

The results of dynamic compression and SHPB tests were then used to verify the DEM code to simulate the dynamic behavior of granite. Micro parameters were calibrated using quasi-static procedures as shown in Table 3-3. Instead of using high numerical damping in modeling quasi-static problems, zero damping was applied to simulate dynamic problems, in which material damping is neglected. In static model, the damping coefficient is artificially set very high to quickly dissipate the kinetic energy and get the steady-state results. In dynamic modeling, usually the material damping for intact rock is very low for intact rock and can be neglected.

3.5.3.1 Numerical Simulation of Compression Tests

In modeling dynamic compression tests, more iterative steps are needed to reach the failure state when a lower strain rate is applied. It took about 12 hours to run a simulation of 2500-sphere packing at strain rate of 0.2 s^{-1} on Lonestar platform at Texas Advanced Computing Center of University of Texas at Austin. Due to the limit of computational resource, only strain rates higher than 0.2 s^{-1} can be simulated when a 2500-sphere packing is used. So only the dynamic compression test with the strain rate of 0.2 s^{-1} can be simulated with a 2500-sphere packing. As shown in Figure 3-37, for strain rate of 0.2 s^{-1} , the simulated strength is close to the experimental one. For a higher strain-rate regime, simulated dynamic strength in uniaxial compression is about 10% higher than the strength of both SHPB simulated and experimental tests, which will be addressed in next section.

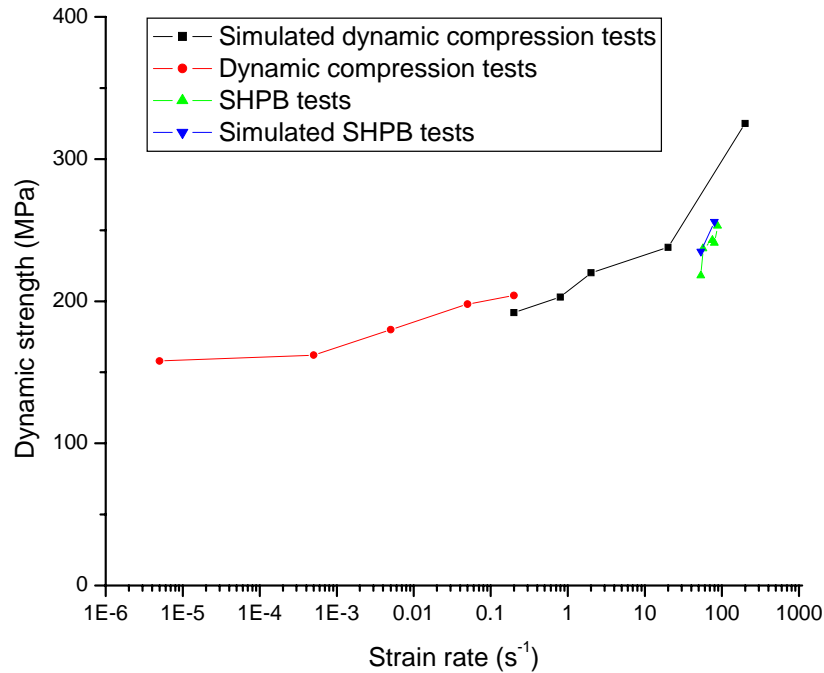


Figure 3-37 Effect of strain rate on dynamic strength observed from both experimental and numerical results

In order to understand the effect of loading rate on dynamic strength within a relatively large range of strain rate from a numerical point of view, a 600-sphere packing was used for the simulation of dynamic compression tests. All the micro model parameters were the same as those calibrated with 2500-sphere packing. With this smaller-number sphere packing, the lowest strain rate of 0.001 s^{-1} can be simulated. Simulations were performed to mimic the actual test conditions by fixing the specimen bottom in the vertical direction and by applying displacement at the top end continuously with a specified velocity. To obtain stress-strain curves, the average vertical normal stresses on bottom and top ends of the specimen were monitored.

The simulated stress-strain curves under different strain rates for dynamic compression tests are shown in Figure 3-38. Strain rate has negligible effect on Young's modulus, which can be estimated from the Figures 3-38 (a) and (b) as about 23.5 MPa. When the applied strain rate is higher than 10.0 s^{-1} , noticeable “stepping” waves occur. For a very large strain rate, such as case (d) in Figure 3-38, one step wave is enough to fail the specimen. Even for a low strain rate, this type of “stepping waves” still exist and can be found when zooming into a small range of strain (Figure 3-38 (a)). The simulated failure evolution of case (c) is shown in Figure 3-39 by monitoring contact failures at different stages. It is found that contact failures progressively propagate from the two ends to the center of the specimen.

The simulated strength dependence on strain rate is shown in Figure 3-39. The tendency of increasing dynamic strength with strain rate exhibits two distinct regimes in strain rate. The strength dependency on strain rate is less prominent for the small strain rate regime ($< 10 \text{ s}^{-1}$) compared to the large strain rate regime ($> 10 \text{ s}^{-1}$). This numerical observation is similar to the experimental results as shown in Figure 3-25, which was also confirmed by the experimental results on granite (dynamic compression and SHPB tests)

shown in Figure 3-40. Note that no rate-dependent constitutive model was used in the DEM model to simulate dynamic behavior. As discussed by Lankford (Lankford 1982) (Lankford 1980), inertia controls the strain rate dependent behavior because the extension of cracks is limited by material inertia. Usually specimens fail at the stress level corresponding to the commencement of the micro crack nucleation processes, and material inertia inhibits crack growth.

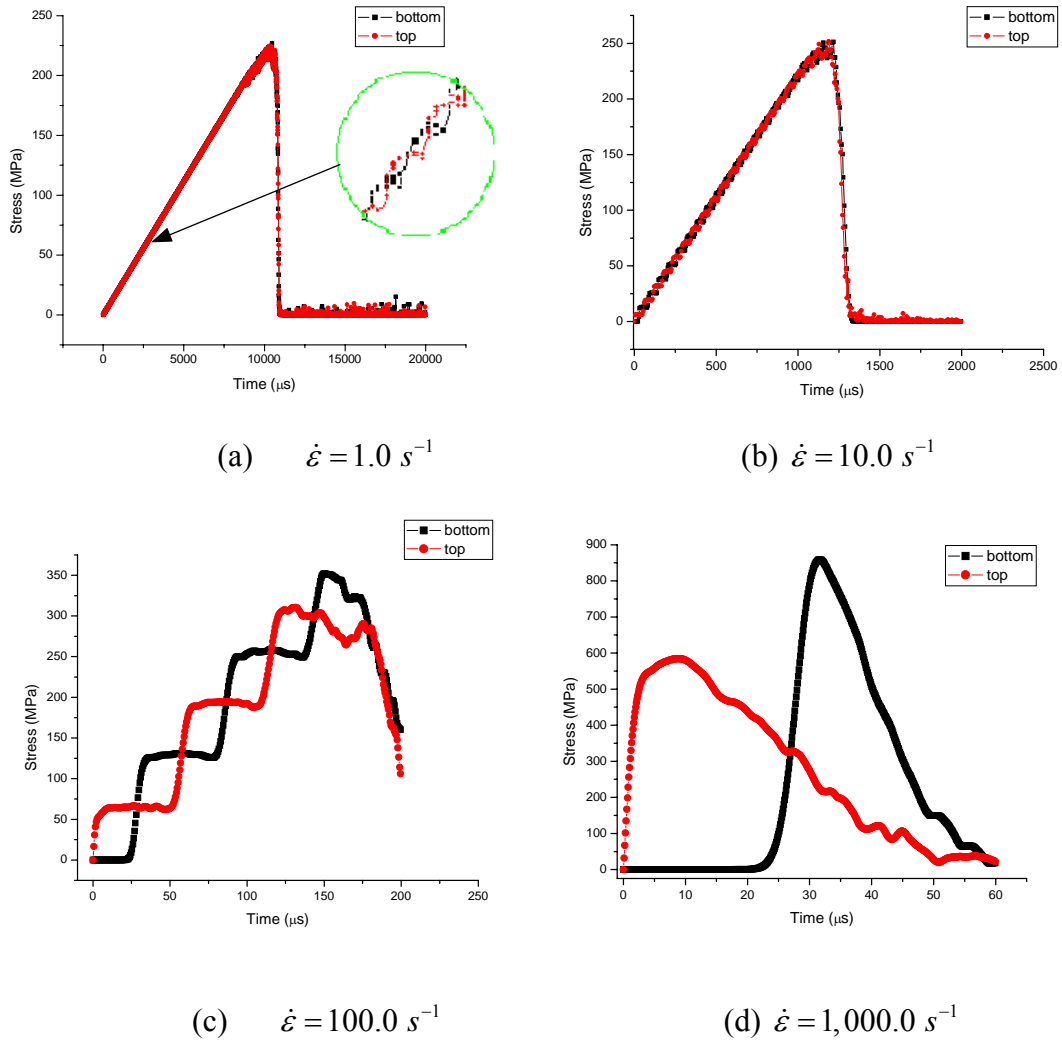


Figure 3-38. Stress-strain curves for different applied strain rates (both stresses on top end and on bottom end were recorded as indicated in the figures)

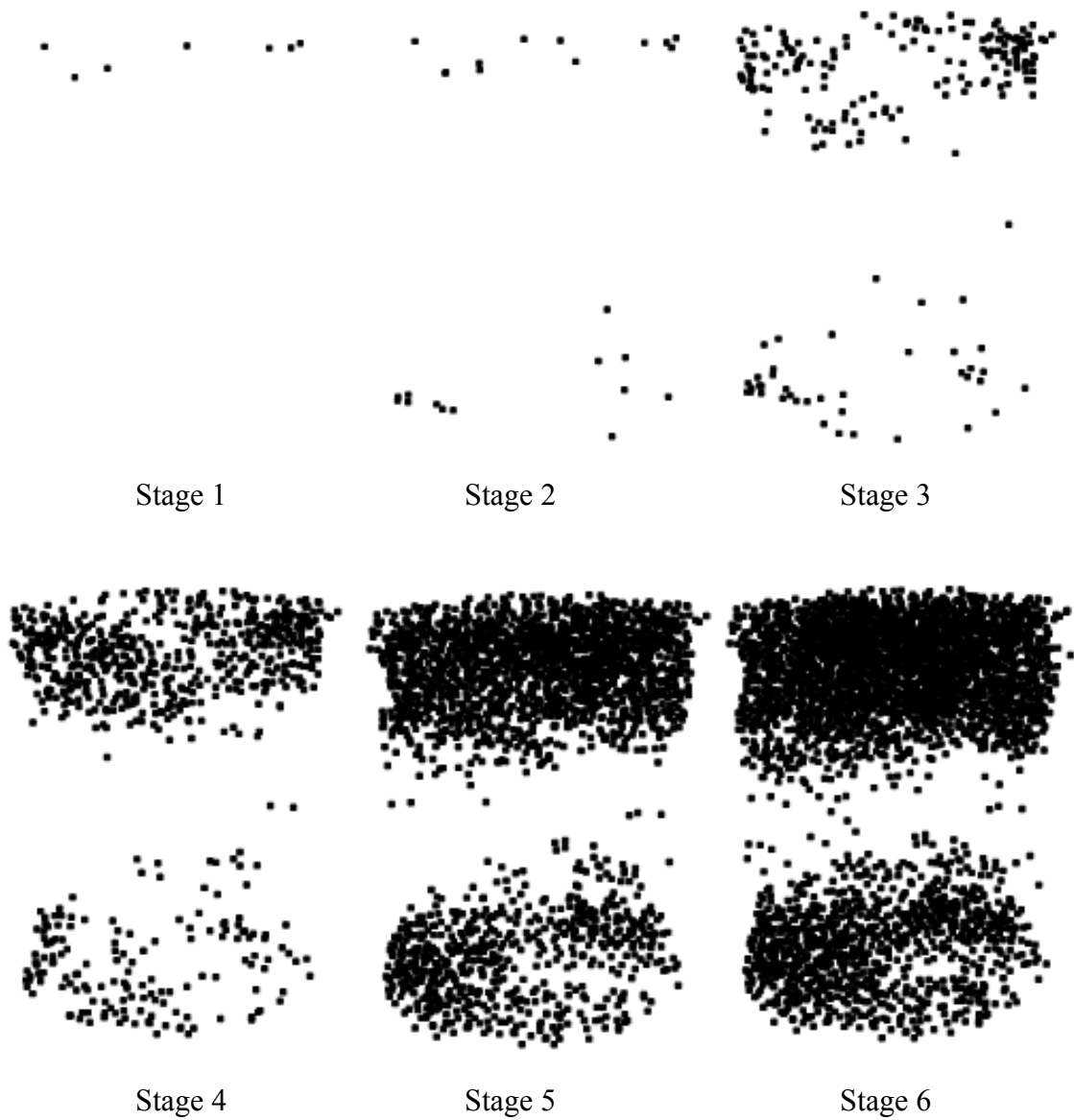


Figure 3-39. Failure evolution by monitoring contact failures at different stages corresponding to the simulation case (c) in Figure 3-38. The black points represent locations of failed contacts.

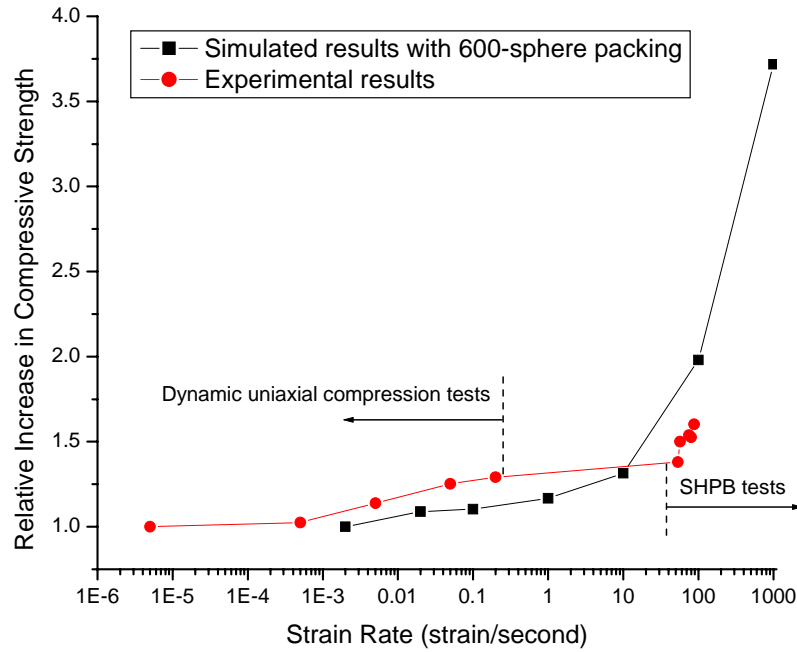


Figure 3-40. Strain-rate dependent dynamic strength for both experimental results and simulated results in modeling dynamic compression tests with 600-sphere packing

3.5.3.2 Numerical Simulations of SHPB Tests

A 2500-sphere packing with diameter of 21.6 mm and length of 13.1 mm was used to build the numerical rock sample. Micro parameters are the same as those calibrated with quasi-static procedures. As discussed previously in Section 3.4.4, identified micro parameters are slightly packing dependent. But this dependence is not very prominent if a similar size distribution is used, hence the same micro parameters as identified in quasi-static model calibrations were applied to the new SHPB specimen to approximately achieve similar material properties. Two SHPB tests with strain rates of 53.4 and 80.1 s^{-1} were simulated.

The experimental input and output velocities were applied to the left and right ends of specimen, respectively. Due to the diameter change from bars to adapters,

deduced particle velocities of bars have to be transformed to particle velocities of adapters. This transformation was achieved by obtaining a velocity reduction factor based on the measured particle velocities of adapters captured by the high speed camera. The reduction factors were determined by comparing the maximum values of deduced particle velocity based on uniform bar and the monitored particle velocity using high speed camera. The final input and output particle velocities are shown in Figures 3-35 and 3-36.

The resulting input and output forces are computed by summing all the forces applied on the two specimen ends. Given the experimental input and output velocity histories, the positions of the two specimen ends are updated at each time step. The simulated stress strain curves are then obtained, and should be compared with experimental stress-strain curves.

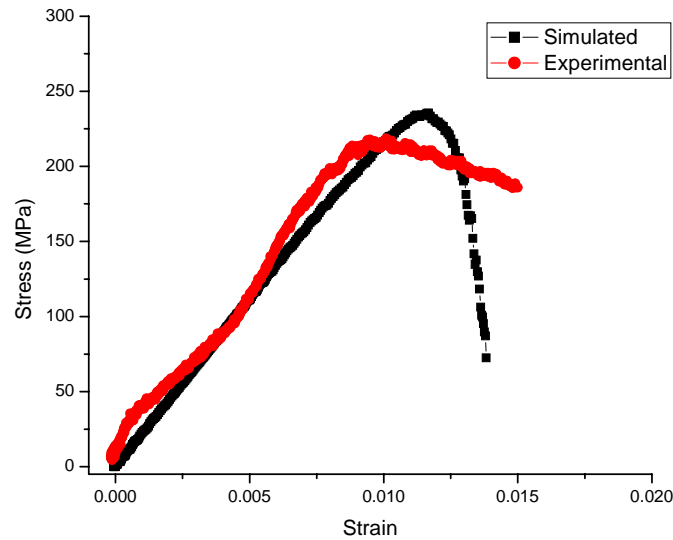


Figure 3-41. Numerical and experimental SHPB stress-strain curves for the strain rate of 53.4 s^{-1}

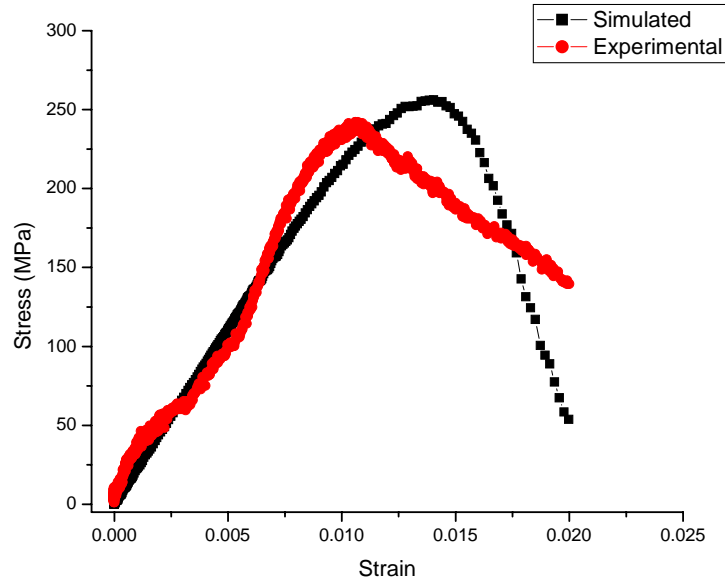


Figure 3-42. Numerical and experimental SHPB stress-strain curves for the strain rate of 80.1 s^{-1}

Figures 3-41 and 3-42 show stress-strain curves for the two tests with the strain rate of 53.4 and 80.1 s^{-1} . The simulated strengths are a little higher (less than 10%) than but are close to the experimental ones. The simulated pre-peak curves well fit the experimental ones, but the post-peak parts do not match well the experimental ones.

3.5.4 Fragment Size Distribution

3.5.4.1 Introduction

Fragment size distribution is the most important outcome of fragmentation processes. It is governed by both a material property (the distribution of flaws) and a kinematic property (the rate of loading) (Grady and Kipp 1980). Figures 3-27, 3-29 and 3-30 show a strain-rate-dependent fragment size distribution from the experimental results. The higher the applied strain rate is, the smaller the average fragment size is.

Different distribution functions were used to describe fragment size distributions (Åström et al. 2004; Behera B 2005; Cheong et al. 2004; Grady 2008; Lu et al. 2002; Wittel et al. 2008), namely, exponential, Voronoi and Weibull distributions.

The exponential distribution is usually used to describe fragment distribution on metals and other more ductile material (Grady 2008). It can be written as

$$Q(s) = 1 - \exp\left(-\frac{s}{s_c}\right), \quad (3-12)$$

in which, $Q(s)$ is accumulated mass of all fragments smaller than a given normalized fragment size normalized by the total mass of the block; the normalized fragment size, s , is the actual fragment size divided by the largest fragment size; s_c is a parameter to be determined representing the average fragment size. Grady also proposed Voronoi distribution to account for depletion of the smaller sizes.

$$Q(s) = 1 - \left(1 + \frac{s}{s_c}\right) \exp\left(-\frac{s}{s_c}\right) \quad (3-13)$$

A two-parameter Weibull distribution was proposed based on a fracture activation and stress-wave interaction model to describe dynamic fragmentation event.

$$Q(s) = 1 - \exp\left[-\left(\frac{s}{s_c}\right)^k\right], \quad (3-14)$$

where k is a parameter to be determined, which is physically related to stress wave propagation (Grady 2008; Grady and Kipp 1980; Mott 1947).

3.5.4.2 Fragmentation Detection in DEM Modelling

In order to analyze the size distributions of fragments in DEM modeling of impact fragmentation processes, a fragmentation detection scheme was developed to predict fragmentation-related information and also post impact behavior. The detecting scheme is directly related to the characteristics of the discrete element method in which particles

can move apart or link together in clusters. The scheme is able to recognize clusters where particles are either linked together or separated after impact. Generally, the particles within the same cluster have the same velocity. The corresponding information such as velocity, mass, etc. associated with each cluster can be easily measured.

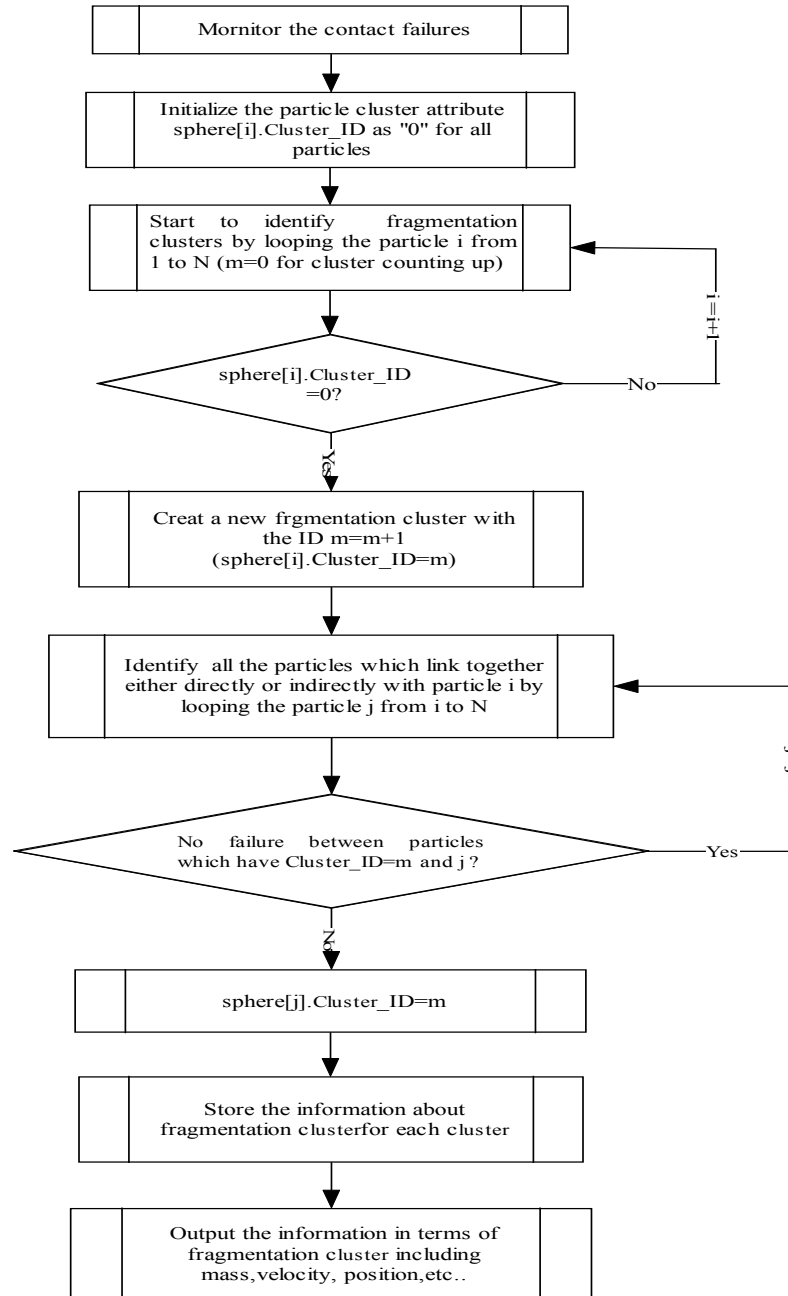


Figure 3-43. Flowchart of fragmentation block detecting scheme in DEM modeling

The detailed fragmentation detecting scheme is shown in the flow chart of Figure 3-43, and an example of detected fragmentation after an impact is given in Figure 3-44, in which all the fragments were separated for better visualization.

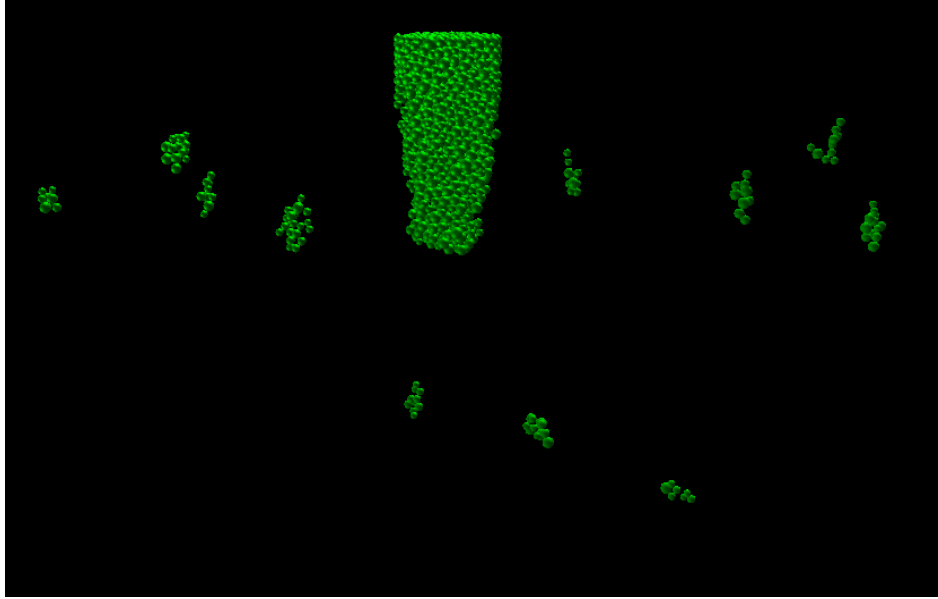


Figure 3-44. Detected fragments after a simulated impact (some very tiny fragments are not shown)

3.5.4.3 Results of Fragment Size Distributions

Sieve analysis was performed on the fragments generated in both dynamic compression and SHPB tests. Figure 3-45 shows normalized size distributions for different strain rates. The normalized cumulative mass and fragment size are defined in Equation (3-12). With increasing strain rate, the average fragment size shifts to smaller values. The fitted curves with different distribution equations are given in Figure 3-46. It shows that Weibull distribution works better than exponential and Voronoi distributions for both high and low strain rates. The exponential distribution can hardly capture the fragment size distribution at a low strain rate. In using two-parameter Weibull

distribution, the value of s_c , which indicates the normalized average fragment size, decreases from 0.75 at strain rate of 0.1 s^{-1} to 0.31 at strain rate of 80.1 s^{-1} . The value of k , representing the shape of the distribution curve, decreases with increasing strain rate.

Size distributions of fragments in simulated dynamic compression and SHPB tests were also analyzed and compared against experimental ones. As shown in Figure 3-47, simulated fragment size distributions are not in good agreement with experimental ones, in particular for low strain rates. This discrepancy comes from the fact that there is a large gap between small fragments and large fragments for the simulation with a low strain rate. The model resolution also affects the fragment size distributions because the smallest fragment can not be smaller than the smallest sphere used in DEM modelling. It has been found that the fragment size distribution can be improved by introducing rolling stiffness to the particles in the model, which will be discussed in Chapter 4. But the development of this improvement will be left for the future research.

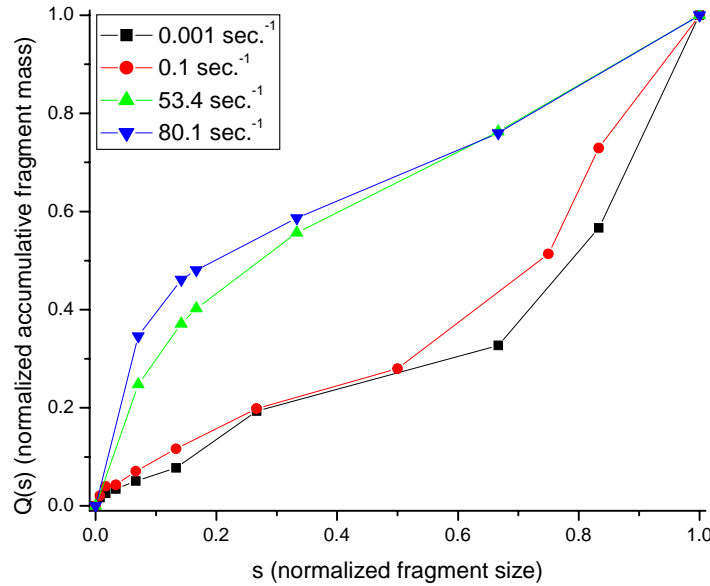


Figure 3-45. Normalized size distributions for the generated fragments in dynamic tests at different strain rates

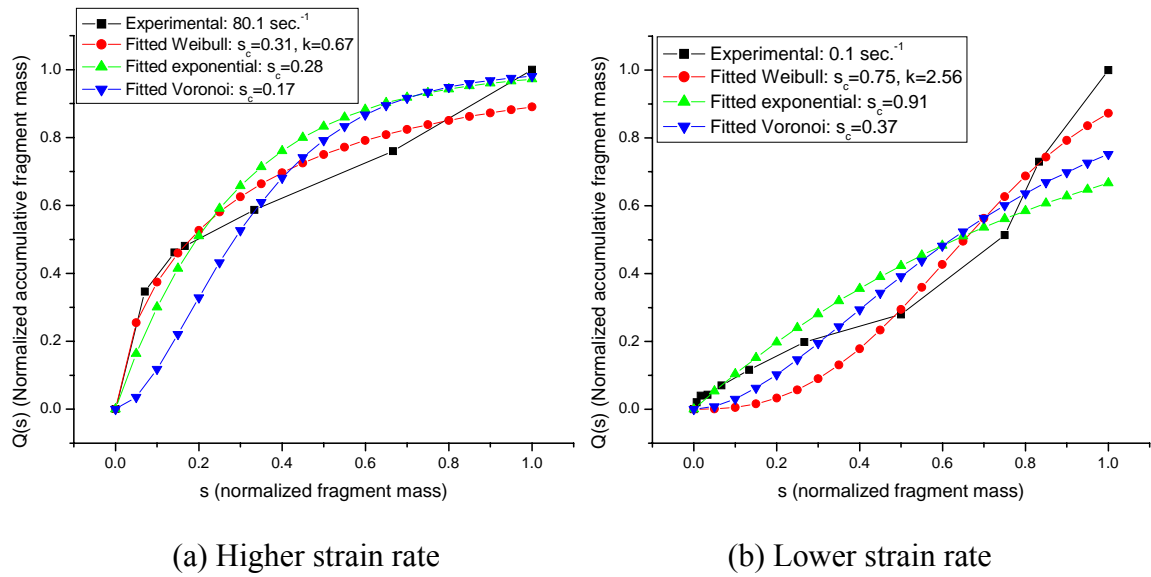


Figure 3-46. Normalized fragment size distributions and fitted curves with different distribution equations at different strain rates

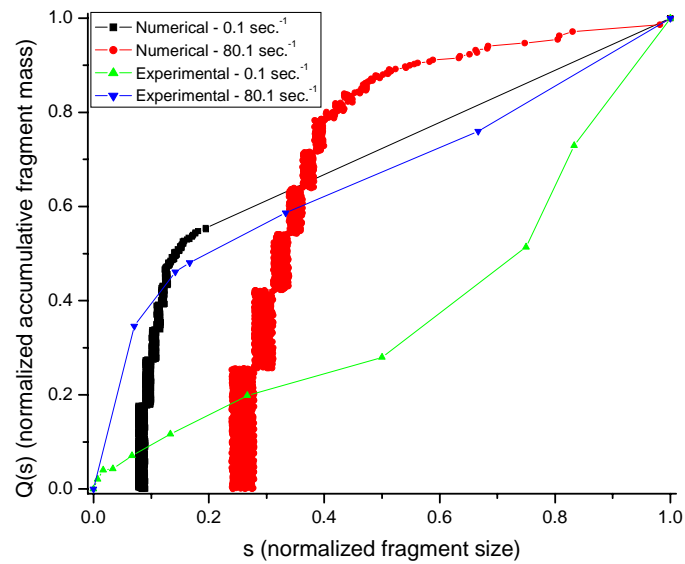


Figure 3-47. Comparison of experimental and numerical fragment size distributions at different strain rates

CHAPTER 4 MODELING ROCK FRAGMENTATION UPON IMPACT

4.1 INTRODUCTION

In the previous chapter, the developed DEM code has been calibrated and verified to be capable of modeling both static and dynamic loading induced rock failure. In this chapter, the DEM code is to be used to simulate impact induced rock fragmentation in rockfall analysis.

The physical process of rockfall impact fragmentation is complex consisting of impact-induced stress wave propagating, generating thermal energy and acoustic wave, and creation of plastic zones, etc. In order to model this type of process using the calibrated DEM code, it is necessary to simplify the problem, such as introducing coefficients of restitution to account for the energy loss during impact, which will be addressed later in the chapter. One of the challenges in modeling rock fall impact, in which a block of rock impacts on the ground with the kinetic energy accumulated from the gravity, is to choose a right model to represent the interaction between rock block and the ground including the stiffness and damping issues of the ground.

4.2 MODEL OF THE INTERACTION BETWEEN ROCK BLOCKS AND THE GROUND

In using DEM to model the rock impacting against the ground, the ground is simplified as a half-space, elastic, homogeneous and isotropic media, while the behavior of rock blocks is simulated by the DEM. The interaction between impacting rock blocks and the ground is essentially the force-displacement relationship, which will be applied to DEM model as boundary conditions. In other words, the impacting forces due to the

penetration of rock blocks into the ground are to be determined and applied as a force boundary in DEM modeling.

In DEM modeling, impact interactions are treated as point loads acting on both impacting boundary particles and the ground. These point loads applied to the half-space medium can induce surface motions, which will, in turn, influence other impacting boundary particles' interactions.

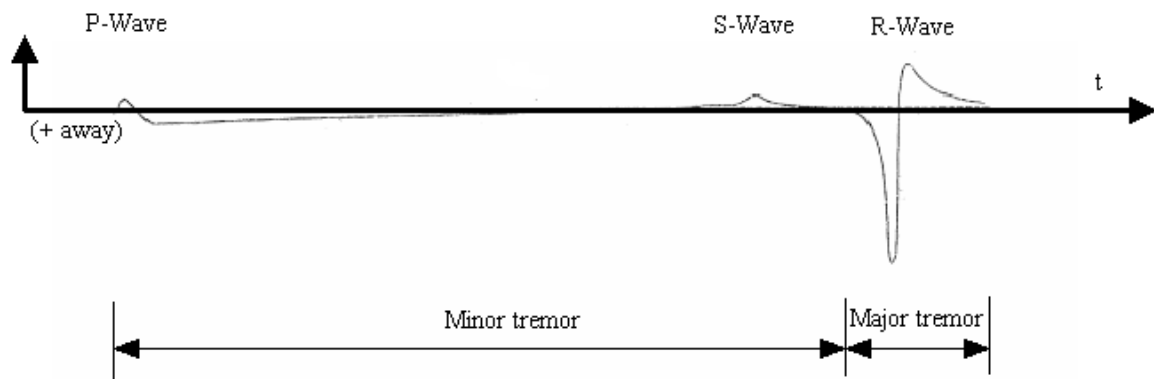


Figure 4-1. Surface motion due to a transient point source (after (Richart et al. 1970))

Lamb first investigated (Lamb 1903 - 1904) the surface motion occurred by a point source at the surface of an linearly elastic isotropic and homogeneous half-space medium. Under the conditions considered by Lamb, an excitation spreads out from the transient point source as a symmetrical annular wave. As shown in Figure 4-1, a particle at the surface first experiences a motion in the form of oscillation at the arrival of P-wave, followed by a relatively quiet period leading up to another oscillation at the arrival of S-wave. These motions are referred by Lamb as the minor tremor and are followed by a much larger oscillation, the major tremor, at the arrival of the R-wave. The results presented by Lamb are in frequency domain, not in time domain, and are very difficult to be implemented into our DEM model because the DEM calculation scheme uses explicit

time integration. Some analytical solutions for surface motions caused by harmonic or Heaviside impact sources were also presented in wave number-time domain (Park and Kausel 2004; Richart et al. 1970). Due to the difficulty of determining the surface motion caused by irregular time-dependent excitation, it is impossible to introduce these results into the DEM modeling to account for the impact behavior. For simplicity, the coupling effects of the interactions due to the surface motions generated by other impacting particles are to be neglected.

In order to use DEM to simulate the rock impact, the rock block is set up as a sphere packing as discussed previously. When an impact occurs, part of the boundary particles (spheres) interact with the ground and the generated interface forces may make the block bounce off the ground. The larger the penetration of those boundary particles into the ground is, the larger the generated “push-back” forces are. The relationship between the “push-back” forces and the penetrations can be depicted by a serial of springs in both normal and tangential direction attached to impacting boundary particles as shown in Figure 4-2. The stiffness of the springs can be estimated from the theory of vibrations for foundations on elastic media. In this approximation, the spherical boundary particles are treated as tiny foundations whose equivalent disk radii are the same as their own spherical radii.

In the theory of vibrations for foundations on elastic media, the vertical and tangential oscillations of a rigid circular disk foundation are possible to be described in terms of mass-spring-dashpot analog (Richart et al. 1970). For disk foundations resting on an elastic half-space, the spring constants are determined from the static response of the rigid disk to vertical or horizontal loads, and are given as (Richart et al. 1970):

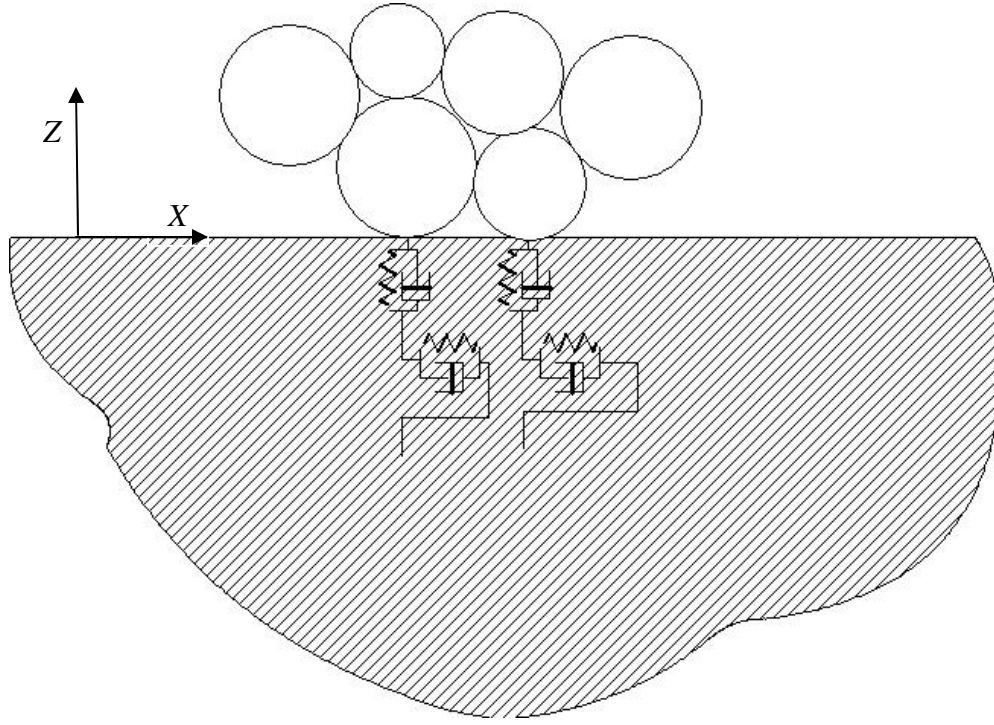


Figure 4-2. Sketch of impact model with springs and dashpots attached to each impacting particle in both normal and shear directions to simulate dynamic interactions between rock block and the ground.

$$\begin{aligned} k_n &= \frac{4Gr_0}{1-\nu} & (\text{Vertical}) \\ k_s &= \frac{32(1-\nu)}{7-8\nu} Gr_0 & (\text{Sliding}) \end{aligned} \quad , \quad (4-1)$$

where k_n and k_s are normal and shear stiffness respectively, G , ν are the shear modulus and Poisson's ratio of the ground respectively, and r_0 is the radius of the disk foundation.

The dashpots are used to provide damping that accounts for the energy loss due to the elastic stress waves propagating away into the ground (geometric damping or radiation damping). The dashpot constants are given as (Richart et al. 1970):

$$\begin{aligned} c_n &= \frac{3.4r_0^2}{1-\nu} \sqrt{\rho G} & (\text{Vertical}) \\ c_s &= \frac{18.4(1-\nu)}{7-8\nu} r_0^2 \sqrt{\rho G} & (\text{Sliding}) \end{aligned} \quad , \quad (4-2)$$

in which c_n and c_s are damping constants for normal and tangential oscillations respectively, and ρ is the density of the ground material.

When particles penetrate into the ground, contacts develop and the interactions between rock block and the ground are set up. The equations of translational motions of particles in normal and tangential directions to the impact plane are then written as:

$$\begin{aligned} m\ddot{z} + \frac{3.4r_0^2}{1-\nu}\sqrt{\rho G}\dot{z} + \frac{4Gr_0}{1-\nu}z &= Q_z(t) & \text{(Vertical)} \\ m\ddot{x} + \frac{18.4(1-\nu)}{7-8\nu}r_0^2\sqrt{\rho G}\dot{x} + \frac{32(1-\nu)}{7-8\nu}Gr_0x &= Q_x(t) & \text{(Sliding)} \end{aligned} \quad (4-3)$$

where $Q_z(t)$ and $Q_x(t)$ are forces exerted by other neighboring particles in normal (z) and tangential (x) directions, respectively.

4.3 INVESTIGATION ON MECHANISM OF IMPACT FRAGMENTATION

The mechanism of impact fragmentation is complicated. There are numerous factors governing the process of impact fragmentation, among which, magnitude of impact velocity, incidence angle, ground conditions and material properties of rock block itself are important and are to be addressed below. Some other factors, such as persistence, orientation and aperture of fractures in the rock block, are also very important for impact rock fragmentation, and will be dealt with in Section 4.3.4.

4.3.1 Model Setup

A spherical rock block was generated to simulate rock fall impact and investigate the mechanism of impact fragmentation. The block consists of 600 randomly distributed spherical particles with average radius of 0.011 m, and has a radius of 0.1 m.

The model parameters are the same as those calibrated for granite in Table 3-3. The model parameters for the spherical block cannot be directly calibrated by using the algorithm used for cylindrical specimens, because there are no standard experiments that

give strength and deformability for spherical specimens. Instead, a similar random internal particle structure was constructed by using a similar distribution of particle sizes. By doing this, one can assume that micro model parameters are approximately equal to those identified from cylindrical specimens. The spring-dashpot impact model is applied to model interaction between the rock block and the ground.

4.3.2 Effect of Impact Velocity

The magnitude of impact velocity and the incidence angle with reference to the slope (ground) are directly related to the dynamic interaction between rock blocks and the ground, and hence play important roles in the process of impact fragmentation. Here, incidence angle is defined as the acute angle between the slope and the incident trajectory. For example, for a normal impact, incidence angle is 90° . Generally, a greater magnitude of impact fragmentation tends to generate higher impact stresses and to break the rock block more easily. A smaller incidence angle has the larger potential to alleviate the impact fragmentation while producing greater angular momentum to rock blocks.

In this section, effects of the magnitude of impact velocity and the incidence angle on impact fragmentation of homogeneous rock blocks (without initial fractures) have been investigated. The ground has Young's modulus of 20 GPa and Poisson's ratio of 0.3, which is representative of relatively hard rock.

4.3.2.1 Magnitude of Impact Velocity

In this case, normal incidences are considered, in which a rock block impacts with the ground perpendicular to the ground slope. The magnitude of impact velocity varies as 40, 50 and 60 m/s, which are reasonable values in practical rockfall analyses. One of the most important concerns on impact fragmentation is the highest impact stress generated during impact. As shown in Table 4-1 and Figure 4-3, at about 50 m/s of impact velocity,

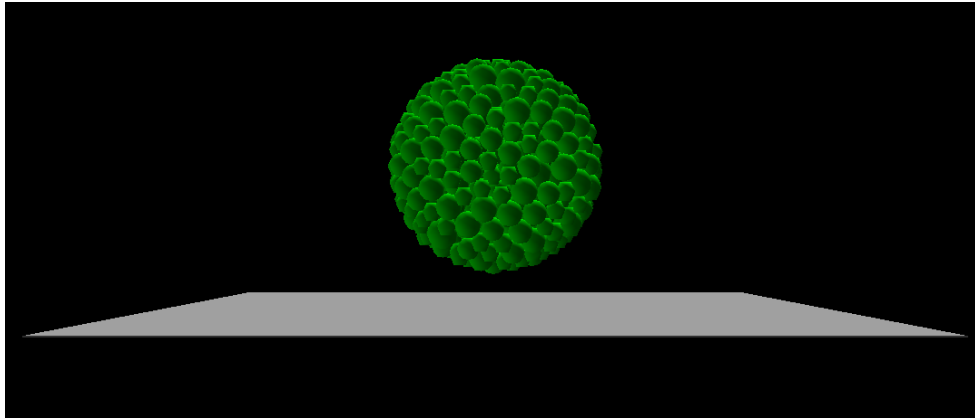
fragmentation starts to occur with 43 fragments. When the impact velocity increases to 60 m/s, the number of fragments goes up to 334.

Table 4-1. Number of fragments of different magnitude of impact velocity under normal incidence

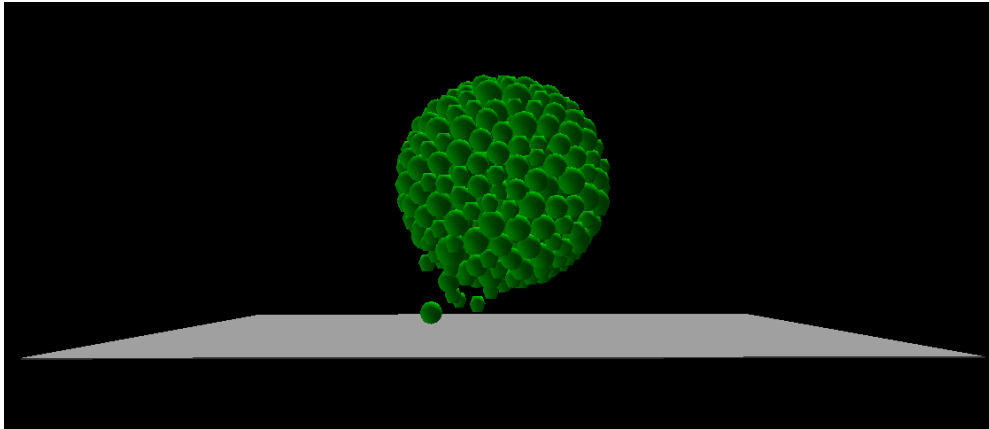
Magnitude of velocity (m/s)	40	50	60
Number of fragments	0	43	334

Note that the fragmentations localize at the impact zone and all the generated fragments during impact are very small consisting of less than 3 spherical particles. In other words, for a homogeneous rock block, impact fragmentations occur locally without generating some relative large fragments as typically observed in the field for large rock block, which may have some inherent fractures. The importance of inherent fractures in rock block to impact fragmentation is to be addressed shortly in Section 4.3.4.

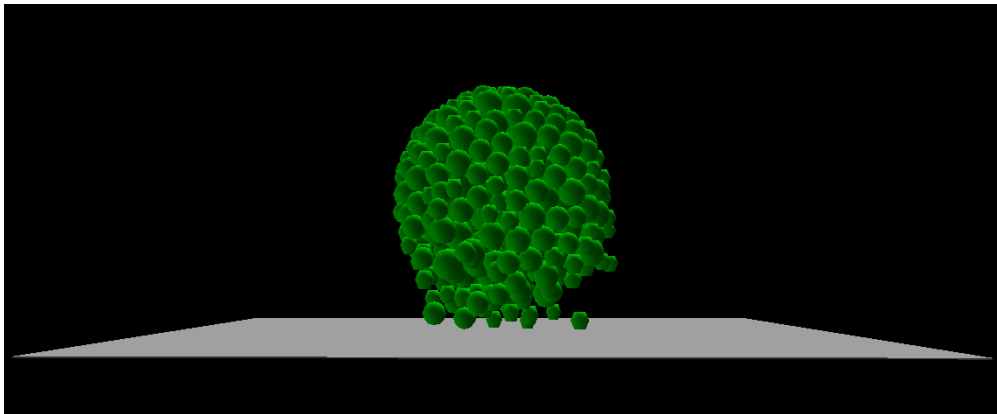
In Figure 4-4, monitored histories of system kinetic energy and impact normal stress give a clear view on an impact process. During the approach period, the system kinetic energy decreases while the block penetrating into the ground and reaches almost zero when the block attains its largest penetration, at which point almost all the system kinetic energy is transformed into strain energy. Impact normal stress increases with penetration and impact normal stress reaches its largest value at about the largest penetration. During the restitution period, the stored strain energy is again transformed into system kinetic energy gradually while impact normal stress decreases until reaching zero when the block bounces off the ground.



a) $V = 40 \text{ m/s}$



b) $V = 50 \text{ m/s}$



c) $V = 60 \text{ m/s}$

Figure 4-3. Fragmentations of different magnitude of impact velocity after the block (in green) bouncing off the ground (in white)

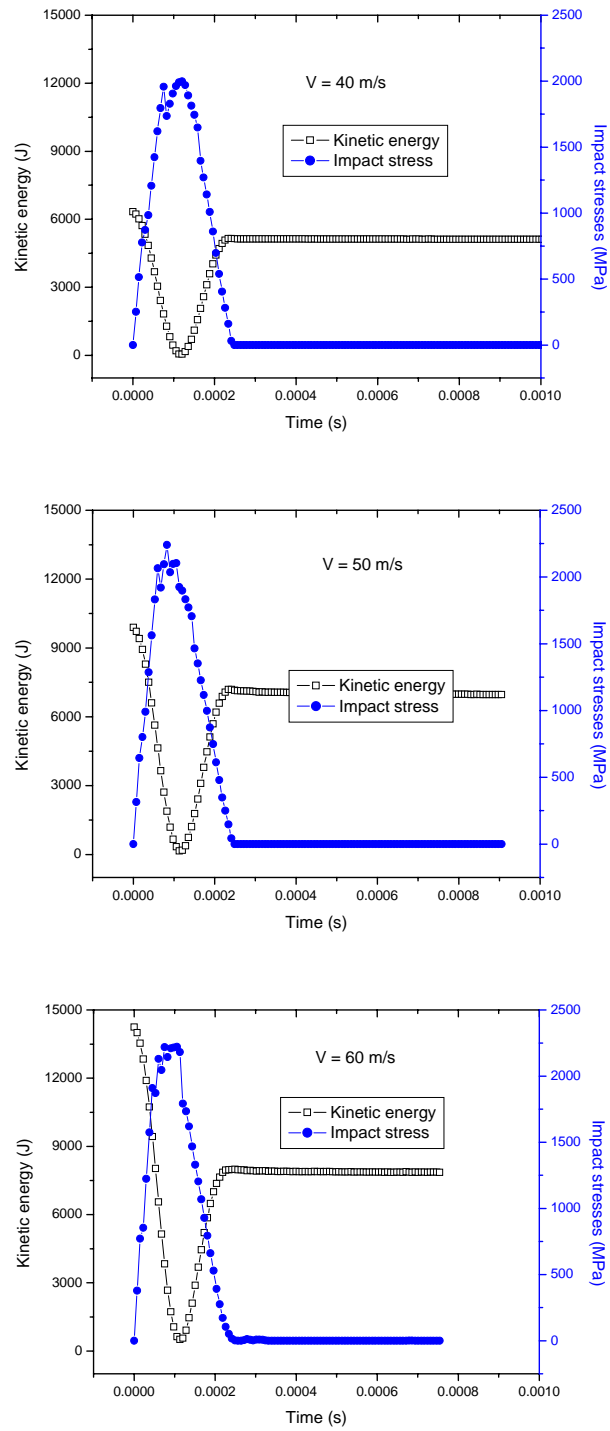


Figure 4-4. Histories of impact stress and system kinetic energy for different impact velocities

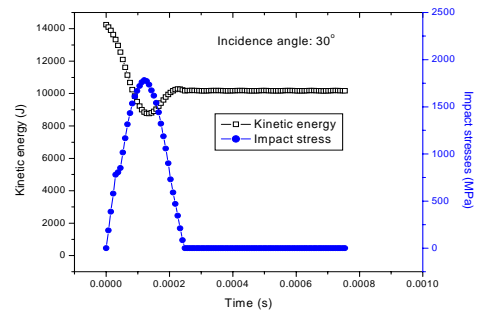
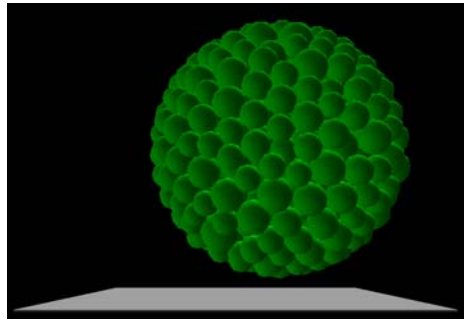
Figure 4-3 shows that the monitored highest impact normal stress increases from about 2,000 MPa to 2,250 MPa when the magnitude of impact velocity increases from 40 to 60 m/s, while the highest impact normal stress does not increase much when impact velocity increases from 50 m/s to 60 m/s. There seems an impact normal stress threshold controlling the fragmentation for a given type of rock block, only above which fragmentation can occur. When fragmentation occurs, impact normal stress is deviated by the generated fragments. This explains why there are no big differences in generated highest impact normal stress between impact velocity of 50 m/s and 60 m/s. The impact duration at different magnitudes of velocity does not vary much. A higher velocity tends to decrease the impact duration. On the other hand, a higher velocity also causes a larger penetration which increases the impact duration.

The monitored impact normal stress was determined by the normal forces divided by the contact areas when impact particles penetrate into the ground. This stress is actually the dynamic contact stress applied to individual particle. This impact contact stress is much higher than material strength because it is calculated on contact areas, and not on gross area. This monitored impact contact stress can reflect the “push-back” effect applied to the block.

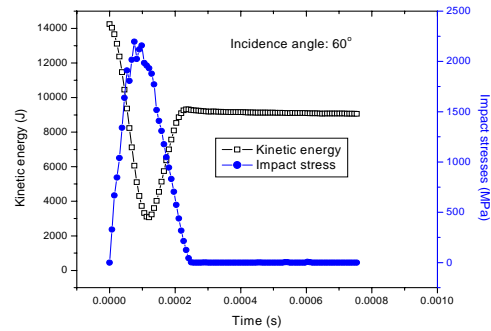
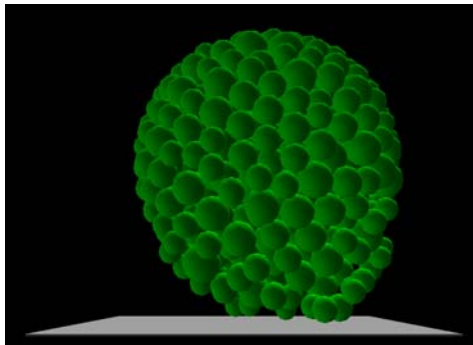
4.3.2.2 Incidence Angle

For a constant magnitude of impact velocity, a change of incidence angle can also affect impact fragmentation because the normal component of impact velocity to the ground really governs the highest impact stress, which is the main drive for impact fragmentation. The normal component increases with incidence angle, so a larger incidence angle has a greater potential to generate fragmentation. The tangential component of impact velocity actually plays a role in changing angular momentum.

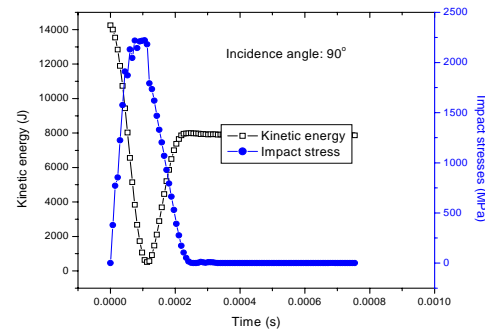
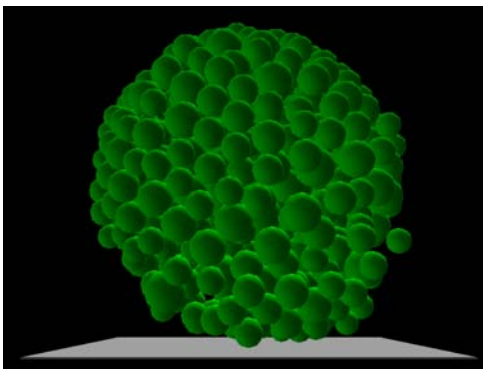
In this case, the magnitude of impact velocity is kept constant as 60 m/s, while the incidence varies as 30° , 60° and 90° . As shown in Table 4-2, for incidence angle of 30° , no fragmentation occurs, while the number of fragments increases to 175 and 334 for an incidence angle of 60° and 90° , respectively.



(a) 30°



(b) 60°



(c) 90°

Figure 4-5. Fragmentation, and histories of impact stress and system kinetic energy for different incidence angles

Table 4-2. Fragmentation of different incidence angles with the magnitude of impact velocity of 50 m/s

Incidence angle	30°	60°	90°
Number of fragments	0	175	334

Figure 4-5 shows that the monitored highest impact normal stress increases from about 1800 MPa for incidence angle of 30° to 2250 MPa for incidence angle of 60°, where fragmentation occurs. The highest impact normal stress does not increase much when incidence angle increases from 60° to 90°, as the highest impact normal stress exceeds the fragmentation stress threshold as discussed in the previous case. For the normal incidence (90° incidence angle) case, system kinetic energy reaches almost zero when the block attains its largest penetration, at which point almost all the system kinetic energy is transformed into strain energy. By contrast, the system kinetic energy changes little when the incidence angle is equal to 30°. For a small incidence angle, most of the system energy is transmitted by the tangential component of velocity rather than the vertical penetration.

4.3.3 Effect of Ground Condition

Not only magnitude of the impact velocity and angle of incidence, but also ground conditions can affect impact fragmentation. A softer ground tends to extend the duration of an impact and produce lower impact stress, so a rigid ground is more likely to cause impact fragmentation compared to a soft ground. As seen in Equations (4-1) and (4-2) on the impact model used to simulate the dynamic interaction between rock block and the ground, the Young's modulus and Poisson's ratio of the ground jointly determine the values of stiffness and geometric damping in both normal and tangential directions. Based on Equations (4-1) and (4-2), the Young's modulus of the ground is proportional to the values of stiffness and the square of geometric damping in both normal and

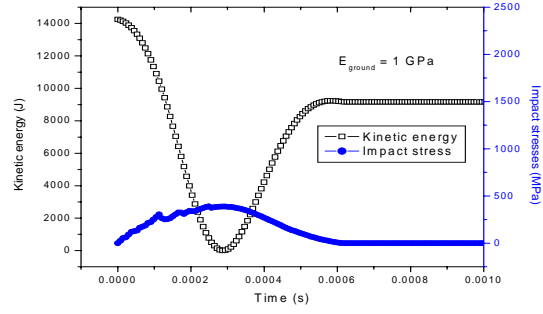
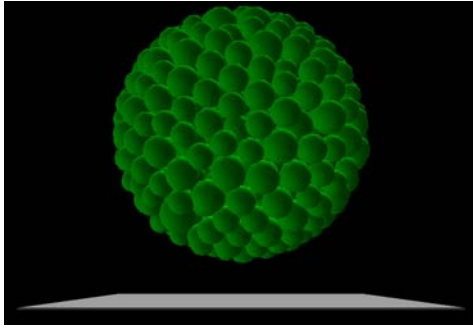
tangential directions, while the Poisson's ratio of the ground has less effect on those values of stiffness and damping especially in tangential direction. Considering that the Poisson's ratio of the ground does not vary much (with typical values ranging from 0.15 to 0.35), the effect of the Poisson's ratio of the ground is not studied here and ground conditions are only characterized by the Young's modulus of the ground.

In this case, normal incidences are considered and the magnitude of impact velocity is kept constant as 60 m/s. The Young's modulus of the ground varies as 1, 10 and 20 GPa. As shown in Table 4-3, for the Young's modulus of the ground of 1 GPa, no fragmentation occurs. Fragmentation occurs with 36 fragments for the Young's modulus of the ground of 10 GPa. When the ground becomes much stiffer with the Young's modulus of the ground of 20 GPa, the number of fragments increases to 334.

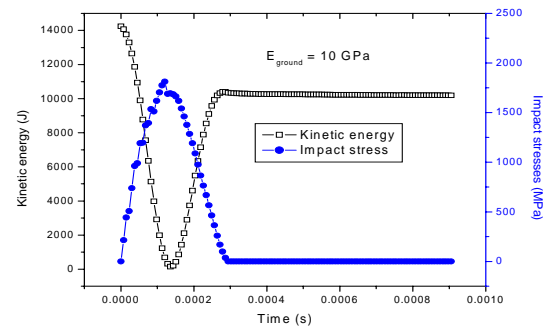
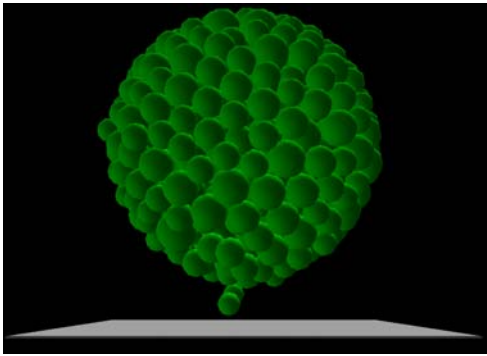
Table 4-3. Fragmentation of different ground conditions under normal incidence

Young's modulus of the ground (GPa)	1	10	20
Number of fragments	0	36	334

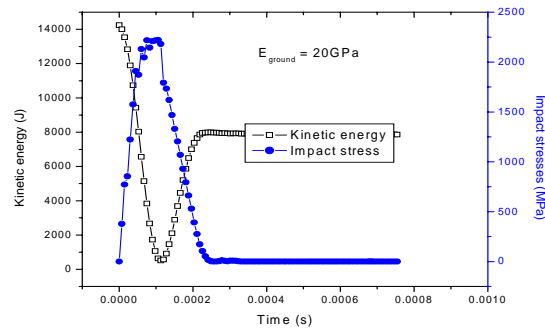
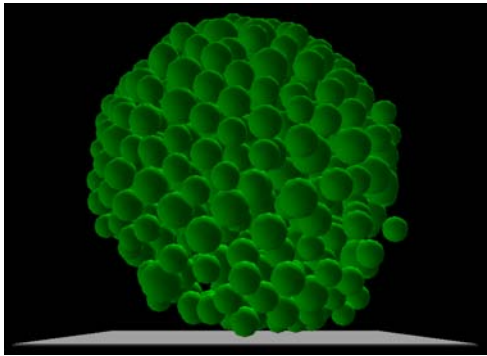
Figure 4-6 shows that impact normal stress increases with the Young's modulus of the ground. The highest impact stress increases from about 400 MPa to 1,900 MPa when the Young's modulus of the ground increases from 1 GPa to 10 GPa. Impact fragmentation occurs with 36 fragments for the ground of 10 GPa and with 334 fragments for the ground of 20 GPa, while the highest impact normal stress increases from about 1,900 MPa to 2,250 MPa. It has been discussed previously that the highest impact normal stress does not overpass the impact fragmentation stress threshold much because the impact normal stress is deviated when impact fragmentation occurs. But for different ground conditions, the impact fragmentation stress threshold may be different.



(a) 1 GPa



(b) 10 GPa



(c) 20 GPa

Figure 4-6. Fragmentation, and histories of impact normal stress and system energy for different ground conditions under normal incidence

Impact duration also plays a role in controlling the impact fragmentation stress threshold needed for occurrence of impact fragmentation. From Section 3.5, the uniaxial compressive strength increases with increasing strain rate. A softer ground tends to

extend impact duration and induces a relatively lower strain-rate loading applied to rock blocks, so the stress threshold of impact fragmentation for a soft ground is lower than that for a rigid ground provided that the dynamic strength of rock blocks is strain-rate dependent. On the other hand, impact stresses are nearly proportional to the ground Young's modulus before generating fragmentation. A soft ground tends to produce lower impact stresses given the same impact profile. Based on the simulated results (Figure 4-6), the effect of the ground Young's modulus on impact stress is much larger than that of strain rate dependent strength, and a soft ground tends to alleviate the impact fragmentation.

4.3.4 Effect of Fracture Properties of Rock Block

Real rock blocks involved in rock fall are seldom homogeneous. Typically, rock blocks contain fractures. These fractures can play very important roles in impact induced rock fragmentation. The effects of fracture persistence, opening, cementation and orientation on impact induced rock fragmentation were investigated and are presented hereafter.

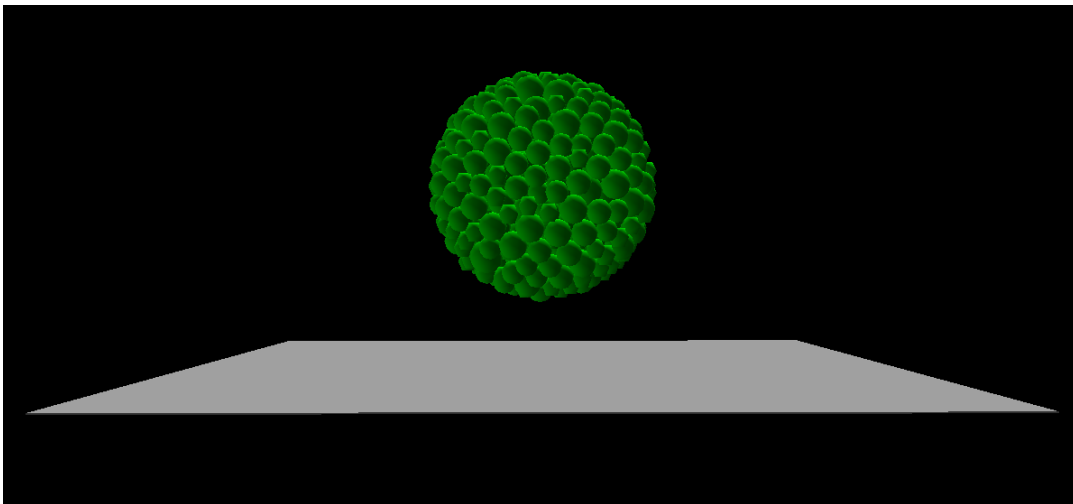


Figure 4-7. Impact of homogeneous rock block on the ground after the block (in green) bouncing off the ground (in white)

In following cases, normal incidences with a magnitude of impact velocity of 30 m/s and Young's modulus of the ground of 20 GPa are considered. Fractures were treated as planar with circular shape. All fractures were modeled as broken contact bonds in DEM modeling. The simulated results of fractured block can be compared to the homogeneous one as shown in Figure 4-7 with no fragmentation occurred, in which no fracture is included in the DEM model.

4.3.4.1 Persistence

In this cases, two fractures, which are perpendicular to each other, are located in the form of “X” centered at the center of the block and are along the angular bisectors of X and Z axis (Figure 4-8). Fractures persistence is defined as the ratio of the radius of circular fracture plane over the largest radius of the circular plane which cuts through the spherical block. In the case of a fracture passing through the sphere center, the largest radius is the radius of the spherical block. Fractures were treated as broken contact bond with frictional angle of 20° .

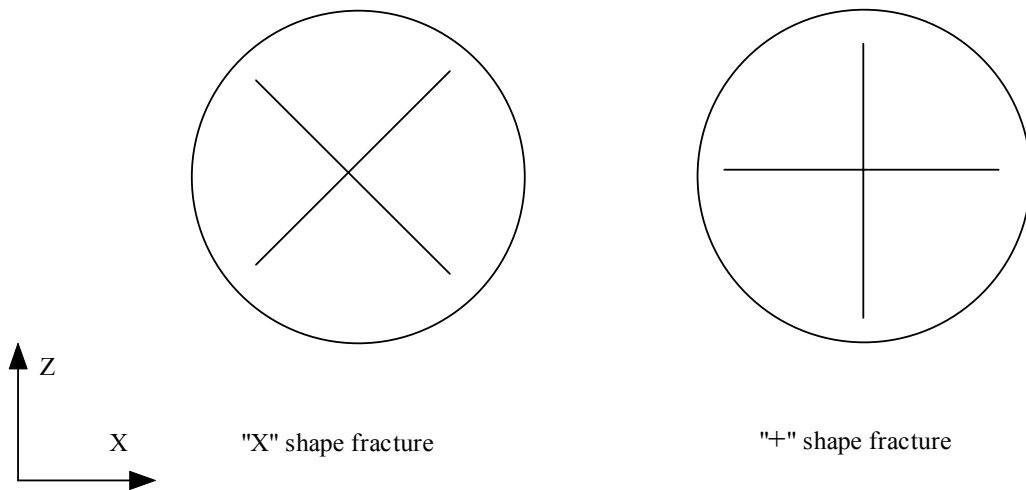
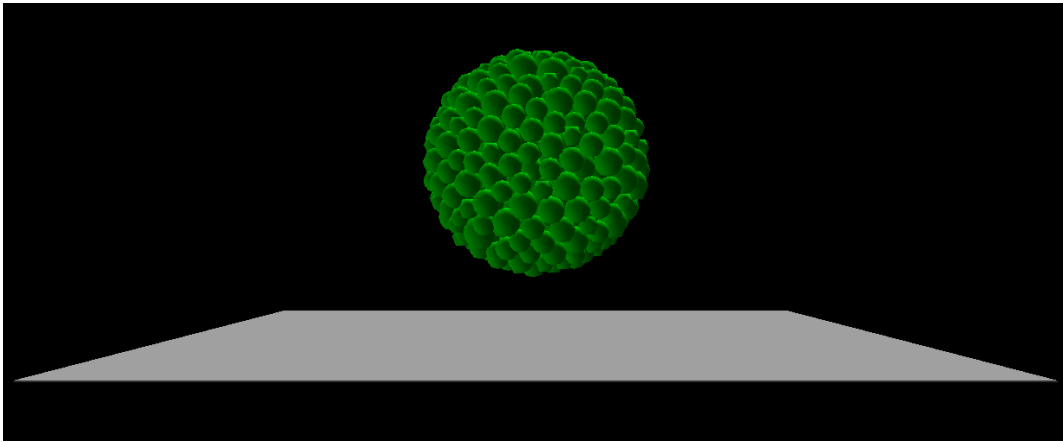
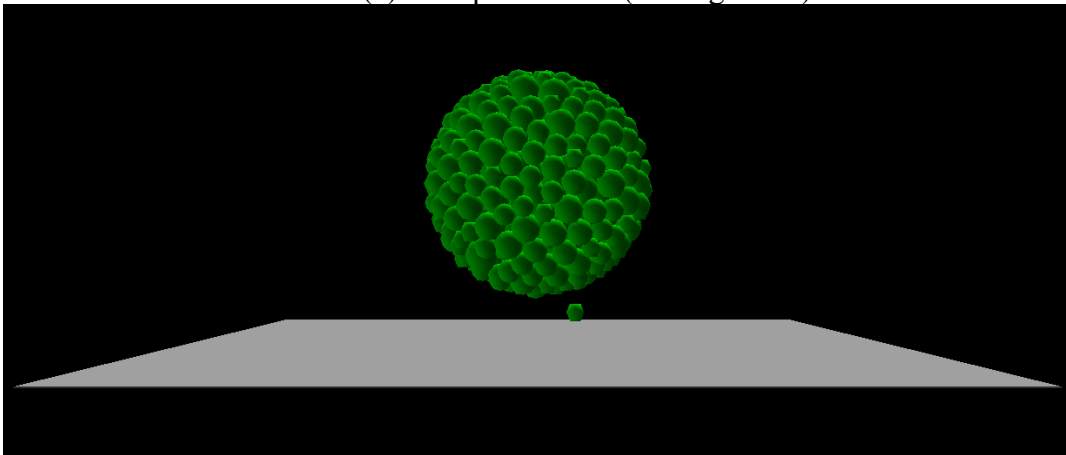


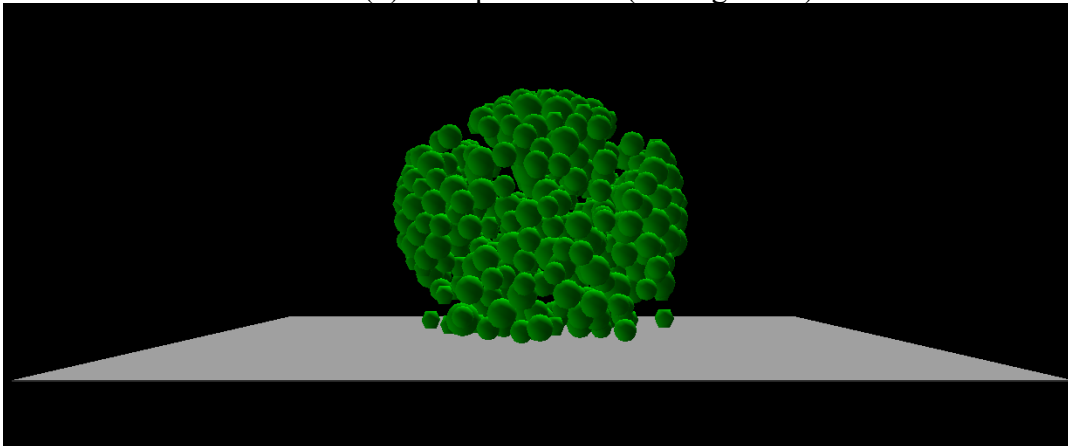
Figure 4-8. Sketch of “X” and “+” shape fractures in a spherical block used for numerically investigating the effect of fracture patterns on fragmentation



(a) 80% persistence (46 fragments)



(b) 90% persistence (55 fragments)



(c) 100% persistence (196 fragments)

Figure 4-9. Impact fragmentation for different fracture persistence after the block (in green) bouncing off the ground (in white)

The simulated results show that fracture persistence has a very important role in governing the degree and the pattern of impact fragmentation. As shown in Figure 4-9, with 80% of fracture persistence, there are 46 fragments generated which cannot be observed from outside the block. These 46 fragments are actually some individual particles along the fractures, de-bonded and separated from the rock block due to the impact. When fracture persistence increases to 90%, the number of fragments is 55 and part of the perimeter of the block, which is not cut through by the fractures, starts to break (Figure 4-9 (b)) due to the fracture propagation from the fractures tips. Only when the fractures are fully persistent, there is a clear pattern of four big fragments with the bottom one more fragmented. The number of fragments for fully persistent case is 196.

4.3.4.2 Fracture Aperture

In this case, in addition to using broken contact bond to describe fracture in DEM modeling, a fracture opening was modeled by introducing a new equilibrium distance, D_{eq} , of a broken contact, which is smaller than the actual center-to-center distance. When two contacting spheres move close together across a fracture, no contact compression force will be generated before reaching the new equilibrium distance.

The fracture aperture was taken as 1% of the actual center-to-center distance and “X” form 80% fracture persistence was used. Compared against the results of 80% fracture persistence (as shown in Figure. 4-9 (b)) with 46 fragments, now 306 fragments are generated with two larger ones for opening fracture case as shown in Figure 4-10. It has been found that impact fragmentation is very sensitive to fracture aperture. This can be attributed to cracks caused by tensile stress waves. When a compressive stress wave produced by impact encounters a free surface (open fracture), it turns into a tensile stress

wave. Usually, rock materials are much weaker to tensile forces than to compression forces. That is why a larger number of fragments were found in the case of open fracture.

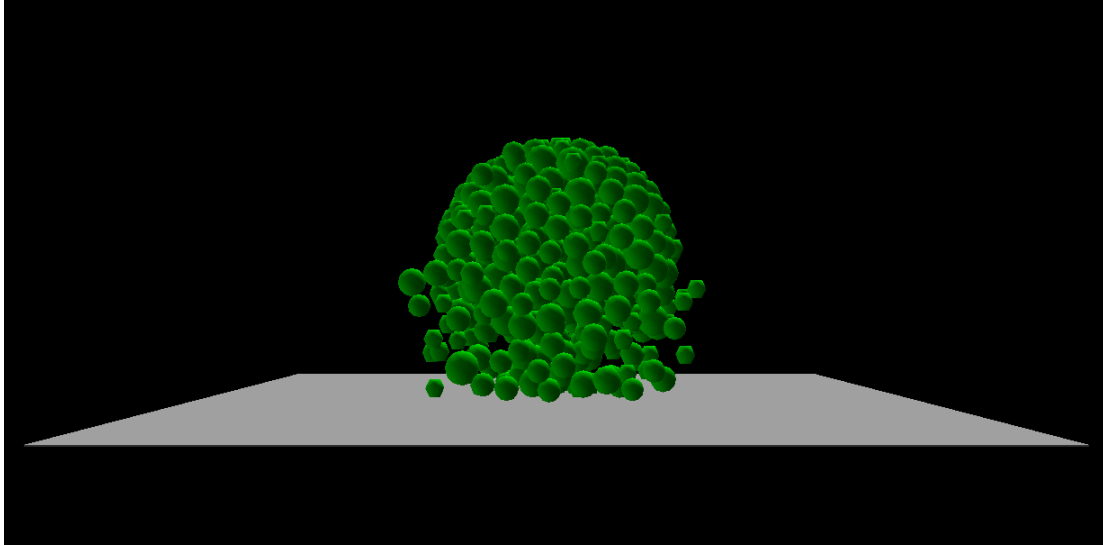
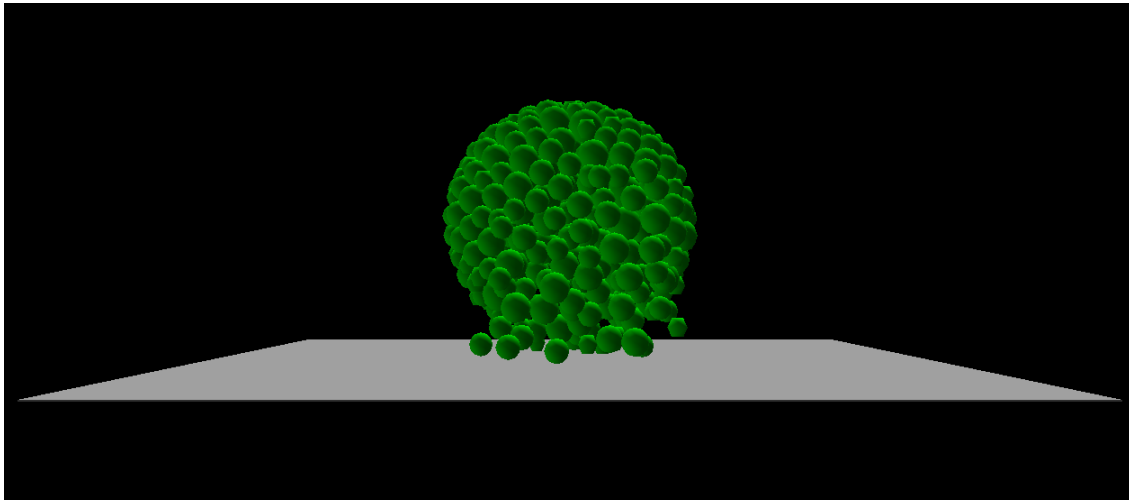


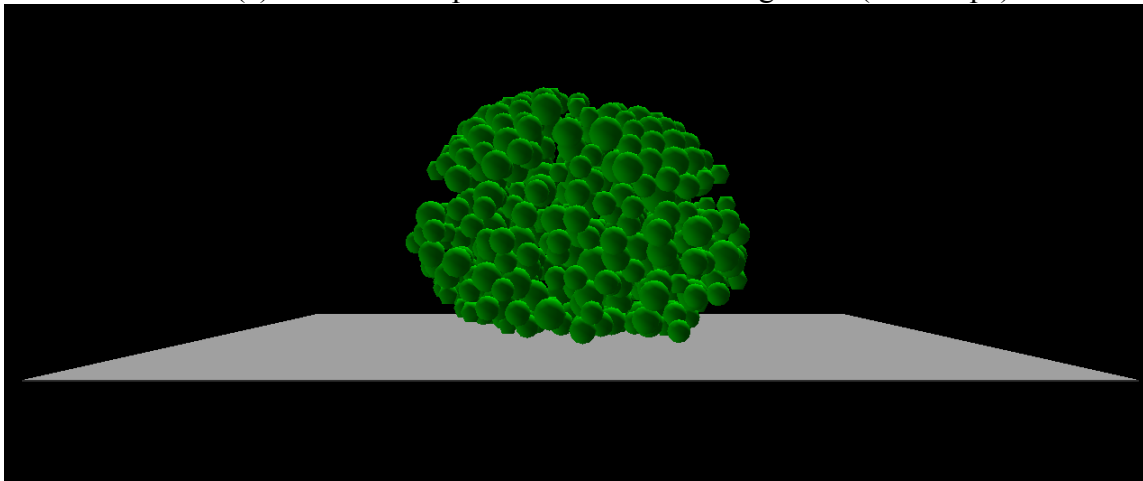
Figure 4-10. Impact fragmentation for opening fractures with 80% persistence after the block (in green) bouncing off the ground (in white)

4.3.4.3 Fracture Orientation

In this case, compared against “X” shape fractures, two fractures in “+” shape centered at the block center were modeled, which are in XY and YZ planes (Figure 4-8), respectively. It shows that “+” shape fractures are more critical to creating fragmentation than “X” form fractures. For fracture persistence of 90%, only 55 fragments were generated for the case of “X” form fractures compared to 224 fragments for “+” shape fractures. As shown in Figure 4-11 (b), 317 fragments were generated with the two bottom part separated by the fractures crashed down. By contrast, there are 196 fragments created after impact with 3 larger fragments for the case of fully persistent “X” shape fractures.



(a) 90% fracture persistence with 224 fragments (“+” shape)



(b) 100% fracture persistence with 317 fragments (“+” shape)

Figure 4-11. Impact fragmentation for different persistence of “+” shape fractures after the block (in green) bouncing off the ground (in white)

4.3.5 Energy Loss during Impact and Dynamic Interaction with the Ground

Energy loss is one of the most concerns in impact modeling. In rock fall impact, considerable kinetic energy is consumed to generate rock fragments, stress waves propagating into the ground, craters into the ground, etc. Usually, the rebound velocity of the rock is significantly less than its impact velocity (An 2006; An and Tannant 2007). In modeling of rock impact against the ground with fragmentation, system energy can be

tracked to understand the energy transformation during impact. Because the ground is idealized as elastic material, the energy loss due to crater generation into the ground cannot be accounted for.

The total system energy (E_T), includes kinetic energy (E_K), strain energy (E_S) and energy loss due to friction (E_F), geometric damping (E_D) and tensile cracking (E_C). According to conservation of energy, the total system energy E_T is equal to the summation of $E_K + E_S + E_F + E_D + E_C$ at any time. The gravity is neglected in impact simulations considering that the gravity of block is much smaller than impact stress during impact for practical impact fragmentation problems.

Kinetic energy consists of translational and angular energy of particles, which can be determined as

$$E_K = \sum_{N_p} \sum_{i=1}^3 \left(\frac{1}{2} M V_i^2 \right) \quad (4-4)$$

where N_p is the number of particles, generalized M includes mass and principal moment of inertial of particles, and generalized V_i includes translational and angular velocity of particles.

Strain energy is the energy stored in normal and tangential springs at all contacts. It can be expressed as

$$E_S = \frac{1}{2} \sum_{i=1}^{N_c} \left(\frac{|F_i^n|^2}{K_i^n} + \frac{|F_i^s|^2}{K_i^s} \right) \quad (4-5)$$

where N_c is the number of contacts, F_i^n and F_i^s are the normal and shear forces, respectively, and K_i^n and K_i^s are normal and shear stiffness, respectively.

Energy losses of friction, geometric damping and tensile cracking are accumulated during impact, and are not recoverable. Friction energy loss occurs after contact shear failure. It can be expressed as (An 2006)

$$E_F \leftarrow E_F - \sum_{i=1}^{N_c} \left(F_i^s \left(\Delta U_i^s - (\Delta U_i^s)^{elastic} \right) \right) \quad (4-6)$$

in which ΔU_i^s is the incremental shear displacement, and $\Delta U_i^s - (\Delta U_i^s)^{elastic}$ stands for the increment of slip displacement.

Geometric damping energy loss is caused by the dashpots associated with the impact model of ground interaction, which is related to stress waves propagating out via the ground. This accumulated damping energy loss is written as

$$E_D \leftarrow E_D + \sum_{N_{p_imp}} \left(c_n v_n \Delta u_n + c_s v_s \Delta u_s \right) \quad (4-7)$$

where N_{p_imp} is the number of particles in direct contact with the ground during impact, c_n and c_s are the damping coefficients determined by Equation (4-2), v_n and v_s are the particle velocity in normal and tangential directions, respectively, and Δu_n and Δu_s are the incremental displacement in normal and tangential directions, respectively.

Tensile cracking energy loss is the energy release of the stored strain energy in normal springs when contact tensile failure occurs. This accumulated tensile crack energy loss is calculated by

$$E_C \leftarrow E_C + \frac{1}{2} \sum_{N_{c_crack}} \left(\frac{(T \cdot A_i^c)^2}{K_i^n} \right) \quad (4-8)$$

where N_{c_crack} is the number of contacts in tensile failure, T is the tensile contact strength, and A_i^c is the contact area.

All of these energies can be tracked to see how the energy is transformed and how the energy transformation is related to failure process. Figure 4-12 shows the energy transformation of a normal impact against a relative stiffer ground (the Young's modulus of the ground: 20 GPa) with an impact velocity of 60 m/s generating 334 fragments. It reveals that:

1) Energy transformation happens mainly during impact period including approach and restitution stages.

2) After the block bounces off the ground, little energy transformation occurs, stored strain energy is released and kinetic energy remains relatively constant.

3) Failure process accompanied by energy loss in friction and tensile cracking only occurs during the period of impact, which means that no further failure occurs after the block bounces off the ground.

4) Friction energy loss takes up the most part of the energy loss, while tensile cracking energy loss is not prominent. For a softer ground condition, the geometric damping energy may go up and exceed frictional energy loss as the impact duration tends to become longer.

5) Total energy, which is the summation of all types of energy, remains constant during the whole simulation, which means energy conservation.

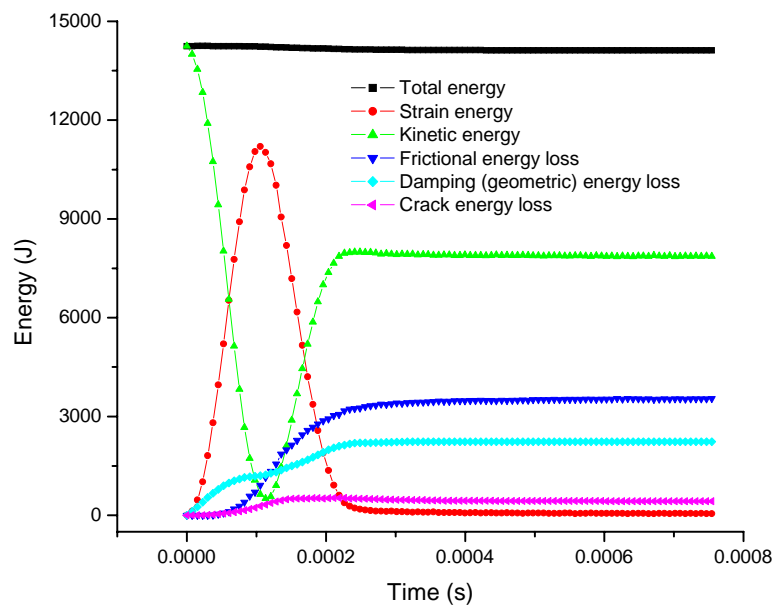


Figure 4-12. System energy transformation and energy loss due to failure and geometric damping during impact

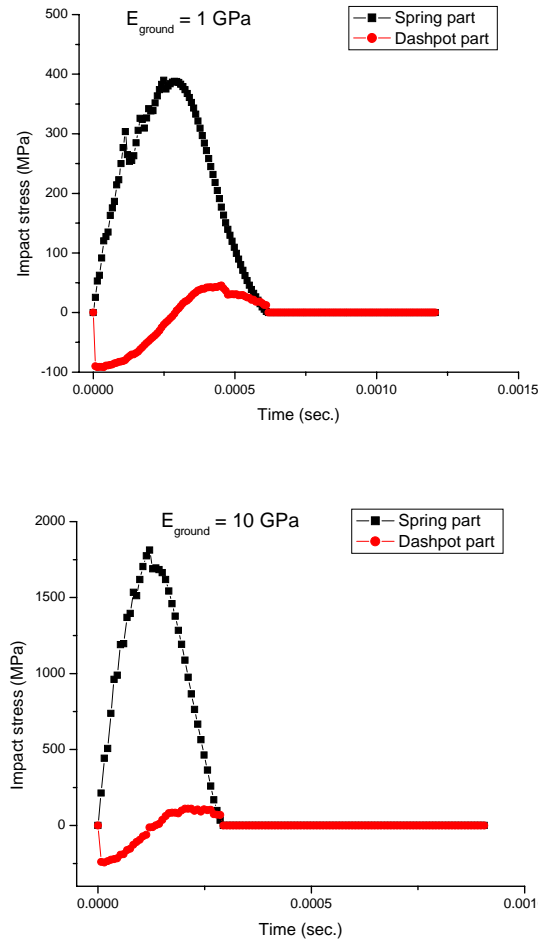


Figure 4-13. Histories of impact stresses resulted from spring and dashpot in normal direction for different ground conditions

In the impact model to simulate the dynamic interaction between rock block and the ground, there are two components directly related to the dynamic interaction, namely stiffness and damping in both normal and tangential directions (Eqs. (4-1) and (4-2)). In terms of impact fragmentation, interaction in normal direction is of the most concern.

The effect of the geometric damping (refer to Section 4.1) on fragmentation was investigated by comparing the contributions of stresses from both spring and dashpot. As seen in Figure 4-13, stresses resulted from both spring and dashpot in the normal

direction were recorded during impact for different ground conditions. The stress related to geometric damping is overshadowed by the stress from the spring, especially for a stiffer ground. For a soft ground, the contribution from damping part is relatively higher than that for a stiffer ground, so the energy dissipation from geometric damping is relatively higher for a softer ground.

4.4 CONCLUSION

The developed DEM code has been used with a simplified impact model inspired by the theory of foundations subjected to dynamic loading to simulate impact induced rock fragmentation in rockfall analysis. This approach can provide us some valuable insights into impact induced rock fragmentation, although the real physical process is too complicated to be fully modeled. It has been shown that the magnitude of impact velocity, the angle of the incidence, ground conditions and fractures all play very important roles in impact fragmentation.

CHAPTER 5 FRAGMENTATION MODULE

5.1 INTRODUCTION

The final rockfall analysis package to be delivered in this research consists of a rockfall analysis platform, HY-STONE (Agliardi and Crosta 2003), and a developed fragmentation module. It takes a relatively long time to run an impact simulation with the developed DEM code depending on the impact conditions. Hence it is not wise to directly invoke DEM code to run impact simulations to obtain fragmentation information in performing rockfall analysis. Alternatively, a large set of impact simulations have been carried out beforehand to build up a database, which is used to develop a fragmentation module by either training a neural network model or linearly interpolating the database. This module is employed to predict impact fragmentation processes during a rockfall analysis.

An interface has been developed by Dr. Crosta's group at the Bicocca University of Milano, Italy, to integrate the developed fragmentation module into HY-STONE. When an impact occurs during rockfall analysis, the module will detect whether fragmentation occurs or not. If fragmentation does not occur, HY-STONE will continue its ordinary rockfall analysis. If fragmentation is detected, HY-STONE will stop the simulation of "ordinary" trajectories at the impact location where fragmentation has been detected, and invoke the fragmentation module to generate detailed fragment information, and continue rockfall analysis by following each generated fragment.

5.2 SIMULATION DATABASE PREPARATION

A large set of impact simulations were carried out to cover different impact scenarios. For simplicity, a spherical block with a diameter of 0.1 m was simulated by using a 2,500-sphere packing. The simulations of different block sizes can be

approximately obtained by scaling the results of 0.1 m diameter packing. Because the failure criteria used in discrete element model are stress dependent rather than scale (particle size) dependent, the effect of scale on simulation results should be negligible especially for fragmentation. This has been confirmed by following two different simulations: uniaxial compression test and impact test.

In the simulations of uniaxial compression test, two types of cylindrical specimen were used. The smaller specimen has radius of 0.0125 m and height of 0.05 m, while the larger one is 0.25 m in radius and 0.1 m in height, which is double size of the smaller one. The larger specimen was directly scaled up from the packing for the smaller specimen, and hence has the same number of particle (2,500) and the same packing structure as the smaller one. Except for the specimen size, all the model parameters used in the simulation were the same for both simulations. Figure 5-1 shows that the simulated stress-strain curves are very close to each other and the scale dependence is negligible.

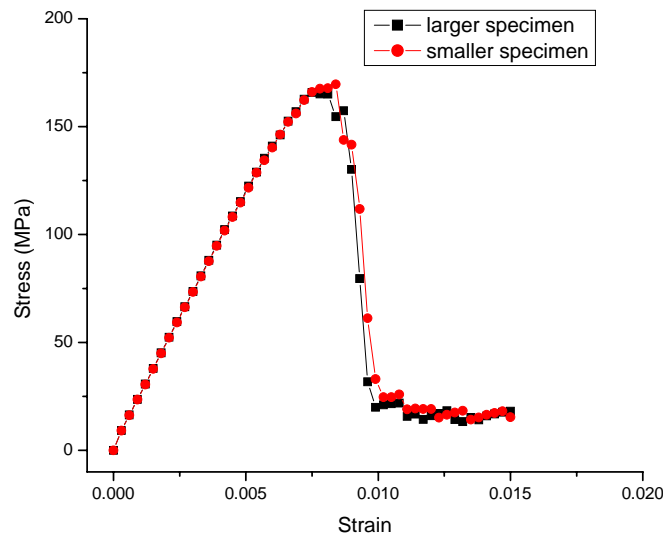


Figure 5-1. Comparisons of simulated stress-strain curves of uniaxial compression test for two different scales of specimen

In impact simulations, two different sizes of spherical block were used to investigate the scaling effect on impact fragmentation. The smaller block has radius of 0.1 m and the larger one is 0.4 m in diameter. The larger specimen of rock block was directly scaled up from the packing for the smaller spherical block, and has the same number of particles (600) and the same packing structure as the smaller one. An oblique impact with incident angle of 60 and velocity of 50 m/s against the ground with a Young's modulus of 50.0 GPa was considered in the simulations. All other model parameters were the same for both simulations. The comparisons on generated fragments for two different sizes of block given in Table 5-1 show that the number of fragments and fragment velocity are approximately close to each other and the scale dependence can also be neglected.

Table 5-1. Comparisons of simulated impact fragmentation for two different sizes of block

Fragment information		Smaller block	Larger block
Number of fragment		103	111
The 1 st large fragment	Number of particle	477	467
	Mass (kg)	6.51	402.8
	Velocity vector (m/s)	(22.4, 1.4, 36.7)	(23.5, 1.0, 38.7)
The 2 nd large fragment	Number of particle	4	5
	Mass (kg)	0.09	4.7
	Velocity vector (m/s)	(8.4, -14.1, 31.1)	(14.7, -20.5, 22.7)
The 3 rd large fragment	Number of particle	3	4
	Mass (kg)	0.04	3.9
	Velocity vector (m/s)	(11.8,-0.4,18.2)	(9.2, 0.3, 40.0)

There are seven input parameters used in building the database of impact simulations. These input parameters consist of three types of properties, namely, material properties of rock block itself, ground conditions and impact profiles. There are five micro model parameters used to describe the material properties: particle Young's modulus, E_c , the ratio K_s / K_n , cohesion, c , friction angle, φ , and tensile strength, T . The ratio K_s / K_n is directly related to material's Poisson's ratio, which does not vary much for most rock materials, and hence is not included in the input parameters. The ratio K_s / K_n was kept as 0.15, which leads a Poisson's ratio of about 0.25. For ground conditions, only Young's modulus of the ground, E_{grd} , is used, while the Poisson's ratio of the ground is not included because it does not significantly affect the results (Section 4.2). The Poisson's ratio of the ground was selected as 0.3. There are two parameters used to describe the impact profile: magnitude of impact velocity, V , and incidence angle, θ , which is defined, in a local reference system, as the acute angle between impact velocity and slope plane, 90° for normal impact, 0° for purely tangential impact.

The possible bounds for each parameter are set to cover possible scenarios, which can happen in reality, as listed as in Table 5-2.

Considering the computational burden of large number of simulations, the number of points for each input parameter should be small. Three points were selected for each micro parameter to describe material properties of rock block. Five points were chosen for each parameter used for ground condition and impact profile. This leads up to a total number of $3^4 \times 5^3 = 10,125$ impact simulations. The number of points chosen for each input parameter may be too sparse to generate acceptable accurate results especially for interpolation method. However, increasing the density of the points for each input parameter may substantially increase the number of impact simulations.

For each simulation, the number of fragments and the mass and average velocities of each fragment are recorded and are used as output parameters for either neural network or interpolation method to predict impact fragmentation.

Table 5-2. Input parameters for impact simulations

Properties	Material properties of rock block (micro parameters)				Ground condition	Impact profile	
Parameter	E_c (GPa)	c (MPa)	φ (°)	T (MPa)	E_{grd} (GPa)	V (m/s)	θ (°)
Low bound.	5.0	50.0	30.0	10.0	0.1	1.0	5.0
High bound.	200.0	500.0	80.0	150.0	50.0	60.0	90.0

5.3 NEURAL NETWORK MODEL

5.3.1 Overview

Neural networks (NNs) (Hecht-Nielsen 1987; Schalkoff 1997) provide a massively parallel computational model that mimics the structure and operation of the human brain. NNs are capable of learning highly non-linear relationships, they are noise tolerant, and truly adaptive (J. G. Cai 1998; Sidarta 2000; Sonmez et al. 2006). These features make NN able to perform predictions for some complex processes, such as impact fragmentation process.

NN learns from examples (training data) to gain and discover the insight information presented in training data. During the learning process, the NN adjusts NN connection weights associated to each neuron to be able to reproduce the training data.

In this section, NN was used to predict impact fragmentation process, specifically, the number of fragments, and the mass and velocities of each fragment, by training the NN with the data included in the simulation database discussed previously in Section 5.2.

5.3.2 Multi-layer Feed Forward NN

The first computational model of an artificial neuron (also referred to as processing unit or node) that was capable of threshold logic operation was proposed by McCulloch and Pitts (McCulloch 1943). Hebb (Hebb 1949) designed the first learning rule for NN, which was based on the premise that if two neurons were activated simultaneously, then the strength of the connection between them should be increased. Then using the McCulloch-Pitts neurons, Rossenblatt (Rosenblatt 1962) developed a two-layer learning system, called perceptron.

5.3.2.1 Neuron Model

A neuron with a single R -element input vector is shown in Figure 5-2 (Howard et al. 2007). The individual elements of inputs $[p_1, p_2, \dots, p_R]$ are multiplied by weights $[w_{1,1}, w_{1,2}, \dots, w_{1,R}]$ and are summed as form of $W \cdot p$, the dot product of the single-row matrix W and the vector p .

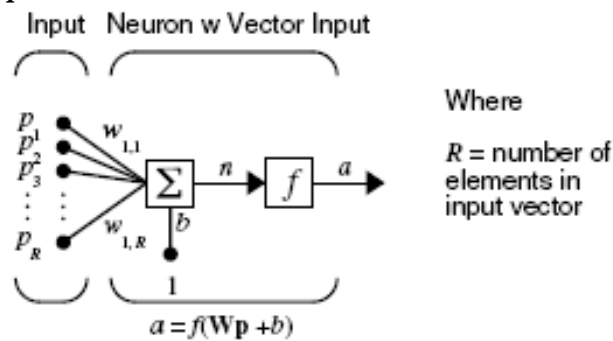


Figure 5-2. A neuron with vector input used in neural network model (Howard et al. 2007)

The neuron has a bias b summed with the weighted inputs to form the net input n as $n = w_{1,1}p_1 + w_{1,2}p_2 + \dots + w_{1,R}p_R + b$, which is the argument of the transfer function f .

5.3.2.2 Network Architecture

Network architecture refers to the topology of the NN that includes the number of layers and the number of neurons in each layer. A method to back-propagate the error information from the output neurons to hidden neurons, which are the neurons in the hidden layers between input layer and output layer, was discovered by Werbos (Werbos 1974). This method led to the development of multi-layer, feed-forward NNs, also called backpropagation NNs (Sidarta 2000).

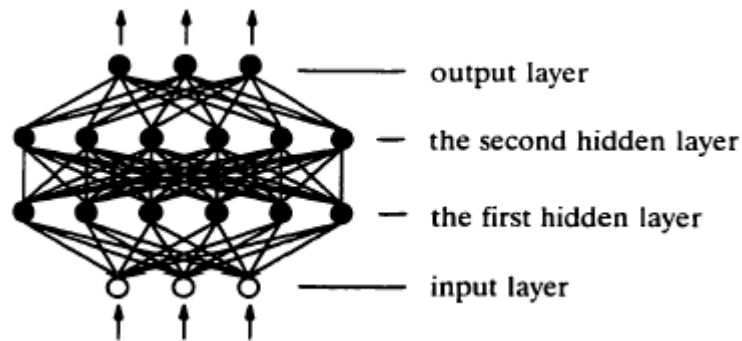


Figure 5-3 A typical multi-layer feed forward NN with two hidden layers (Howard et al. 2007)

In the multi-layer, feed-forward NN, as illustrated in Figure 5-3, the artificial neurons are in layers. All neurons in each layer have connections to all neurons in the next layer. A NN starts with the operation by presenting input signals to the input neurons. These signals forwardly travel through the connections, and reach the output neurons to produce the output of the NN.

A layer can consist of two or more of the neurons. A network can have several such layers. Each layer has a weight matrix \mathbf{W} (\mathbf{IW} : Input weight matrix, \mathbf{LW} : Layer

weight matrix), a bias vector \mathbf{b} , and an output vector \mathbf{a} . To distinguish between the weight matrices, output vectors, etc., for each of these layers in Figure 5-4, the number of the layer is appended as a superscript to the variable of interest. The network shown in Figure 5-4 has R inputs, S^1 neurons in the first layer, S^2 neurons in the second layer, etc.

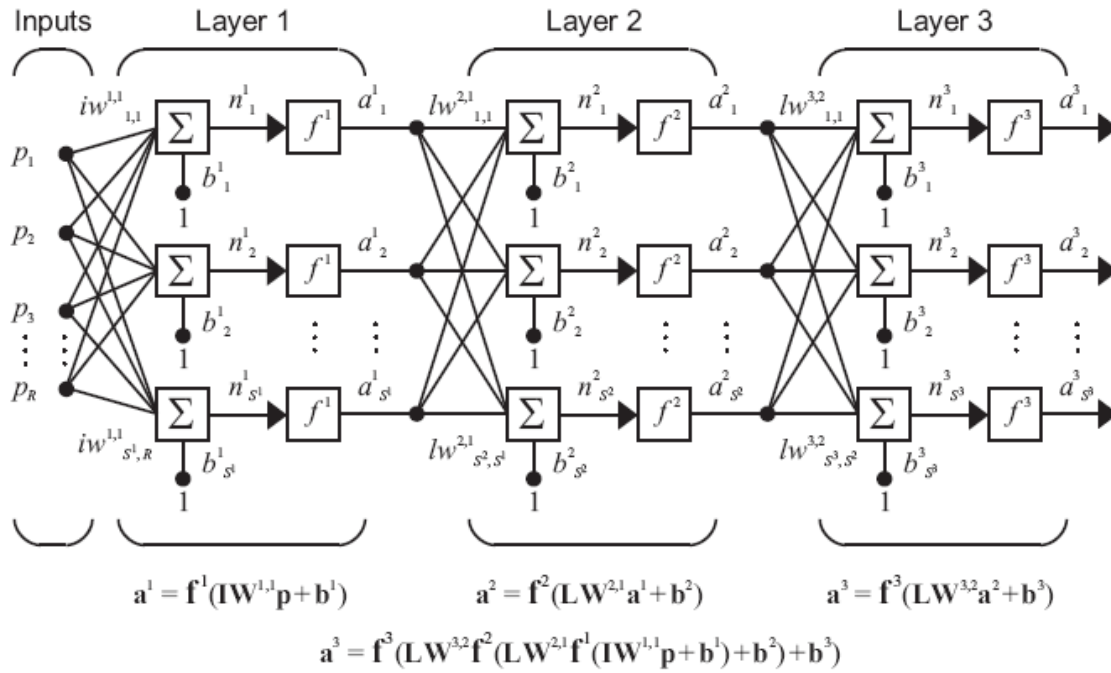


Figure 5-4. A multi-layer neural network (Howard et al. 2007)

There are three types of layers in a multilayer network. A layer that used to feed the input elements is called an input layer. A layer that produces the network output is called an output layer. All other layers are called hidden layers.

The number of layers is essentially determined from the number of hidden layers. The number of neurons in the input and output layers can be easily determined from the problem representation, but the number of neurons in hidden layers, which determines the capacity of the NN, is difficult to determine in priori, since it is deeply related to the complexity of the underlying knowledge base in the training data and the degree of

complexity of the problem. The relation between the degree of complexity of the problem and the network architecture is not well understood at present (Schalkoff 1997; Sidarta 2000).

5.3.2.3 Neural Network Training

“The purpose of NN training is to allow the NN to learn and discover the underlying information present in the training data in the form of input-output pairs and to self-organize to adapt to the database environment” (Schalkoff 1997; Sidarta 2000). NN adapts to the presented training data by changing the values of its connection weights. The learned knowledge during the NN training is stored in NN connection weights.

The training process consists of three major steps (Schalkoff 1997; Sidarta 2000): (1) initialization of connection weights, (2) presentation of training examples, and (3) adjustment of connection weights. The connection weights are randomly initialized within a small range of values. An input signal is then forwardly passed through the NN to produce an output signal by applying corresponding NN connection weights. The output error is backpropagated through the NN, and the connection weights are adjusted by adopting a specified learning rule. The training process is repeated until a satisfactory learning is achieved. During iterative training of a neural network, a single pass through the entire training set is called a training epoch.

5.3.3 Input and Output Neurons

Input layer consists of seven input parameters as shown in Table 5-2, which have already been discussed in Section 5.2.

Output layer is formed by 41 parameters, which include the total number of fragments, mass and velocities of the largest 10 fragments generated in an impact

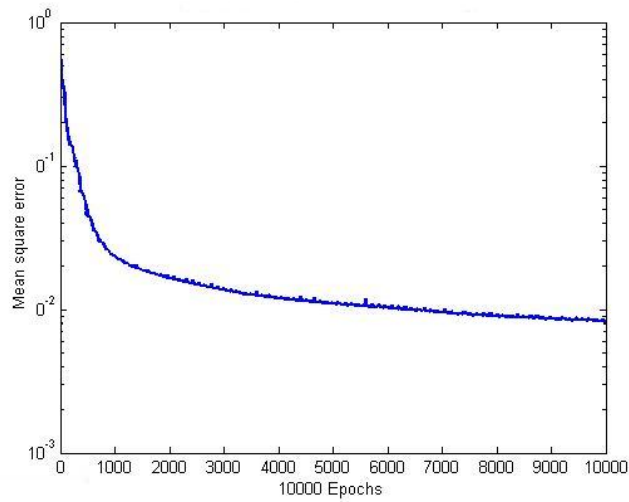
simulation. If the total generated number of fragments is less than 10, the remaining output parameters are set as zero.

5.3.4 Training and Testing Network

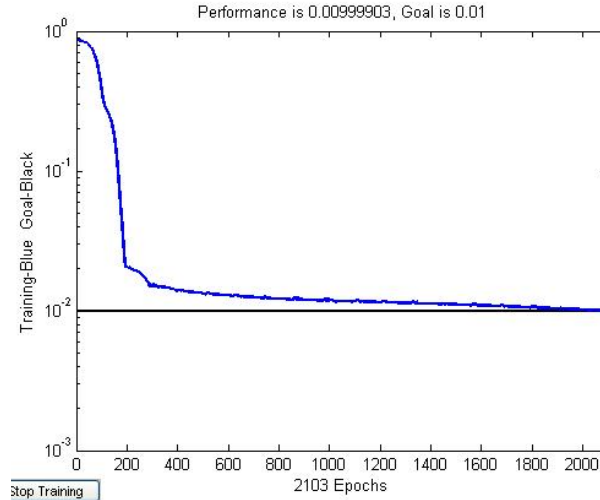
The selection of an adequate number of training patterns is extremely important, both the size and range of training set affect the performance of the network. If there are too few training patterns, the network can memorize all of the correct outputs because of the large capacity of the weights. Therefore the resulting network is accurate on the training set but makes poor predictions on the testing set. When the number of training patterns is large, the learning procedure finds common features among the patterns in the training set that enable the network to correctly predict the desired outputs that were not included in the training set, but the training time will be prolonged. Because at present neural networks are not good at extrapolating information outside the training domain, patterns chosen for training should cover ranges of parameters values used in practice. 10,125 patterns from the simulation database were chosen to train the neural network and additional 40 cases were used to test the trained neural network.

The purpose of utilizing NN is to form a fragmentation module to be integrated into HY-STONE for predicting impact fragmentation in rock fall analysis. In many cases, impacts occur but no fragmentation happens or just local failure occurs. Under such situations, in order to save computational resource no complete fragmentation information needs to be output. Therefore, the prediction process was divided into two stages. In the first stage, a trained neural network is employed to determine whether a rock block is heavily fragmented or not after impact. Only when a heavily fragmented impact is detected, the second stage is activated to predict the detailed fragmentation. In

the second stage, the masses and velocities of fragments are predicted by a second trained neural network. Both networks have one hidden layer.



(a) First stage prediction with 27 hidden neurons



(b) Second stage prediction with 20 hidden neurons

Figure 5-5. Convergence characteristics of training for the two neural networks

Since NN requires a few trials to establish a desired network, a parametric study were carried out by changing the number of neurons in the hidden layer. The number of neurons in the hidden layer has been decided based on reasonable errors from repeated trainings. The mean square error plotted as a function of the training epochs is shown in Figure 5-5. Experiments indicated that there was no significant improvement in convergence as the number of neurons in hidden layer increased beyond 27 for first stage prediction and 20 for second stage prediction.

5.3.5 Performance of Trained Neural Networks

In order to make sure that the network is capable of generalization, a set of unseen patterns were used to check network performance. Forty patterns not included in the database (i.e. whose values do not coincide with grid points) were chosen to evaluate the interpolation performance. The number of fragments, the mass and velocity component in Z direction (V_z) (referred to Figure 4-2) of the largest fragment were selected to evaluate interpolation performance.

5.3.5.1 Performance of the First Stage NN Prediction

To evaluate the capability of the network, the scatter diagram of the output values and target values of network for prediction of number of fragments was plotted as shown in Figure 5-6. Ideally, on a plot of output versus target, the points should be aligned along the 1:1 diagonal straight line. The results plotted in Figure 5-6 show that the trained neural network can be used to approximately predict the number of fragments in impact simulations.

5.3.5.2 Performance of the Second Stage NN Prediction

There are 40 output parameters in the network of the second stage of prediction. In order to observe the performance of network, the mass (m) and velocity in Z direction

(V_z) (referred to Figure 4-2) of the largest fragment are selected. These two parameters are the first and second, respectively.

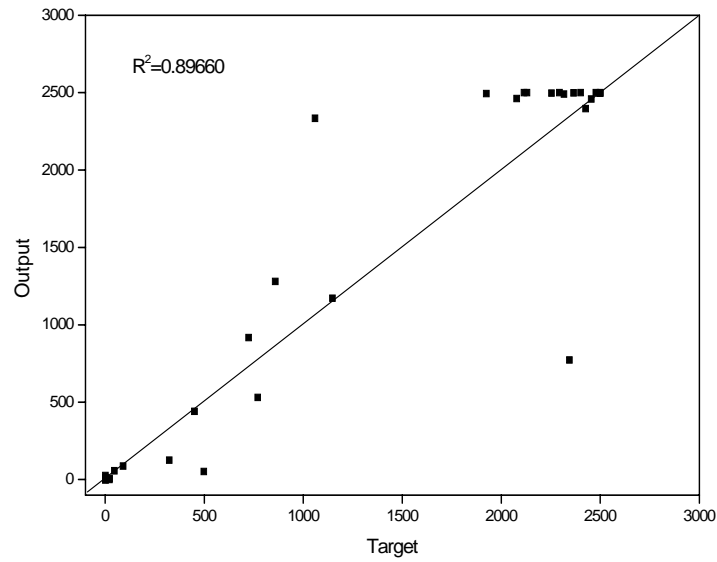


Figure 5-6. Network performance for the number of fragments in the first trained neural network

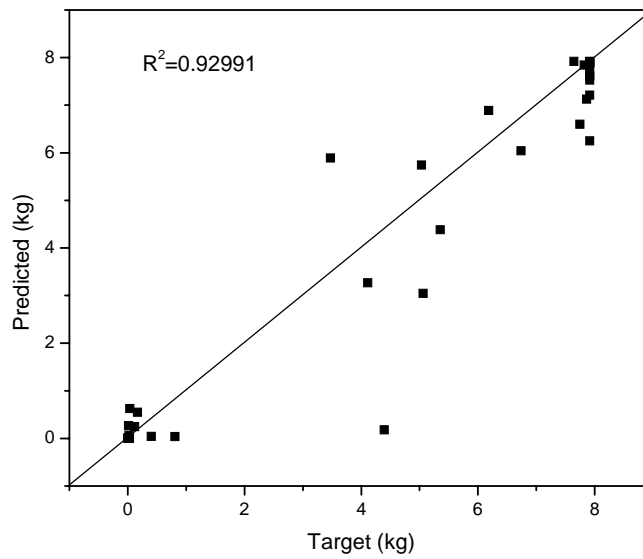


Figure 5-7. Network performance for the mass of the largest fragment (the 1st output) in the 2nd trained neural network

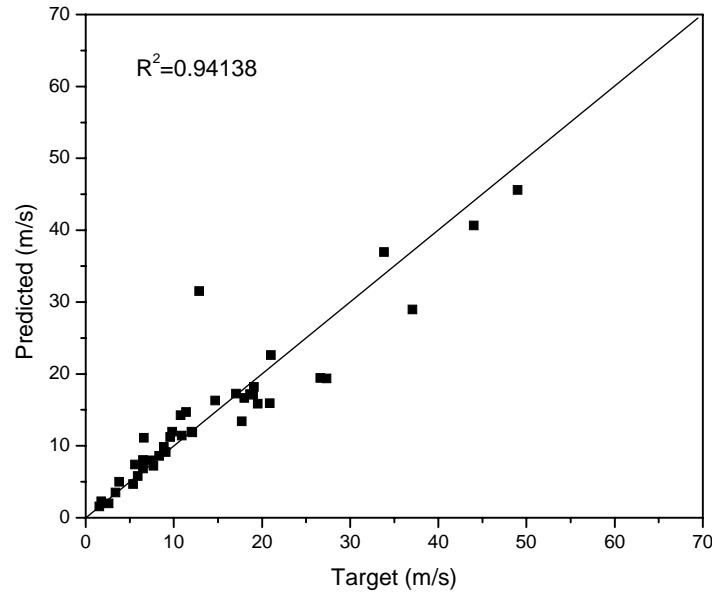


Figure 5-8. Network performance for the V_z component of the largest fragment (the 2nd output) in the 2nd trained neural network

Figures 5-7 and 5-8 show the performance of the two outputs in the 2nd trained neural network. Overall, the network has good prediction performance. By comparing Figure 5-6 against Figure 5-7, it is seen that the velocity correlation is better than the mass correlation. This difference is due to the fact that velocity depends on input parameters more smoothly than mass, which can be seen from the statistic analyses on fragment information in training database prescribed below. The network performance is actually related to the underlying smoothness in the training database, because NN can more easily capture a smooth database.

Some statistical analyses were performed on all fragments in the numerical simulations used for training. Figure 5-9 shows that the distribution of fragment mass is highly concentrated in two regions: either smaller than 0.5 kg or larger than 7.5 kg, which means that for most of the simulations, the rock blocks are either fully shattered or nearly

unbroken. This highly non-smooth behavior is difficult to be predicted by using neural network. Unlike the distribution of mass, the distributions of velocity components are highly concentrated and related to the input parameters of impact profiles as seen in Figure 5-10.

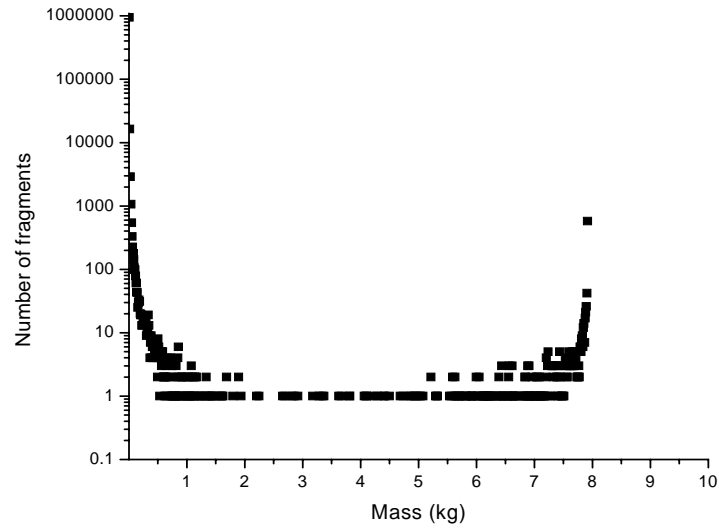


Figure 5-9. Statistic distribution of fragment mass in the database of impact simulation

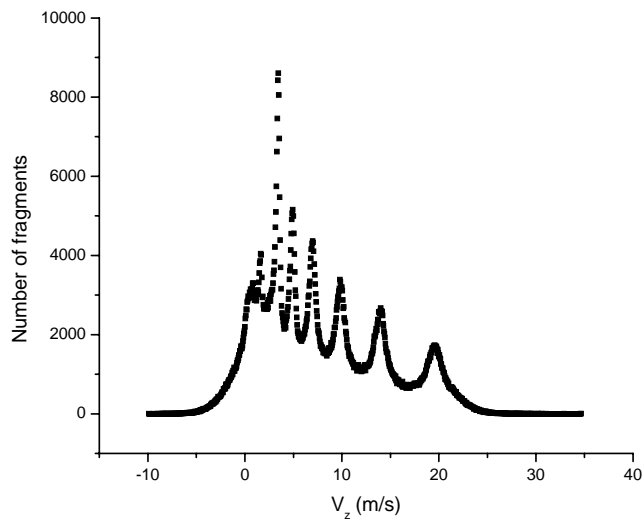


Figure 5-10. Statistic distribution of fragments velocity component in the Z direction in the database of impact simulation

5.4 INTERPOLATION METHOD

5.4.1 Multilinear Interpolation

As the impact simulation database is rectangular-grid-based with respect to the seven input parameters, multi-dimensional interpolation method is of the option for the prediction approximation. Multilinear interpolation was chosen, in which one-dimensional linear interpolation is applied in each separate coordinate dimension (Judd 1998). Following algorithms are taken from Kenneth's work (Kenneth 2006).

Interpolating function $y[\mathbf{x}]$ is based on a sampling of y at point $\mathbf{x} = \mathbf{x}^{[m]}$, wherein \mathbf{x} is defined as $\mathbf{x} = (x_1, x_2, \dots, x_n)$, $\mathbf{x}^{[m]} = (x_1^{[m]}, x_2^{[m]}, \dots, x_n^{[m]})$ in an n -dimensional Cartesian space, and \mathbf{m} is an integer-valued, n -dimensional index list ($\mathbf{m}=(m_1, m_2, \dots, m_n)$).

This multilinear interpolation algorithm requires a rectangular sampling grid. For multilinear interpolation, it has the following form,

$$yFit^{[m]}[\mathbf{x}] = \sum_{\substack{\mathbf{s}=(s_1, \dots, s_n), \\ s_j \in \{0,1\}}} u_s^{[m]}[\mathbf{x}] y[\mathbf{m} + \mathbf{s}], \quad (5-1)$$

where the functions $u_s^{[m]}[\mathbf{x}]$ are defined so that at grid points

$$yFit^{[m]}[\mathbf{m} + \mathbf{s}] = y[\mathbf{m} + \mathbf{s}]; \quad s_j \in \{0,1\}; \quad j \in \{1, \dots, n\} \quad (5-2)$$

This require that the functions satisfy the following conditions,

$$u_s^{[m]}[\mathbf{m} + \mathbf{s}'] = \begin{cases} 1, & \mathbf{s} = \mathbf{s}' \\ 0, & \mathbf{s} \neq \mathbf{s}' \end{cases}, \quad s_j, s'_j \in \{0,1\}; \quad j \in \{1, \dots, n\} \quad (5-3)$$

$u_s^{[m]}[\mathbf{x}]$ is linear in each coordinate x_j and can be expressed as

$$u_s^{[m]}[\mathbf{x}] = \prod_{j \in \{1, \dots, n\}} (1 - |x_j - m_j - s_j|) \quad \text{with } m_j \leq x_j \leq m_j + 1 \quad (j \in \{1, \dots, n\}) \quad (5-4)$$

5.4.2 Performance

The accuracy of the prediction in impact fragmentation depends on the density of grid points. Due to the limit of computational resource, the density of grid points is

relatively low, which may lead to poor prediction accuracy. The number of grid points over a given interval of input values varies from 3 to 5 depending on the input parameter.

The 40 patterns used for testing NN performance were also chosen to evaluate the interpolation performance. The number of fragments, the mass and velocity component in Z direction (V_z) of the largest fragment were selected to evaluate interpolation performance. Figures 5-11 to 5-13 show the interpolation performance for these three output parameters, respectively. The overall performance of interpolation method is poorer than that of trained neural network, but it still can be used to reasonably predict the impact fragmentation.

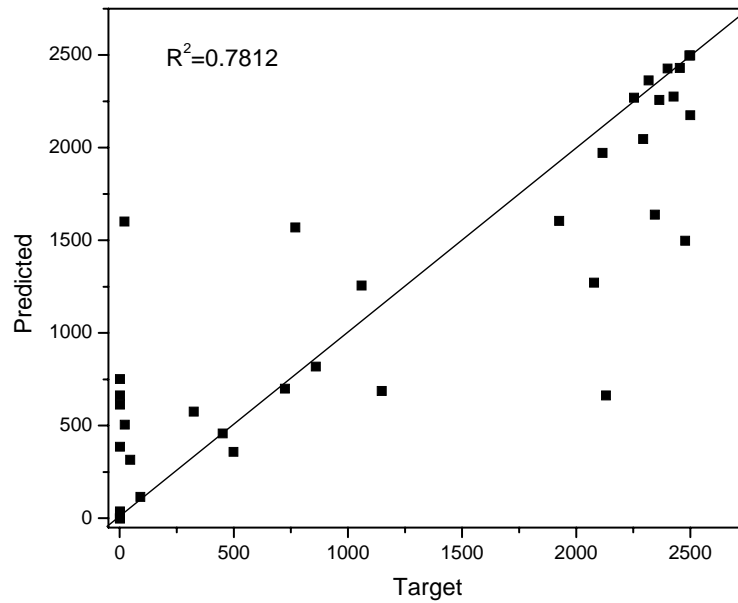


Figure 5-11. Performance of interpolation method for the number of fragments (1st output)

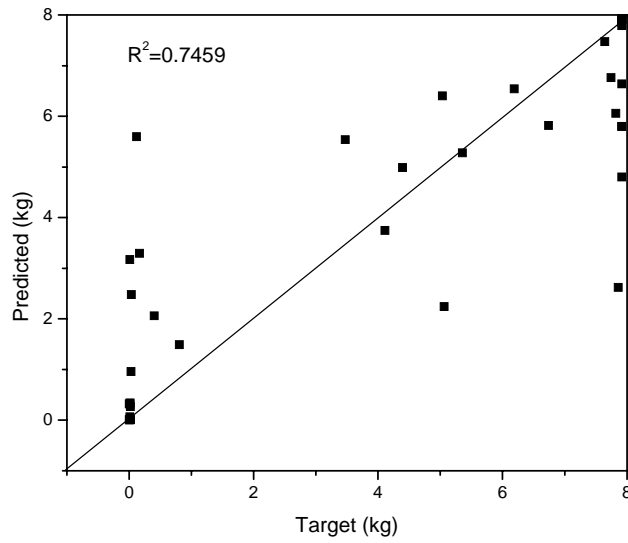


Figure 5-12. Performance of interpolation method for the mass of the largest fragment (2nd output)

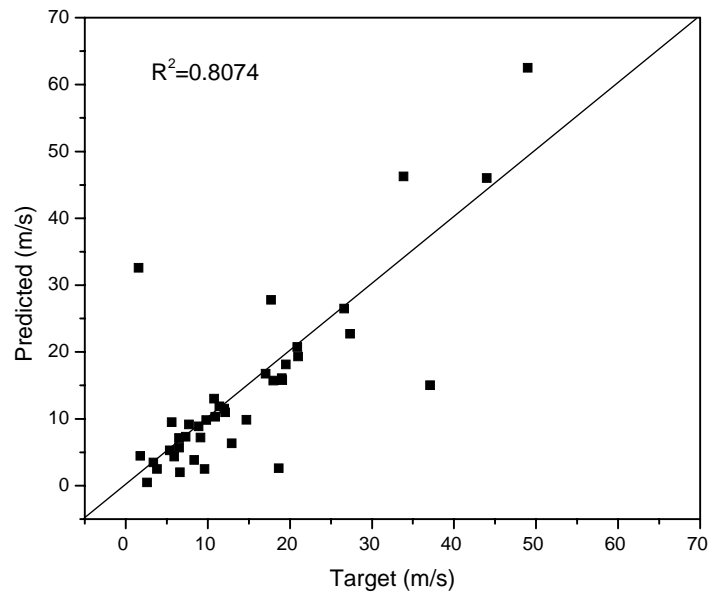


Figure 5-13. Performance of interpolation method for the velocity component in Z direction of the largest fragment (3rd output)

5.5 FRAGMENTATION MODULE

5.5.1 Overview

The fragmentation module to be integrated into HY-STONE is based either on trained neural network or on the interpolation method. Because the neural network was developed and trained in MATLAB environment, the MATLAB should be activated whenever the fragmentation module is recalled. This may extensively increase the computational burden while running HY-STONE for rockfall analysis by considering impact fragmentation. The interpolation method is a standalone program which can be directly recalled to predict impact fragmentation. Compared to neural network method, interpolation method is less accurate due to relatively sparse grid points.

The fragmentation module has input and output which are directly fed and read, respectively, by HY-STONE when impact fragmentations are considered during rock fall analysis. This is explained in Section 5.5.2.

As impact simulations were performed based on a local reference system with a unique block size, transformation and scaling should be applied to the predicted results for both neural network and interpolation methods so that HY-STONE can directly use them for rock fall analysis. This is explained in Section 5.5.4.

5.5.2 Input and Output

The following input parameters should be input before HY-STONE calls the fragmentation module:

E_c (GPa):	Particle Young's modulus
c (MPa):	Micro cohesion
ϕ ($^{\circ}$):	Micro frictional angle
T (MPa):	Micro tensile strength

E_{grd} (GPa):	Ground Young's modulus
V (m/s):	Impact velocity
θ ($^{\circ}$):	Incidence angle
COR_n :	Coefficient of restitution in normal direction
COR_s :	Coefficient of restitution in tangential direction
Dimensional scaling factor:	$\lambda = \frac{R_{Equivalent}}{0.1 \text{ m}}$

The first seven parameters are the same as those used for simulation database preparation, which have already been discussed in Section 5.2. Coefficients of restitution in normal (COR_n) and tangential (COR_s) directions are defined respectively as the ratio of the magnitudes of velocity components in normal and tangential directions (with respect to an impact plane) before and after an impact. The dimensional scaling factor, λ , is defined as the ratio of actual equivalent block size (radius) over the simulated block size (0.1 m in radius).

The output parameters are similar to those in simulation database preparation except that velocity of each fragment should be transformed into the global reference system used in HY-STONE. These parameters are:

N :	Number of fragments
m_i :	Mass of fragment i
R_i :	Equivalent radius of fragment i
\vec{V}_{i_glb} :	Velocity vector of fragment i in a global reference system

Only the largest 10 fragments are output. If the total number of fragments is less than 10, all the output parameters of remaining virtual fragments will be set to “zero”.

5.5.3 Preprocessor

Impact simulations are performed based on a local reference system (refer to Figure 4-2 and Section 4.2), in which the effect of gravity is neglected compared to the large impact forces. The purpose of the preprocessor is to prepare input parameters in the local reference system at the point of impact. The local reference system is formed as follows based on a global reference system:

- The origin of the local reference system is located right at the impact point;

- The unit vector Z_{loc} , with components $\begin{bmatrix} x_3 \\ y_3 \\ z_3 \end{bmatrix}$ in the global reference system,

points upward normal to the slope;

- The unit vector X_{loc} , with components $\begin{bmatrix} x_1 \\ y_1 \\ z_1 \end{bmatrix}$ in the global reference system,

points in the direction of projected impact velocity on the slope plane;

- The unit vector Y_{loc} , with components $\begin{bmatrix} x_2 \\ y_2 \\ z_2 \end{bmatrix}$ in the global reference

system, can be then determined by considering the right-hand rule ($Y_{loc} = Z_{loc} \times X_{loc}$).

The transformation matrix from the local to the global reference system, M is

$$M = \begin{bmatrix} X_{loc} & Y_{loc} & Z_{loc} \end{bmatrix} = \begin{bmatrix} x_1 & x_2 & x_3 \\ y_1 & y_2 & y_3 \\ z_1 & z_2 & z_3 \end{bmatrix}. \quad (5-5)$$

The transformation matrix from the global to the local reference system is M^T .

5.5.4 Postprocessor

The purpose of the postprocessor is to transform the predicted results from a local (XYZ_{loc}) to a global (XYZ_{glb}) reference system, and to apply coefficients of restitution and scaling factor to the results, so that HY-STONE can directly continue the rockfall analysis with the predicted fragmentation information.

The output impact velocity is adjusted by taking account of coefficients of restitution in both normal and tangential directions. The adjusted velocity components for the i -th fragment in local reference system are computed by considering coefficients of restitution as:

$$\begin{cases} V'_{i_x} = V_{i_x} \cdot COR_s \\ V'_{i_y} = V_{i_y} \cdot COR_s \\ V'_{i_z} = V_{i_z} \cdot COR_n \end{cases} \quad (5-6)$$

The velocity vector of the i -th fragment, $(V'_{i_x}, V'_{i_y}, V'_{i_z})$, is then transformed from local reference system to global reference system as $V_{i_glb} = M \cdot V_{i_loc}$.

The mass of each fragment is scaled up by the factor λ^3 , and the equivalent radius of each fragment is scaled up by a factor λ .

CHAPTER 6 Case Studies

6.1 INTRODUCTION

In this chapter, three rockfall case histories (namely, the California quarry rockfall field tests, the Rossing drop tests, and the Argyle rockfall event) have been used to validate the developed impact fragmentation module in rockfall analysis. Among the three case histories, only the California case has detailed topographical information on the slope, and hence it has been selected to validate the rockfall package that integrates the fragmentation module into STONE. The other two case histories have been selected to directly validate the impact model, where only single impacts were simulated to evaluate fragmentation.

6.2 CALIFORNIA ROCKFALL TESTS

6.2.1 Overview

In an effort to evaluate the environmental impact of conversion of the Guadalupe Valley Quarry, located in Brisbane, CA, to a civil development, drop tests were carried out with the aim of determining the runout distance of possible rockfalls down a 165-m high slope. The drop tests were documented in detail by using a high-speed camera including fragmentation information.

Sixty three blocks were dropped with a wheel loader from two different locations following two possible different cross sections F-F' and G-G' as shown in Figures 6-1 to 6-4. The rock blocks were composed of sandstone either with isolated fractures or highly fractured. The run-out distance and the sample condition after fall were recorded.

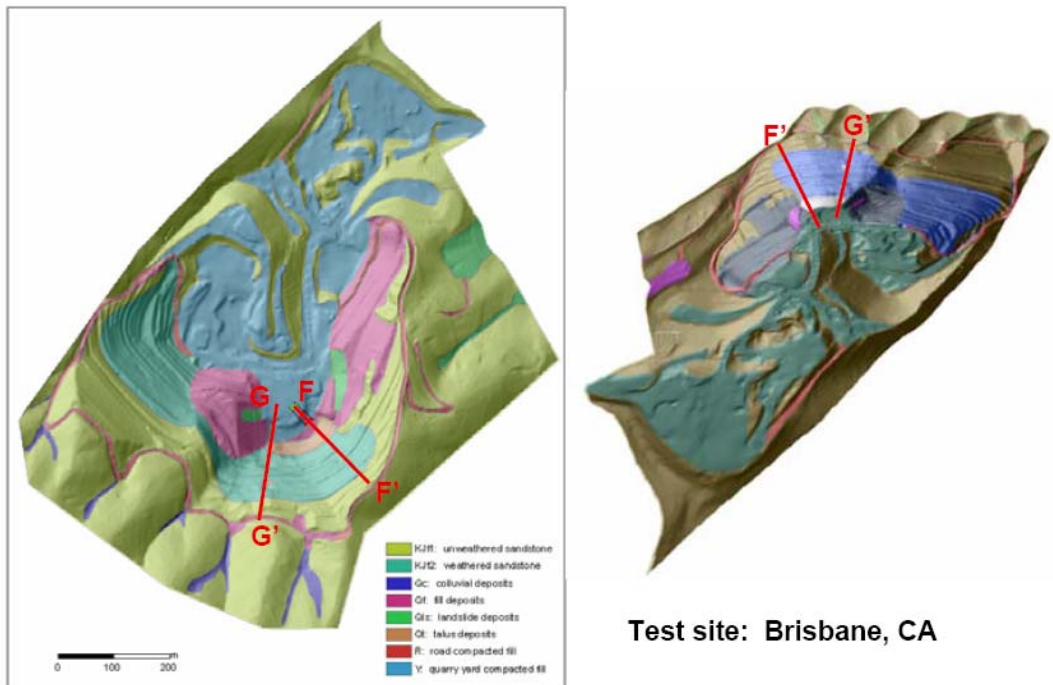


Figure 6-1. 3D topographic map of the test site in Brisbane, CA with the sketch of two cross-sections used for dropping tests

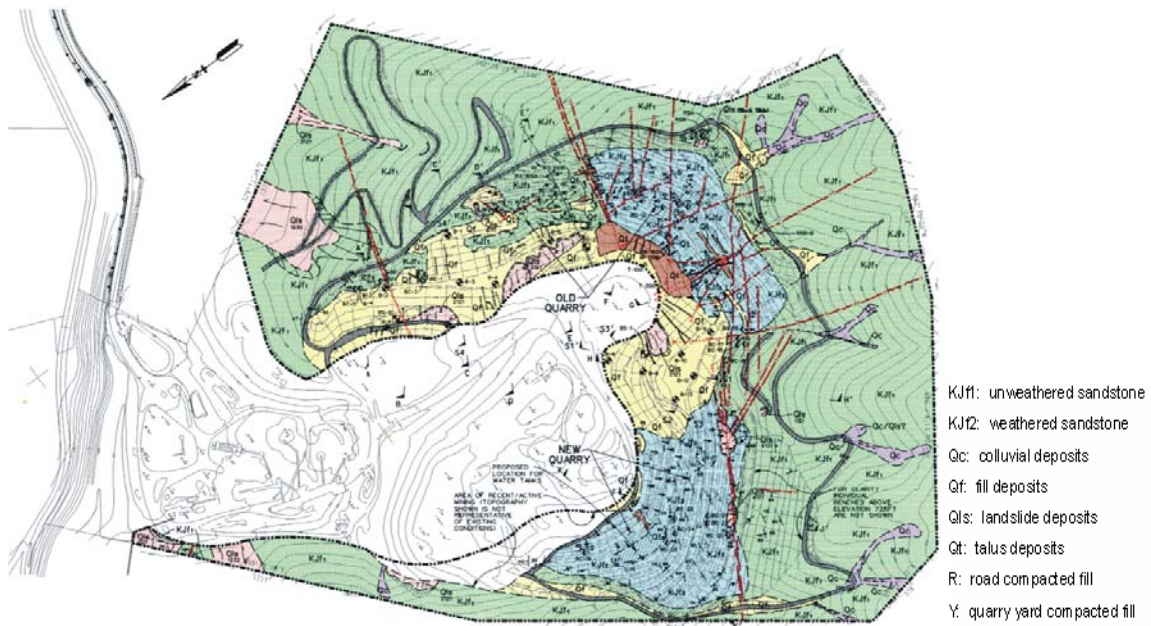


Figure 6-2. Geological map of the test site in Brisbane, CA

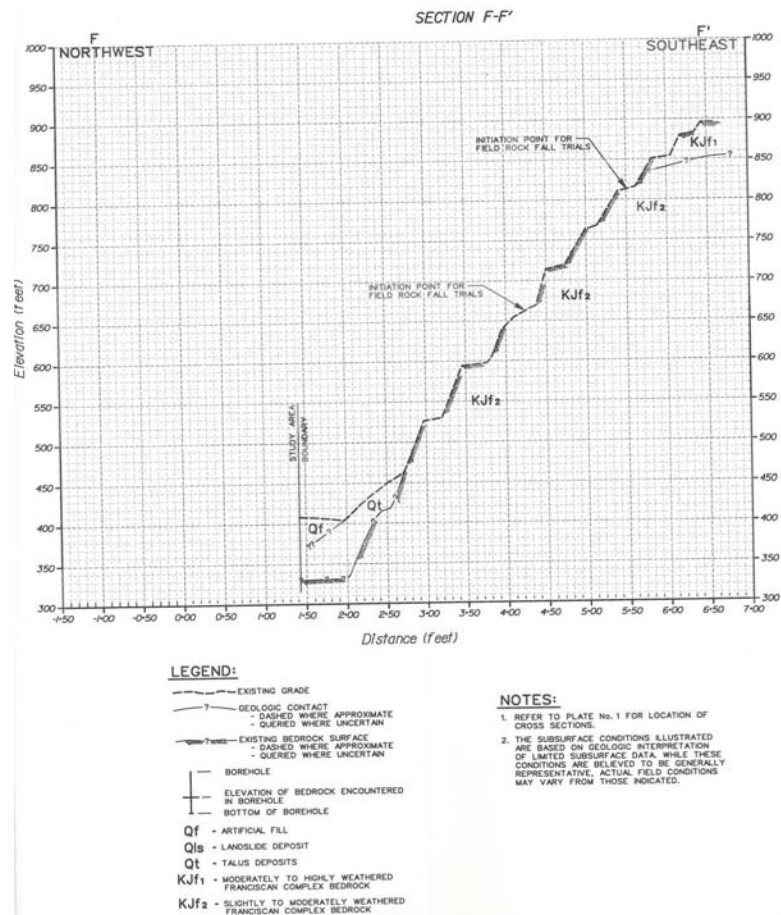


Figure 6-3. Cross section of F-F' for dropping tests

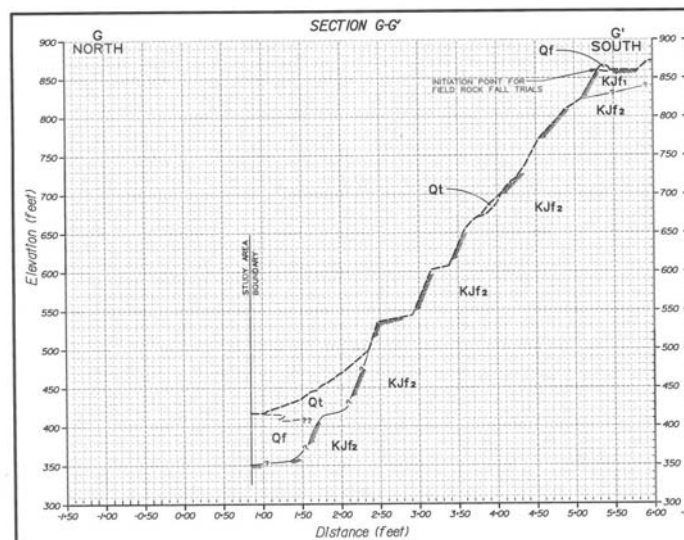


Figure 6-4. Cross section of G-G' for dropping tests

6.2.2 Model Calibration

The material properties of sandstone were analyzed based on uniaxial compressive experimental data (given in Appendix B) provided by Prof. Scott Kieffer from University of Graz. Only uniaxial compressive strength (UCS) and Young's modulus data were available. The intact rock Young's modulus was picked as the highest value of 64.7 GPa among those determined experimentally. Similarly, the highest UCS (97.0 MPa) was chosen as the intact rock UCS. m_i , one of the parameters used in Hoek-Brown failure criterion (Hoek 1983; Hoek and Brown 1997), was chosen as the average value of 17.0. Geologic strength index (GSI) for the rock blocks was determined as 85.0 to reach a UCS of about 61.1 MPa for the rock mass, which is actually the average value of tested UCSs on intact rock.

The deformation modulus, E_m , for the rock blocks was obtained by using the following correlation (Hoek and Diederichs 2006):

$$E_m = E_i \left(0.02 + \frac{1 - D / 2}{1 + e^{((60 + 15D - GSI)/11)}} \right) \quad (6-1)$$

where E_i is the deformation modulus for intact rock, and D is the disturbance factor.

The strength envelope depicted in Figure 6-5 is based on the following Hoek-Brown failure criterion (Hoek and Brown 1997):

$$\sigma_1' = \sigma_3' + \sigma_{ci} \left(m_b \frac{\sigma_3'}{\sigma_{ci}} + s \right)^a \quad (6-2)$$

where σ_1' and σ_3' are the maximum and minimum effective stresses at failure respectively, m_b is the value of the Hock-Brown constant m for the rock mass, s and a are constants which depend upon the characteristics of the rock mass, and σ_{ci} is the uniaxial compressive strength of the intact rock.

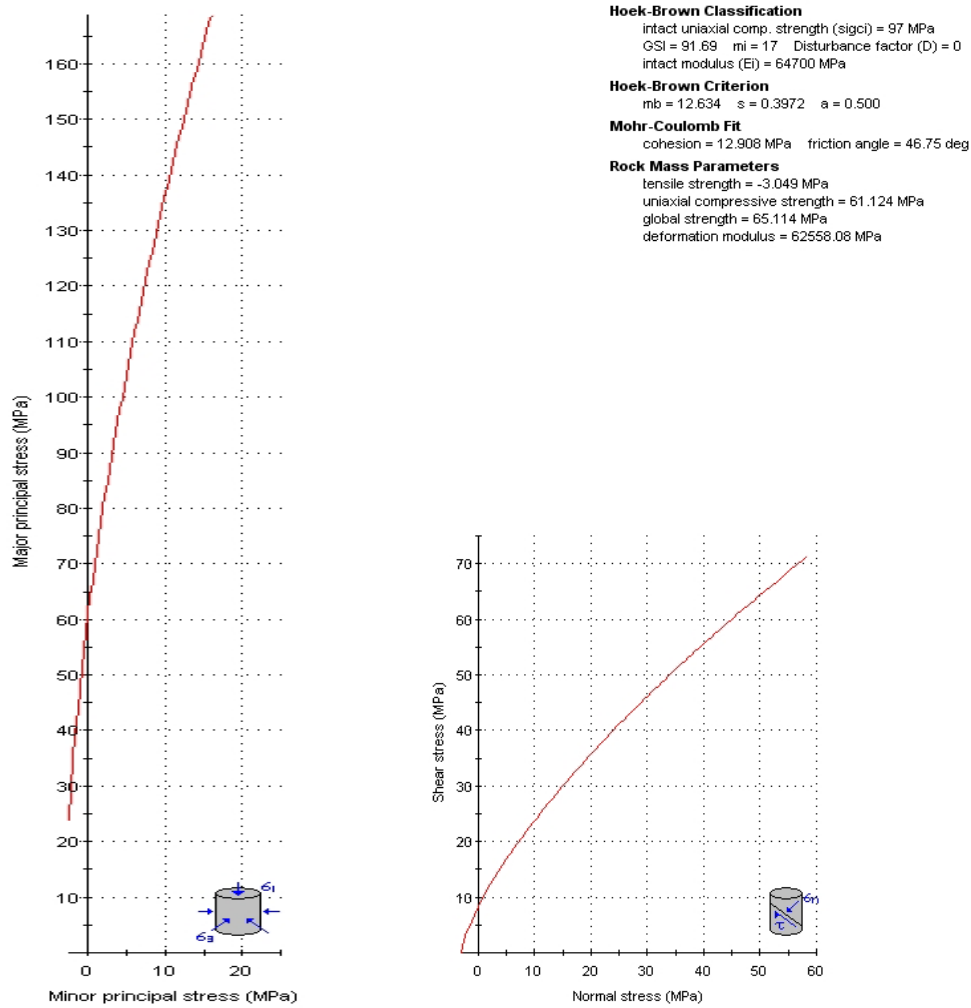


Figure 6-5. Material properties of generalized sandstone with RockData

The strength of a fractured rock mass depends on the properties of the intact rock and also on fracture structures. The Geological Strength Index (GSI) provides a system for estimating the reduction in rock mass strength for different geological conditions.

Once the Geological Strength Index has been estimated, the parameters which describe the rock mass strength characteristics are calculated as follows:

$$m_b = m_i \exp\left(\frac{GSI - 100}{28}\right) \quad (6-3)$$

For $GSI > 25$, the original Hoek-Brown criterion is applicable

$$\begin{cases} s = \exp\left(\frac{GSI - 100}{9}\right) \\ a = \frac{1}{2} \end{cases} \quad (6-4)$$

For $GSI < 25$, the original Hoek-Brown criterion applies with

$$\begin{cases} s = 0 \\ a = 0.65 - \frac{GSI}{200} \end{cases} \quad (6-5)$$

The following parameters were then chosen for calibrating the DEM model.

1) Deformability

The deformability properties of generalized rock mass were obtained as Young's modulus: $E=62.0$ GPa and Poisson's ratio: $\nu=0.18$ (picked as average value of experimental data for uniaxial compression tests as seen in Appendix B). With these deformability properties, the micro DEM deformability parameters: $E_c = 59.0$ GPa and $K_s/K_n = 0.29$ were then identified (Section 3.4.1).

2) Strength

In order to identify the micro model strength parameters, the following points in the (σ_1, σ_3) plane were picked from the strength envelope in Figure 6-6: (0.0, 61.1), (1.0, 71.5), (2.0, 81.0), (5.0, 104.5), (10.0, 136.5) in the units of MPa. By performing optimization-based calibration process (Section 3.4.2), the micro strength parameters were calibrated as: $c = 108.5$ MPa, $\varphi = 57.0^\circ$ and $T = 26.2$ MPa. The produced failure envelope is shown in Figure 6-6, which shows that the experimental and calculated failure envelopes are reasonably close to one another in the confinement range of interest to rockfall analysis (0-2 MPa).

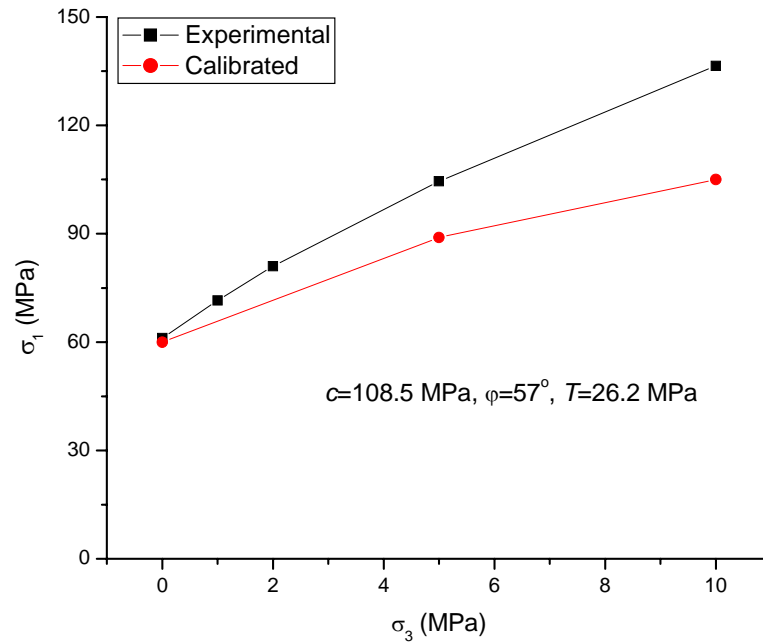


Figure 6-6. Calibrated and experimental failure envelopes of sandstone for California case study

6.2.3 Rockfall Analysis using HY-STONE

The developed fragmentation module using the interpolation method has been successfully integrated into HY-STONE to perform rockfall analysis by accounting for impact fragmentation. The program HY-STONE simulates in three dimensions the fall of a boulder along a slope. The program was designed to use thematic data already available for large areas, or that could be obtained from geological and geomorphologic maps or through reconnaissance investigations, and to generate spatially distributed information useful to assess rock-fall hazard at the regional and local scales. Rockfall analyses along cross-section FF' in California case history were performed with and without considering impact fragmentation and the effects of impact fragmentation in rockfall analysis were evaluated.

6.2.3.1 Input Data

HY-STONE requires the following input data (Guzzetti et al. 2002) and some input data are shown in Table 6-1:

- 1) a digital terrain model (DTM), representing topography in raster format, which was converted from the original digital map in AutoCAD dwg format provided by Dr. Scott Kieffer;
- 2) a raster map (a grid) showing the location of the starting cells, i.e., the cells from which rock falls occur, also specifying the number of boulders to be triggered;
- 3) grids for the normal and tangential restitution coefficients, the rolling friction coefficient, and ground Young's modulus (used for fragmentation module);
- 4) calibrated model parameters for rock blocks if fragmentation module is activated; and
- 5) other initial and controlling parameters specifying the input grid filenames, the initial conditions and the simulation specifications required by the code (threshold values, ranges of stochastic variability, etc.).

Table 6-1. Input data used for HY-STONE rockfall model in California case study

Field	Value
Normal restitution coefficient	weathered sandstone: 0.55; talus/debris: 0.35
Tangential restitution coefficient	weathered sandstone: 0.70; talus/debris: 0.70
Rolling friction coefficient	weathered sandstone 0.4; talus/debris: 0.65
Block shape	sphere
Block average radius	0.3 m
Block maximum radius	0.5 m
Start velocity	1 m/s
Start rotational velocity	0.5 radius/s

Min velocity (stop below)	0.25 m/s
E_c	59.0 GPa
c	108.5 MPa
ϕ	57.0°
T	26.2 MPa
Rock density	2.59 kg/m ³
Ground Young's modulus	0.25 GPa (talus deposit), 2.5 GPa (weathered sandstones)
Stochastic ranges (applied to Restitution coefficients, Rolling friction coefficient, Start velocity, and Ground Young's modulus)	normal distribution, standard deviation: 5% of mean value

6.2.3.2 Kinematic Modeling

HY-STONE uses a “lumped mass” approach to simulate rock falls, i.e., the boulder is considered dimensionless with all the mass concentrated in a point (the centre of mass). The size, shape and mass of the boulder are not considered and a kinematics simulation of the rock-fall process is performed where the movement is computed through a series of discrete time intervals. The advantage of the lumped mass approach lays in its simplicity and in the computational speed. Taking into account the mass of the boulder, its shape and size would allow for a complete dynamic modeling, but would introduce uncertainties (particularly due to the irregular shape of the boulder), would increase the computation time, and would generate a large variability in the results making it more difficult to ascertain rock-fall hazard at the regional scale.

The trajectory (or travel path) of a boulder is computed automatically from the DTM in HY-STONE. The trajectory depends on the starting point, the topography, and the coefficients used to simulate the loss of velocity at the impact point or where the boulder is rolling (Guzzetti et al. 2002).

HY-STONE is capable of modeling three of the four “states” that a rock fall can take, namely: free falling, bouncing and rolling. Starting from a source point, HY-STONE “shoots” a boulder horizontally out of the point along the steepest slope and at an initial velocity set by the user. After the horizontal start, the boulder, driven by gravity, follows a parabolic (ballistic) trajectory (free falling) until it hits the ground.

When the location of the impact point has been determined, HY-STONE invoke the fragmentation module to check whether this impact can cause fragmentation or not. If fragmentation does not occur, rebound velocity and angle are computed by accounting for the energy loss using coefficients of restitutions. If fragmentation occurs, the fragmentation module outputs the rebound velocity of each fragment and different new rockfall trajectories are then computed and followed in the rockfall analysis.

6.2.3.3 Natural Variability and Uncertainty in the Input Data

Parameters such as the rockfall starting velocity and direction, the rolling friction coefficient and the normal and tangential energy restitution coefficients vary largely in nature and are difficult to define precisely, particularly over large areas. HY-STONE provides a way to cope with the natural variability and local uncertainty associated with such information by adding to these values a random component. The user can select a range of variation (in percentage) around the given (default or central) values. During the computation, where needed (i.e., at the beginning of a new trajectory for the starting angle, at each impact point for the normal and tangential energy restitution coefficients, and where the boulders roll for the dynamic friction coefficient), STONE draws randomly a value from the selected range around the given (default) values.

Adding the random components to the simulation proves very useful to test the program outputs for errors or inconsistencies due to local conditions. When combined

with the possibility of triggering a large number of boulders from each starting cell, the use of the random components provides a way of coping with the natural variability and the intrinsic uncertainty associated with rock falls. The statistic analyses of computed rockfall trajectories by considering the natural variability and the intrinsic uncertainty can be used for assessing rockfall invasion areas in terms of frequency and intensity.

6.2.3.4 Results

Rockfall modeling along cross-section FF' was performed with and without activating fragmentation module using HY-STONE. Simulated rockfall trajectories using probabilistic modeling by accounting for the natural variability of parameters were used to assess rockfall invasion areas. In the probabilistic modeling of rockfall analysis, the areas with higher density of rockfall trajectories are considered as higher frequency or intensity of rockfall invasions.

Figures 6-7 to 6-16 shows different views of simulated 3D rockfall trajectories with and without activating fragmentation along cross-section FF' using HY-STONE. Trajectories are represented as points, classified by translational velocity. By comparing the rockfall trajectories with and without activation fragmentation module, following observations can be made:

- 1) Impact fragmentation occurs when activating the fragmentation module for calibrated input parameters of rock blocks used in the case study, which is confirmed by the recorded experimental results.
- 2) Simulated rockfall invasion areas with activating the fragmentation module are much larger than those computed without activating fragmentation module.

- 3) The average values of velocity and height (relative height from the slope in the vertical direction) of small fragments are higher than those for rock blocks without activating the fragmentation module.

It is then natural to draw the conclusion that impact fragmentation is very important in rockfall analysis in assessing rockfall invasion areas in terms both of frequency and intensity. Without considering impact fragmentation, the assessment of the areas prone to rockfall would be underestimated and hence may mislead the design of protection measurement or other rockfall risk analyses.

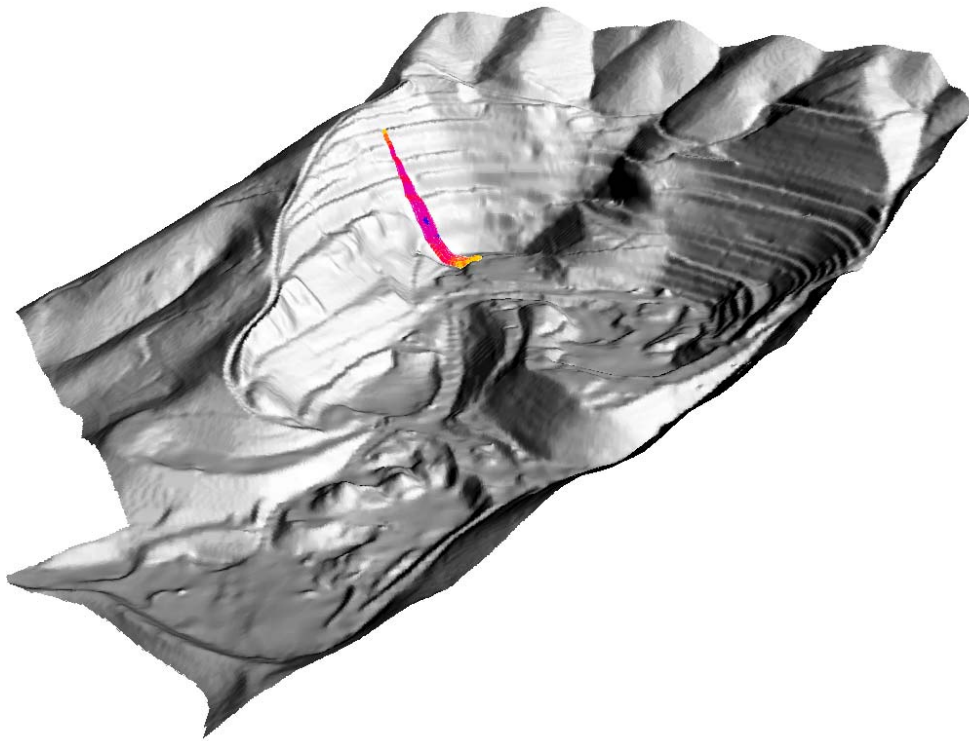


Figure 6-7. Full view (NE) of simulated 3D rockfall trajectories with fragmentation along cross-section FF' using HY-STONE

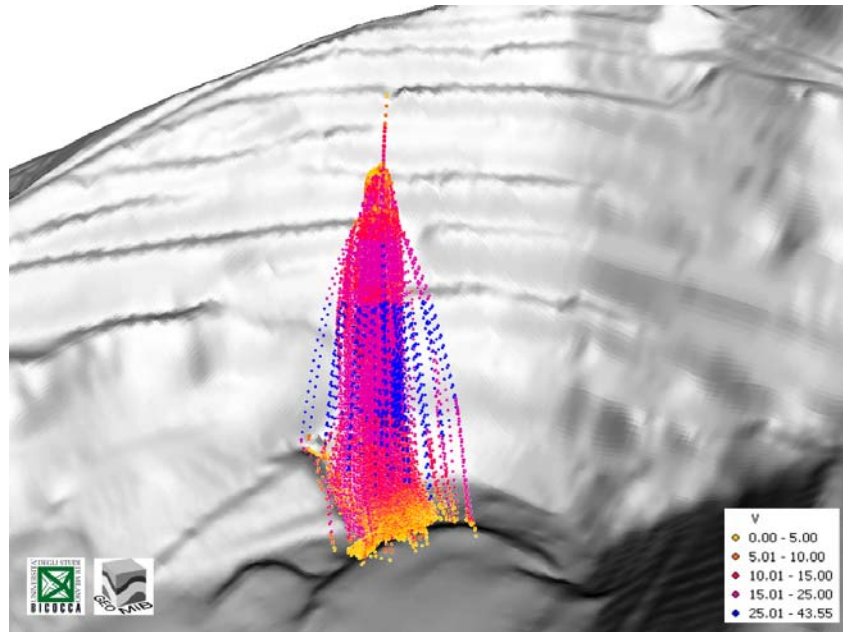


Figure 6-8. Front view of simulated 3D rockfall trajectories with fragmentation along cross-section FF' using HY-STONE. Trajectories are represented as points, classified by translational velocity.

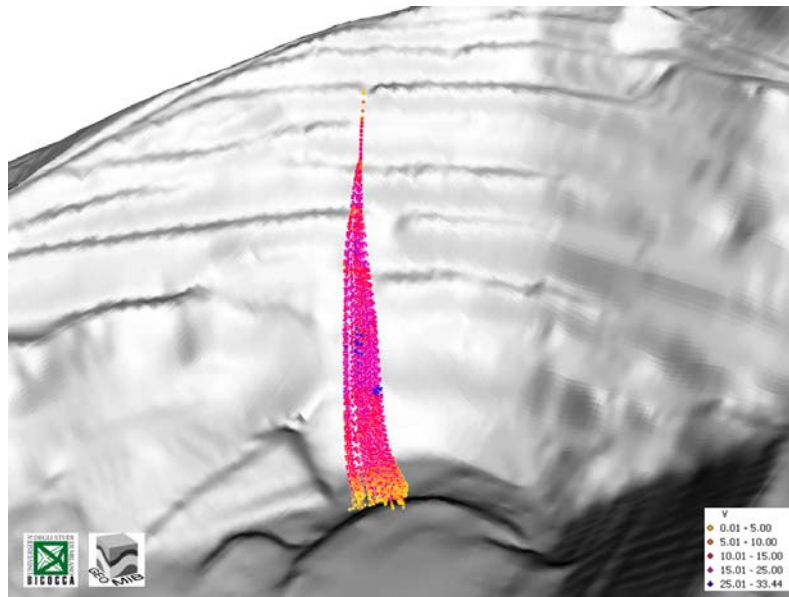


Figure 6-9. Front view of simulated 3D rockfall trajectories without fragmentation along cross-section FF' using HY-STONE. Trajectories are represented as points, classified by translational velocity.

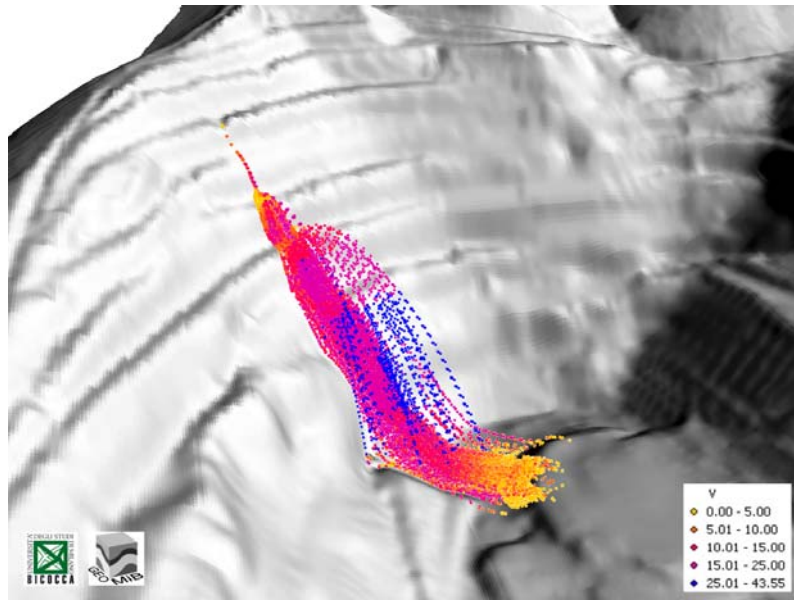


Figure 6-10. NE-view of simulated 3D rockfall trajectories with fragmentation along cross-section FF' using HY-STONE. Trajectories are represented as points, classified by translational velocity.

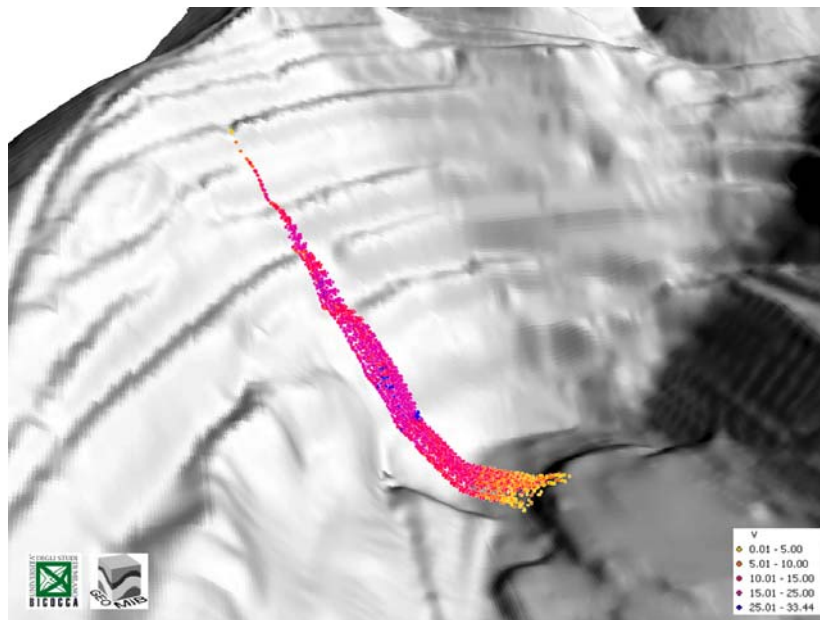


Figure 6-11. NE-view of simulated 3D rockfall trajectories without fragmentation along cross-section FF' using HY-STONE. Trajectories are represented as points, classified by translational velocity.

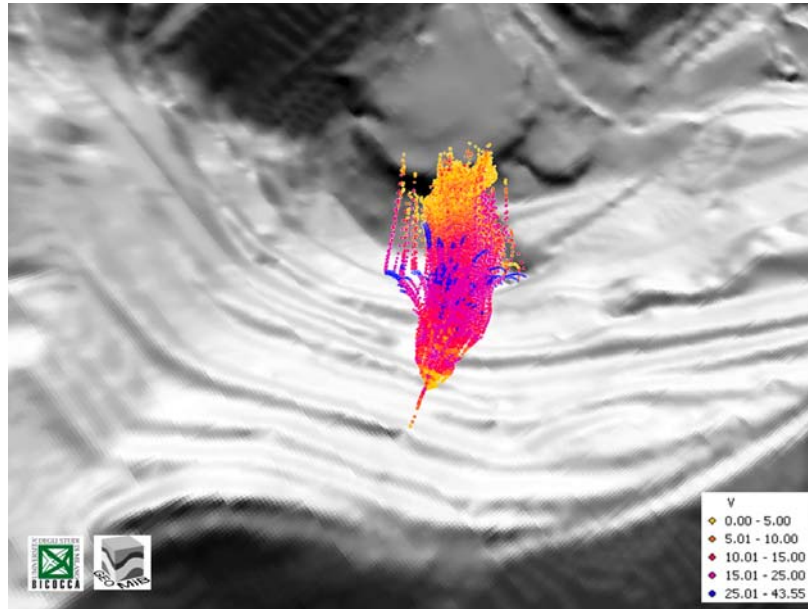


Figure 6-12. Top view of simulated 3D rockfall trajectories with fragmentation along cross-section FF' using HY-STONE. Trajectories are represented as points, classified by translational velocity.

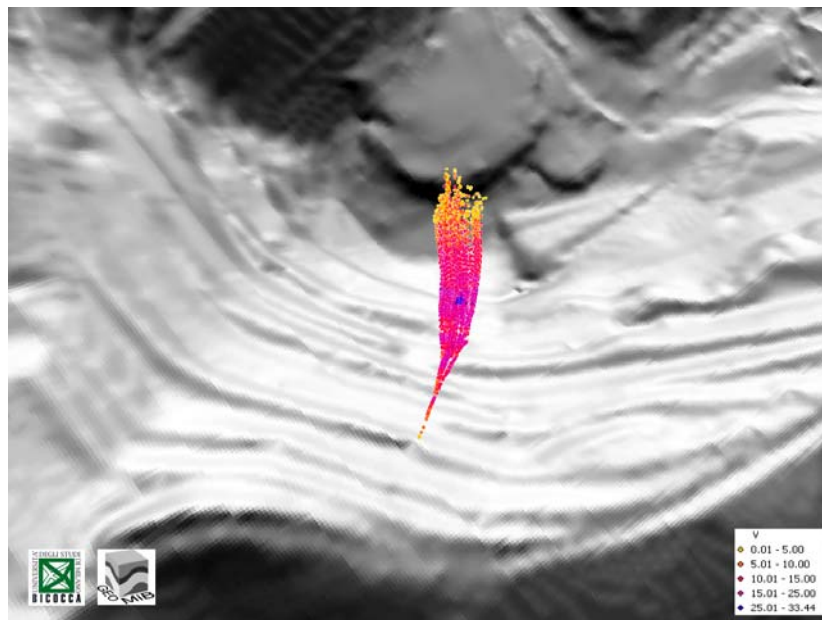


Figure 6-13. Top view of simulated 3D rockfall trajectories without fragmentation along cross-section FF' using HY-STONE. Trajectories are represented as points, classified by translational velocity.

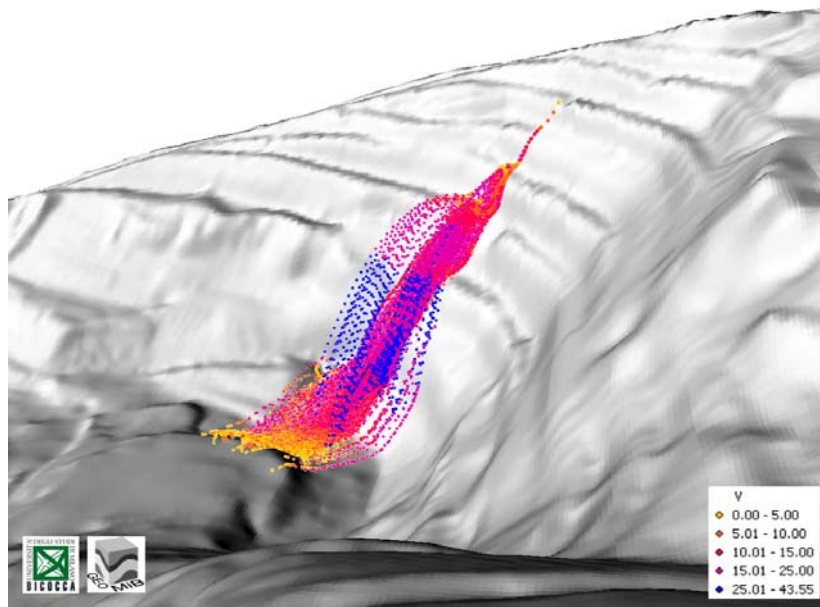


Figure 6-14. N-view of simulated 3D rockfall trajectories with fragmentation along cross-section FF' using HY-STONE. Trajectories are represented as points, classified by translational velocity.

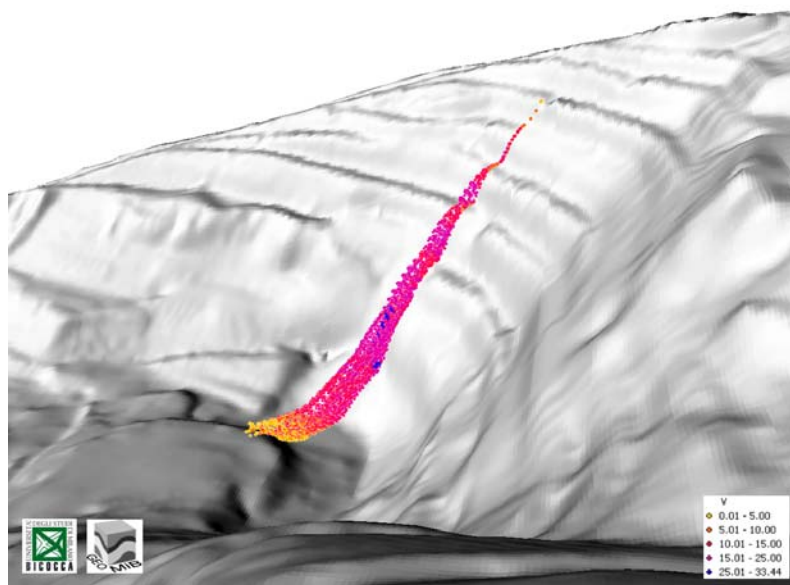


Figure 6-15. N-view of simulated 3D rockfall trajectories without fragmentation along cross-section FF' using HY-STONE. Trajectories are represented as points, classified by translational velocity.

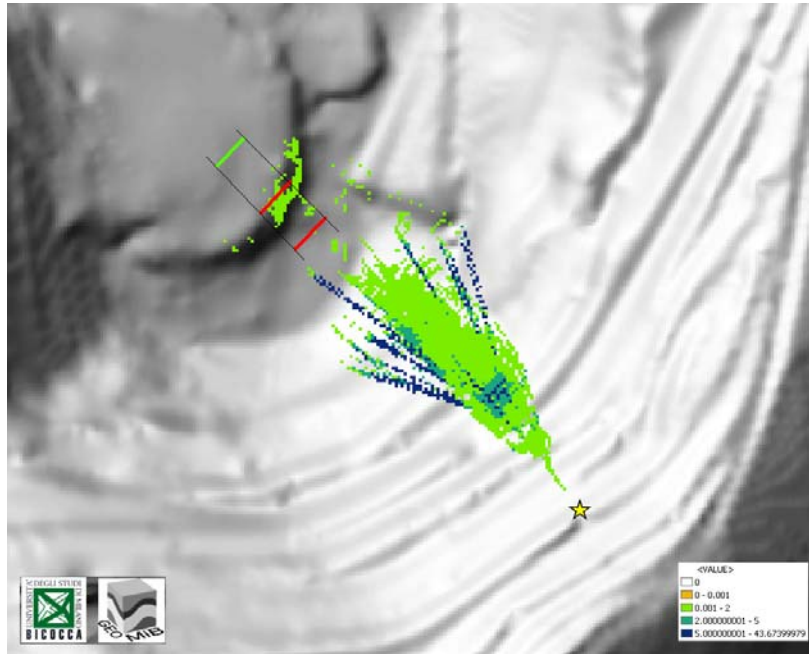


Figure 6-16. Average height of flying fragments of each cell with fragmentation along cross-section FF' using HY-STONE

6.3 ROSSING DROP TESTS

6.3.1 Overview

The experimental work at Rossing Uranium Mine in Australia comprised free falling tests onto a nearly horizontal surface of rock and scree-covered rock, respectively. The initial purpose of this drop tests was to measure the normal coefficient of restitution. Because fragmentation was observed in the drop tests, it was then proposed to validate our DEM impact model based on these results.

Selected equidimensional rock blocks, ranging in size from 200 to 300 mm, were vertically dropped from a height of 9.6 m onto the prepared test surfaces. Approximately 60 rock blocks, including marble, quartzite and skarn, were released during the testing and dropped onto a cordierite gneiss hard rock surface as well as a scree covered surface as shown in Figure 6-17. The falling rock blocks were recorded by a high speed video

camera. From the provided video files, about 6 drops resulted in rock block fragmentation, and they were all tested on the hard rock surface. However, it is now impossible to identify the rock type from those video files, which makes it difficult to use the test results to directly validate our DEM code. But it can at least provide us with useful *in situ* data to compare with the simulation results.

6.3.2 Model Calibration

The provided test data on rock properties were very limited and displayed large variation (Appendix C). Due to the insufficiency of provided experimental data, only marble was selected for the validation, which has relatively more data. Because of the large scatter of the provided data, higher and lower parameter bounds were selected and used for validating the dropping tests as follows:

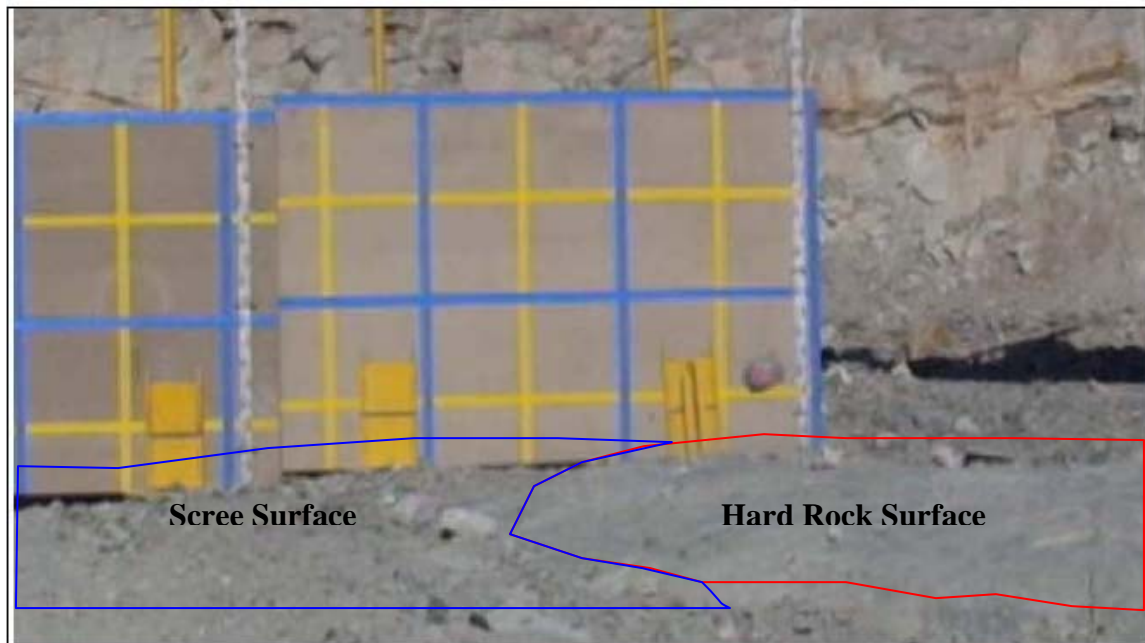


Figure 6-17. Testing arrangement for Rossing dropping tests

1) High bound

The high-bound deformability properties for the rock blocks were estimated as: Young's modulus: $E=66.0$ GPa and Poisson's ratio: $\nu=0.25$. With these deformability properties, the micro DEM deformability parameters: $E_c = 74.8$ GPa and $K_s/K_n = 0.115$ were then identified (Section 3.4.1).

Points in the (σ_1, σ_3) plane were picked from the high-bound strength envelope for the rock blocks: (0.0, 115.0), (10.0, 144.1), (20.0, 167.4), (30.0, 197.3) in the units of MPa. By performing optimization-based calibration process (Section 3.4.2), the micro strength parameters were calibrated as: $c = 80.0$ MPa, $\varphi = 60^\circ$, $T = 110.0$ MPa. The experimental and simulated failure envelopes are shown in Figure 6-18, in which the simulated failure envelope is fairly close to the target one.

2) Low bound

The low-bound deformability properties for the rock blocks were estimated as Young's modulus: $E=41.0$ GPa and Poisson's ratio: $\nu=0.25$. With these deformability properties, the micro DEM deformability parameters: $E_c = 45.3$ GPa and $K_s/K_n = 0.115$ were then identified.

Points in the (σ_1, σ_3) plane were picked from the low-bound strength envelope for the rock blocks: (0.0, 44.0) (10.0, 58.0), (20.0, 71.0) in the units of MPa. By performing optimization-based calibration process, the micro strength parameters were calibrated as: $c = 65.0$ MPa, $\varphi = 60^\circ$, $T = 12.0$ MPa. The experimental and simulated failure envelopes are shown in Figure 6-19, in which the simulated failure envelope is not very close to the target one at high confining pressures, but matches the target envelope at low confining pressures. Considering the interest of modeling rock fragmentation upon impact in the research, confining pressure is not of a big concern. As a result, these calibrated model parameters are acceptable for the case study.

6.3. 3 Impact Simulations

For simplicity, a spherical block of 0.2 m in diameter was used for simulations. The block was represented by a sphere packing consisting of 2,500 particles. The impact was simulated as a normal impact (incident angle of 90°) with the magnitude of impact velocity of 13.7 m/s, which is directly determined from the dropping height of 9.6 m as $v = \sqrt{2gh} = \sqrt{2 \times 9.8 \times 9.6} \text{ m/s} = 13.7 \text{ m/s}$. Drops onto both cordierite gneiss hard rock and the scree covered surfaces were modeled. Ground Young's modulus of 21.0 GPa for a hard rock) surface (considering a Young's modulus of 50.0 GPa for intact cordierite gneiss rock and a GSI of 55 for estimation) and 0.5 GPa (estimated based on a medium dense gravel (Lequang and Junichi 2003)) for a scree-covered surface, respectively, were chosen in the following impact simulations.

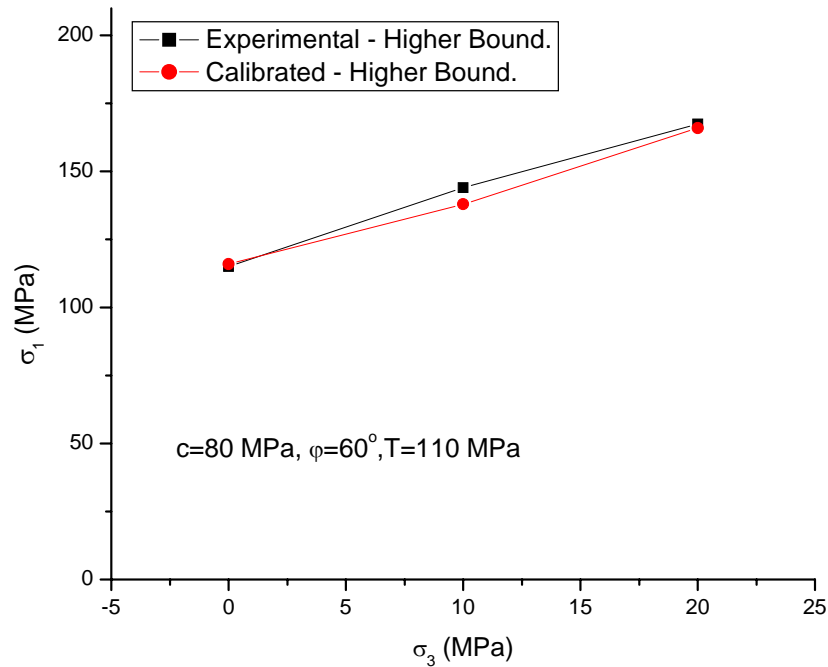


Figure 6-18. Experimental and calibrated failure envelopes for the high-bound properties

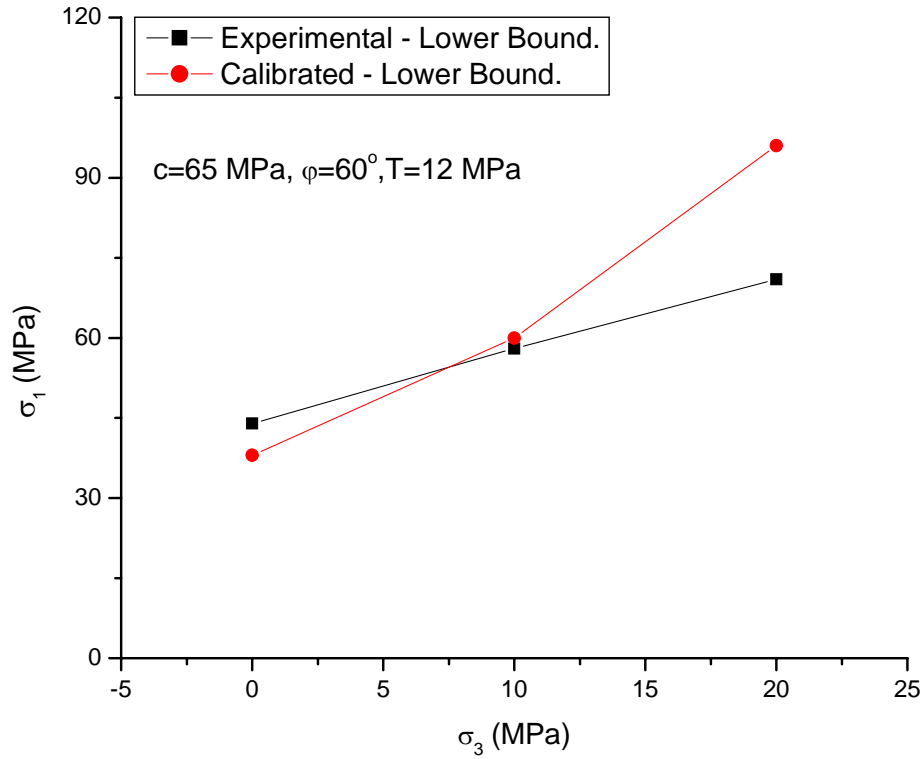


Figure 6-19. Experimental and calibrated failure envelope for the lower-bound properties

1) **High bound**

First, the calibrated model for high-bound properties of marble was used to simulate the impact against both the hard rock surface and scree-covered surface. As exemplified in Figure 6-20, the simulated results show that no fragmentation occurs for the impacts against the scree-covered surface, while for impacts against rock, a few small fragments developed at the impact zone as seen in Figure 6-21. For high bound marble, dropping vertically from a height of 9.6 m may not create severe fragmentation when landing either onto the hard rock surface or onto the scree-covered surface.

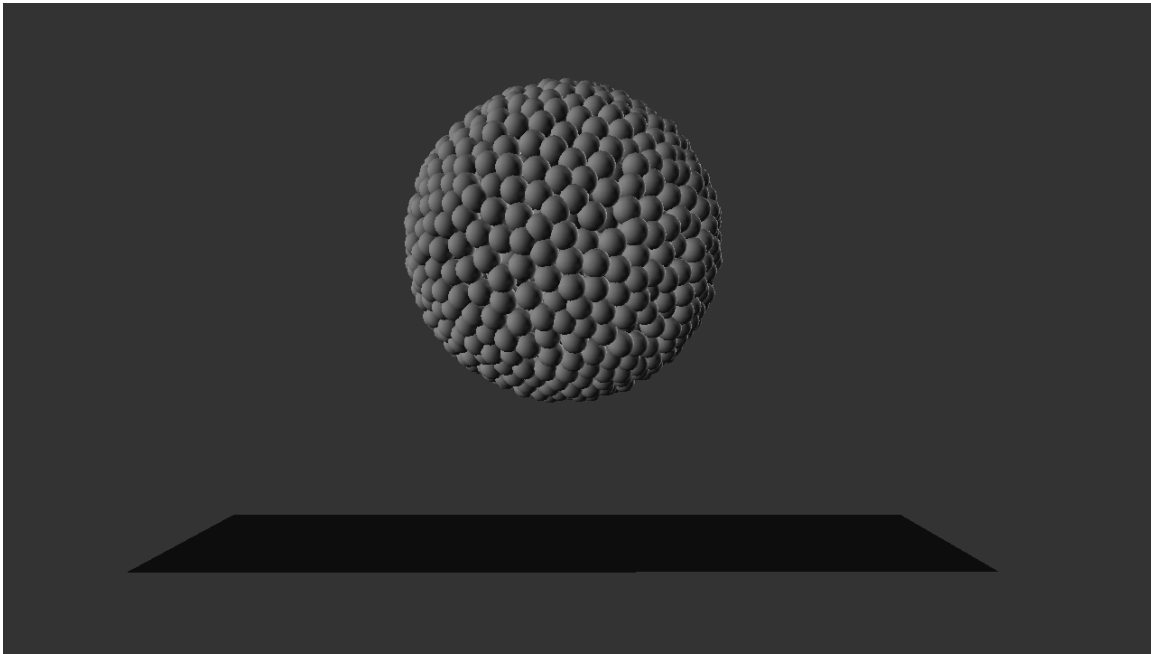


Figure 6-20. Simulated high-bound marble block after bouncing off the ground for dropping onto the scree-covered surface

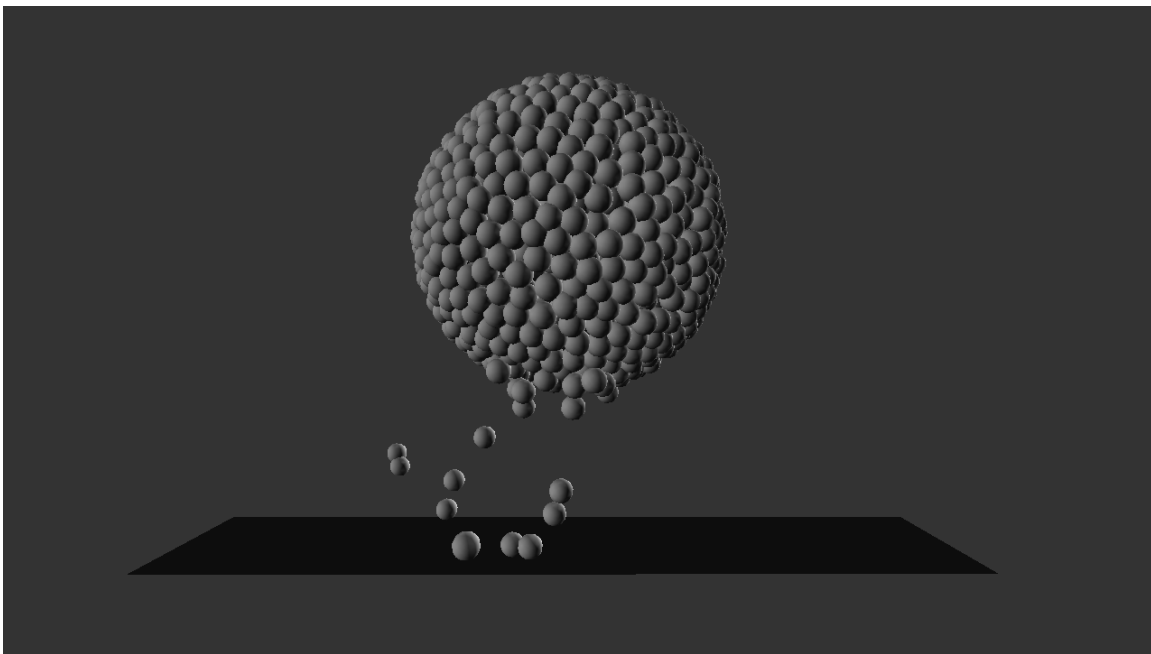


Figure 6-21. Simulated high-bound marble block after bouncing off the ground for dropping onto the hard rock surface

2) Low bound

The calibrated model for low-bound properties of marble was then used to simulate the impact upon both the hard rock surface and the scree-covered surface. The simulated results show that fragmentation occurs under both ground conditions for low-bound marble block. When the low-bound marble rock impacts against the scree covered surface, about 120 fragments were generated, in which two relatively big fragments account for up to 90% of the total volume and the remaining are just tiny fragments consisting of one to 3 spherical DEM particles. The two big fragments move at a similar speed, so it is not easy to visually differentiate the two fragments from Figure 6-22. When the low-bound marble rock impacts onto the hard rock surface, it suddenly smashes generating about 1,380 fragments with the biggest fragments only consisting of 290 DEM spherical particles as seen in Figure 6-23. This large number of fragments is caused by the low strength of rock block itself and the high stiffness of the ground. This process is similar to the situation where a dry soil block impacts onto a hard rock surface.

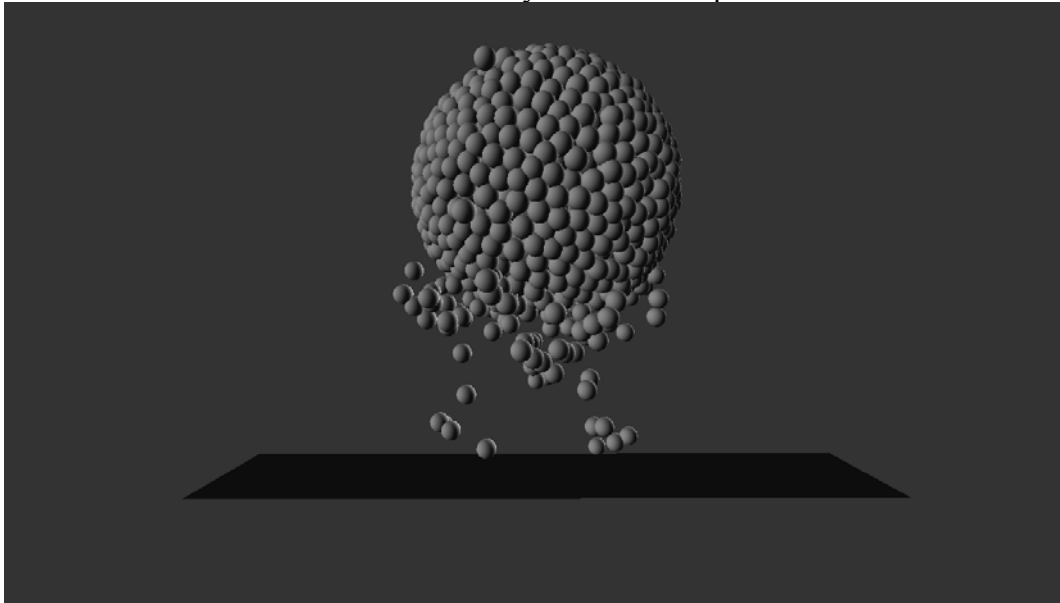


Figure 6-22. Simulated low-bound marble block after bouncing off the ground for dropping onto the scree-covered surface

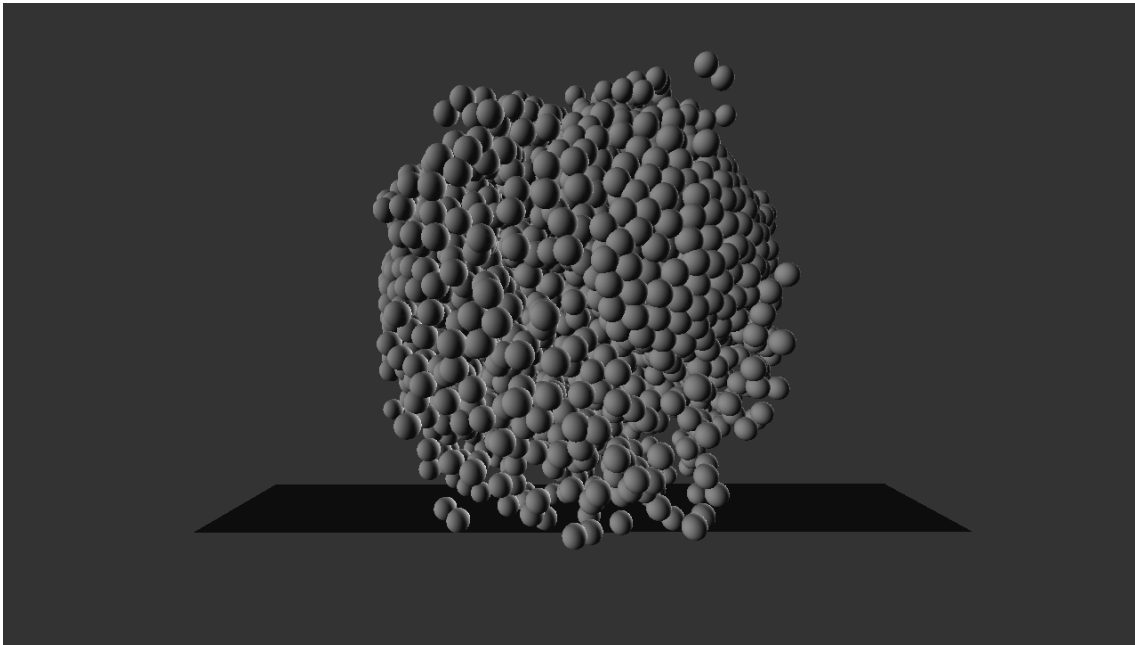


Figure 6-23. Simulated low-bound marble block after bouncing off the ground for dropping onto the hard rock surface

6.3. 4 Conclusion

Based on the simulation results using estimated possible high and low bound properties of marble, it is reasonable to draw the conclusion that the DEM impact model can be used to predict the impact fragmentation. Considering the large uncertainty of rock properties, it is impossible to fully simulate the fragmentation process in real tests. Especially, when real fragments are smaller than the sizes of DEM particles, the simulated fragments cannot be compared to the real situations any more. However, the DEM impact model can provide good reference results in evaluating impact fragmentation in rock fall analysis. It is also very useful to carry out statistical analysis in impact fragmentation using the DEM impact model by introducing uncertainties in model parameters. By accounting for the possible variations in rock properties, valuable results

with respect to impact fragmentation in rock fall analysis may be obtained to guide the design of protective measures against rock fall events with impact fragmentation.

6.4 ARGYLE ROCKFALL EVENT

6.4.1 Introduction

According to a report from Rio Tinto, a rockfall incident with impact fragmentation happened at Borefield in Argyle, Australia on Dec. 2nd 2001 with no injuries to personnel, in which a Motor Control Centre (MCC) was severely damaged due to flying fragments as shown in Figure 6-24. Though a tire fence (about 2.5 m high) was used to prevent rock fall damage, the impact created rock fragments that jumped over the bench and hit the MCC. The damaged MCC had to be replaced at cost of \$77,000.



Figure 6-24. Rock fall damage to Motor Control Center with impact fragmentation at an Argyle mine

As shown in Figures 6-25 and 6-26, the slope of a typical Argyle quartzite waste rock dump is about 37 degrees and the point of origin of the rockfall was estimated at approximately 280 m relative level (RL) near the crest of the waste dump. The point of impact at the waste dump toe is at approximately 235 m RL. The dump toe was relatively soft, which is not enough to fragment the falling rock block. It was then speculated that the falling rock block possibly impacted with another boulder and got fragmented. Those fragments flew over a tire fence to hit the facility which is at 235m elevation. The size of the original block is unknown but can be estimated as about 300×300×400 mm based on the broken fragments in the photographs.

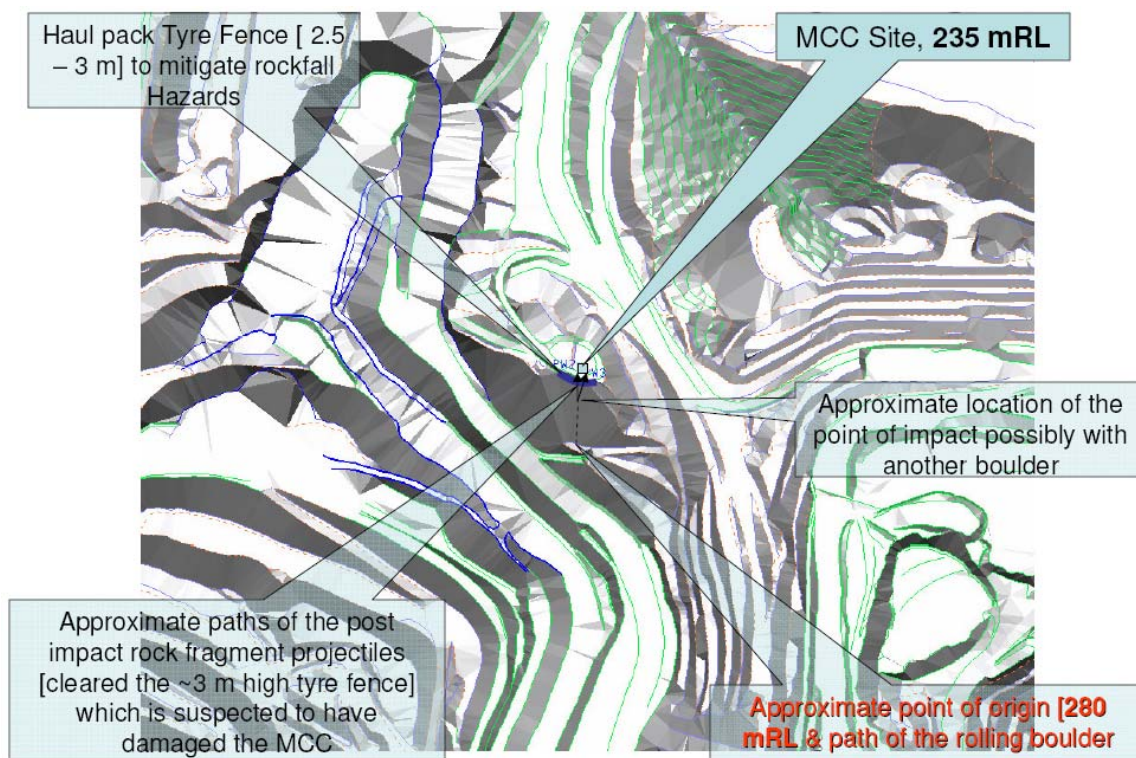


Figure 6-25. Location of rockfall incident with possible impact point

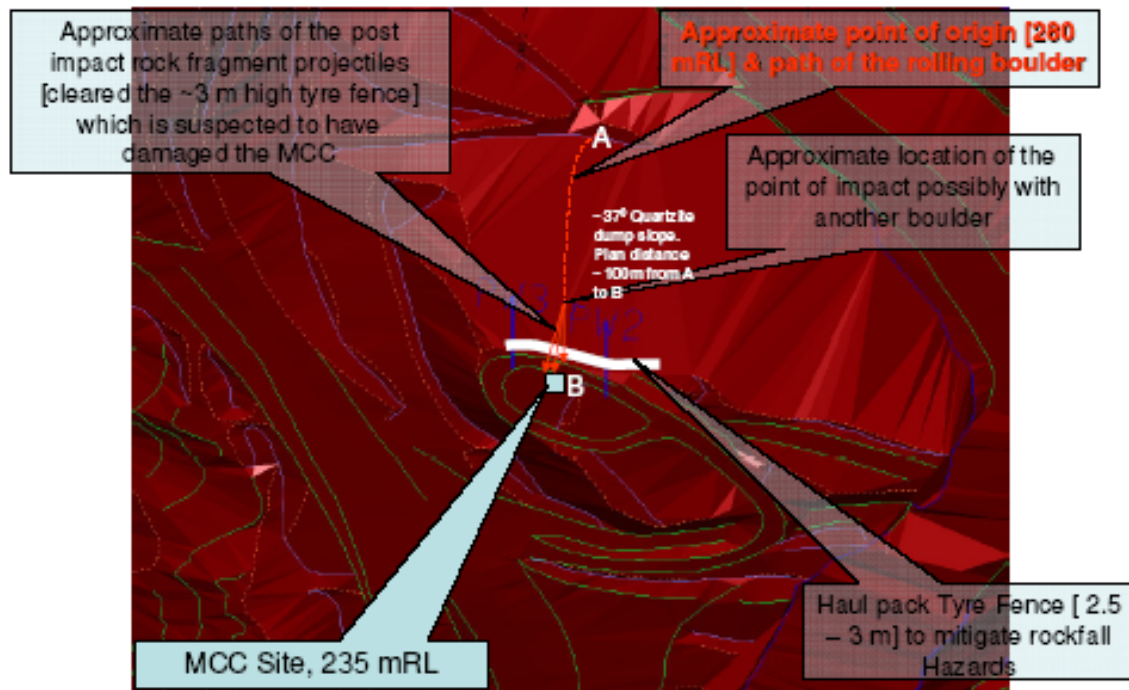


Figure 6-26. An oblique view of the local site of the rockfall incident

6.4.2 Model Calibration for Intact Rock

As part of this research, a quartzite block sourced and shipped from Argyle in Australia was cored and specimens were tested by using triaxial tests. Some fractures oriented mainly in two sets of directions were observed while coring the sample. The tested specimens were almost intact with no visible fractures as seen from a CT scanned cross section of a representative specimen in Figure 6-27. Hence the tested results can be viewed as properties for intact quartzite. In this case study, firstly, intact rock properties were used for impact simulation to check whether it can get fragmented or not. Then, a calibrated equivalent continuum model was employed to simulate the impact fragmentation of rock mass.

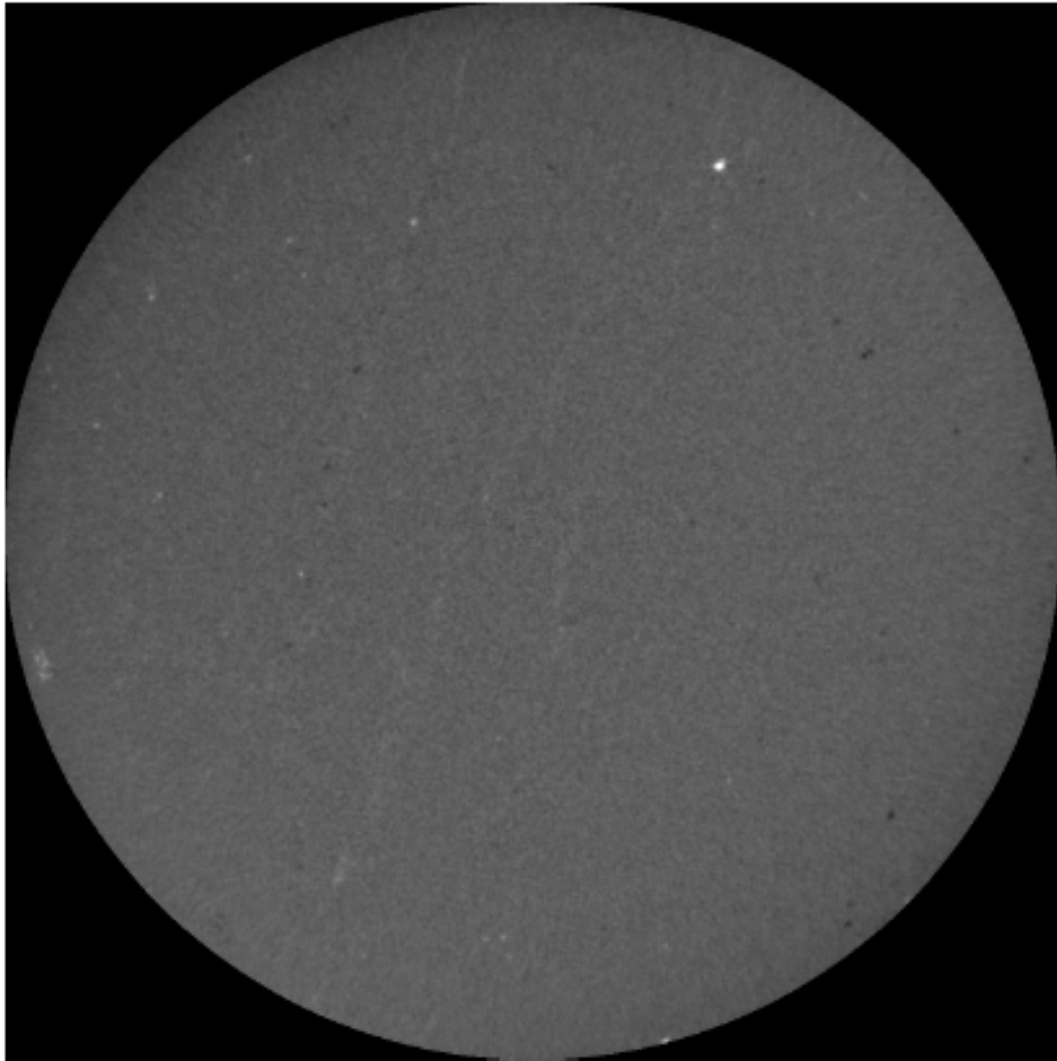


Figure 6-27. A CT scanned cross section of the tested quartzite sample

For the tested intact quartzite specimens, the average Young's modulus and Poisson's ratio are 122.0 GPa and 0.25, respectively. The tested failure envelope is shown in Figure 6-28.

With these tested material properties, the micro model parameters were then identified with the developed calibration algorithms (Section 3.4). The identified model parameters are shown in Table 6-2.

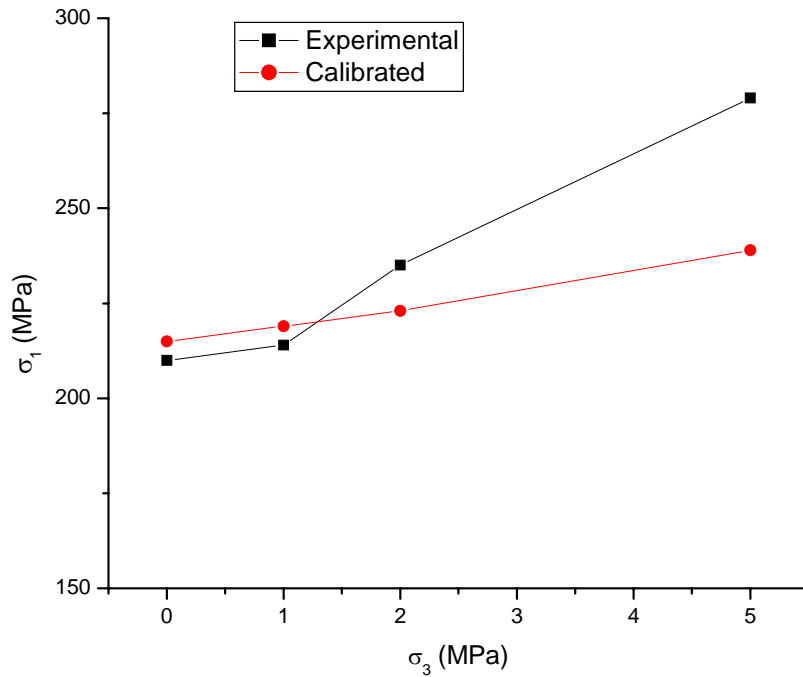


Figure 6-28. Experimental and calibrated of failure envelopes of the tested intact quartzite sample

Table 6-2 Micro model parameters for intact quartzite

E_c (GPa)	K_s / K_n	c (MPa)	φ (°)	T (MPa)
138.3	0.12	350.0	60.0	120.0

6.4.3 Model Calibration for Equivalent Continuum Model

The material properties of equivalent continuum quartzite were obtained by using the same approach as used in Section 6.2. The Young's modulus and the UCS for the tested intact rock are 122 GPa and 210 MPa, respectively. The Hoek-Brown parameter, m_i , was chosen as 20 for quartzite. GSI was estimated 85 based on the observation of fractures in the cored block. Eventually, the deformability and strength parameters were obtained for the generalized rock mass properties as shown in Figure 6-29.

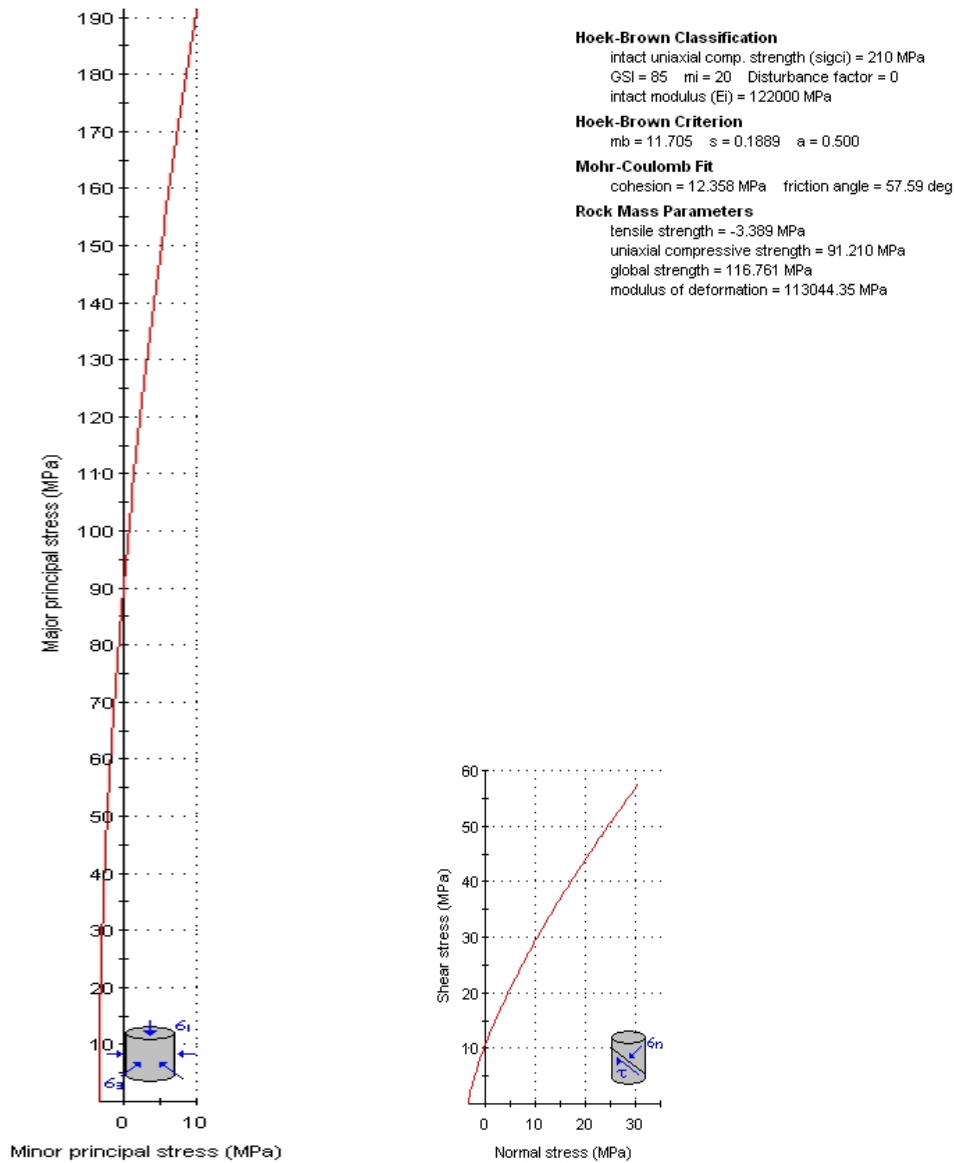


Figure 6-29. Material properties of quartzite rock mass obtained based on intact rock properties and characterization of fractured rock

Deformability and strength properties were then chosen for calibrating the DEM model to simulate equivalent quartzite rock mass. Young's modulus and Poisson's ratio are 113.0 GPa and 0.24, respectively, for the equivalent continuum material. Points in the

(σ_1, σ_3) plane were picked from the generalized failure envelope to identify the micro strength model parameters. The selected points were (0.0, 91.2), (1.0, 104.0), (2.0, 117.0) and (5.0, 148) in the units of MPa. Identified micro model parameters are shown in Table 6-3.

Table 6-3. Micro model parameters for intact quartzite

E_c (GPa)	K_s / K_n	c (MPa)	φ ($^\circ$)	T (MPa)
125	0.13	125	60	65

The computed failure envelope is shown in Figure 6-30, which is not very close to the target one at high confining pressures, but is fairly close to the target envelope at low confining pressures.

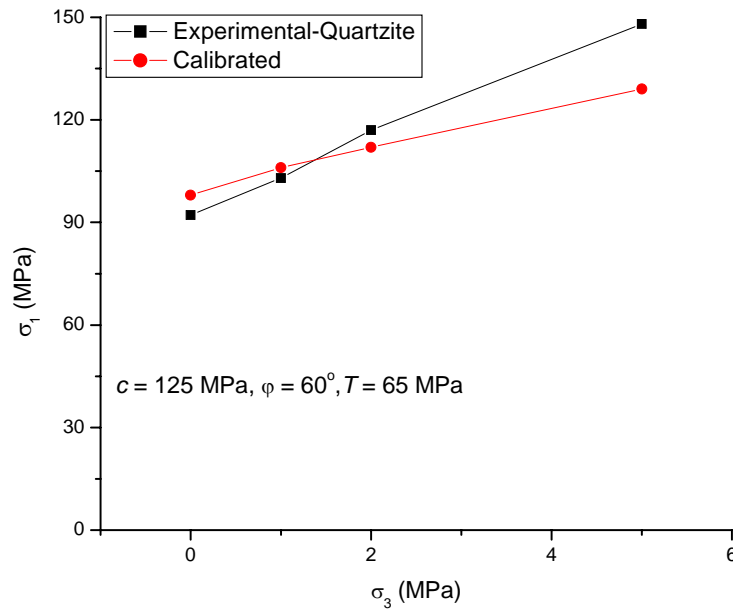


Figure 6-30. Comparison between the calibrated and generalized failure envelopes for fractured quartzite

6.4.4 Impact Simulation

As shown in Figure 6-31, a block rolling along the slope and then impacting against a horizontally placed big boulder was considered. For simplicity, a spherical block consisting of 2,500 spherical particles was used for impact simulations. The radius of the block is 0.2 m. The impact was configured as an oblique impact with an incident angle of 37° , which is the slope angle provided by Rio Tinto. The impact velocity was calculated as $v = \alpha\sqrt{2gh} = 0.8 \times \sqrt{2 \times 9.8 \times 35.0} \text{ m/s} = 21.0 \text{ m/s}$, in which a coefficient $\alpha = 0.8$ was used to account for the energy loss during rolling. The ground Young's modulus was chosen as 20.0 GPa to represent the big boulder against which the falling rock landed. The coordinate system was set up as shown in Figure 6-31.

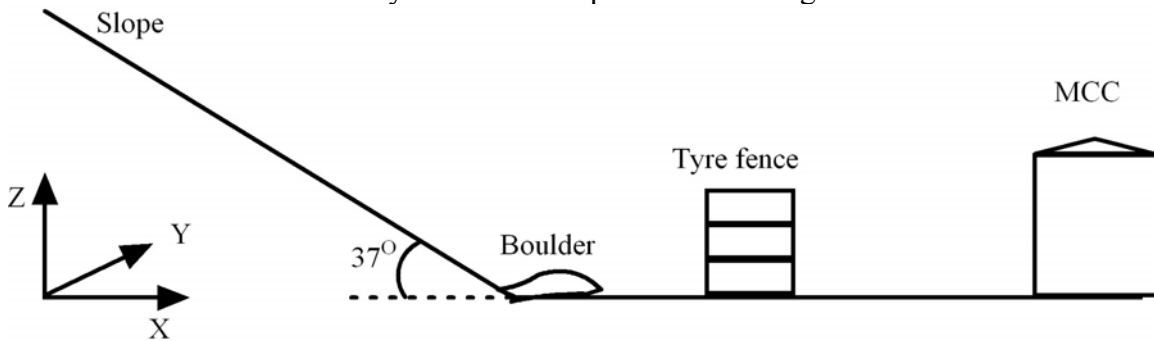


Figure 6-31. Sketch of impact simulation with coordinate reference system

Firstly, calibrated intact model was used to simulate the impact to check whether an intact rock block can fragment in the impact. As shown in Figure 6-32, no fragmentation was observed in the simulation with the intact model. The average reflected velocity of the block is about 19.5 m/s, which is slightly lower than the incident velocity because part of the translational energy is transformed into rotational energy and part of kinetic energy is dissipated by geometric damping. Unlike an ideal oblique impact, the horizontal component of reflected velocity was smaller than the horizontal component of incident velocity because tangential resistance was applied to the block, which causes the slight block rotation.

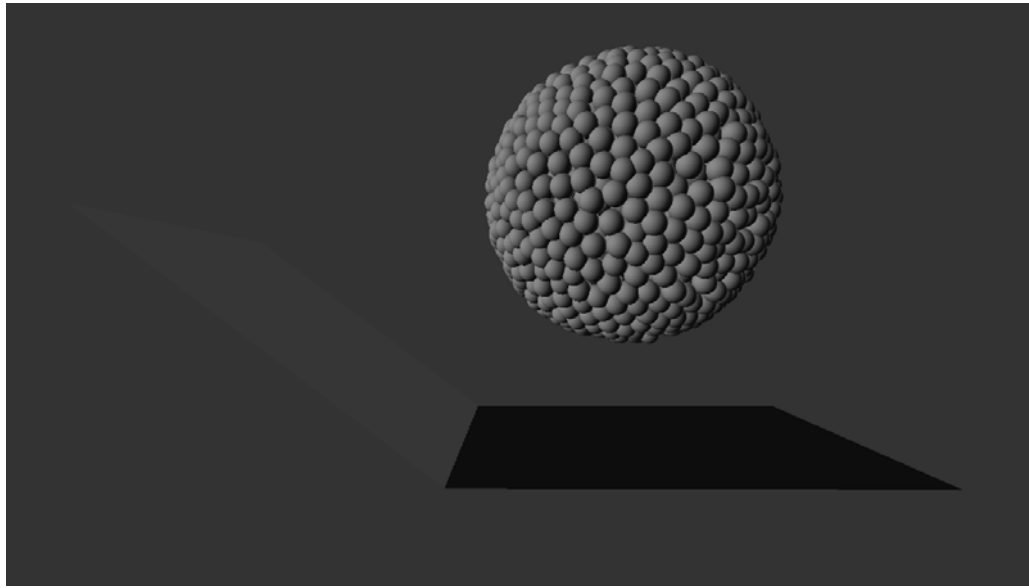


Figure 6-32. Simulated intact block rolling down a slope and impacting against a horizontal placed big boulder

The calibrated equivalent continuum model to represent fractured rock was then applied to simulate the impact. As shown in Figure 6-33, about 200 fragments were generated. The biggest fragment accounts for about 85% of the total volume and the rest are just some small and tiny particles. The reflected velocity of the 5 biggest fragments is shown in Table 6-4. By performing a simple analysis on fragment trajectories, three of them can likely fly over the tire fence and hit the MCC. Compared with the actual fragments observed on site (Figure 6-24), simulated fragment sizes do not agree well with the actual fragment sizes. It is always difficult to fully model rock fragmentations because rock blocks are discontinuous and internal structures are complex. In modeling impact fragmentations, an equivalent continuum model was employed to simplify the problem, which may lead the deference from the actual observations on fragment sizes. However, by using this developed model it is able to perform some risk analysis on impact fragmentation.

Table 6-4. Velocity of the largest five fragments after impact

Fragment No.		1 st	2 nd	3 rd	4 th	5 th
Velocity (m/s)	X	12.3	0.5	5.7	12.9	14.0
	Y	0.2	5.6	3.7	-0.03	1.1
	Z	8.6	3.2	8.3	10.3	1.0
Fly over the tire fence?		Yes	No	Yes	Yes	No

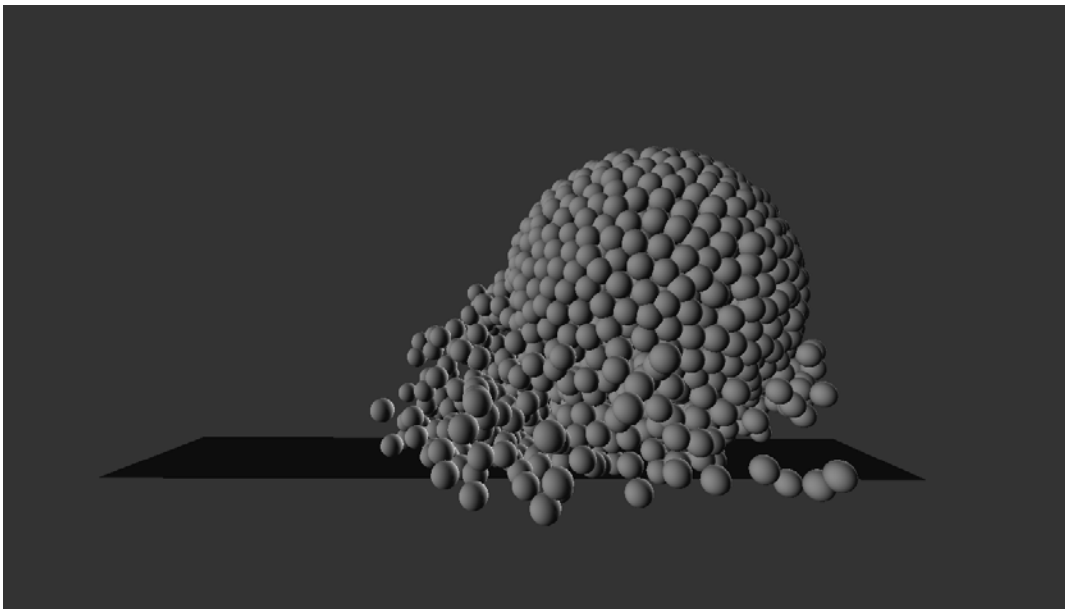


Figure 6-33. Simulated equivalent fractured block rolling down a slope and impacting against a horizontal placed big boulder

6.5 IMPROVEMENT ON FRAGMENT SIZE DISTRIBUTION

The DEM impact model can reasonably predict fragmentation, especially predict whether a rock block fragments or not in a given impact condition. However, due to the limit of current model to accurately account for the uncertainty and complexity of rock materials, it is very difficult to fully match the real fragmentation process such as fragment sizes.

We have made some improvements to our current model to more realistically reproduce the fragment size distribution by adding rolling stiffness and strength disorder to obtain better fragment size distributions. However, this will lead to a more complex model calibration because more parameters should be identified. A brief description of the improved model and some preliminary results by using the improved model are presented below.

6.5.1 Rolling Stiffness and Strength Disorder

A rolling stiffness, K_r , is introduced to resist particle rotation (Iwashita and Oda 2000):

$$K_r = aK_s r, \quad (6-6)$$

where K_s is contact shear stiffness, r is the particle radius, and a is a constant. The moment, M_r , due to a rotation vector, $\theta = (\theta_x, \theta_y, \theta_z)$, of a particle in a global reference system, is then calculated as

$$M_r = -K_r \theta = (-K_r \theta_x, -K_r \theta_y, -K_r \theta_z). \quad (6-7)$$

This rolling resistance is added to the contribution of the particle's motion equation for rotation (Equation 2-17).

A rotation angle threshold, θ_{lim} , is also used, above which the rolling resistance M_r remains constant. This is similar to a perfectly elastic-plastic behavior.

In order to describe the internal defects in rock materials, strength disorder was introduced to contact strength parameters, c , φ and T , according to Weibull distributions (Wittel et al. 2008)

$$\begin{aligned} P(c) &= \frac{k}{c_0} \left(\frac{c}{c_0} \right)^{k-1} \exp\left(-\left(\frac{c}{c_0}\right)^k\right), \\ P(\varphi) &= \frac{k}{\varphi_0} \left(\frac{\varphi}{\varphi_0} \right)^{k-1} \exp\left(-\left(\frac{\varphi}{\varphi_0}\right)^k\right), \end{aligned} \quad (6-8)$$

$$P(T) = \frac{k}{T_0} \left(\frac{T}{T_0} \right)^{k-1} \exp\left(-\left(\frac{T}{T_0}\right)^k\right).$$

Here c_0 , φ_0 and T_0 are the average values for c , φ and T , and k is the shape factor which controls the distribution shape. A larger k value gives a lower disorder.

6.5.2 Fragment Size Distribution

A normal impact was simulated by using the impact model that accounts for rolling stiffness. The number of generated fragments was 742. A two-parameter Weibull distribution as discussed in Section 3.5.4.1 was employed here to fit the size distribution of calculated fragments. Figure 6-34 shows that the normalized fragmentation mass distribution can be well represented by a two-parameter Weibull distribution, which is much better than the fragment size distribution shown in Figure 3-46. The simulated fragment size distribution curve with improved model is more uniform than the previous one. Without introducing rolling stiffness and strength disorder, it is difficult to simulate a fragmentation with several relative big fragments, which is typically observed in reality for rock fragmentation as seen also in Argyle case.

6.6 CONCLUSION

Three case studies have been performed to validate the developed impact fragmentation module in rockfall analysis. It has been demonstrated that the DEM impact model can reasonably predict impact fragmentation, especially predict whether a rock block fragments or not in a given impact condition. Due to the limit of current model to accurately account for the uncertainty and complexity of rock materials, it is not able to fully match the real fragmentation process such as fragment sizes. An improved model was then proposed by introducing rolling stiffness and strength disorders to better

simulate fragment size distributions. However, additional extensive calibration work is required.

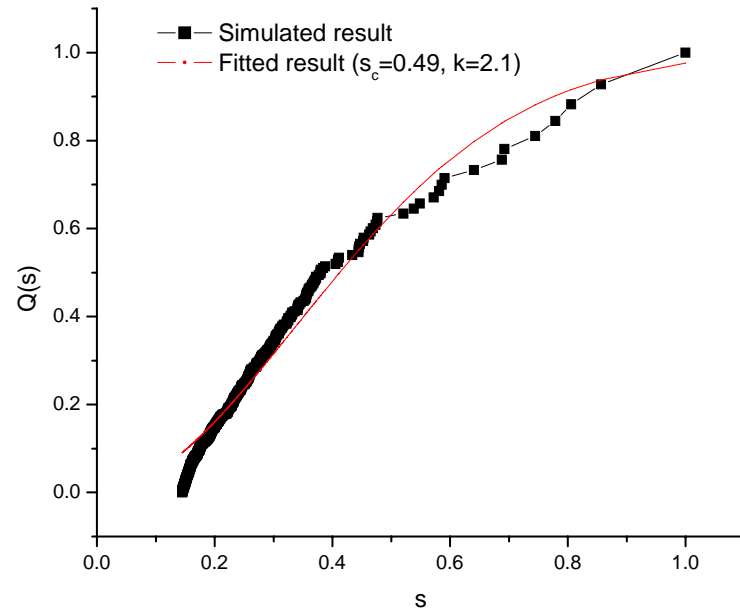


Figure 6-34. Fragmentation size distribution of simulated rock impact using improved model with rolling stiffness

CHAPTER 7 CONCLUSIONS AND RECOMMENDATIONS

7.1 OVERALL CONCLUSIONS

An impact fragmentation module was developed and integrated into HY-STONE to perform rock fall analysis by taking into account rock fragmentation upon impact and fly-rock. A discrete element model was employed to model impact fragmentation. The model was first calibrated and verified with experimental results to demonstrate the capability of modeling both quasi-static and dynamic material behavior. Some fundamental mechanisms of impact fragmentation associated with rockfalls were then investigated. The impact fragmentation module was finally developed to quickly predict the fragmentation process in rockfall analysis using either an interpolation method or a neural network model based on a simulation database.

A DEM code was developed from scratch. A radius expansion packing method was used to prepare specimens for modeling. A contact-level based constitutive model consisting of spring-dashpot systems and failure criteria was then applied to describe material's constitutive behavior. Some numerical issues such as packing structure, particle size and damping effects, and computational time were addressed.

A new membrane boundary that applies realistic fluid confining pressure was developed for modeling triaxial tests. To realistically simulate the confining pressure, the new approach applies updated boundary forces rather than a rigid-wall boundary. The applied forces only act on the boundary particles, which are identified and updated periodically. Comparisons between rigid-wall boundary and membrane boundary have shown that rigid-wall boundary can significantly alter the material response especially the material strength, and hence is not appropriate to realistically simulate confining pressures.

When three-dimensional, bonded discrete element models are deployed to model intact rock, a basic question is how to determine the micro-parameters that control macro-properties of the modeled rock. Algorithms to calibrate the model's micro-parameters against standard laboratory tests, such as uniaxial and triaxial tests, were presented. Sensitivity analyses are used to identify the deformability micro-parameters by obtaining relationships between microscopic and macroscopic deformability properties. The strength model parameters were identified by a global optimization process aimed at minimizing the difference between computed and experimental failure envelopes. When applied to the experimental results of tested granite, this calibration process produced a good agreement between simulated and experimental results for both deformability and strength properties.

Investigation on failure evolution of simulated granite was also performed in modeling triaxial tests. The monitored evolution of the number and type of contact failures (micro cracks) reveals that at micro level tensile failures occur first followed by mobilization of residual friction, and that three distinct stages of stress-strain curve can be well represented by the accumulated number of contact failures and the mode of contact failures.

After identifying the micro model parameters, dynamic compression and SHPB tests were performed to verify the dynamic model. A strain-rate-dependent dynamic strength was observed in the experimental results. Different from modeling quasi-static problems, in which a high damping was used to quickly dissipate kinetic energy, material damping was neglected by using zero damping in modeling dynamic problems. This strain-rate-dependent dynamic strength was also confirmed by the numerical results. No rate-dependent constitutive model was used in the DEM model to simulate dynamic

behavior. This simulated rate-dependent dynamic strength can be attributed to material inertia because the inertia inhibits crack growth.

The developed DEM code was coupled with a simplified impact model inspired by the theory of dynamic foundations. This approach can provide us with some valuable insights into impact induced rock fragmentation, although the real physical process is too complicated to be fully modeled. It has been shown that the magnitude of impact velocity, the angle of the incidence, the ground condition all play very important roles in impact fragmentation. The effects of fracture orientation, opening and persistence are also prominent in modeling fractured rock. The energy loss due to failure process and energy transformation in modeling impact fragmentation can be well tracked.

Because it takes relatively long time to run an impact simulation with the developed DEM code, it may be impractical to directly invoke the DEM code and run an impact simulation each time a rock block impacts the ground during a rockfall analysis. Alternatively, a large set of impact simulations, which cover different impact scenarios, have been carried out beforehand to build up a database of possible impacts. The database was used to train a neural network and to set up an interpolation module to quickly predict impact fragmentation processes in rockfall analysis. The prediction performances of trained neural network and interpolation method were evaluated and compared with each other. Both approaches can be used to approximately predict impact fragmentation. The overall performance of interpolation method is poorer than the trained neural network's.

Several studies were performed to validate the developed impact fragmentation module in rockfall analysis. It has been demonstrated that the DEM impact model can reasonably predict impact fragmentation, especially predict whether a rock block fragments or not in a given impact condition. Due to the limit of current model to

accurately account for the uncertainty and complexity of rock materials, the DEM impact model is not able to fully match the real fragmentation process such as fragment size distribution. An improved model was then proposed by introducing rolling stiffness and strength disorders to better simulate fragment size distributions. However, additional extensive calibration work is required.

7.2 RECOMMENDATIONS FOR FUTURE WORK

Although detailed work on impact fragmentation in rock fall analysis has been made in this work, our understanding to this complicated process is still limited. In order to improve our understanding of impact fragmentation in rock fall analysis, the following additional work is recommended for future work:

1. The effects of fracture orientation, aperture and persistence on impact fragmentation have been preliminarily studied. However these fracture properties have not been explicitly considered in the fragmentation module (interpolation module or neural network) because the number of parameters (and thus extent of database) would have significantly increased. It is recommended that these fracture properties be included in the development of a specific fragmentation module for given site conditions and rock properties, where the values of those parameters are fixed, and do not need to be varied in a sensitivity analysis.
2. In modeling an impact against the ground, the ground was simplified as a half-space composed of an elastic and homogeneous medium, and the ground failure was not directly accounted for. Instead, coefficients of restitution were employed to account for the energy dissipation due to ground local yielding. It is recommended that ground yielding be accounted for in modeling impact

fragmentation and correlations between coefficients of restitution and ground yielding be developed.

3. Without any improvement, the current model has some difficulties in reproducing the fragment size distribution as observed in reality. As discussed in Section 6.5, by introducing rolling stiffness the model may be improved to reproduce a realistic fragment size distribution. Once this additional feature is introduced into the DEM code, model validation should be carried out, the effect of the rolling stiffness on model behavior can be further investigated, the micro-parameter calibration algorithm should be accordingly augmented, and the database and fragmentation modules should be accordingly extended.

APPENDIX

APPENDIX A TRANSFORMATION MATRIX (ARFKEN 1985)

a) In 3D space, the transformation matrix for a rotation around a given unit vector

$\bar{v} = [x, y, z]$ by counterclockwise angle θ is defined as

$$M(\bar{v}, \theta) = \begin{bmatrix} \cos \theta + (1 - \cos \theta)x^2 & (1 - \cos \theta)xy - (\sin \theta)z & (1 - \cos \theta)xz + (\sin \theta)y \\ (1 - \cos \theta)xy + (\sin \theta)z & \cos \theta + (1 - \cos \theta)y^2 & (1 - \cos \theta)yz - (\sin \theta)x \\ (1 - \cos \theta)xz - (\sin \theta)y & (1 - \cos \theta)yz + (\sin \theta)x & \cos \theta + (1 - \cos \theta)z^2 \end{bmatrix}$$

(A.1)

b) Let (O, X, Y, Z) be a global Cartesian coordinate system. The rotations with angles θ_x, θ_y and θ_z , respectively along these axes can be defined as follows:

- Rotation along the X-axis:

$$R_x(\theta_x) = \begin{bmatrix} 1 & 0 & 0 \\ 0 & \cos \theta_x & \sin \theta_x \\ 0 & -\sin \theta_x & \cos \theta_x \end{bmatrix}$$

- Rotation along the Y-axis:

$$R_y(\theta_y) = \begin{bmatrix} \cos \theta_y & 0 & -\sin \theta_y \\ 0 & 1 & 0 \\ \sin \theta_y & 0 & \cos \theta_y \end{bmatrix}$$

- Rotation along the Z-axis:

$$R_z(\theta_z) = \begin{bmatrix} \cos \theta_z & \sin \theta_z & 0 \\ -\sin \theta_z & \cos \theta_z & 0 \\ 0 & 0 & 1 \end{bmatrix}$$

The total rotation matrix can be written

$$\text{as } M(\theta_x, \theta_y, \theta_z) = R_x(\theta_x)R_y(\theta_y)R_z(\theta_z)$$

$$M(\theta_x, \theta_y, \theta_z) = \begin{bmatrix} \cos \theta_y \cos \theta_z & \cos \theta_y \sin \theta_z & -\sin \theta_y \\ \sin \theta_x \sin \theta_y \cos \theta_z - \cos \theta_x \sin \theta_z & \sin \theta_x \sin \theta_y \sin \theta_z + \cos \theta_x \cos \theta_z & \sin \theta_x \cos \theta_y \\ \cos \theta_x \sin \theta_y \cos \theta_z + \sin \theta_x \sin \theta_z & \cos \theta_x \sin \theta_y \sin \theta_z - \sin \theta_x \cos \theta_z & \cos \theta_x \cos \theta_y \end{bmatrix} \quad (\text{A.2})$$

APPENDIX B UNIAXIAL COMPRESSIVE TEST DATA ON SANDSTONE FOR CALIFORNIA ROCKFALL TESTS

Table 7 - Summary of Unconfined Compressive Strength and Modulus Test Results

Block Number*	Block Elevation (feet)	Rock Type	Modulus (x10 ⁶ psi)	Poisson's Ratio	Unconfined Compressive Strength (ksi)	Density (pcf)
T_100	405	Sandstone	8.96	0.24	6.27	162.6
T_300	405	Sandstone	--	--	11.56	160.6
B1_150A	530	Sandstone	3.41	0.11	3.13	164.9
B1_150B	530	Sandstone	--	--	10.24	163.7
B1_375A	535	Sandstone	8.11	0.21	14.10	166.0
B1_375B	535	Sandstone	--	--	13.48	164.9
B3_100A	660	Sandstone	--	--	8.92	160.9
B3_100B	665	Sandstone	--	--	12.81	163.2
B3_A	665	Sandstone	2.5	0.15	9.20	143.9
RS_BA	940	Sandstone	3.3	0.15	4.97	152.1
RS_BB	940	Sandstone	--	--	5.30	164.0
RR_BA	860	Sandstone	3.45	0.15	7.14	158.0
RR_BB	860	Sandstone	--	--	7.87	160.8
T21_B		Sandstone	9.38	0.22	9.13	163.1

* Block Samples are shown on Plate 1

APPENDIX C RESULTS OF UNIAXIAL COMPRESSION TESTS WITH ELASTIC MODULUS AND POISSON'S RATIO MEASUREMENTS BY MEANS OF STRAIN GAUGES

SPECIMEN PARTICULARS				SPECIMEN DIMENSIONS					SPECIMEN TEST RESULTS								
Rocklab Specimen No	Sample ID	Borehole Depth	Rock Type	Diameter	Height	Ratio of Height to diameter	Mass	Density	Failure Load	Strength (UCS)	Tangent Elastic Modulus @ 50% UCS	Secant Elastic Modulus @ 50% UCS	Poisson's Ratio Tangent @ 50% UCS	Poisson's Ratio Secant @ 50% UCS	Linear Axial Strain at Failure	Failure Code	Note
3165-		m		mm	mm		g	g/cm ³	kN	MPa	GPa	GPa			mm/mm		
UCM-01	SKRS 1		Marble	62.60	175.8	2.8	576.3	1.06	214.1	69.6	68.1	63.5	0.34	0.29	0.002065	XA	
UCM-02a	SKRS 2		Marble	47.19	109.1	2.3	576.3	3.02	250.7	143.3	108.0	114.0	0.35	0.30	0.001375	1B	
UCM-02b				47.20	104.8	2.2	513.8	2.80	202.5	115.7	92.6	96.4	0.31	0.28	0.001735	3B	
UCM-02c				47.37	104.6	2.2	507.1	2.75	165.0	93.6	56.8	60.1	0.14	0.15	0.001869	XA	
UCM-03a	SKRS 3		Marble	47.34	112.3	2.4	536.7	2.72	77.8	44.2	50.5	44.3	0.27	0.20	0.001129	1B	
UCM-03b				47.48	96.9	2.0	455.9	2.66	100.1	56.5	50.9	48.2	0.30	0.22	0.001825	XA	
UCM-06a	SKRS 6		Pyritic Quartzite	47.22	116.7	2.5	573.6	2.81	129.1	73.7	57.0	61.1	0.32	0.27	0.001290	3B	
UCM-06b				47.34	115.7	2.4	558.6	2.74	192.2	109.2	65.9	68.1	0.24	0.24	0.001665	XB	
UCM-08A				47.42	101.9	2.1	486.1	2.70	185.8	105.2	40.4	41.0	0.33	0.25	0.002615	XB	
UCM-08B	SKRS 8		Skarn	47.52	90.9	1.9	475.5	2.95	91.5	51.6	70.6	69.9	0.56	0.35	0.000705	0B	

References

- Agliardi, F., and Crosta, G. (2003). "High resolution three-dimensional numerical modelling of rockfalls." *International Journal of Rock Mechanics and Mining Sciences*, 40, 455-471.
- An, B. (2006). "A study of energy loss during rock impact using PFC2D," M.Sc., University of Alberta (Canada), Canada.
- An, B., and Tannant, D. (2007). "Discrete element method contact model for dynamic simulation of inelastic rock impact." *Computers & Geosciences*, 33(4), 513-521.
- Arfken, G. (1985). "Mathematical Methods for Physicists, 3rd ed." *Orlando, FL: Academic Press*.
- ASTM. (2007). "Designation: D 4543, Standard Practices for Preparing Rock Core as Cylindrical Test Specimens and Verifying Conformance to Dimensional and Shape Tolerances." *ASTM*.
- Åström, J. A., Linna, R. P., Timonen, J., Moller, P. F., and Oddershede, L. (2004). "Exponential and power-law mass distributions in brittle fragmentation." *Physical Review E*, 70(2), 026104.
- Behera B, K. F., McNamara S, Herrmann HJ. (2005). "Fragmentation of a circular disc by impact on a frictionless plate." *J Phys-Condens Mater*, 17, S2439–S2456.
- Bozzolo, D., and Pamini, R. (1986). "Simulation of rock falls down a valley side." *Acta Mechanica*, 63(1), 113-130.
- Chau K.T., W. S. Z., Zhu W.C., Tang C.A., Yu T.X. . (2003). "Dynamic fracture and fragmentation of spheres." In: *16th ASCE Engineering Mechanics Conference*, University of Washington, Seattle.
- Cheong, Y. S., Reynolds, G. K., Salman, A. D., and Hounslow, M. J. (2004). "Modelling fragment size distribution using two-parameter Weibull equation." *International Journal of Mineral Processing*, 74(Supplement 1), S227-S237.

- Cho, N., Martin, C. D., and Sego, D. C. (2007). "A clumped particle model for rock." *International Journal of Rock Mechanics and Mining Sciences*, 44(7), 997-1010.
- Cook, B., Lee, M., DiGiovanni, A., Bronowski, D., Perkins, E., Williams, J. (2004). "Discrete Element Modeling Applied to Laboratory Simulation of Near-Wellbore Mechanics." *International Journal of Geomechanics*, 4(1), 19-27.
- Cooreman, S., Lecompte, D., Sol, H., Vantomme, J., and Debruyne, D. (2007). "Elasto-plastic material parameter identification by inverse methods: Calculation of the sensitivity matrix." *International Journal of Solids and Structures*, 44(13), 4329-4341.
- Crosta, G., Agliardi, F. . (2003). "A methodology for physically based rockfall hazard assessment." *Natural Hazard and Earth Systems Science*, 3, 407-422.
- Cundall, P. A. (1971). "A computer model for simulating progressive large scale movements in blocky rock systems." *In: Proceedings of the Symposium of International Society of Rock Mechanics, Nancy: France*, 1, Paper No. II-8.
- Cundall, P. A. (1988). "Formulation of a three-dimensional distinct element model--Part I. A scheme to detect and represent contacts in a system composed of many polyhedral blocks." *International Journal of Rock Mechanics and Mining Science & Geomechanics Abstracts*, 25(3), 107-116.
- Cundall, P. A., and Hart, R. (1992). "Numerical modeling of discontinua." *J. Engr. Comp*, 9, 101-113.
- Cundall, P. A., and Strack, O. D. L. (1979). "A Discrete Element Model for Gralular Assemblies." *Geotechnique*, 29(1), 47-65.
- D'Addetta, G. A., Kun, F., Ramm, E., and Herrmann, H. J. (2001). "From solids to granulates - Discrete element simulations of fracture and fragmentation processes in geomaterials. ." *Lecture Notes in Physics*, Volume 568, 231.
- Donze, F. V., Bouchez, J., and Magnier, S. A. (1997). "Modeling fractures in rock blasting." *International Journal of Rock Mechanics and Mining Sciences*, 34(8), 1153-1163.
- Dorren, L. K. A. (2003). "A review of rockfall mechanics and modelling approaches." *Progress in Physical Geography*, 27(1), 69-87

- Fakhimi, A., and Villegas, T. (2007). "Application of Dimensional Analysis in Calibration of a Discrete Element Model for Rock Deformation and Fracture " *Rock Mechanics and Rock Engineering*, 40(2), 193-211.
- Ferrez, J. A., and Liebling, T. M. (2001). "Parallel DEM Simulations of Granular Materials " *Lecture Notes in Computer Science (book chapt)*, High-Performance Computing and Networking, 211-220.
- Fraige, F. Y., and Langston, P. A. (2004). "Integration schemes and damping algorithms in distinct element models " *Advanced Powder Technology*, 15(2), 227-245.
- Frew, D., Forrestal, M., and Chen, W. (2001). "A split Hopkinson pressure bar technique to determine compressive stress-strain data for rock materials." *Experimental Mechanics*, 41(1), 40-46.
- Frew, D., Forrestal, M., and Chen, W. (2002). "Pulse shaping techniques for testing brittle materials with a split hopkinson pressure bar." *Experimental Mechanics*, 42(1), 93-106.
- Giacomini, A., Buzzi, O., Renard, B., and Giani, G. P. "Experimental studies on fragmentation of rock falls on impact with rock surfaces." *International Journal of Rock Mechanics and Mining Sciences*, In Press, Corrected Proof.
- Giani, G. P., Giacomini, A., Migliazza, M., and Segalini, A. (2004). "Experimental and Theoretical Studies to Improve Rock Fall Analysis and Protection Work Design." *Rock Mechanics and Rock Engineering*, 37(5), 369-389.
- Grady, D. E. (2008). "Fragment size distributions from the dynamic fragmentation of brittle solids." *International Journal of Impact Engineering*, 35(12), 1557-1562.
- Grady, D. E., and Kipp, M. E. (1980). "Continuum modelling of explosive fracture in oil shale." *International Journal of Rock Mechanics and Mining Sciences & Geomechanics Abstracts*, 17(3), 147-157.
- Guzzetti, F., Crosta, G., Detti, R., and Agliardi, F. (2002). "STONE: a computer program for the three-dimensional simulation of rock-falls." *Computers & Geosciences*, 28(9), 1079-1093.

- Hajiabdolmajid, V., Kaiser, P. K., and Martin, C. D. (2002). "Modelling brittle failure of rock." *International Journal of Rock Mechanics and Mining Sciences*, 39(6), 731-741.
- Hebb, D. O. (1949). *The organization of Behavior*, John Wiley and Sons, New York, NY.
- Hecht-Nielsen, R. (Year). "Kolmogorov's mapping neural network existence theorem." *Proceedings of the first IEEE international conference on neural networks*, San Diego CA, USA, 11-14.
- Henty, D. S. (2000). "Performance of hybrid message-passing and shared-memory parallelism for discrete element modeling." In: *Proceedings of the 2000 ACM/IEEE conference on Supercomputing (CDROM)*, IEEE Computer Society, Dallas, Texas, United States.
- Hentz, S., Daudeville, L., and Donze, F. (2004a). "Identification and Validation of a Discrete Element Model for Concrete." *Journal of Engineering Mechanics*, 130(6), 709-719.
- Hentz, S., Donze, F. V., and Daudeville, L. (2004b). "Discrete element modelling of concrete submitted to dynamic loading at high strain rates." *Computers & Structures*, 82(29-30), 2509-2524.
- Hoek, E. (1983). "Strength of jointed rock masses." *Géotechnique*, 23(3), 187-223.
- Hoek, E., and Brown, E. T. (1997). "Practical estimates of rock mass strength." *International Journal of Rock Mechanics and Mining Sciences*, 34(8), 1165-1186.
- Hoek, E., and Diederichs, M. S. (2006). "Empirical estimation of rock mass modulus." *International Journal of Rock Mechanics and Mining Sciences*, 43(2), 203-215.
- Howard, D., Mark, B., and Martin, H. (2007). *MATLAB Neural Network Toolbox 6 User's Guide*, The MathWorks.
- Itasca. (1999). "PFC3D Manual, 1st Edition."
- Iwashita, K., and Oda, M. (2000). "Micro-deformation mechanism of shear banding process based on modified distinct element method." *Powder Technology*, 192-205, 192-205.

- J. G. Cai, J. Z., J. A. Hudson. (1998). "Computerization of Rock Engineering Systems Using Neural Networks with an Expert System " *Rock Mechanics and Rock Engineering*, 31(3), 135-152.
- Jensen, R. P., Bosscher, P. J., Plesha, M. E., and Edil, T. B. (1999). "DEM simulation of granular media - structure interface: effects of surface roughness and particle shape." *International Journal for Numerical and Analytical Methods in Geomechanics*, 23(6), 531-547.
- Jodrey, W. S. (1985). "Computer simulation of close random packing of equal spheres." *Physical Review A*, 32(4), 2347- 2351.
- Judd, K. L. (1998). *Numerical methods in Economics*, MIT Press, Cambridge, Mass.
- Kenneth, C. J. (2006). "Multidimensional Interpolation Methods." <http://software.kjinnovation.com/InterpMethods.pdf>.
- Kuhn, M. R. (1995). "A flexible boundary for three-dimensional dem particle assemblies." *Engineering Computations*, 12(2).
- Lamb, H. (1903 - 1904). "On the Propagation of Tremors over the Surface of an Elastic Solid." *Proceedings of the Royal Society of London*, 72, 128-130.
- Lankford, J. (1980). "Mechanisms Responsible for Strain-rate-dependent Compressive Strength in Ceramic Materials." *Communications of the American Ceramic Society*, c-33.
- Lankford, J. (1982). "Inertia as a Factor of Dynamic Strength of Brittle Materials." *Communications of the American Ceramic Society*, C-122.
- Lequang, A., and Junichi, K. (2003). *Deformation Characteristics of Geomaterials*, Lyon, France.
- Liao, C., Chang, T., Young, D., Chang, C. (1997). "Stress-strain relationship for granular materials based on the hypothesis of best fit." *International Journal of Solids and Structures*, 34(31-32), 4087-4100.
- Lu, C., Danzer, R., and Fischer, F. D. (2002). "Fracture statistics of brittle materials: Weibull or normal distribution." *Physical Review E*, 65(6), 067102.

- McCulloch, W. S. a. P., W. H. (1943). "A logical calculus of the ideas immanent in nervous activity." *Bulletin of Mathematical Biophysics*, 5(115-133).
- Mott, N. F. (Year). "Fragmentation of Shell Cases " *Proceedings of the Royal Society of London. Series A, Mathematical and Physical Sciences*.
- Mougin, J.-P., Perrotin, P., Mommessin, M., Tonnelo, J., and Agbossou, A. (2005). "Rock fall impact on reinforced concrete slab: an experimental approach." *International Journal of Impact Engineering*, 31(2), 169-183.
- Neumaier, W. H. a. A. (2008). "Snobfit - Stable Noisy Optimization by Branch and Fit." *ACM Trans. Math.*(Software 35), Article 9.
- Ng, T.-T. (2006). "Input Parameters of Discrete Element Methods." *Journal of Engineering Mechanics*, 132(7), 723-729.
- Nocilla, N., Evangelista, A., and Scotto di Santolo, A. (2008). "Fragmentation during Rock Falls: Two Italian Case Studies of Hard and Soft Rocks." *Rock Mechanics and Rock Engineering*.
- O'Sullivan, C., and Bray, J. D. (2004). "Selecting a suitable time step for discrete element simulations that use the central difference time integration scheme." *Engineering Computations*, 21(2/3/4), 278 - 303
- Olson, J. E., Narayanasamy, R., Holder, J., Rauch, A., and Camacho, B. (2002). "DEM Study Of Wave Propagation In Weak Sandstone." In: *Third International Conference on Discrete Element Methods*, Santa Fe, NM.
- Onate, E., and Rojek, J. (2004). "Combination of discrete element and finite element methods for dynamic analysis of geomechanics problems." *Computer Methods in Applied Mechanics and Engineering*, 193(27-29), 3087-3128.
- Oreskes, N., Shrader-Frechette, K., and Belitz, K. (1994). "Verification, Validation, and Confirmation of Numerical Models in the Earth Sciences " *Science*, 263(5147), 641-646.
- Park, J., and Kausel, E. (2004). "Impulse Response of Elastic Half-Space in the Wave Number--Time Domain." *Journal of Engineering Mechanics*, 130(10), 1211-1222.

- Pierce, M., Cundall, P., and Potyondy, D. (Year). "A synthetic rock mass model for jointed rock." *Rock mechanics : meeting society's challenges and demands : proceedings of the 1st Canada-US Rock Mechanics Symposium*, Vancouver, B.C., 341-349.
- Potyondy, D. O., and Cundall, P. A. (2004). "A bonded-particle model for rock." *International Journal of Rock Mechanics and Mining Sciences*, 41(8), 1329-1364.
- Richart, F. E., Hall, J. R., and Woods, R. D. (1970). "Vibrations of Soils and Foundations" *Englewood Cliffs, N.J., Prentice-Hall*
- Rosenblatt, F. (1962). *Principles of Neurodynamics*, sPARTAN, New York, NY.
- Schalkoff, R. (1997). *Artificial neural network*, New York: McGraw-Hill.
- Sidarta, D. E. (2000). "Neural network-based constitutive modeling of granular material," Ph.D., University of Illinois at Urbana-Champaign, United States -- Illinois.
- Sonmez, H., Gokceoglu, C., Nefeslioglu, H. A., and Kayabasi, A. (2006). "Estimation of rock modulus: For intact rocks with an artificial neural network and for rock masses with a new empirical equation." *International Journal of Rock Mechanics and Mining Sciences*, 43(2), 224-235.
- Wang, Y., and Tonon, F. (2008). "Calibration of a Discrete Element Model for Intact Rock." *International Journal for Numerical and Analytical Methods in Geomechanics*, (Accepted).
- Wang, Y., and Tonon, F. (2009a). "Calibration of a Discrete Element Model for Intact Rock." *International Journal for Numerical and Analytical Methods in Geomechanics*, (Accepted).
- Wang, Y., and Tonon, F. (2009b). "Modeling Lac du Bonnet Granite Using a Discrete Element Model " *International Journal of Rock Mechanics and Mining Sciences* In press.
- Werbos, P. (1974). "Beyond Regression: New Tools for Prediction and Analysis in the Behavior Sciences," Harvard University, Cambridge, MA.

- Whittles, D. N., Kingman, S., Lowndes, I., and Jackson, K. (2006). "Laboratory and numerical investigation into the characteristics of rock fragmentation." *Minerals Engineering*, 19(14), 1418-1429.
- Wittel, F., Carmona, H., Kun, F., and Herrmann, H. (2008). "Mechanisms in impact fragmentation." *International Journal of Fracture*, 154(1), 105-117.
- Yoon, J. (2007). "Application of experimental design and optimization to PFC model calibration in uniaxial compression simulation." *International Journal of Rock Mechanics and Mining Sciences*, 44(6), 871-889.
- Zhang, R., and Sture, S. (1996). "Flexible Boundary for Discrete Element Simulation of Granular Assemblies." In: *11th ASCE Engineering Mechanics Conference* ASCE, Ft. Lauderdale, Florida.
- Zhang, Z. X., Kou, S. Q., Jiang, L. G., and Lindqvist, P. A. (2000). "Effects of loading rate on rock fracture: fracture characteristics and energy partitioning." *International Journal of Rock Mechanics and Mining Sciences*, 37(5), 745-762.
- Zhao, H. (2003). "Material behaviour characterisation using SHPB techniques, tests and simulations." *Computers & Structures*, 81(12), 1301-1310.
- Zhao, J., Li, H. B., Wu, M. B., and Li, T. J. (1999). "Dynamic uniaxial compression tests on a granite." *International Journal of Rock Mechanics and Mining Sciences*, 36(2), 273-277.

VITAE

Yuannian Wang was born in a small village called “Spring-Autumn” in Shucheng, Anhui, China, on December 4, 1975 as the 3rd son of Yeliu Wang and Daoshu Li. He spent most of his childhood time farming and playing in the fields and hills. He started his Bachelor’s of Science degree in 1994 in Mining Engineering at Shandong Institute of Mining and Technology. In 1998, immediately after receiving his bachelor’s degree, he worked for a coal mine as a mining engineer. After two years of working, he started his Master of Science’s degree in Solid Mechanics at Institute of Mechanics, Chinese Academy of Sciences. After his receiving his first master degree in 2003, he spent one more year working as a research engineer at Institute of Mechanics, Chinese Academy of Sciences. In 2004, he came to United State and started his research and study in Geotechnical Engineering at Wayne State University and received his master degree in 2004. In the same year, he started his doctoral study at The University of Texas at Austin in the Department of Civil, Architectural and Environmental Engineering under supervision of Dr. Fulvio Tonon. He specialized in computational geomechanics and underground engineering.

Permanent address: Shucheng, Chunqiuxiang Chunqiucun Chengdazhuang, Anhui, China 231337

The dissertation was typed by the author.